UNIVERSITÉ DE GRENOBLE

THÈSE

Pour obtenir le grade de

DOCTEUR DE L'UNIVERSITÉ DE GRENOBLE

Spécialité : **Mécanique des fluides, Énergétique, Procédés**

Arrêté ministériel : 7 août 2006

Présentée par

Kunkun TANG

Thèse dirigée par **Christophe CORRE**
et codirigée par **Alberto BECCANTINI**

préparée au sein du **Laboratoire des Applications en Thermohydraulique et Mécanique des Fluides, CEA Saclay**
dans **l'École Doctorale I-MEP2 – Ingénierie – Matériaux, Mécanique, Environnement, Énergétique, Procédé, Production**

Combining Discrete Equations Method and Upwind Downwind-Controlled Splitting for Non-Reacting and Reacting Two-Fluid Computations

Thèse soutenue publiquement le **14 décembre 2012**,
devant le jury composé de :

M. Frédéric LAGOUTIÈRE
Professeur, Université Paris-Sud (Paris XI), Président
M. Rémi ABGRALL
Professeur, Université Bordeaux I, Rapporteur
M. Eleuterio F. TORO
Professeur, University of Trento – Italy, Rapporteur
M. Éric GONCALVES
Maître de Conférences – HDR, Grenoble INP – ENSE3, Examinateur
M. Christophe CORRE
Professeur, Grenoble INP – ENSE3, Directeur de thèse
M. Alberto BECCANTINI
Ingénieur de recherche, CEA Saclay, Co-Directeur de thèse

Contents

List of Tables

List of Figures

Introduction

Computational Fluid Dynamics (CFD) is widely used today in industrial applications in general and in nuclear engineering in particular where it complements experiments in a crucial way (*e.g.* [Yadigaroglu 05, Bestion 11]). When investigating more specifically the safety issues involved in nuclear reactor containment, the use of CFD often implies the capability of dealing with geometries which are large with respect to the characteristic dimensions of the physical phenomena. Such situations arise when computing the pressure loads generated by a hydrogen-air combustion occurring in a nuclear reactor containment during a postulated Loss of Coolant Accident. The free volume of the European Pressurized Reactor building is about 75000 m^3 while the characteristic physical lengths of the combustion flame are much smaller: the reaction zone in a laminar deflagration at atmospheric condition can vary from about 1 mm to 10 mm; consequently, the “Direct Numerical Simulation (DNS)” of flame propagation and deflagration-to-detonation transition (DDT) in such a large-scale geometry would require a discretization mesh with a prohibitively large number of elements. Alternatively, with the purpose of performing computationally efficient simulations, DNS can be avoided by considering the flame as an infinitely thin interface (sharp interface) and by modeling the (thermal and species) diffusion effects through phenomenological laws for the flame speed (see for instance [Efimenko 01]). The combustion-induced pressure loads can then be correctly predicted provided the flame speed is correctly estimated. This pressure loads prediction is of great importance from the viewpoint of the investigation of its impact on the containment structure.

Numerical context: Reactive Discrete Equations Method for interface propagation

In [Efimenko 01], a combustion algorithm called CREBCOM is proposed to study fast deflagrations and detonations in large geometries. In this algorithm the species diffusion and the thermal diffusivity are neglected and replaced by the introduction of a burning rate constant, which has the dimension of speed and plays the same role as the fundamental flame speed. The CREBCOM algorithm is very simple to be implemented in a CFD code: it resolves the non-reactive Euler equations, and the reactive contribution is added by simply introducing a source term. It has been successfully implemented in several industrial purpose CFD codes, such as TONUS [Kudriakov 07] and COM3D [Bielert 01], to investigate turbulent combustion flows. The main drawback of the CREBCOM algorithm is that it involves a binary criterion function that specifies whether the control volume is burnt or not. Numerical experiments [García 10] have shown that this criterion function can create numerical pressure oscillations which strongly affect the flow when the flame speed is low with respect to the sound speed (low Mach number regime).

When looking for a combustion model which retains the simplicity of CREBCOM (no flame surface reconstruction) while not involving a combustion criterion, the Reactive Discrete Equations Method (RDEM) appears as an attractive strategy. Initially proposed in [Le Métayer 05] to compute evaporation fronts and Chapman-Jouguet detonation waves, the RDEM method extends to the reactive Euler equations the Discrete Equations Method (DEM) previously introduced in [Abgrall 03] for two-phase physical or numerical mixtures and interface problems. Let us mention at this stage non-reacting flows will also be studied is in this work, as a preliminary step for the developed numerical strategies. Within the framework of our targeted applications, namely both reactive and non-reactive cases, the main properties and advantageous features of the DEM/RDEM method can be listed as follows:

- The DEM/RDEM method is a numerical strategy which aims at discretizing the full two-fluid model of two-phase flows [Delhaye 68, Ishii 75, Drew 98]. Two pressures and two velocities are essentially needed in this work, since the pressure and velocity jump across a reactive discontinuity is not negligible. Because of this, reduced two-fluid models with a single pressure and/or a single velocity, *e.g.* [Kapila 01, Murrone 05, Kokh 10, Chang 07], are not suitable for large-scale combustion simulations.

- A Riemann solver for the full two-fluid model (see for instance [Tokareva 10]) is not needed. The DEM/RDEM approach consists essentially in the integration of one-fluid and two-fluid interface problem solutions over a two-phase control volume where the solutions can be provided by Riemann solvers for Euler equations. Let us emphasize that the purpose of this work is not looking for accurate, robust and/or efficient Riemann solvers. Instead, the exact available Riemann solver for non-reacting problems [Toro 97] will be used when dealing with non-reacting flows. Alternatively, any suitable approximate Riemann solver can also be considered. A quasi exact reactive Riemann solver is employed for combustion problems [Beccantini 10a]. However, there are no approximate reactive Riemann solvers available today in the literature which do not involve Newton type iterations.

- The DEM/RDEM method can be regarded as the extension of the Godunov's method [Godunov 59] in the case of two-phase problems. The single phase limit is recovered when dealing with the same fluids. On the other hand, when considering two-phase problems in which the gradient of the phase volume fractions vanishes, the DEM/RDEM approach reduces to the Godunov's method for each individual phase. In fact, no phase interaction is taken into account in DEM/RDEM in this case.

- The same equations are solved in each computational cell for both phases. No specific interface capturing treatment is needed. The difficult physical modeling of the interface conditions, *i.e.* the non-conservative terms in the two-fluid model, is avoided by considering two-phase or reactive Riemann problem solutions. This idea is also of paramount importance in the computation of these non-conservative terms in the two-fluid model. Indeed, these terms can be easily discretized as a flux moving with the numerical interface velocity already obtained via the Riemann problem solution. A Lagrangian type concept is thus used to define the moving flux; note however this Lagrangian technique is not linked to the moving mesh. In this sense, the DEM/RDEM is an Eulerian approach. It can be furthermore extended as an Arbitrary Lagrangian-Eulerian approach without difficulty.

- When computing two-phase mixture or interface problems, it is well known that the global averaging of a variable in a control cell would lead to unacceptable numerical errors [Abgrall 96, Abgrall 01]. DEM studies the two-phase problems by separately solving the two phases. Thus, both flow conservative variables and thermodynamic properties are considered separately. This property is essential because it implies that numerical mixing errors are no longer involved in the computational process. It follows that any equation of state (EOS) can be employed without producing a non-physical oscillation, even when the fluids have vastly different thermodynamic closures.

- Regarding the reacting case, a reactive Riemann solver has been proposed in [Beccantini 10a] for thermally perfect gases and used to design an “all shock” approximate Riemann solver which is eventually combined with the RDEM approach to successfully compute high speed combustion waves. The resolution of the reactive Riemann problem between burnt and unburnt gases is a key ingredient in the RDEM approach, which yields a correct flame speed after imposing the fundamental flame speed, while the global averaging of variables would lead to significant errors in terms of flame speeds.

- An additional interesting feature of RDEM for computing combustion problems is that it does not require any flame surface reconstruction and can be used for both deflagration and denotation in their full combustion regimes.

- DEM/RDEM is fully conservative, which means that total mass, momentum and energy are conserved in a closed and isolated system. This property is fundamental for long-term simulations, for instance when computing the combustion in large geometry if the Adiabatic Isochoric Complete Combustion (AICC) state is to be recovered at the end of the combustion process. The enforcement of conservation is in fact one of the main reasons why some non-conservative approaches, such as ghost fluid type methods (*e.g.* [Farhat 08]), are not retained for our applications even though they can be computationally simpler.

In spite of the above lengthy list of advantages, some drawbacks of the DEM/RDEM approach must nonetheless be mentioned. First of all, the DEM/RDEM approach appears as rather complex from an algorithmic viewpoint, since it involves two complete phases plus their interactions. Secondly, even though the exact Riemann solver can be replaced by more efficient approximate solvers for non-reacting problems, the need to solve an expensive reactive Riemann problem between the burnt and unburnt regions cannot be avoided. Another current drawback lies in the computation of the interface evolution velocity in the multi-dimensional case [Beccantini 10a, Tang 12]. The approximate direction and/or speed of interface velocity resulting from the DEM/RDEM approach is not always correct in the case of reacting problems where a mass flux takes place across the discontinuity.

Keeping in mind the large scale of the geometry in the targeted applications, the use of rather coarse meshes is hardly avoidable. The preliminary numerical results obtained in [Beccantini 10a] with a first-order version of the RDEM approach do not yield a sufficient accuracy of the flame profile, especially for fast deflagration and denotation configuration. Following the initial proposal made in [Abgrall 03], a limited second-order semi-discrete approach could be used. In such an approach, internal Riemann problems are required to be resolved at the interface diffusion zone. The present thesis work builds on these existing numerical strategies to further improve the reactive interface accuracy and better predict in consequence the pressure loads exerted on a containment. The further accuracy improvement is achieved through the use of the downwind-controlled (anti-diffusive) method initially proposed in [Lagoutière 00, Després 02]; this specific contribution of the present work is now briefly reviewed.

Thesis contribution: Upwind downwind-controlled splitting for high resolution of interfaces

The downwind-controlled method [Lagoutière 00, Després 02, Kokh 10] has been designed for computing impermeable fronts and yields exact interfaces capturing in one-dimensional case. This downwind-controlled (anti-diffusive) reconstruction method was coupled with the RDEM approach in the hope of improving accuracy and compared with the second-order approach. The downwind-controlled method coupled with the RDEM approach was found to be very accurate for computing detonation fronts but unstable for deflagration fronts [Beccantini 10b]. In order to better understand the coupling between the RDEM approach and the downwind-controlled method for combustion simulation, it was decided to investigate in detail the impermeable interface problems (non-reacting flows) using DEM and the downwind-controlled method. The computation of liquid-gas flows, where each phase is described by the stiffened gas equation of state (SG-EOS), led to the development of an original upwind downwind-controlled splitting (UDCS) method with attractive accuracy, robustness and efficiency properties when coupled with the DEM approach; this UDCS strategy was also successfully inserted into RDEM. Some key features of this original approach are:

- If combined with a second-order TVD limiter, the UDCS is equivalent to the conventional second-order reconstruction method when applied to the scalar linear advection equation.
- The UDCS anti-diffusive approach is equivalent to the original downwind- controlled method when applied to the scalar linear advection problem.
- The extension of UDCS in multi-dimensional cases with unstructured grids is feasible (and has been performed).
- When combined with DEM/RDEM method, the UDCS provides numerical stability properties which are similar to those of a first-order upwind method.
- Less diffused fronts also leads to a reduced number of (expensive) reactive Riemann problems to solve. This makes the UDCS anti-diffusive approach computationally more efficient than an upwind method.
- The improvement brought by the UDCS with respect to [Kokh 10] where an anti-diffusive numerical scheme is introduced for the simulation of interfaces between compressible fluids lies in the capability of the newly developed method

to solve both non-reacting and reacting flows, including flame fronts at all combustion regimes, on general multi-dimensional unstructured meshes.

This newly developed strategy of UDCS has been implemented in the fast dynamic fluid-structure interaction code EUROPLEXUS (developed by CEA and Joint Research Centre (JRC)), with the aim of performing reliable nuclear safety investigations.

Outline

The thesis is devoted to the description of the newly proposed numerical strategy upwind downwind-controlled splitting, for both non-reacting and reacting flows, and is organized as follows:

- Chapter 1 briefly reviews the physical modeling ingredients involved in the study, such as the equations of state, the phase characteristic function (also the volume fraction) and the balance equations governing the evolution of sharp interfaces (between liquid/gas phases for non-reacting flows, and between unburnt/burnt gas mixtures for reacting flows).
- Chapter 2 describes in detail the (Reactive) Discrete Equations Method applied to the two-fluid model of two-phase flow, particularly its first-order and standard second-order versions together with their numerical results for both non-reactive and reactive interfaces.
- Chapter 3 introduces the proposed upwind downwind-controlled splitting approach for an accurate and robust computation of the interface. In particular, the extension of UDCS anti-diffusive method in multiple space dimensions for irregular unstructured meshes is given.
- Numerical results obtained by combining DEM/RDEM with UDCS are displayed and analyzed in Chapter 4 for one-dimensional test problems and in Chapter 5 for two-dimensional cases.
- Conclusions are eventually drawn and some perspectives are outlined.

Chapter 1

Physical modeling by two-fluid model

When considering the physical modeling of the applications targeted in this work, the full two-fluid model [Delhaye 68, Ishii 75, Drew 98] resolved by the DEM/RDEM method in [Abgrall 03, Le Métayer 05] seems particularly appropriate. It involves two sets of one-phase balance equations (one for each phase), which implies the use of two distinct pressures and velocities. This property is important when computing with the DEM/RDEM approach the reactive interfaces across which the jumps of pressure, velocity and density are in general significant [Beccantini 10a]. In fact, reduced models resulting from mechanical equilibrium [Kapila 01, Murrone 05, Kokh 10] are not suitable for reacting flow unless additional mass transfer is modeled, such as in [Saurel 08], which implies an added complexity of modeling and computation. Meanwhile, it is straightforward for the DEM/RDEM approach, once the fundamental flame speed is imposed, to deal with the mass transfer phenomenon which is in fact included in the reactive Riemann solver. At the same time, two pressures and two velocities do not introduce additional difficulties, since they are also easily handled within the Riemann solver.

In this chapter, the baseline two-fluid model for the DEM/RDEM approach is briefly reviewed. Some newly developed numerical methods will be subsequently applied to this starting point. The rigorous mathematical features (derivations and properties) of the two-fluid model are not of concern here and we rather refer to [Drew 98] for these issues. Alternative approaches are available either from other types of averaging procedures [Ishii 75, Nigmatulin 79, Buyevich 71] or from continuum mechanics.

The main ingredients of the one-phase flow modeling, such as the governing equations and their thermodynamic closures, are first recalled in Section 1.1 and 1.2 respectively.

The phase characteristic function and related topics, such as the volume fraction and the topological equation, are next presented in Section 1.3 with the purpose of linking the two phases together. Finally, the two-fluid balance equations are introduced in Section 1.4, followed by the interface jump conditions described in Section 1.5. The particular case of non-reacting flow without mass transfer is discussed in Section 1.6.

1.1 Conservation equations

The two-fluid model for two-phase flow already mentioned above considers each phase separately and thus includes two sets of conservation equations. From a distribution viewpoint, a local fluid particle is either inside phase Σ_1 or phase Σ_2. It follows that its local behavior is governed by single phase balance equations. Neglecting the body force, the fluid viscosity and any heat transfer phenomena, the exact equations of motion, valid inside each phase locally, are the Euler equations of gas dynamics:

$$\begin{aligned}
&\frac{\partial \rho}{\partial t} + \nabla \cdot (\rho \mathbf{v}) = 0,\\
&\frac{\partial (\rho \mathbf{v})}{\partial t} + \nabla \cdot (\rho \mathbf{v}\mathbf{v}) + \nabla p = 0,\\
&\frac{\partial (\rho e^t)}{\partial t} + \nabla \cdot \left(\rho e^t \mathbf{v}\right) + \nabla \cdot (p\mathbf{v}) = 0.
\end{aligned} \tag{1.1}$$

where ρ is the density of the phase under study, $\mathbf{v}$ its velocity field, p its pressure, e^t its total energy containing the kinetic energy $\frac{1}{2}|\mathbf{v}|^2$, the internal energy e and the enthalpy of formation h_0 useful in the case of reactions.

We emphasize that the Euler equations (1.1) are also valid from a macroscopic point of view. The involved variables are therefore the global ones. Specifically when considering interface problems, since no physical mixture is considered, it is assumed in this work that the macroscopic individual phase variables can be evaluated by the local values.

1.2 Thermodynamic considerations

The reacting or non-reacting flow problems considered in this work are described by the two-fluid model which involves two phases with their own thermodynamic variables. A physical mixture is not involved in the modeling of the interface problems investigated in this study, but a numerical mixture is unavoidable from a numerical viewpoint. However, as will be detailed in Chapter 2, it is not necessary to define the mixture EOS within the numerical mixture when using the two-fluid model along with the Discrete Equations Method (DEM). Thus, the EOS involved in present work are only related to each single phase.

Any suitable EOS can be employed to represent gases and liquids in the framework of DEM approach. For the sake of simplicity, we restrict our attention to single component gases and use a stiffened gas EOS (SG-EOS) for the computation of non-reacting problems. Compressible liquids and polytropic gases can be described using SG-EOS. The reactive Riemann solver introduced in [Beccantini 10a] is developed for thermally perfect gases where the specific heats can vary with respect to the temperature. The same assumptions will be retained in the present study when investigating reacting flows.

1.2.1 Stiffened gas EOS (SG-EOS) for non-reacting flow

A popular EOS for describing in a unified way a liquid and a gaseous phase is the stiffened gas EOS [Harlow 71]:

$$p(\rho, e) = (\gamma - 1)\rho e - \gamma p_\infty, \tag{1.2}$$

where ρ is the density, p is the pressure, and e is the specific internal energy (we do not take account of the enthalpy of formation for the non-reacting case). The polytropic constant γ and pressure constant p_∞ are fluid-dependent. Values for these two constants can be found in [Lennon 94, Le Métayer 03] for several different liquids. For water, typical values retained in the present work are $\gamma = 4.4$ and $p_\infty = 6 \times 10^8$. The gases considered in this work for the study of two-phase flow without phase change are governed by the polytropic gas EOS that can be obtained by setting $p_\infty = 0$ in SG-EOS (1.2) (note that $1 < \gamma < 2$ for the polytropic gas).

Speed of sound for SG-EOS

The sound speed in media governed by SG-EOS is given by:

$$c^2 = \left(\frac{\partial p}{\partial \rho}\right)_s = \frac{\gamma(p + p_\infty)}{\rho}. \tag{1.3}$$

It is implied from (1.3) that, from mathematical point of view, there should be

$$p > -p_\infty. \tag{1.4}$$

Note that negative pressure p can thus arise for liquids, for instance when strong rarefaction waves occur, which can create serious numerical difficulties. No specific treatment concerning negative pressure is done in this work since system (1.1) remains hyperbolic and mathematically well-posed as long as the square of sound speed c^2 remains positive. Alternatively, [Le Métayer 05] proposes an evaporation solver for (1.2) in which liquid is transformed into vapor or liquid-vapor mixture when its pressure is inferior to the saturated one.

Other relationships for SG-EOS

Applying the Maxwell relations of thermodynamics for a single component system in equilibrium governed by SG-EOS leads to the following thermal EOS [Le Métayer 03, Le Métayer 05],

$$p(\rho, T) = (\gamma - 1)\rho c_v T - p_\infty, \tag{1.5}$$

where the specific heat at constant volume c_v is assumed constant and has been defined by

$$c_v = \left(\frac{\partial e}{\partial T}\right)_\tau, \tag{1.6}$$

with τ the specific volume. The following relations can be furthermore obtained:

$$e(p, T) = \frac{p + \gamma p_\infty}{p + p_\infty} c_v T, \tag{1.7}$$

$$h(p, T) = e(p, T) + p\tau(p, T) = \gamma c_v T = h(T). \tag{1.8}$$

It follows from (1.8) that the specific heat at constant pressure c_p is given by

$$c_p = \left(\frac{\partial h}{\partial T}\right)_p = \gamma c_v. \tag{1.9}$$

Using again the Maxwell relations yields the specific entropy s for SG-EOS:

$$s(p, \tau) = c_v \ln((p + p_\infty)\tau^\gamma) + s_0. \tag{1.10}$$

The speed of sound (1.3) can be easily derived from (1.10); it can be alternatively expressed as

$$c^2 = (\gamma - 1)c_p T. \tag{1.11}$$

1.2.2 Thermally perfect gas EOS for reacting flow

The EOS of thermally perfect gases is used to describe the unburnt and burnt gas mixtures [Beccantini 10a]:

$$\begin{aligned} p &= \rho \mathcal{R} T, \\ \tilde{e} &= h_0 + \int_0^T c_v(\psi)\,\mathrm{d}\psi, \end{aligned}$$

where $\mathcal{R}$ is the gas constant, $\tilde{e}$ is the specific internal energy, and $c_v(T)$ is the specific heat at constant volume which depends on the temperature. In the reaction problem, the enthalpy of formation of the unburnt gas is released and transformed into the heat of reaction and the sensible energy of the burnt gas.

The sound speed of thermally perfect gases is given by:

$$c^2 = \frac{\gamma(T)p}{\rho} = \gamma(T)\mathcal{R}T, \tag{1.12}$$

with $\gamma(T)$ the heat capacity ratio expressed as:

$$\gamma(T) = \frac{c_p(T)}{c_v(T)} = \frac{c_v(T) + \mathcal{R}}{c_v(T)}.$$

1.3 Phase characteristic function X_k and volume fraction α_k

1.3.1 Definitions

When simulating the interface evolution between two phases, it is useful to determine the position of the interface. In [Drew 98], the *characteristic function* $X_k(\mathbf{x}, t; \Sigma_k)$ of phase Σ_k is defined for this purpose:

$$X_k(\mathbf{x}, t; \Sigma_k) = \begin{cases} 1, & \text{if } \mathbf{x} \text{ lies in phase } \Sigma_k \text{ at } t; \\ 0, & \text{otherwise.} \end{cases}$$

The function X_k (see Fig. 1.1) indicates locally the phase Σ_k and ignores all other phases and interfaces. The interface is thus characterized by the discontinuity of the characteristic function X_k. This function is of fundamental importance in the theoretical multiphase flow modeling, as well as for the development of the numerical method DEM/RDEM. The average (for instance the ensemble average of [Drew 98]) of $X_k(\mathbf{x}, t; \Sigma_k)$ means the average fraction of the presence of phase Σ_k at point $\mathbf{x}$ at time t; this macroscopic variable is commonly called the "volume fraction" in the literature:

$$\alpha_k = \overline{X_k}. \tag{1.13}$$

We remind that, as far as the interface problems involved in our applications are concerned, physical mixtures are not considered. For this reason, α_k and X_k have an analogous meaning from a physical viewpoint. However, when considering the numerical mixtures involved in the computations, we assume that the macroscopic variable α_k can have intermediate values between 0 and 1, while the microscopic variable X_k still has two possible values 0 or 1 only.

1.3.2 The topological equation

According to [Drew 98], the *topological equation* for X_k reads:

$$\frac{\partial X_k}{\partial t} + \mathcal{D}_I \cdot \nabla X_k = 0, \tag{1.14}$$

where $\mathcal{D}_I$ is the propagation velocity of the phase interface (or of the reactive shock in a reacting problem). Since (1.14) means, from a distribution point of view (see [Drew 98]), that the material derivative of X_k following the interface vanishes, this topological equation describes the geometrical evolution of the interface. It can be interpreted through the following two cases: i) when looking at a point not located at the interface, *i.e.* either such that $X_k = 1$ or $X_k = 0$, both partial derivatives vanish, ii) on the other hand, when considering a point on the interface, both derivatives are

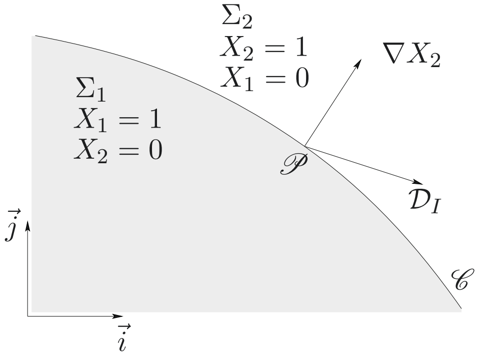

Figure 1.1: Characteristic function X. The phase Σ_1 is shaded, and characterized by $X_1 = 1$ whereas the phase Σ_2 is in white, and characterized by $X_2 = 1$. The interface between the phases is represented by the curve $\mathscr{C}$, and $\mathcal{D}_I$ is its velocity at point $\mathscr{P}$. ∇X_1 and ∇X_2 are both perpendicular to the interface curve $\mathscr{C}$ at $\mathscr{P}$.

defined from a distribution point of view. This point, following the interface with the velocity of $\mathcal{D}_I$, has its characteristic function X_k described by a jump that remains constant. Thus its material derivative following the interface vanishes.

Averaging the topological equation (1.14) gives

$$\frac{\partial \alpha_k}{\partial t} + \overline{\mathcal{D}_I \cdot \nabla X_k} = 0. \tag{1.15}$$

Following [Perrier 07], we can write the term $\overline{\mathcal{D}_I \cdot \nabla X_k}$ as the average term $\mathbf{D}_I \cdot \nabla \alpha_k$ plus a fluctuation term which will be neglected in this work so that:

$$\overline{\mathcal{D}_I \cdot \nabla X_k} \approx \mathbf{D}_I \cdot \nabla \alpha_k.$$

We also refer to [Abgrall 03] for this modeling task. It then follows the averaged topological equation is expressed by

$$\frac{\partial \alpha_k}{\partial t} + \mathbf{D}_I \cdot \nabla \alpha_k = 0. \tag{1.16}$$

Note that for applications to interface problems, (1.16) can be interpreted analogously to (1.14). In fact, after assuming that only macroscopic interfaces are involved, α_k takes two values (0 or 1) and its discontinuity indicates the material interface. Thus (1.16) also means the material derivative vanishes following the interface.

When dealing with numerical two-phase mixtures with intermediate values of α_k between 0 and 1, we need to model the average interface velocity where the gradient of α_k is non-zero. This will be discussed in Chapter 2 in the framework of the Discrete Equations Method.

1.4 Balance equations of two-fluid model for interfaces

When dealing with (macroscopic) interface problems, each phase can be governed by the (macroscopic) Euler equations. We assume the phase vector of variables and fluxes can be analogously defined as in the local Euler equations (1.1):

$$\mathbf{u}_k = \begin{bmatrix} \rho_k \\ \rho_k \, \mathbf{v}_k \\ \rho_k {e^t}_k \end{bmatrix}, \quad \mathbb{F}_k = \begin{bmatrix} \rho_k \, \mathbf{v}_k \\ \rho \, \mathbf{v}_k \, \mathbf{v}_k + p_k \\ \rho_k {e^t}_k \mathbf{v}_k + p_k \mathbf{v}_k \end{bmatrix}, \tag{1.17}$$

Multiplying the single phase macroscopic Euler equations

$$\frac{\partial \mathbf{u}_k}{\partial t} + \nabla \cdot \mathbb{F}_k = 0 \tag{1.18}$$

by the phase volume fraction α_k yields

$$\alpha_k \frac{\partial \mathbf{u}_k}{\partial t} + \alpha_k \nabla \cdot \mathbb{F}_k = 0. \tag{1.19}$$

Coupled with the averaged topological equation (1.16) which describes the interface evolution, (1.19) can be rearranged as

$$\frac{\partial (\alpha_k \mathbf{u}_k)}{\partial t} + \nabla \cdot (\alpha_k \mathbb{F}_k) = (\mathbb{F}_k - \mathbf{u}_k \mathbf{D}_I) \cdot \nabla \alpha_k. \tag{1.20}$$

As done in [Abgrall 03], the so-called Lagrangian flux function is defined by

$$\mathbb{F}_k^{\mathrm{Lag}} = \mathbb{F}_k - \mathbf{u}_k \mathbf{D}_I.$$

Since $\nabla \alpha_k$ vanishes everywhere except on the interface, $\mathbb{F}_k^{\mathrm{Lag}}$ needs to be defined only on the interface. The two-fluid system (1.20) can then be expressed by

$$\frac{\partial (\alpha_k \mathbf{u}_k)}{\partial t} + \nabla \cdot (\alpha_k \mathbb{F}_k) = \mathbb{F}_{k,I}^{\mathrm{Lag}} \cdot \nabla \alpha_k. \tag{1.21}$$

It is emphasized that the two-fluid model (1.21) reduces to the single phase Euler equations (1.18) when looking at a point that is not located on the interface, that is, when $\nabla \alpha_k = 0$.

Let us denote $\Gamma_{k,I}$ the source of mass at the interface (linked to the chemical reaction in this work):

$$\Gamma_{k,I} = \rho_{k,I} \left(\mathbf{v}_{k,I} - \mathbf{D}_I \right) \cdot \nabla \alpha_k \tag{1.22}$$

In the momentum conservation equation, the interfacial momentum source is directly related to the mass generation source:

$$\Gamma_{k,I} \mathbf{v}_{k,I} = \rho_{k,I} \mathbf{v}_{k,I} \left(\mathbf{v}_{k,I} - \mathbf{D}_I \right) \cdot \nabla \alpha_k \tag{1.23}$$

The interfacial pressure source related to phase interaction is denoted $\mathbf{P}_{k,I}$ and such that:

$$\mathbf{P}_{k,I} = p_{k,I} \nabla \alpha_k \tag{1.24}$$

In the energy conservation equation, the interfacial energy source is also directly related to the mass generation source:

$$\Gamma_{k,I} e^t_{k,I} = \rho_{k,I} e^t_{k,I} \left(\mathbf{v}_{k,I} - \mathbf{D}_I \right) \cdot \nabla \alpha_k \tag{1.25}$$

The interfacial power source related to phase interaction is such that:

$$\mathbf{P}_{k,I} \cdot \mathbf{v}_{k,I} = p_{k,I} \mathbf{v}_{k,I} \cdot \nabla \alpha_k \tag{1.26}$$

Injecting these quantities in the compact conservation equations (1.21) yields:

Mass

$$\frac{\partial (\alpha_k \rho_k)}{\partial t} + \nabla \cdot (\alpha_k \rho_k \mathbf{v}_k) = \Gamma_{k,I}$$

Momentum

$$\frac{\partial (\alpha_k \rho_k \mathbf{v}_k)}{\partial t} + \nabla \cdot (\alpha_k \rho_k \mathbf{v}_k \mathbf{v}_k) + \nabla (\alpha_k p_k) = \Gamma_{k,I} \mathbf{v}_{k,I} + \mathbf{P}_{k,I}$$

Energy

$$\frac{\partial \alpha_k \rho_k {e^t}_k}{\partial t} + \nabla \cdot (\alpha_k \rho_k {e^t}_k \mathbf{v}_k) + \nabla \cdot (\alpha_k p_k \mathbf{v}_k) = \Gamma_{k,I} e^t_{k,I} + \mathbf{P}_{k,I} \cdot \mathbf{v}_{k,I}$$

Coupling the local (microscopic) Euler equations with the characteristic function X_k, the two-fluid model (1.21) can be alternatively derived in a rigorous way from the averaging theory (see *e.g.* [Drew 98, Abgrall 03, Perrier 07]), with all the involved fluctuation terms appearing throughout the averaging procedures neglected. We emphasize that, for the macroscopic interface problems of interest in our applications, the averaging procedures are not essential from a physical point of view. However, we can alternatively employ the averaging method for interpreting the numerical two-phase mixtures in discrete situations. This is the reason why we have distinguished the characteristic function X_k and the volume fraction α_k in Section 1.3. Thus, when studying the numerical two-phase mixtures, the variables in (1.17) for each phase can be considered as the following averaging terms in discrete situations:

- The density ρ_k of Σ_k is given by the average weighted with the characteristic function X_k (called component-weighted average):

$$\rho_k = \frac{\overline{X_k \rho}}{\alpha_k}.$$

The component-weighted average can be similarly applied to the phase pressure p_k:

$$p_k = \frac{\overline{X_k p}}{\alpha_k}.$$

- The velocity $\mathbf{v}_k$ of Σ_k is defined by the average weighted by $X_k\rho$ (called mass-weighted average):

  $$\mathbf{v}_k = \frac{\overline{X_k \rho \mathbf{v}}}{\alpha_k \rho_k}.$$

  The mass-weighted average can be analogously applied to the phase internal energy e_k:

  $$e_k = \frac{\overline{X_k \rho e}}{\alpha_k \rho_k}.$$

1.5 Interface conditions and mixture equations

At the interface between fluids, properties can be discontinuous but mass, momentum and energy must be conserved, after neglecting the surface tension and other interfacial energy source. Thus, the following jump conditions hold:

$$\begin{aligned} \sum_k \Gamma_{k,I} &= 0, \\ \sum_k (\Gamma_{k,I}\mathbf{v}_{k,I} + \mathbf{P}_{k,I}) &= 0, \\ \sum_k (\Gamma_{k,I} e^t_{k,I} + \mathbf{P}_{k,I} \cdot \mathbf{v}_{k,I}) &= 0, \end{aligned} \tag{1.27}$$

When solving the two-fluid model here considered, it is essentially needed to determine the various interfacial terms involved in (1.27). The mass transfer term $\Gamma_{k,I}$ is, in general, described by empirical relations depending on the problem under study: evaporation, condensation, combustion, etc. The modeling of interfacial pressure $p_{k,I}$ and interfacial velocity $\mathbf{v}_{k,I}$ is delicate [Saurel 99a]. As far as our applications are concerned (thermally perfect reacting gases), many of the available approaches of this modeling in the literature are not suitable, since they assume that the interfacial pressure and velocity are equal for both phases. When dealing with burnt and unburnt gases separated by a reacting front, however, these values can be dramatically different [Beccantini 10a]. It will be shown in Chapter 2 that this modeling difficulty can be successfully overcome by considering the reactive Riemann problem [Beccantini 10a] in the framework of the RDEM approach. In fact, the solution of the reactive Riemann problem will allow to determine at once the interfacial pressure $p_{k,I}$ and the interfacial velocity $\mathbf{v}_{k,I}$ on the reactive interface for both phases, as well as the mass transfer term $\Gamma_{k,I}$, provided that the fundamental flame speed K_0 is given in case of deflagration.

Summing the balance equations of two-fluid model for phase Σ_1 and Σ_2, and taking into account the jump conditions at the interface, the mixture equations take the form of the Euler equations.

1.6 Case of impermeable interfaces

When considering two-phase interfaces with neither chemical reaction nor phase change (*i.e.* impermeable interfaces), the mass transfer term $\Gamma_{k,I}$ in (1.22) vanishes. As a consequence,

$$\mathbf{D}_I = \mathbf{v}_{1,I} = \mathbf{v}_{2,I} = \mathbf{v}_I. \tag{1.28}$$

Inserting this relation into the interface jump conditions (1.27) yields

$$p_{1,I} = p_{2,I} = p_I. \tag{1.29}$$

Thus, pressure and velocity are continuous across the chemically inert fronts. The physical modeling of interface conditions thus becomes easier in this case (see for instance the model proposed in [Saurel 99a]). However, as previously pointed out in the case of permeable fronts, it is also possible to resort to the solution of a Riemann problem in the framework of the DEM approach: the values of p_I and $\mathbf{v}_I$ can be exactly known (on the contact discontinuity) if the exact Riemann solver is used. As a consequence, the numerical errors of the DEM approach for non-reactive interfaces, coupled with an exact solution of local Riemann problems, are only due to the numerical averaging procedures of the phase variables inside the control volumes. Alternatively, approximate Riemann solvers could also be used, which would add another source of error to that induced by the averaging procedure.

To summarize, the two-fluid model for impermeable interfaces can be written as:

$$\begin{aligned}
&\frac{\partial \alpha_k}{\partial t} + \mathbf{v}_I \cdot \nabla \alpha_k = 0,\\
&\frac{\partial (\alpha_k \rho_k)}{\partial t} + \nabla \cdot (\alpha_k \rho_k \mathbf{v}_k) = 0,\\
&\frac{\partial (\alpha_k \rho_k \mathbf{v}_k)}{\partial t} + \nabla \cdot (\alpha_k \rho_k \mathbf{v}_k \mathbf{v}_k) + \nabla (\alpha_k p_k) = p_I \nabla \alpha_k,\\
&\frac{\partial (\alpha_k \rho_k {e^t}_k)}{\partial t} + \nabla \cdot (\alpha_k \rho_k {e^t}_k \mathbf{v}_k) + \nabla \cdot (\alpha_k p_k \mathbf{v}_k) = p_I \mathbf{v}_I \cdot \nabla \alpha_k.
\end{aligned} \tag{1.30}$$

Chapter 2

(Reactive) Discrete Equations Method for two-fluid model

This second chapter is devoted to the presentation of the (Reactive) Discrete Equations Method (DEM/RDEM) [Abgrall 03, Le Métayer 05] which will be used throughout this work to obtain numerical solutions of the two-fluid system (1.16)-(1.21).

Looking back at the previous Chapter 1, the two-fluid system is composed of the averaged topological equation (1.16) combined with two sets of conversation laws (Euler-type equations) for each phase. The numerical discretization of (1.16) is thus of fundamental importance when solving the full two-fluid system; this discretization will be performed in Section 2.1 using the first-order upwind DEM/RDEM method, with the aim of giving a first introduction to the method.

The extension of this upwind DEM/RDEM method to the full two-fluid system can then be realized by making use of the important concept of *intercell boundaries partition*. This concept will be reviewed in Section 2.2: it will be shown in particular how it is consistent with an averaging procedure for the solution of the topological equations.

Section 2.3 is devoted to a general qualitative overview of the DEM/RDEM discretization strategy for the full two-fluid system. It can be regarded as an extension to two-phase problems of the single phase Godunov's method. Three local Riemann problems must be solved, with one of them a (non-reacting or reacting) Riemann problem between two different phases. This section will also describe how DEM/RDEM copes with the modeling issues of the interface conditions, such as interfacial pressure and velocity, as well as the mass transfer term in case of chemical reactions.

Next, Section 2.4 provides a complete quantitative description of the DEM/RDEM method, generalizing the upwind approach presented in Section 2.1.

Specific time marching conditions for the DEM/RDEM approach are investigated in Section 2.5.

Second-order extension and extension to the multi-dimensional case are eventually discussed in Section 2.6 and 2.7 respectively.

Numerical results for one-dimensional interfaces computed with DEM are provided in Section 2.8 and motivate the need for a further improvement both of the interface accuracy and of the method robustness. The present work proposes to achieve such an improvement using an original upwind downwind-controlled splitting approach that will be presented in the next Chapter 3.

Note finally that the rather simple DEM/RDEM description proposed in this chapter is given with the hope to make the practical implementation of the DEM/RDEM approach easier for the interested reader. We refer to [Abgrall 03] for a more rigorous derivation of the method.

2.1 First-order upwind DEM/RDEM approach for averaged topological equation (scalar case)

Let us consider the one-dimensional averaged topological equation

$$\frac{\partial \alpha}{\partial t} + D_I(x,t)\frac{\partial \alpha}{\partial x} = 0, \tag{2.1}$$

where the phase indicator k has been omitted.

It is emphasized that α can be discontinuous, which reflects the location of the interfaces. According to [Drew 98], the following relationship, similar to the product rule for ordinary derivatives, holds:

$$D_I\frac{\partial \alpha}{\partial x} = \frac{\partial(\alpha D_I)}{\partial x} - \alpha\frac{\partial D_I}{\partial x}.$$

Equation (2.1) can thus be rewritten as:

$$\frac{\partial \alpha}{\partial t} + \frac{\partial(\alpha D_I)}{\partial x} = \alpha\frac{\partial D_I}{\partial x} \tag{2.2}$$

The conservative term $\dfrac{\partial(\alpha D_I)}{\partial x}$ can be discretized using a standard finite volume technique

$$\left[\frac{\partial(\alpha D_I)}{\partial x}\right]_i^n = \frac{\alpha^n_{i+\frac{1}{2}} D^n_{I,i+\frac{1}{2}} - \alpha^n_{i-\frac{1}{2}} D^n_{I,i-\frac{1}{2}}}{\Delta x}. \tag{2.3}$$

The discrete interface velocities $D^n_{I,i-\frac{1}{2}}$ and $D^n_{I,i+\frac{1}{2}}$ here involved can, in fact, be given by the local Riemann problem solution, in the numerical context of DEM/RDEM approach for full two-fluid system. For instance, these quantities can be evaluated by the speed of the reactive shock wave within the reactive Riemann problem solution. Since we are only interested, in this section, with the scalar topological equation, it is assumed that $D^n_{I,i-\frac{1}{2}}$ and $D^n_{I,i+\frac{1}{2}}$ are known variables. Their specific evaluation will be further discussed in Section 2.3.2 and 2.3.3. For a first-order approach, the numerical solution $\alpha(x,t)$ at time t^n can be approximated by a piecewise constant reconstruction function $\alpha^n(x,t^n)$, such that for the control volume $[x_{i-\frac{1}{2}}, x_{i+\frac{1}{2}}]$

$$\alpha^n(x,t^n) = \alpha^n_i, \; x_{i-\frac{1}{2}} < x < x_{i+\frac{1}{2}}.$$

Thus, the non-conservative term $\alpha\frac{\partial D_I}{\partial x}$ can be simply discretized as

$$\left[\alpha\frac{\partial D_I}{\partial x}\right]_i^n = \alpha^n_i \frac{D^n_{I,i+\frac{1}{2}} - D^n_{I,i-\frac{1}{2}}}{\Delta x}. \tag{2.4}$$

Using the above relations and the first-order Euler method for the time discretization, the numerical scheme for the modified topological equation (2.2) takes the form:

$$\alpha^{n+1}_i = \alpha^n_i + \frac{\Delta t}{\Delta x}\left[D^n_{I,i-\frac{1}{2}}(\alpha^n_{i-\frac{1}{2}} - \alpha^n_i) - D^n_{I,i+\frac{1}{2}}(\alpha^n_{i+\frac{1}{2}} - \alpha^n_i)\right]. \tag{2.5}$$

The intercell value $\alpha^n_{i-\frac{1}{2}}$ at $x = x_{i-\frac{1}{2}}$ of an upwind method is classically given by

$$\alpha^n_{i-\frac{1}{2}} = \begin{cases} \alpha^n_{i-1}, \text{ if } D^n_{I,i-\frac{1}{2}} > 0, \\ \alpha^n_i, \text{ if } D^n_{I,i-\frac{1}{2}} < 0. \end{cases} \tag{2.6}$$

Here we define an interface velocity indicator β on each intercell boundary by

$$\beta_{i-\frac{1}{2}} = \begin{cases} 1, \text{ if } D^n_{I,i-\frac{1}{2}} \geq 0, \\ 0, \text{ if } D^n_{I,i-\frac{1}{2}} < 0. \end{cases} \tag{2.7}$$

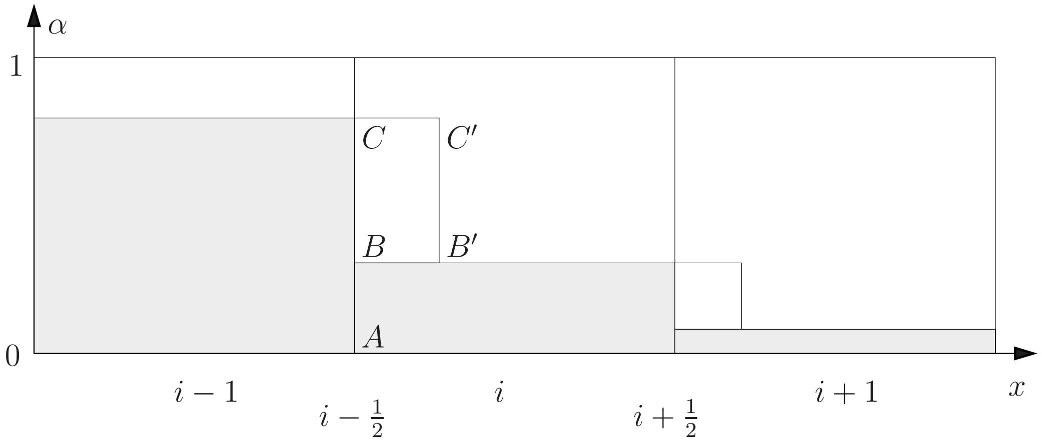

Figure 2.1: First-order upwind method for averaged topological equation.

Scheme (2.5) can then be rewritten as

$$\alpha_i^{n+1} = \alpha_i^n + \frac{\Delta t}{\Delta x}\left[\beta_{i-\frac{1}{2}} D^n_{I,i-\frac{1}{2}}(\alpha^n_{i-1} - \alpha^n_i) + (1-\beta_{i+\frac{1}{2}}) D^n_{I,i+\frac{1}{2}}(\alpha^n_i - \alpha^n_{i+1})\right]. \tag{2.8}$$

The upwind scheme (2.8) implies that the value of α_i is only modified by the numerical interfaces (*i.e.* numerical fluxes) entering into cell i from its boundaries. The flux contributions at boundaries $x_{i-\frac{1}{2}}$ and $x_{i+\frac{1}{2}}$ are respectively:

$$\begin{aligned} \beta_{i-\frac{1}{2}} D^n_{I,i-\frac{1}{2}}(\alpha^n_{i-1} - \alpha^n_i), \\ (1-\beta_{i+\frac{1}{2}}) D^n_{I,i+\frac{1}{2}}(\alpha^n_i - \alpha^n_{i+1}), \end{aligned} \tag{2.9}$$

The method is also graphically illustrated in Fig. 2.1 for the specific case where the propagation speeds are positive. In that particular case:

$$\beta_{i-\frac{1}{2}} = 1,\ 1-\beta_{i+\frac{1}{2}} = 0,$$

so that the flux contribution from intercell boundary $x_{i+\frac{1}{2}}$ vanishes. The term

$$\beta_{i-\frac{1}{2}} D^n_{I,i-\frac{1}{2}} \Delta t(\alpha^n_{i-1} - \alpha^n_i)$$

in the numerical scheme (2.8) can also be interpreted as the area $A_{BB'C'C}$ displayed in Fig. 2.1. Thus,

$$\alpha_i^{n+1} = \alpha_i^n + \frac{A_{BB'C'C}}{\Delta x}. \tag{2.10}$$

2.2 Partition of intercell boundaries

In order to extend scheme (2.5) to the full two-fluid model, the concept of intercell boundaries partition is now graphically described, using Fig. 2.2. The quantity $S^{(12)}_{i-\frac{1}{2}}$ or $S^{(21)}_{i-\frac{1}{2}}$ denotes the interface between two phases in the discrete situation. In the specific case shown in Fig. 2.2, it is simply assumed that no such interface exists with phase Σ_2 on the left and phase Σ_1 on the right (*i.e.* $S^{(21)}_{i-\frac{1}{2}} = 0$). Note that a non-zero volume fraction of phase Σ_k is assumed in each computational cell in our computations in order for the problem to be well-posed [Murrone 05, Zein 10]. Thus, according to the configuration illustrated in Fig. 2.2, it is certain that two single-phase non-zero sub-surfaces are present at each intercell boundary. For instance, at $x_{i-\frac{1}{2}}$, the sub-surface linked to the single-phase contact of Σ_1 can be quantified by

$$S^{(11)}_{i-\frac{1}{2}} = \min\left\{\alpha_{1,i-1}, \alpha_{1,i}\right\} = 1 - \max\left\{\alpha_{2,i-1}, \alpha_{2,i}\right\}. \tag{2.11}$$

The sub-surface linked to the single-phase contact of Σ_2 is given by

$$S^{(22)}_{i-\frac{1}{2}} = 1 - \max\left\{\alpha_{1,i-1}, \alpha_{1,i}\right\} = \min\left\{\alpha_{2,i-1}, \alpha_{2,i}\right\}. \tag{2.12}$$

The sub-surface linked to the numerical interface between phase Σ_1 and Σ_2 can be computed as:

$$S^{(12)}_{i-\frac{1}{2}} = \max\left\{0, \alpha_{1,i-1} - \alpha_{1,i}\right\} = \max\left\{0, \alpha_{2,i} - \alpha_{2,i-1}\right\}. \tag{2.13}$$

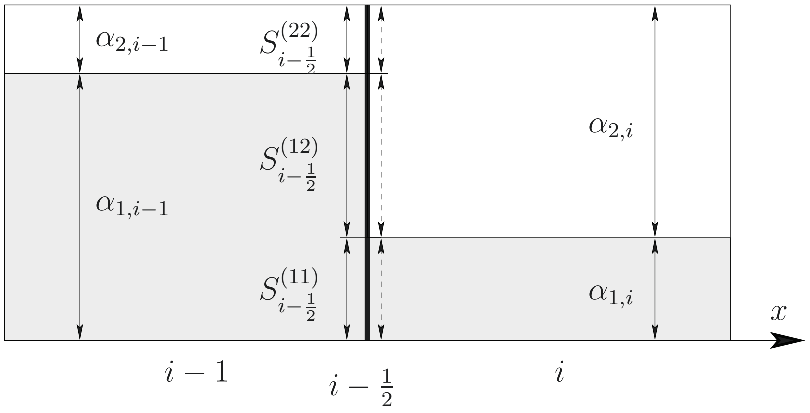

Figure 2.2: Partition of the intercell boundary, The phase Σ_1 is shaded whereas the phase Σ_2 is in white.

Similarly, we have for the sub-surface between phase Σ_2 and Σ_1:

$$S^{(21)}_{i-\frac{1}{2}} = \max\left\{0, \alpha_{1,i} - \alpha_{1,i-1}\right\} = \max\left\{0, \alpha_{2,i-1} - \alpha_{2,i}\right\}. \tag{2.14}$$

It is easy to observe that one of the sub-surface $S^{(12)}_{i-\frac{1}{2}}$, $S^{(21)}_{i-\frac{1}{2}}$, should be zero. Moreover, in exact algebra, the following relationship holds:

$$S^{(11)}_{i-\frac{1}{2}} + \max\left\{S^{(12)}_{i-\frac{1}{2}}, S^{(21)}_{i-\frac{1}{2}}\right\} + S^{(22)}_{i-\frac{1}{2}} = 1. \tag{2.15}$$

2.2.1 Upwind scheme for averaged topological equation by means of intercell boundary partition

From the above definitions, the quantity $\alpha^n_{k,i-1} - \alpha^n_{k,i}$ in the upwind scheme (2.8) for phase Σ_k can also be expressed in terms of sub-surfaces:

$$\alpha^n_{k,i-1} - \alpha^n_{k,i} = S^{(kk')}_{i-\frac{1}{2}} - S^{(k'k)}_{i-\frac{1}{2}}, \tag{2.16}$$

where k' is the phase indicator different from k. Similarly, the quantity $\alpha^n_{k,i} - \alpha^n_{k,i+1}$ can also be written as:

$$\alpha^n_{k,i} - \alpha^n_{k,i+1} = S^{(kk')}_{i+\frac{1}{2}} - S^{(k'k)}_{i+\frac{1}{2}}. \tag{2.17}$$

The upwind method for the averaged topological equation of phase Σ_k can then be rewritten as

$$\alpha^{n+1}_{k,i} = \alpha^n_{k,i} + \frac{\Delta t}{\Delta x}\left[\beta_{i-\frac{1}{2}} D^n_{I,i-\frac{1}{2}}(S^{(kk')}_{i-\frac{1}{2}} - S^{(k'k)}_{i-\frac{1}{2}}) + (1-\beta_{i+\frac{1}{2}}) D^n_{I,i+\frac{1}{2}}(S^{(kk')}_{i+\frac{1}{2}} - S^{(k'k)}_{i+\frac{1}{2}})\right]. \tag{2.18}$$

That is, the scheme (2.18) with intercell boundary partition is equivalent to the upwind scheme (2.8).

2.3 Qualitative overview of DEM/RDEM for two-fluid system

2.3.1 General principles

In this section, the (Reactive) Discrete Equations Method (DEM/RDEM) [Abgrall 03, Le Métayer 05] is qualitatively presented for the full two-fluid model aiming to deal with reacting and non-reacting interfaces. The DEM/RDEM described here, as the upwind method for the volume fraction described in the previous Sections, is an Eulerian approach (fixed space grid). The two-phase flow here considered is characterized by the volume fraction of each phase. Even though only the interfaces (permeable or impermeable) separating the pure fluids should be involved in the problem, non-zero volume fractions must be defined at each location to preserve the hyperbolicity of the two-fluid model with two pressures and two velocities [Murrone 05, Zein 10]. Due to numerical dissipation, the volume fraction at the interface is diffused, which artificially creates numerical mixture. In Fig. 2.3, the diffused volume fractions illustrate the numerical mixture of material interface in one space dimension (note this diffused volume fraction model corresponds to the piecewise constant representation of α used in Section 2.1 and 2.2).

As in the Godunov's method for the single phase compressible Euler equations, local Riemann problems are considered in the DEM/RDEM method for the averaging of conservative variables, or more practically for computing the intercell numerical flux functions. At each intercell boundary in the interface diffusion zone for the volume fraction model in Fig. 2.4, the unitary surface can be divided into three parts, depending upon the phase configuration across the intercell boundary (see Section 2.2). This intercell boundary partition results in three different local Riemann problems at each intercell location, for instance at the position $x_{i-\frac{1}{2}}$ in the case where $\alpha_{1,i-1} > \alpha_{1,i}$ (and $\alpha_{2,i-1} < \alpha_{2,i}$ since the flow is assumed saturated):

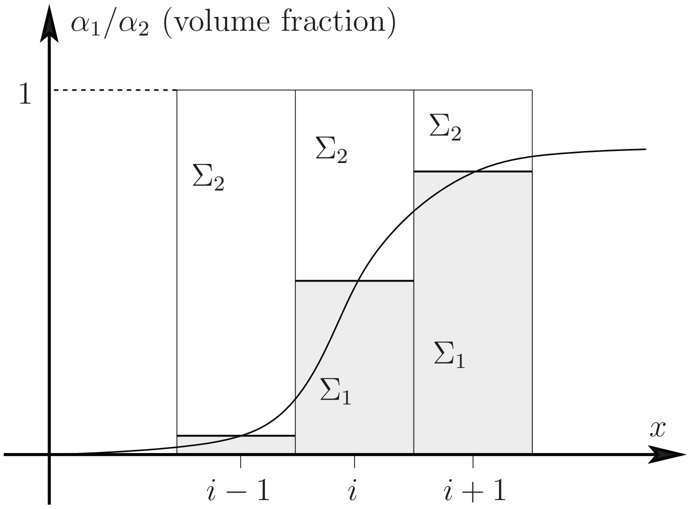

Figure 2.3: Numerically diffused volume fractions. The phase Σ_1 is shaded, and characterized by the volume fraction α_1 whereas the phase Σ_2 is in white, and characterized by α_2. $\alpha_1 + \alpha_2 = 1$.

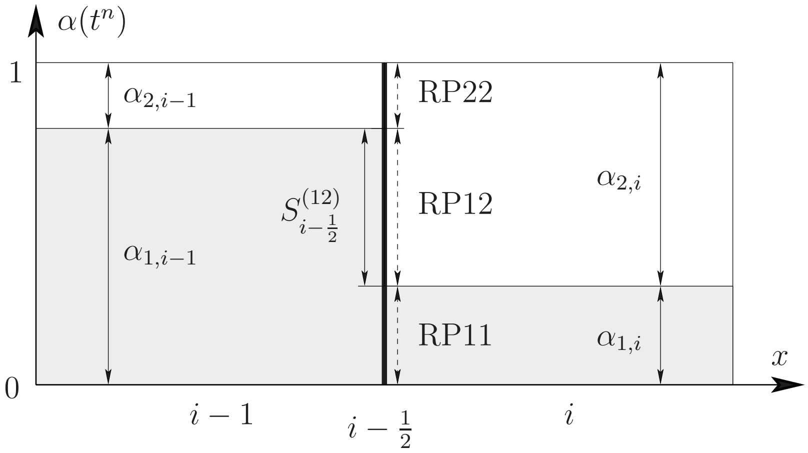

Figure 2.4: Three Riemann problems at the intercell boundary $i-\frac{1}{2}$. The phase Σ_1 is shaded whereas the phase Σ_2 is in white.

- RP11$\big(\mathbf{U}^n_{1,i-1}, \mathbf{U}^n_{1,i}\big)$,
- RP12$\big(\mathbf{U}^n_{1,i-1}, \mathbf{U}^n_{2,i}\big)$,
- RP22$\big(\mathbf{U}^n_{2,i-1}, \mathbf{U}^n_{2,i}\big)$.

Let us emphasize that, with the DEM/RDEM approach, the Riemann problem

- RP21$\big(\mathbf{U}^n_{2,i-1}, \mathbf{U}^n_{1,i}\big)$

is not taken into account in the specific case shown in Fig. 2.4. Firstly, from a physical viewpoint, the interface considered in the present work cannot involve both RP12 and RP21 at the same time and the same location. Secondly, from a numerical viewpoint, the sub-surface $S^{(21)}_{i-\frac{1}{2}}$ vanishes in scheme (2.18) for the present case where $S^{(12)}_{i-\frac{1}{2}} > 0$.

As far as the one-phase local Riemann problems RP11 and RP22 are concerned, the conventional Godunov flux for the Euler equations $\mathbf{F}^{\mathrm{G}}(\mathbf{U}^{(11)}_{i-\frac{1}{2}})$ and $\mathbf{F}^{\mathrm{G}}(\mathbf{U}^{(22)}_{i-\frac{1}{2}})$ (see [Ivings 98] for stiffened gases, [Beccantini 00, Beccantini 10a] for thermally perfect gases) can be used for updating the phase variables. Alternatively, any suitable approximate Riemann solver [Toro 97] can be employed for RP11 and RP22.

The two-phase local Riemann problem RP12 requires a specific treatment for the discretization of the non-conservative transport equation for volume fractions (1.16) (see Section 2.1) and the updating of the corresponding phase variables. This treatment for the two-phase local Riemann problem RP12 depends on whether the interface velocity D_I is positive or negative. If $D_I > 0$, the phase Σ_1 enters into cell i with the velocity D_I; otherwise, the phase Σ_2 enters into cell $i-1$ with the velocity D_I. In the following description, focused on cell i, D_I is supposed to be positive at $x_{i-\frac{1}{2}}$ and $x_{i+\frac{1}{2}}$ with $\alpha_{1,i-1} > \alpha_{1,i} > \alpha_{1,i+1}$. The overall configuration of the two-phase control volumes at time $t^{n+1} = t^n + \Delta t$ is sketched in Fig. 2.5. The two-phase interface (Σ_1, Σ_2) represented by BC at $x_{i-\frac{1}{2}}$ at time t^n moves to the right with velocity D_I and reaches position $B'C'$ $(x = x_{i-\frac{1}{2}} + D_I\Delta t)$ at t^{n+1}. The sub-volume of $BCC'B'$ initially occupied by phase Σ_2 (Fig. 2.4) is now occupied by Σ_1 (Fig. 2.5). Thus, the variations of the phase volume fraction in the cell element i can be quantified as:

$$\begin{aligned}\Delta\alpha_{1,i}^n &= S_{i-\frac{1}{2}}^{(12)}\frac{D_I\Delta t}{\Delta x};\\ \Delta\alpha_{2,i}^n &= -S_{i-\frac{1}{2}}^{(12)}\frac{D_I\Delta t}{\Delta x}.\end{aligned} \tag{2.19}$$

Formulation (2.19) corresponds to the discretization of the volume fraction equation (1.16), which can be interpreted by the volume $BCC'B'$ in Fig. 2.5 (see scheme (2.18)). To explain the averaging procedure of phase variables in the DEM/RDEM approach, the Riemann problems for surface segment BC at location $x_{i-\frac{1}{2}}$ and for DE at location $x_{i+\frac{1}{2}}$ are illustrated in Fig. 2.6 in the case of non-reacting stiffened gas flows, where the interface velocity D_I is equal to the velocity of contact discontinuity. It is worthwhile to notice that in order to perform the variables averaging for both

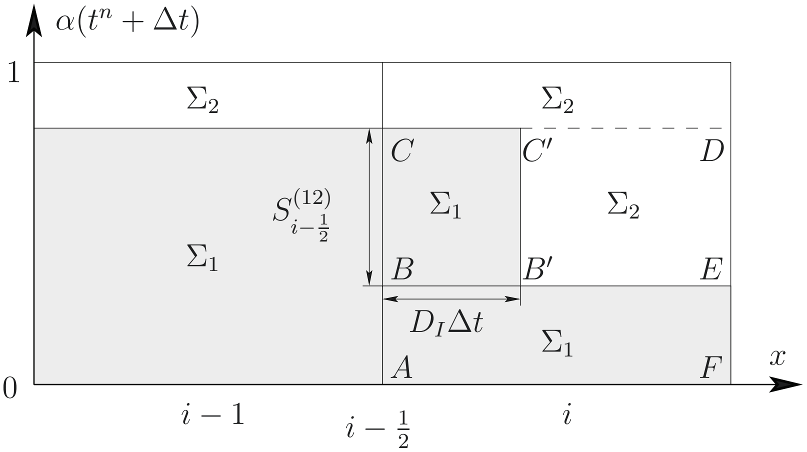

Figure 2.5: Two-phase control volumes at time $t^n + \Delta t$. The interface represented by BC at $x_{i-\frac{1}{2}}$ at time t^n moves to the right with the velocity of D_I and arrives at position $B'C'$ $(x = x_{i-\frac{1}{2}} + D_I\Delta t)$ at $t^{n+1} = t^n + \Delta t$.

phases in DEM/RDEM method, it is sufficient to assume that no wave interaction occurs within the computational cells. This is satisfied by enforcing the CFL restriction CFL $\leq \frac{1}{2}$. Thus, the averaging of conservative variables for each phase concerning the sub-cell $BCDE$ in Fig. 2.5 inside the element i can be expressed, by integrating over the line segment $[x_{i-\frac{1}{2}}, x_{i+\frac{1}{2}}] \times t^{n+1}$ in Fig. 2.6, as

$$\mathbf{U}^{n+1}_{1,i}\big|_{BCC'B'} = \int_{x_{i-\frac{1}{2}}}^{x_{i-\frac{1}{2}}+D_I\Delta t} \mathbf{U}^{(12)}_{i-\frac{1}{2}}\left(x, t^{n+1}\right) \mathrm{d}x,$$

$$\mathbf{U}^{n+1}_{2,i}\big|_{B'C'DE} = \int_{x_{i-\frac{1}{2}}+D_I\Delta t}^{x_{i-\frac{1}{2}}+\frac{1}{2}\Delta x} \mathbf{U}^{(12)}_{i-\frac{1}{2}}\left(x, t^{n+1}\right) \mathrm{d}x + \int_{x_{i+\frac{1}{2}}-\frac{1}{2}\Delta x}^{x_{i+\frac{1}{2}}} \mathbf{U}^{(22)}_{i+\frac{1}{2}}\left(x, t^{n+1}\right) \mathrm{d}x,$$

where $\mathbf{U}^{(12)}_{i-\frac{1}{2}}$ is the solution of local Riemann problem RP12 at $x_{i-\frac{1}{2}}$, and $\mathbf{U}^{(22)}_{i+\frac{1}{2}}$ is the solution of local Riemann problem RP22 at $x_{i+\frac{1}{2}}$ (surface area DE in Fig. 2.5 is covered by RP22 at $x_{i+\frac{1}{2}}$). The conservative variables in the volume $ABEF$ in Fig. 2.5 for phase Σ_1 are updated by the conventional Godunov's flux (or an approximate Riemann solver) at the surface areas AB and EF. Concluding for the cell element i, the volumes $BCC'B'$ and $ABEF$ in Fig. 2.5 are responsible for the averaging of conservative variables for phase Σ_1, and in the same manner, the remaining volume inside cell i is linked to the averaging for phase Σ_2. In other words, the averaging of conservative variables is realized separately for the two phases, which, consequently, also avoids averaging the thermodynamic properties. This (important) specific property of the DEM/RDEM method prevents the occurrence of non-physical pressure oscillations at the material interface [Abgrall 96].

However, it is difficult to handle the averaging of conservative variable when a more efficient time-marching scheme is required. Indeed, due to the nonlinear wave interactions when CFL $> \frac{1}{2}$, the determination of phase variables at the next time step is no longer obvious. On the other hand, as for the conservative form of the Godunov's method, the DEM/RDEM method can be written in terms of numerical flux for practical computations (see [Abgrall 03, Le Métayer 05] or the following section of this chapter). Since a moving interface is involved in the two-phase Riemann problem RP12, a so-called Lagrangian flux is required. It can be understood as a Lagrangian projection on the Eulerian mesh, which is equivalent to a flux function across a moving boundary of the corresponding phase, representing the phase interactions. By applying the DEM/RDEM method with the numerical flux for two-phase Riemann problems (Eulerian one and Lagrangian one), the CFL restriction of CFL $\leq \frac{1}{2}$ can be extended to CFL ≤ 1, provided that no wave acceleration takes place as a consequence of wave interaction [Toro 97]. Note however that, within the framework of

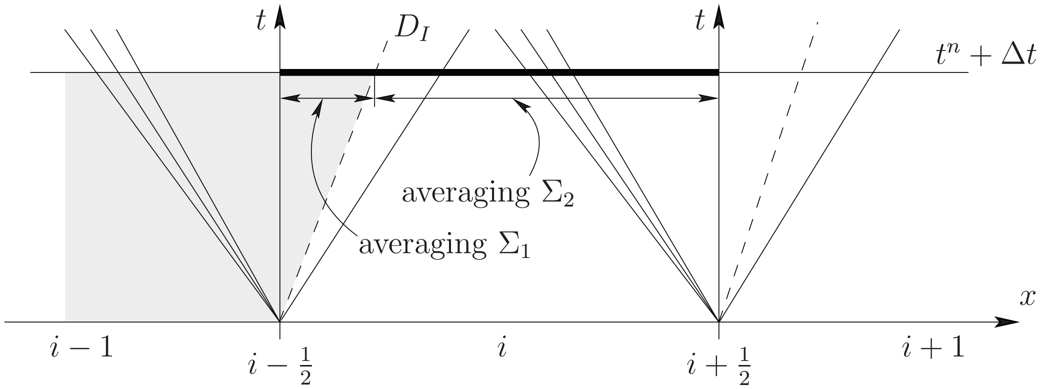

Figure 2.6: Two-phase local Riemann problem RP12 at intercell position $x_{i-\frac{1}{2}}$ linked to the surface segment BC in Fig. 2.5, and the corresponding one-phase local Riemann problem RP22 at intercell position $x_{i+\frac{1}{2}}$ linked to the surface segment DE in Fig. 2.5. At t^n, the sub-volume $BCDE$ of element i (Fig. 2.5) is entirely occupied by the phase Σ_2 (in white). D_I corresponds to the interface velocity. At t^{n+1}, one part of $[x_{i-\frac{1}{2}}, x_{i-\frac{1}{2}} + D_I\Delta t]$ in the sub-volume $BCDE$ is occupied by the phase Σ_1 (shaded). So Σ_1 is averaged aver $[x_{i-\frac{1}{2}}, x_{i-\frac{1}{2}} + D_I\Delta t] \times t^{n+1}$, and Σ_2 is averaged aver $[x_{i-\frac{1}{2}} + D_I\Delta t, x_{i+\frac{1}{2}}] \times t^{n+1}$.

DEM/RDEM approach, additional restriction for time step Δt must be respected for the volume fraction (see condition (2.35)).

2.3.2 Local Riemann problem in the non-reacting case

For the stiffened gas problem in the non-reacting case within the DEM approach, any suitable approximated Riemann solver [Toro 97, Ivings 98] can be used to evaluate the numerical flux. The numerical results presented in this work, except when specified, are obtained with the exact Riemann solver. The one-phase local Riemann problems RP11 and RP22 have the same solution structure as the two-phase Riemann problems RP12 or RP21. For instance, the typical solutions of RP22 and RP12 are illustrated in Fig. 2.7. The velocity of contact discontinuity v^* in the two-phase Riemann problem (*e.g.* Fig. 2.7(b)) is inserted into the non-reacting system (1.30) as the average interface velocity v_I in one space dimension. On the other hand, the pressure p^* inside the star region in the two-phase Riemann problem is set as the interface pressure p_I when calculating the moving flux (Lagrangian flux) across the interface. Consequently, the difficult physical modeling for interface conditions (v_I and p_I) in two-phase flow is avoided by using numerical data [Saurel 99a, Abgrall 03].

Regarding the general multi-dimensional case, rotational invariance is valid for the governing equations of two-fluid model (1.16)-(1.21). Thus, one-dimensional Riemann problem can be used for computing the multi-dimensional numerical flux. At each intercell boundary of a general mesh, the solution of a local one-dimensional two-phase Riemann problem gives the propagation speed of the volume fraction in the normal direction of the intercell boundary. This kind of approximation reflects the averaged interface velocity $\mathbf{D}_I$ in the averaged topological equation (1.16) within the framework of DEM/RDEM approach.

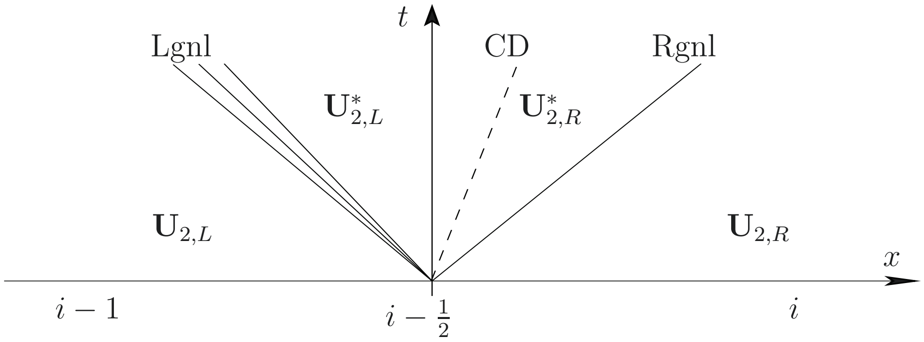

(a) RP22

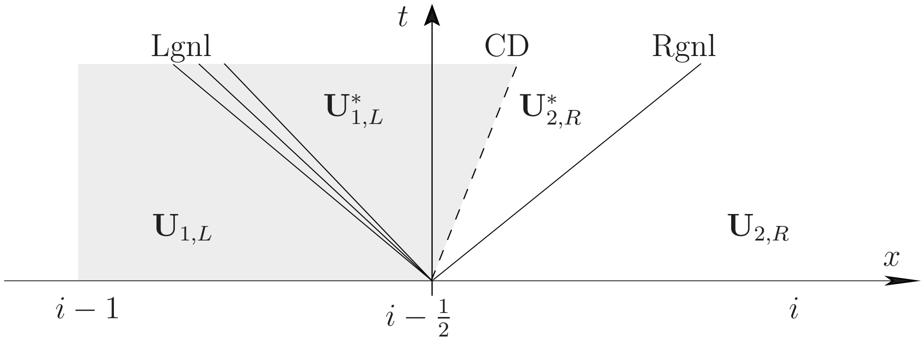

(b) RP12

Figure 2.7: Local Riemann problems in case of non-reacting stiffened gas flows at intercell position $x_{i-\frac{1}{2}}$. (a) is the solution structure of one-phase Riemann problem RP22($\mathbf{U}^n_{2,i-1}, \mathbf{U}^n_{2,i}$) which contains a left genuinely nonlinear wave (Lgnl), a contact discontinuity (CD), and a right genuinely nonlinear wave (Rgnl); (b) is the two-phase Riemann problem RP12($\mathbf{U}^n_{1,i-1}, \mathbf{U}^n_{2,i}$) with the same structure as the one-phase problem (a). The velocity of the contact discontinuity in (b) is the interface velocity D_I.

2.3.3 Local Riemann problem in the reacting case

The reacting interface problem also involves the local Riemann problems RP11, RP22, and RP12 or RP21 within the RDEM approach. As far as the one-phase non-reacting problems (RP11, RP22) are concerned, any approximated Riemann solver [Toro 97, Beccantini 00] or exact Riemann solver [Beccantini 00] can be applied for thermally perfect gases with temperature-dependent specific heats. The exact wave structure of RP11 or RP22 is similar to the one of non-reacting stiffened gas (Fig. 2.7(a)). The wave structure of the two-phase reactive Riemann problem RP12 or RP21 is fully studied in [Beccantini 10a] at all combustion regimes. The general case is shown in Fig. 2.8 for RP12. The phase Σ_1 is the burnt gas mixture (shaded in Fig. 2.8), and Σ_2 is the unburnt one (in white). The velocity of the reactive shock wave (RS) is the average interface velocity D_I in Equation (1.16) for one-dimensional problems. In deflagration configurations, for which the visible flame velocity is calculated by adding the unburnt gas velocity to the imposed fundamental flame speed K_0, the right genuinely nonlinear wave (Rgnl) is the precursor shock wave of the flame (RS), while in detonations (K_0 is not needed), the Rgnl is caught up by the RS, and these two waves overlap in $x - t$ plane. In case of Chapman-Jouguet deflagrations or detonations, a Taylor expansion wave appears behind the reacting shock where the flow is sonic.

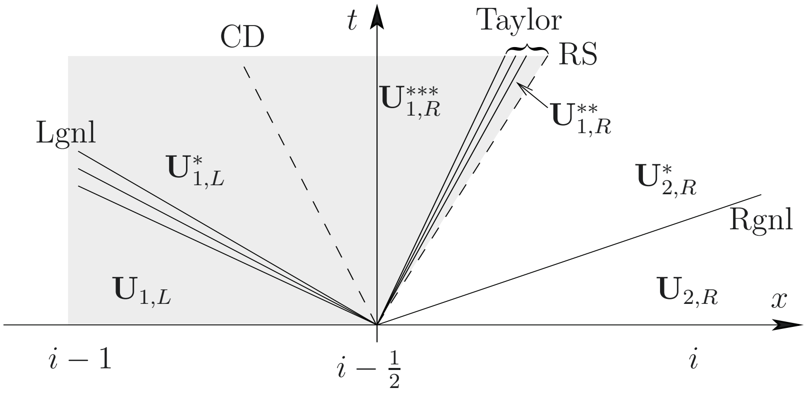

Figure 2.8: General case of two-phase local Riemann problem RP12($\mathbf{U}^n_{1,i-1}, \mathbf{U}^n_{2,i}; K_0$) in reacting case at intercell position $x_{i-\frac{1}{2}}$ [Beccantini 10a]. The left side is the burnt phase Σ_1, and the right side is the unburnt phase Σ_2. The solution structure contains a left genuinely nonlinear wave (Lgnl), a contact discontinuity (CD), a Taylor expansion wave in case of Chapman-Jouguet deflagration or detonation, a reacting shock wave (RS), and a right genuinely nonlinear wave (Rgnl). The velocity of reacting shock is the interface velocity D_I in averaged topological equation (1.16).

The interfacial pressure $p_{k,I}$ and velocity $v_{k,I}$, as well as the mass transfer flux $\rho_{k,I}(v_{k,I} - D_I)$ and other linked terms across the reactive interface in system (1.16)-(1.21) are defined by considering the reactive Riemann problem. They are the variables on the reactive shock evaluated by the variables of phase Σ_k: if $\mathscr{P}$ is a point located on the interface, the interface variable of interest $Q_{k,I}(\mathscr{P})$ is the limit of $Q(\mathscr{M})$ when the point $\mathscr{M}$ stays inside the phase Σ_k and $\mathscr{M} \to \mathscr{P}$. These variables are not continuous in general on the reactive interface. The interface conditions (1.27) are guaranteed by the Rankine-Hugoniot jump relations across the reactive shock wave.

According to [Beccantini 10a], the velocity of the reacting interface in the multi-dimensional case is modeled as a function of the fundamental flame speed K_0 and the unburnt gas velocity $\mathbf{v}^{\mathrm{u}}$:

$$\mathbf{D}_I = \mathbf{v}^{\mathrm{u}} + K_0 \mathbf{n} \tag{2.20}$$

where $\mathbf{n}$ is the normal to the reacting interface going from the burnt gas mixture to the unburnt one. For a multi-dimensional general grid, the one-dimensional reactive Riemann problem is resolved on intercell boundary in the local frame. As suggested in [Beccantini 10a], the fundamental flame speed used for this one-dimensional Riemann problem, is computed by $K_0|\mathbf{n} \cdot \mathbf{n}_f|$ with $\mathbf{n}_f$ the cell interface normal which can be different from the flame surface normal $\mathbf{n}$.

2.4 Quantitative description of DEM/RDEM for two-fluid system

In this section, the first-order upwind scheme (2.5) or (2.8) for the averaged topological equation is generalized for the full two-fluid system, taking into account the main concepts qualitatively discussed in Section 2.3.

Let us recast system (1.21) into the following one-dimensional form:

$$\frac{\partial(\alpha_k \mathbf{u}_k)}{\partial t} + \frac{\partial(\alpha_k \mathbf{f}_k)}{\partial x} = \mathbf{f}_k^{\mathrm{Lag}} \frac{\partial \alpha_k}{\partial x}. \tag{2.21}$$

where $\mathbf{u}_k = (\rho_k, \rho_k v_k, \rho_k e_k^t)^{\mathrm{T}}$, $\mathbf{f}_k = (\rho_k v_k, \rho_k v_k^2 + p_k, \rho_k e_k^t v_k + p_k v_k)^{\mathrm{T}}$, and the so-called Lagrangian flux $\mathbf{f}_k^{\mathrm{Lag}}$ is defined on the interface by

$$\mathbf{f}_k^{\mathrm{Lag}} = \mathbf{f}_{k,I} - D_I \mathbf{u}_{k,I}.$$

According to [Drew 98], the non-conservative term $\mathbf{f}_k^{\text{Lag}} \frac{\partial \alpha_k}{\partial x}$ can be rewritten as

$$\mathbf{f}_k^{\text{Lag}} \frac{\partial \alpha_k}{\partial x} = \frac{\partial(\alpha_k \mathbf{f}_k^{\text{Lag}})}{\partial x} - \alpha_k \frac{\partial \mathbf{f}_k^{\text{Lag}}}{\partial x},$$

which is a rule similar to the product rule for ordinary derivatives. The two-fluid system (2.21) can therefore be modified as

$$\frac{\partial(\alpha_k \mathbf{u}_k)}{\partial t} + \frac{\partial(\alpha_k \mathbf{f}_k)}{\partial x} = \frac{\partial(\alpha_k \mathbf{f}_k^{\text{Lag}})}{\partial x} - \alpha_k \frac{\partial \mathbf{f}_k^{\text{Lag}}}{\partial x}. \tag{2.22}$$

The conservative flux terms involved in (2.22) can be discretized using a classical finite volume technique:

$$\left[\frac{\partial(\alpha_k \mathbf{f}_k)}{\partial x}\right]_i = \frac{\alpha_{k,i+\frac{1}{2}} \mathbf{F}_{k,i+\frac{1}{2}} - \alpha_{k,i-\frac{1}{2}} \mathbf{F}_{k,i-\frac{1}{2}}}{\Delta x},$$

$$\left[\frac{\partial(\alpha_k \mathbf{f}_k^{\text{Lag}})}{\partial x}\right]_i = \frac{\alpha_{k,i+\frac{1}{2}} \mathbf{F}^{\text{Lag}}_{k,i+\frac{1}{2}} - \alpha_{k,i-\frac{1}{2}} \mathbf{F}^{\text{Lag}}_{k,i-\frac{1}{2}}}{\Delta x}.$$

where $\mathbf{F}_k$ and $\mathbf{F}_k^{\text{Lag}}$ are the numerical fluxes approximating respectively $\mathbf{f}_k$ and $\mathbf{f}_k^{\text{Lag}}$. The non-conservative flux term $\alpha_k \dfrac{\partial \mathbf{f}_k^{\text{Lag}}}{\partial x}$ can be discretized, for a first-order approach, as:

$$\alpha_k \left[\frac{\partial \mathbf{f}_k^{\text{Lag}}}{\partial x}\right]_i = \alpha_{k,i} \frac{\mathbf{F}^{\text{Lag}}_{k,i+\frac{1}{2}} - \mathbf{F}^{\text{Lag}}_{k,i-\frac{1}{2}}}{\Delta x}.$$

Employing the above results and applying the first-order forward Euler method for the time derivative term $\dfrac{\partial \alpha_k \mathbf{u}_k}{\partial t}$ in (2.22) yields:

$$\begin{aligned} &\frac{(\alpha \mathbf{U})^{n+1}_{k,i} - (\alpha \mathbf{U})^{n}_{k,i}}{\Delta t} + \frac{(\alpha \mathbf{F})_{k,i+\frac{1}{2}} - (\alpha \mathbf{F})_{k,i-\frac{1}{2}}}{\Delta x} \\ = &\frac{\mathbf{F}^{\text{Lag}}_{k,i+\frac{1}{2}}\left(\alpha_{k,i+\frac{1}{2}} - \alpha_{k,i}\right) - \mathbf{F}^{\text{Lag}}_{k,i-\frac{1}{2}}\left(\alpha_{k,i-\frac{1}{2}} - \alpha_{k,i}\right)}{\Delta x}. \end{aligned} \tag{2.23}$$

which is in fact the final form of the first-order DEM/RDEM scheme for the full two-fluid model. We note that $\alpha^{n+1}_{k,i}$ in (2.23) has already been solved in Section 2.1 by (2.5) or (2.8) with the interface velocity given by the solution of a local two-fluid Riemann problem (see Section 2.3). On the other hand, the intercell value $\alpha_{k,i-\frac{1}{2}}$ at

$x = x_{i-\frac{1}{2}}$ is given by the upwind strategy

$$\alpha_{k,i-\frac{1}{2}} = \begin{cases} \alpha^n_{k,i-1}, \text{ if } D_{I,i-\frac{1}{2}} > 0, \\ \alpha^n_{k,i}, \text{ if } D_{I,i-\frac{1}{2}} < 0. \end{cases}$$

The remaining task consists in evaluating the numerical fluxes $\mathbf{F}_{k,i-\frac{1}{2}}$ and $\mathbf{F}^{\text{Lag}}_{k,i-\frac{1}{2}}$. Considering the intercell boundary partition procedure in Section 2.2 and taking into account the general principles of the DEM/RDEM approach such as reviewed in Section 2.3 concerning the one-phase and two-phase Riemann problems (see Fig. 2.4 and Fig. 2.5), the convective flux contribution $(\alpha\mathbf{F})_{k,i-\frac{1}{2}}$ can be evaluated by

$$(\alpha\mathbf{F})_{k,i-\frac{1}{2}} = \begin{cases} S^{(kk)}_{i-\frac{1}{2}}\mathbf{F}^{(kk)}_{k,i-\frac{1}{2}} + S^{(kk')}_{i-\frac{1}{2}}\mathbf{F}^{(kk')}_{k,i-\frac{1}{2}}, \text{ if } D_{I,i-\frac{1}{2}} > 0, \\ S^{(kk)}_{i-\frac{1}{2}}\mathbf{F}^{(kk)}_{k,i-\frac{1}{2}} + S^{(k'k)}_{i-\frac{1}{2}}\mathbf{F}^{(k'k)}_{k,i-\frac{1}{2}}, \text{ if } D_{I,i-\frac{1}{2}} < 0. \end{cases}$$

where $\mathbf{F}^{(kk)}_{k,i-\frac{1}{2}}$ is the numerical conservative flux of the one-phase Riemann problem RPkk evaluated on $x_{i-\frac{1}{2}}$, and $\mathbf{F}^{(kk')}_{k,i-\frac{1}{2}}$ is the numerical conservative flux of the two-phase Riemann problem RPkk'. Using the interface velocity indicator β introduced in Section 2.1, the above relation can be rearranged in the form:

$$(\alpha\mathbf{F})_{k,i-\frac{1}{2}} = S^{(kk)}_{i-\frac{1}{2}}\mathbf{F}^{(kk)}_{k,i-\frac{1}{2}} + \beta_{i-\frac{1}{2}}S^{(kk')}_{i-\frac{1}{2}}\mathbf{F}^{(kk')}_{k,i-\frac{1}{2}} + (1-\beta_{i-\frac{1}{2}})S^{(k'k)}_{i-\frac{1}{2}}\mathbf{F}^{(k'k)}_{k,i-\frac{1}{2}}, \tag{2.24}$$

and $(\alpha\mathbf{F})_{k,i+\frac{1}{2}}$ is expressed analogously. As previously performed for the topological equation in Section 2.1, the Lagrangian flux contributions in (2.23) can be written in a similar way:

$$\begin{aligned} \mathbf{F}^{\text{Lag}}_{k,i-\frac{1}{2}}\left(\alpha_{k,i-\frac{1}{2}} - \alpha_{k,i}\right) &= \beta_{i-\frac{1}{2}}\mathbf{F}^{\text{Lag}}_{k,i-\frac{1}{2}}\left(\alpha_{k,i-1} - \alpha_{k,i}\right), \\ \mathbf{F}^{\text{Lag}}_{k,i+\frac{1}{2}}\left(\alpha_{k,i+\frac{1}{2}} - \alpha_{k,i}\right) &= (1-\beta_{i-\frac{1}{2}})\mathbf{F}^{\text{Lag}}_{k,i+\frac{1}{2}}\left(\alpha_{k,i+1} - \alpha_{k,i}\right). \end{aligned}$$

and even expressed in terms of partitioned sub-surfaces:

$$\begin{aligned} \mathbf{F}^{\text{Lag}}_{k,i-\frac{1}{2}}\left(\alpha_{k,i-\frac{1}{2}} - \alpha_{k,i}\right) &= \beta_{i-\frac{1}{2}}\mathbf{F}^{\text{Lag}}_{k,i-\frac{1}{2}}\left(S^{(kk')}_{i-\frac{1}{2}} - S^{(k'k)}_{i-\frac{1}{2}}\right), \\ \mathbf{F}^{\text{Lag}}_{k,i+\frac{1}{2}}\left(\alpha_{k,i+\frac{1}{2}} - \alpha_{k,i}\right) &= -(1-\beta_{i-\frac{1}{2}})\mathbf{F}^{\text{Lag}}_{k,i+\frac{1}{2}}\left(S^{(kk')}_{i+\frac{1}{2}} - S^{(k'k)}_{i+\frac{1}{2}}\right). \end{aligned}$$

Since $S^{(kk')}$ is associated to the local Riemann problem RPkk' and $S^{(k'k)}$ to RP$k'k$, the Lagrangian flux contributions are modified as follows:

$$\begin{aligned}
\mathbf{F}^{\mathrm{Lag}}_{k,i-\frac{1}{2}}\left(\alpha_{k,i-\frac{1}{2}}-\alpha_{k,i}\right) &= \beta_{i-\frac{1}{2}}\left(\mathbf{F}^{\mathrm{Lag},(kk')}_{k,i-\frac{1}{2}}S^{(kk')}_{i-\frac{1}{2}}-\mathbf{F}^{\mathrm{Lag},(k'k)}_{k,i-\frac{1}{2}}S^{(k'k)}_{i-\frac{1}{2}}\right),\\
\mathbf{F}^{\mathrm{Lag}}_{k,i+\frac{1}{2}}\left(\alpha_{k,i+\frac{1}{2}}-\alpha_{k,i}\right) &= -(1-\beta_{i-\frac{1}{2}})\left(\mathbf{F}^{\mathrm{Lag},(kk')}_{k,i+\frac{1}{2}}S^{(kk')}_{i+\frac{1}{2}}-\mathbf{F}^{\mathrm{Lag},(k'k)}_{k,i+\frac{1}{2}}S^{(k'k)}_{i+\frac{1}{2}}\right).
\end{aligned} \tag{2.25}$$

where $\mathbf{F}^{\mathrm{Lag},(kk')}_{k,i-\frac{1}{2}}$ is the numerical Lagrangian flux evaluated on the numerical interface (contact discontinuity for SG-EOS or reactive shock for reacting gases) of the two-phase Riemann problem RPkk' at intercell boundary $x_{i-\frac{1}{2}}$. The Rankine-Hugoniot conditions ensure the equality:

$$\mathbf{F}^{\mathrm{Lag},(kk')}_{k,i-\frac{1}{2}} = \mathbf{F}^{\mathrm{Lag},(kk')}_{k',i-\frac{1}{2}}. \tag{2.26}$$

2.4.1 Summary of the DEM/RDEM scheme

Inserting the relations (2.24) and (2.25) into (2.23) yields an expression for the DEM/RDEM scheme in terms of partitioned sub-surfaces, which can be summarized as follows:

$$\begin{bmatrix}\alpha\\ \alpha\mathbf{U}\end{bmatrix}^{n+1}_{k,i} = \begin{bmatrix}\alpha\\ \alpha\mathbf{U}\end{bmatrix}^{n}_{k,i} + \frac{\Delta t}{\Delta x}\left[(\mathscr{R}^{C}_{k,i-\frac{1}{2}}+\mathscr{R}^{\mathrm{Lag}}_{k,i-\frac{1}{2},i}) - (\mathscr{R}^{C}_{k,i+\frac{1}{2}}+\mathscr{R}^{\mathrm{Lag}}_{k,i+\frac{1}{2},i})\right], \tag{2.27}$$

where $\mathscr{R}^{C}_{k,i\pm\frac{1}{2}}$ denotes the conservative flux contribution at intercell boundary $x_{i\pm\frac{1}{2}}$. The explicit expression for $\mathscr{R}^{C}_{k,i-\frac{1}{2}}$ reads:

$$\mathscr{R}^{C}_{k,i-\frac{1}{2}} = \begin{bmatrix} 0\\ S^{(kk)}_{i-\frac{1}{2}}\mathbf{F}^{(kk)}_{k,i-\frac{1}{2}} + \beta_{i-\frac{1}{2}}S^{(kk')}_{i-\frac{1}{2}}\mathbf{F}^{(kk')}_{k,i-\frac{1}{2}} + (1-\beta_{i-\frac{1}{2}})S^{(k'k)}_{i-\frac{1}{2}}\mathbf{F}^{(k'k)}_{k,i-\frac{1}{2}}\end{bmatrix}, \tag{2.28}$$

where the conservative flux contribution for the volume fraction vanishes. Similarly, $\mathscr{R}^{\mathrm{Lag}}_{k,i\pm\frac{1}{2},i}$ denotes the Lagrangian flux contribution to cell i at $x_{i\pm\frac{1}{2}}$. The explicit expression for $\mathscr{R}^{\mathrm{Lag}}_{k,i-\frac{1}{2},i}$ reads:

$$\mathscr{R}^{\mathrm{Lag}}_{k,i-\frac{1}{2},i} = -\beta_{i-\frac{1}{2}}\begin{bmatrix} -(S^{(kk')}_{i-\frac{1}{2}} - S^{(k'k)}_{i-\frac{1}{2}})D_{I,i-\frac{1}{2}}\\ S^{(kk')}_{i-\frac{1}{2}}\mathbf{F}^{\mathrm{Lag},(kk')}_{k,i-\frac{1}{2}} - S^{(k'k)}_{i-\frac{1}{2}}\mathbf{F}^{\mathrm{Lag},(k'k)}_{k,i-\frac{1}{2}}\end{bmatrix}, \tag{2.29}$$

while $\mathscr{R}^{\text{Lag}}_{k,i+\frac{1}{2},i}$ is given by:

$$\mathscr{R}^{\text{Lag}}_{k,i+\frac{1}{2},i} = (1-\beta_{i+\frac{1}{2}}) \begin{bmatrix} -(S^{(kk')}_{i+\frac{1}{2}} - S^{(k'k)}_{i+\frac{1}{2}})D_{I,i+\frac{1}{2}} \\ S^{(kk')}_{i+\frac{1}{2}}\mathbf{F}^{\text{Lag},(kk')}_{k,i+\frac{1}{2}} - S^{(k'k)}_{i+\frac{1}{2}}\mathbf{F}^{\text{Lag},(k'k)}_{k,i+\frac{1}{2}} \end{bmatrix}. \tag{2.30}$$

Considering the cells i and $i-1$, it can be checked the Lagrangian flux is non-conservative by computing on $x_{i-\frac{1}{2}}$:

$$\mathscr{R}^{\text{Lag}}_{k,i-\frac{1}{2},i-1} - \mathscr{R}^{\text{Lag}}_{k,i-\frac{1}{2},i} = \begin{bmatrix} -(S^{(kk')}_{i-\frac{1}{2}} - S^{(k'k)}_{i-\frac{1}{2}})D_{I,i-\frac{1}{2}} \\ S^{(kk')}_{i-\frac{1}{2}}\mathbf{F}^{\text{Lag},(kk')}_{k,i-\frac{1}{2}} - S^{(k'k)}_{i-\frac{1}{2}}\mathbf{F}^{\text{Lag},(k'k)}_{k,i-\frac{1}{2}} \end{bmatrix} \neq 0. \tag{2.31}$$

However, adding the Lagrangian flux contributions together for one cell for both phases yields:

$$\sum_k \mathscr{R}^{\text{Lag}}_{k,i-\frac{1}{2},i} = \sum_k \mathscr{R}^{\text{Lag}}_{k,i-\frac{1}{2},i-1} = 0. \tag{2.32}$$

The DEM/RDEM method thus remains conservative for the two-fluid ensemble ($\Sigma_1 + \Sigma_2$). This property is fundamental for combustion computations in our applications. The various conservative and Lagrangian fluxes involved in the DEM/RDEM scheme are graphically summarized in Fig. 2.9.

2.4.2 Limiting case of zero interface velocity

When $D_{I,i-\frac{1}{2}} = 0$ and/or $D_{I,i+\frac{1}{2}} = 0$, the DEM/RDEM scheme (2.27) is still valid with the following specific identities for the Lagrangian fluxes:

$$\mathbf{F}^{\text{Lag},(kk')}_{k,i-\frac{1}{2}} = \mathbf{F}^{\text{Lag},(kk')}_{k',i-\frac{1}{2}} = \mathbf{F}^{(kk')}_{k,i-\frac{1}{2}} = \mathbf{F}^{(kk')}_{k',i-\frac{1}{2}}.$$

2.4.3 Limiting case of zero two-fluid contact

This limiting case means that there is no numerical two-phase contact at the inter-cell boundary $x_{i-\frac{1}{2}}$. In fact, when the volume fraction is uniform for two adjacent cell elements, even though flow properties can be different, it is considered in the DEM/RDEM approach that no numerical interface is present. In that particular case, the conventional Godunov's method is recovered from (2.27) for both phases:

$$\mathbf{U}^{n+1}_{k,i} = \mathbf{U}^{n}_{k,i} + \frac{\Delta t}{\Delta x}\left(\mathbf{F}^{(kk)}_{k,i-\frac{1}{2}} - \mathbf{F}^{(kk)}_{k,i+\frac{1}{2}}\right),$$

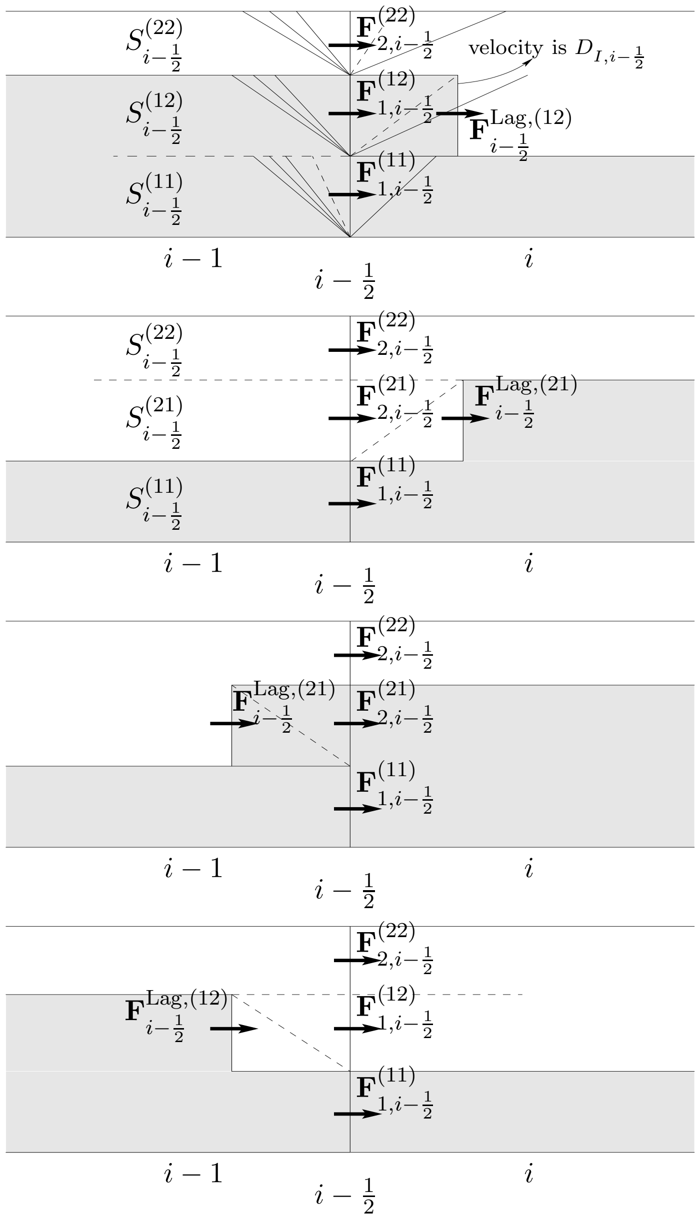

Figure 2.9: Conservative and Lagrangian fluxes at the intercell boundary $x_{i-\frac{1}{2}}$ for cases of different phase contacts and interface propagation directions. The phase Σ_1 is shaded whereas the phase Σ_2 is in white. The characteristic curves are not drawn in $x-t$ space here. They give a qualitative illustration of involved wave propagations in DEM/RDEM method. The Lagrangian flux $\mathbf{F}^{\text{Lag}}_{i-\frac{1}{2}}$ is generated at the numerical phase interface, whose value is evaluated on the corresponding characteristic curve.

The DEM/RDEM method can thus be regarded as an extension of Godunov's method to two-phase problems.

2.5 Time step investigation

As already mentioned in Section 2.3, in order for wave interaction not to occur between the waves generated by the local Riemann problems, the nonlinear stability condition of the DEM/RDEM scheme is

$$\Delta t \leq \frac{1}{2}\frac{\Delta x}{\delta^n_{\max}}, \ \textit{i.e.}\ \mathrm{CFL} \leq \frac{1}{2}$$

where $\delta^n_{\max}$ is the maximum wave speed in the whole computational domain. This time step condition can be relaxed to

$$\mathrm{CFL} \leq 1 \tag{2.33}$$

if assuming no wave acceleration and taking into account the aspects detailed in the following subsections.

2.5.1 Condition on the volume fraction

Local Extremum Diminishing (LED) scheme

A class of monotonic schemes has been developed in [Jameson 95, Jameson 01], based on the Local Extremum Diminishing (LED) property. These schemes, when used to discretize the averaged topological equation, satisfy the discrete maximum principle, which states that a local maximum can not increase and a local minimum can not decrease. Therefore, this class of schemes precludes from developing numerical oscillations. It is worthwhile to notice that a one-dimensional scheme which is LED is also TVD [Jameson 95]. The converse is not true, since when shifting a pair of adjacent maxima and minima, the total variation is unchanged, whilst the local maximum is increased [Jameson 01]. Furthermore, LED ideas can be readily extended to multi-dimensional case, whilst TVD remains unclear except for one-dimensional problems. LED property is in fact widely used in this work to develop the upwind downwind-controlled splitting approach (UDCS) for multi-dimensional two-phase problems with unstructured grids, including reacting problems involving mass transfer phenomenon (Chapter 3).

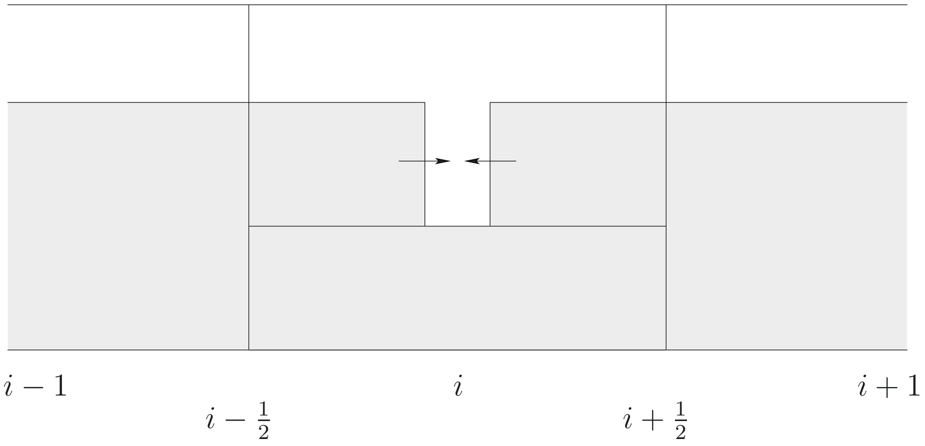

Figure 2.10: Evolution of volume fraction in DEM/RDEM approach with opposite interface velocity linked to adjacent intercell boundaries. New volume fraction α_i^{n+1} in cell element i at time t^{n+1} can not exceed the value of $\max\{\alpha_{i-1}^n, \alpha_i^n, \alpha_{i+1}^n\}$ according to LED property.

LED condition on the volume fraction

The LED property is introduced in this section to emphasize that the DEM/RDEM approach ought not to generate any new local extremum of volume fraction. In one space dimension, this condition is satisfied by (2.33) as far as the numerical interface velocity D_I is unidirectional in the whole computational domain. Proof of this is straightforward using the discretization of the equation (1.16) developed in Section 2.1.

On the other hand, when the numerical interface velocity D_I is not unidirectional, additional condition on the time step Δt should be taken into consideration. For instance, in Fig. 2.10, due to the contribution of intercell boundaries $x_{i-\frac{1}{2}}$ and $x_{i+\frac{1}{2}}$, an amount of generated volume of the same sign is added to cell i from both sides. It is then possible that condition (2.33) is no longer sufficient to ensure the following LED property is satisfied:

$$\min\left\{\alpha_{i-1}^n, \alpha_i^n, \alpha_{i+1}^n\right\} \leq \alpha_i^{n+1} \leq \max\left\{\alpha_{i-1}^n, \alpha_i^n, \alpha_{i+1}^n\right\}. \tag{2.34}$$

In order to avoid such a problem, the following additional condition is imposed in this work for any cell element i:

$$\Delta t \leq \frac{\Delta x}{\max\{D_{I,i-\frac{1}{2}}, 0\} + \left|\min\{D_{I,i+\frac{1}{2}}, 0\}\right|}. \tag{2.35}$$

It is emphasized that the time step restriction (2.35) is a sufficient (but not necessary) condition to satisfy (2.34) [Tang 12].

2.5.2 Acoustic wave contribution over numerical interface

When CFL $> \frac{1}{2}$, wave interaction occurs within computational cells, as for the second version of Godunov's method (see [Toro 97]). While assuming in Godunov's method that no wave acceleration takes place after the wave interaction (this is a linear assumption), the numerical fluxes at the intercell boundaries can be considered constant within the time step Δt. This property is still true in DEM/RDEM approach for two phase problems at the intercell boundaries. On the other hand for the Lagrangian flux on the moving numerical interface, this property is no longer true.

Consider the simple case illustrated in Fig. 2.11. The characteristic curves of the Riemann problems RP12 at $x_{i-\frac{1}{2}}$ and RP22 at $x_{i+\frac{1}{2}}$ in the $x-t$ plane cross each over in the volume fraction diagram. The value of the Lagrangian flux and the numerical interface velocity from $x_{i-\frac{1}{2}}$ over the characteristic curve $\dot{x} = D_{I,i-\frac{1}{2}}$ is modified from time t^m, the time at which the numerical interface interacts with the left-going nonlinear wave coming from the intercell boundary $x_{i+\frac{1}{2}}$. Our experience with a wide range of test cases shows that this kind of interaction between a nonlinear wave and a numerical interface can be neglected in the DEM/RDEM approach without creating serious problems. Robustness problems appear in extreme situations only, such as in the case of a very strong shock wave interacting with a fast traveling interface (*e.g.* detonations and fast deflagrations). The CFL value should be decreased in this case (see in particular the subsequent test case in Section 2.8.2).

2.6 Extension to the limited second-order approach

Higher-accuracy for scheme (2.27) is achieved by improving the accuracy of the intercell flux contributions $\mathscr{R}^C$ and $\mathscr{R}^{\text{Lag}}$. Such a second-order extension for the DEM/RDEM scheme has been previously proposed in [Abgrall 03] and the details of this version of the DEM/RDEM approach are reviewed in the present Section.

Note that a computationally more efficient and robust version of the second-order DEM/RDEM method will be proposed in Chapter 3 based on the upwind downwind-controlled splitting (UDCS) approach [Tang 12], whose basic idea is to perform an extra phase splitting step, right after using first-order DEM/RDEM scheme, with the aim of achieving higher order accuracy of interfaces. As will be observed in the last Section 2.8 of this chapter, devoted to some 1D applications of the DEM/RDEM approach, the "conventional" second-order formulation reviewed in this Section is not sufficiently accurate for our targeted applications, which motivates the original development of the UDCS approach proposed in Chapter 3.

2.6.1 Preliminary remarks on volume fraction reconstruction

Fig. 2.12 illustrates the (quasi) second-order reconstruction process for the volume fractions α_1 and α_2 in two adjacent computational cells $i-1$ and i. The interested reader is referred to Appendix A for a few basics on variable reconstruction. The reconstructed volume fractions at the intercell boundary $x_{i-\frac{1}{2}}$ are given by:

$$\begin{aligned}\alpha_{k,i-1,i-\frac{1}{2}} &= \alpha_{k,i-1} + \frac{1}{2}\Delta x \Delta_{i-1},\\ \alpha_{k,i,i-\frac{1}{2}} &= \alpha_{k,i} - \frac{1}{2}\Delta x \Delta_{i}\end{aligned}$$

where the slope Δ_i inside cell i is computed as:

$$\Delta_i = \frac{\alpha_{k,i+1}-\alpha_{k,i}}{\Delta x}\phi\left(\frac{\alpha_{k,i}-\alpha_{k,i-1}}{\alpha_{k,i+1}-\alpha_{k,i}}\right) \tag{2.36}$$

with ϕ a limiter function. In this work, unless specified otherwise, the minmod limiter is used:

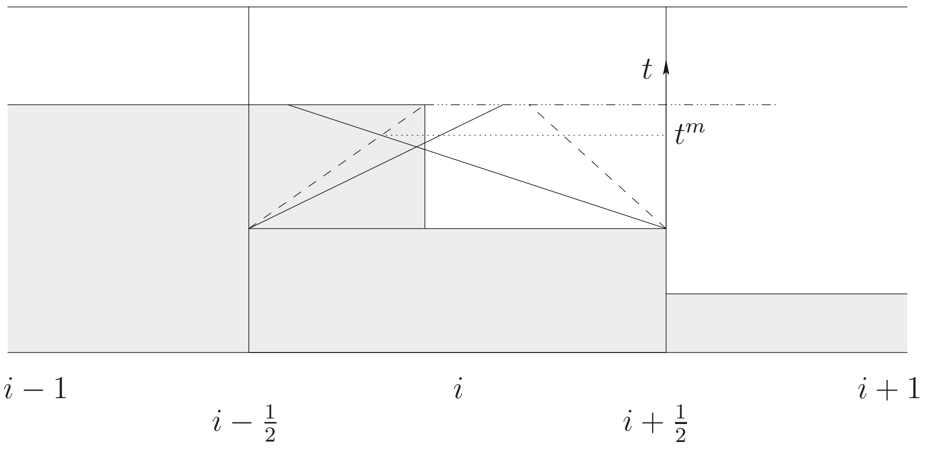

Figure 2.11: The wave interaction bewteen right-going numerical interface from $x_{i-\frac{1}{2}}$ and left-going shock wave from $x_{i+\frac{1}{2}}$. The value of Lagrangian flux (and the numerical interface velocity) from $x_{i-\frac{1}{2}}$ over the characteristic curve $\dot{x} = D_{I,i-\frac{1}{2}}$ is modified at the time t^m due to the shock wave strength.

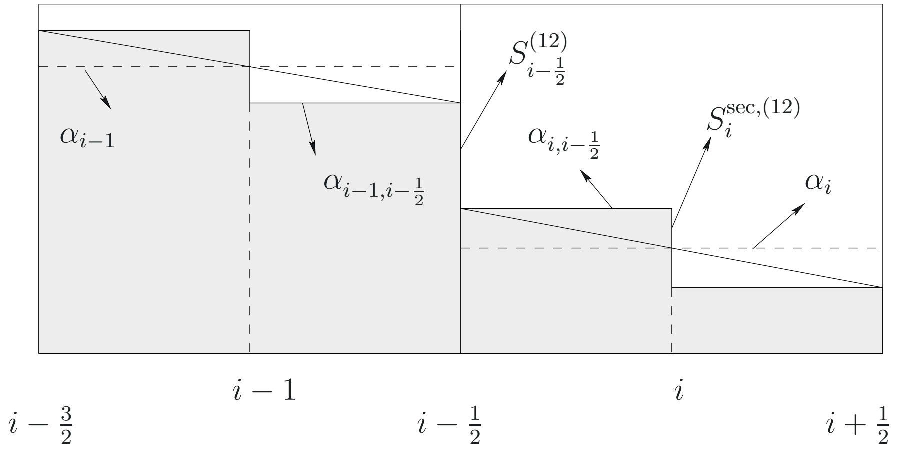

Figure 2.12: (Quasi) second-order reconstruction for volume fractions. The phase Σ_1 is shaded whereas the phase Σ_2 is in white. Two constant values are used instead of linear reconstruction function inside cells. Hence, internal discontinuity of numerical phase interface appears at each cell center. So-called internal Riemann problem is solved with the aim of taking account of the internal wave propagations.

$$\phi(\theta_i) = \max(0, \min(1, \theta_i)) = \begin{cases} 0 & \text{if } \theta_i \leq 0, \\ \theta_i & \text{if } 0 \leq \theta_i \leq 1, \\ 1 & \text{if } \theta_i \geq 1. \end{cases}$$

It follows from (2.6.1) that the partition of intercell boundary with phase contacts (2.11)-(2.14) needs to be rewritten as:

$$\begin{aligned} S^{(11)}_{i-\frac{1}{2}} &= \min\left\{\alpha_{1,i-1,i-\frac{1}{2}}, \alpha_{1,i,i-\frac{1}{2}}\right\}, \\ S^{(22)}_{i-\frac{1}{2}} &= \min\left\{\alpha_{2,i-1,i-\frac{1}{2}}, \alpha_{2,i,i-\frac{1}{2}}\right\}, \\ S^{(12)}_{i-\frac{1}{2}} &= \max\left\{0, \alpha_{1,i-1,i-\frac{1}{2}} - \alpha_{1,i,i-\frac{1}{2}}\right\} = \max\left\{0, \alpha_{2,i,i-\frac{1}{2}} - \alpha_{2,i-1,i-\frac{1}{2}}\right\}, \\ S^{(21)}_{i-\frac{1}{2}} &= \max\left\{0, \alpha_{1,i,i-\frac{1}{2}} - \alpha_{1,i-1,i-\frac{1}{2}}\right\} = \max\left\{0, \alpha_{2,i-1,i-\frac{1}{2}} - \alpha_{2,i,i-\frac{1}{2}}\right\}. \end{aligned} \tag{2.37}$$

The following additional internal two-phase sub-surfaces for cell i (see Fig. 2.12) are also defined:

$$\begin{aligned} S_i^{\mathrm{sec},(12)} &= \max\left\{0, \alpha_{1,i,i-\frac{1}{2}} - \alpha_{1,i,i+\frac{1}{2}}\right\} = \max\left\{0, \alpha_{2,i,i+\frac{1}{2}} - \alpha_{2,i,i-\frac{1}{2}}\right\}, \\ S_i^{\mathrm{sec},(21)} &= \max\left\{0, \alpha_{1,i,i+\frac{1}{2}} - \alpha_{1,i,i-\frac{1}{2}}\right\} = \max\left\{0, \alpha_{2,i,i-\frac{1}{2}} - \alpha_{2,i,i+\frac{1}{2}}\right\}. \end{aligned}$$

We refer to Appendix B for the second-order DEM/RDEM discretization for the scalar topological equation, which is a direct extension of the first-order method presented in Section 2.1. In what follows we concentrate on the cell-internal discontinuity and the related Lagrangian flux contributions to the second-order DEM/RDEM for full two-fluid system. Note that both conservative and non-conservative flux contributions of intercell discontinuity can be calculated analogously as in Section 2.4.

2.6.2 Internal Lagrangian flux contributions

Using the reconstruction illustrated in Fig. 2.12, an additional two-phase Riemann problem should be resolved on the internal discontinuity located at x_i for cell i. Briefly speaking, the contribution of this internal Riemann problem can be obtained by carrying out successively:

- First, a whole computational cell element can be considered to be divided into two semi-cells (with respect to the internal discontinuity), and the first-order DEM/RDEM approach is performed for these two semi-cells. This can in fact be regarded as a first numerical averaging for separate phases.

- Next, we merge these two semi-cells into the original entire one, *i.e.* we complete a second averaging of the separate phase variables for the whole computational element. As a consequence, the conservative fluxes corresponding to the internal semi-cell boundary do not give any contribution to each phase. The only flux contribution to be taken into account is linked to the internal Lagrangian flux.

This internal Lagrangian flux contribution, denoted here by $\delta\mathscr{R}^{\text{Lag}}_{k,i}$ for phase Σ_k, can be evaluated on the sub-surface $S_i^{\text{sec},(kk')}$ or $S_i^{\text{sec},(k'k)}$ by (see Section 2.4):

$$\delta\mathscr{R}^{\text{Lag}}_{k,i} = -\begin{bmatrix} -(S_i^{\text{sec},(kk')} - S_i^{\text{sec},(k'k)})D_{I,i} \\ S_i^{\text{sec},(kk')}\mathbf{F}_i^{\text{Lag},(kk')} - S_i^{\text{sec},(k'k)}\mathbf{F}_i^{\text{Lag},(k'k)} \end{bmatrix}. \tag{2.38}$$

However, the extension of this idea of internal Riemann problem solution to multi-dimensional unstructured grids remains unclear. In fact, the very definition of internal discontinuity of the volume fraction in the case of unstructured meshes is not straightforward. For this reason, instead of considering one internal Riemann problem per element (inside the element), we consider, for each element, one internal Riemann problem for each intercell boundary, as represented in Fig. 2.13. Although computationally more expensive than the previous approach, the extension to unstructured grids is straightforward. Let us consider the representation of Fig. 2.13. Basically, three constant values are present inside each computational cell. For instance, $\alpha_{i,i-\frac{1}{2}}$,

α_i and $\alpha_{i,i+\frac{1}{2}}$ are reconstructed values for cell i in Fig. 2.13. Note that this reconstruction is equivalent to the one in Fig. 2.12, when a second-order TVD limiter is used for gradient calculation. Indeed, we have in this case

$$S^{\text{sec},(12)}_{i,i-\frac{1}{2}} = \max\left\{0, \alpha_{1,i,i-\frac{1}{2}} - \alpha_{1,i}\right\} = \max\left\{0, \alpha_{2,i} - \alpha_{2,i,i-\frac{1}{2}}\right\} = \frac{1}{2}S^{\text{sec},(12)}_{i}, \tag{2.39}$$

$$S^{\text{sec},(21)}_{i,i-\frac{1}{2}} = \max\left\{0, \alpha_{1,i} - \alpha_{1,i,i-\frac{1}{2}}\right\} = \max\left\{0, \alpha_{2,i,i-\frac{1}{2}} - \alpha_{2,i}\right\} = \frac{1}{2}S^{\text{sec},(21)}_{i}, \tag{2.40}$$

and

$$S^{\text{sec},(12)}_{i,i+\frac{1}{2}} = \max\left\{0, \alpha_{1,i} - \alpha_{1,i,i+\frac{1}{2}}\right\} = \max\left\{0, \alpha_{2,i,i+\frac{1}{2}} - \alpha_{2,i}\right\} = \frac{1}{2}S^{\text{sec},(12)}_{i}, \tag{2.41}$$

$$S^{\text{sec},(21)}_{i,i+\frac{1}{2}} = \max\left\{0, \alpha_{1,i,i+\frac{1}{2}} - \alpha_{1,i}\right\} = \max\left\{0, \alpha_{2,i} - \alpha_{2,i,i+\frac{1}{2}}\right\} = \frac{1}{2}S^{\text{sec},(21)}_{i}, \tag{2.42}$$

Hence, for the intercell boundary $x_{i-\frac{1}{2}}$, three two-phase Riemann problems are considered:

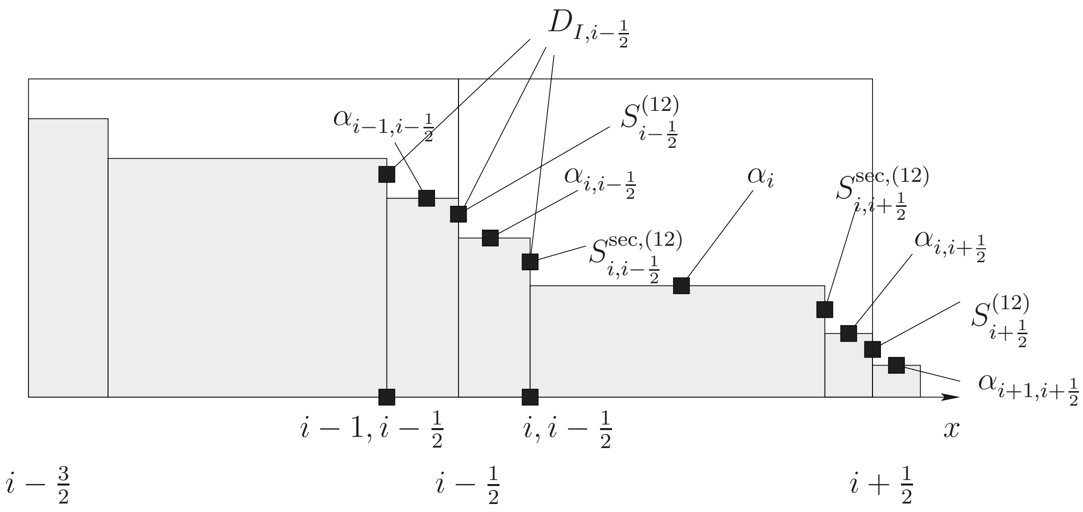

Figure 2.13: Alternative representation of second-order reconstruction for volume fractions. The phase Σ_1 is shaded whereas the phase Σ_2 is in white. Three constant values are used instead of two in Fig. 2.12. Hence, for the intercell boundary $x_{i-\frac{1}{2}}$, three two-phase Riemann problems are considered: the intercell Riemann problem at $x = x_{i-\frac{1}{2}}$ on $S^{(12)}_{i-\frac{1}{2}}$, the internal Riemann problem at $x = x_{i-1,i-\frac{1}{2}}$ on $S^{\text{sec},(12)}_{i-1,i-\frac{1}{2}}$, and the internal Riemann problem at $x = x_{i,i-\frac{1}{2}}$ on $S^{\text{sec},(12)}_{i,i-\frac{1}{2}}$. Their solutions can be all evaluated by the one of the intercell two-phase Riemann problem at $x = x_{i-\frac{1}{2}}$.

- the intercell Riemann problem at $x = x_{i-\frac{1}{2}}$ on $S^{(kk')}_{i-\frac{1}{2}}$ (or $S^{(k'k)}_{i-\frac{1}{2}}$),
- the internal Riemann problem at $x = x_{i-1,i-\frac{1}{2}}$ on $S^{\text{sec},(kk')}_{i-1,i-\frac{1}{2}}$ (or $S^{\text{sec},(k'k)}_{i-1,i-\frac{1}{2}}$),
- and the internal Riemann problem at $x = x_{i,i-\frac{1}{2}}$ on $S^{\text{sec},(kk')}_{i,i-\frac{1}{2}}$ (or $S^{\text{sec},(k'k)}_{i,i-\frac{1}{2}}$).

The internal Lagrangian flux contribution $\delta\mathscr{R}^{\text{Lag}}_{k,i}$ for phase Σ_k can then be generally evaluated on the sub-surfaces $S^{\text{sec},(kk')}_{i,i-\frac{1}{2}}$ (or $S^{\text{sec},(k'k)}_{i,i-\frac{1}{2}}$) and $S^{\text{sec},(kk')}_{i,i+\frac{1}{2}}$ (or $S^{\text{sec},(k'k)}_{i,i+\frac{1}{2}}$) by

$$\delta\mathscr{R}^{\text{Lag}}_{k,i} = \delta\mathscr{R}^{\text{Lag}}_{k,i-\frac{1}{2},i} + \delta\mathscr{R}^{\text{Lag}}_{k,i+\frac{1}{2},i} \tag{2.43}$$

where

$$\delta\mathscr{R}^{\text{Lag}}_{k,i-\frac{1}{2},i} = -\begin{bmatrix} -(S^{\text{sec},(kk')}_{i,i-\frac{1}{2}} - S^{\text{sec},(k'k)}_{i,i-\frac{1}{2}})D_{I,i,i-\frac{1}{2}} \\ S^{\text{sec},(kk')}_{i,i-\frac{1}{2}}\mathbf{F}^{\text{Lag},(kk')}_{i,i-\frac{1}{2}} - S^{\text{sec},(k'k)}_{i,i-\frac{1}{2}}\mathbf{F}^{\text{Lag},(k'k)}_{i,i-\frac{1}{2}} \end{bmatrix}, \tag{2.44}$$

and

$$\delta\mathscr{R}^{\text{Lag}}_{k,i+\frac{1}{2},i} = -\begin{bmatrix} -(S^{\text{sec},(kk')}_{i,i+\frac{1}{2}} - S^{\text{sec},(k'k)}_{i,i+\frac{1}{2}})D_{I,i,i+\frac{1}{2}} \\ S^{\text{sec},(kk')}_{i,i+\frac{1}{2}}\mathbf{F}^{\text{Lag},(kk')}_{i,i+\frac{1}{2}} - S^{\text{sec},(k'k)}_{i,i+\frac{1}{2}}\mathbf{F}^{\text{Lag},(k'k)}_{i,i+\frac{1}{2}} \end{bmatrix}. \tag{2.45}$$

If setting

$$\begin{aligned} &D_{I,i,i-\frac{1}{2}} = D_{I,i,i+\frac{1}{2}} = D_{I,i}, \\ &\mathbf{F}^{\text{Lag},(kk')}_{i,i-\frac{1}{2}} = \mathbf{F}^{\text{Lag},(kk')}_{i,i+\frac{1}{2}} = \mathbf{F}^{\text{Lag},(kk')}_{i}, \\ &\mathbf{F}^{\text{Lag},(k'k)}_{i,i-\frac{1}{2}} = \mathbf{F}^{\text{Lag},(k'k)}_{i,i+\frac{1}{2}} = \mathbf{F}^{\text{Lag},(k'k)}_{i}, \end{aligned}$$

formulation (2.43) reduces to (2.38).

An alternative approximation of the internal Riemann problem solutions can be found in [Beccantini 10b]: the three Riemann problems on $x = x_{i-\frac{1}{2}}$, $x = x_{i-1,i-\frac{1}{2}}$ and $x = x_{i,i-\frac{1}{2}}$ have the same solutions which are evaluated by the intercell two-phase Riemann problem at $x = x_{i-\frac{1}{2}}$ on $S^{(kk')}_{i-\frac{1}{2}}$ (or $S^{(k'k)}_{i-\frac{1}{2}}$). (2.44) and (2.45) can then be rewritten as

$$\delta\mathscr{R}^{\text{Lag}}_{k,i-\frac{1}{2},i} = -\begin{bmatrix} -(S^{\text{sec},(kk')}_{i,i-\frac{1}{2}} - S^{\text{sec},(k'k)}_{i,i-\frac{1}{2}})D_{I,i-\frac{1}{2}} \\ S^{\text{sec},(kk')}_{i,i-\frac{1}{2}}\mathbf{F}^{\text{Lag},(kk')}_{i-\frac{1}{2}} - S^{\text{sec},(k'k)}_{i,i-\frac{1}{2}}\mathbf{F}^{\text{Lag},(k'k)}_{i-\frac{1}{2}} \end{bmatrix}, \tag{2.46}$$

and

$$\delta\mathscr{R}^{\text{Lag}}_{k,i+\frac{1}{2},i} = -\begin{bmatrix} -(S^{\text{sec},(kk')}_{i,i+\frac{1}{2}} - S^{\text{sec},(k'k)}_{i,i+\frac{1}{2}})D_{I,i+\frac{1}{2}} \\ S^{\text{sec},(kk')}_{i,i+\frac{1}{2}}\mathbf{F}^{\text{Lag},(kk')}_{i+\frac{1}{2}} - S^{\text{sec},(k'k)}_{i,i+\frac{1}{2}}\mathbf{F}^{\text{Lag},(k'k)}_{i+\frac{1}{2}} \end{bmatrix}. \tag{2.47}$$

The Lagrangian flux formulation defined by (2.46) and (2.47) can be readily extended to multi-dimensional problems (see Section 2.7), since it only involves the Riemann problem solutions at intercell boundaries and the internal sub-surfaces can be locally evaluated from each intercell boundary. An extra benefit of the scheme defined with (2.46) and (2.47) in one space dimension is the computational efficiency, since the additional internal Riemann problem solution is no longer required.

2.6.3 Time marching

The semi-discrete DEM/RDEM method using the (quasi) second-order space reconstruction described in the previous section takes the form:

$$\frac{\mathrm{d}}{\mathrm{d}t}\begin{bmatrix}\alpha \\ \alpha\mathbf{U}\end{bmatrix}_{k,i} = \frac{1}{\Delta x}\left[(\mathscr{R}^{C}_{k,i-\frac{1}{2}} + \mathscr{R}^{\text{Lag}}_{k,i-\frac{1}{2},i}) - (\mathscr{R}^{C}_{k,i+\frac{1}{2}} + \mathscr{R}^{\text{Lag}}_{k,i+\frac{1}{2},i})\right] + \frac{1}{\Delta x}\delta\mathscr{R}^{\text{Lag}}_{k,i}. \tag{2.48}$$

The first-order Euler method and a second-order Runge-Kutta (RK) stepping scheme are used in this work for time integration.

First-order forward Euler method

Applying the first-order forward Euler method to (2.48) yields the following fully discrete scheme:

$$\begin{bmatrix}\alpha \\ \alpha\mathbf{U}\end{bmatrix}^{n+1}_{k,i} = \begin{bmatrix}\alpha \\ \alpha\mathbf{U}\end{bmatrix}^{n}_{k,i} + \frac{\Delta t}{\Delta x}\left[(\mathscr{R}^{C}_{k,i-\frac{1}{2}} + \mathscr{R}^{\text{Lag}}_{k,i-\frac{1}{2},i}) - (\mathscr{R}^{C}_{k,i+\frac{1}{2}} + \mathscr{R}^{\text{Lag}}_{k,i+\frac{1}{2},i})\right] + \frac{\Delta t}{\Delta x}\delta\mathscr{R}^{\text{Lag}}_{k,i}. \tag{2.49}$$

This scheme is non-linearly stable for

$$\Delta t \leq \frac{1}{4}\frac{\Delta x}{\delta^{n}_{\max}}, \ \ i.e. \text{ CFL} \leq \frac{1}{4}, \tag{2.50}$$

where $\delta^{n}_{\max}$ is the maximum wave speed involved in the whole computational domain. Condition (2.50) guarantees that no wave propagation occurs in the entire computational domain (see [Toro 97]). In fact, the scheme remains stable as long as the wave propagation process does not modify the time-averaged fluxes at intercell and internal boundaries. This stability region can thus be relaxed to

$$\Delta t \leq \frac{1}{2}\frac{\Delta x}{\delta^n_{\max}}, \ \ i.e.\ \mathrm{CFL} \leq \frac{1}{2}, \tag{2.51}$$

provided that we assume no wave acceleration takes place resulting from the wave interaction [Toro 97], and that the elements previously discussed in Section 2.5.2 can be neglected.

Predictor-corrector method

A second-order RK scheme in predictor-corrector formulation is also implemented for time-integration, as an alternative to the previous first-order Euler explicit time-marching. For an ordinary differential equation linked to a semi-discrete numerical scheme

$$\frac{\mathrm{d}Q_i}{\mathrm{d}t} = \mathscr{H}(Q(t);i),$$

the two-stage RK approach reads:

$$\begin{aligned} Q_i^{n+\frac{1}{2}} &= Q_i^n + \frac{1}{2}\Delta t \mathscr{H}(Q^n;i), \\ Q_i^{n+1} &= Q_i^n + \Delta t \mathscr{H}(Q^{n+\frac{1}{2}};i). \end{aligned} \tag{2.52}$$

In the case of DEM/RDEM approach, the RK2 method (2.52) becomes:

- predictor-step:

$$\begin{bmatrix} \alpha \\ \alpha \mathbf{U} \end{bmatrix}^{n+\frac{1}{2}}_{k,i} = \begin{bmatrix} \alpha \\ \alpha \mathbf{U} \end{bmatrix}^{n}_{k,i} + \frac{1}{2}\frac{\Delta t}{\Delta x}\left[(\mathscr{R}^{C,n}_{k,i-\frac{1}{2}} + \mathscr{R}^{\mathrm{Lag},n}_{k,i-\frac{1}{2},i}) - (\mathscr{R}^{C,n}_{k,i+\frac{1}{2}} + \mathscr{R}^{\mathrm{Lag},n}_{k,i+\frac{1}{2},i}) \right] + \frac{1}{2}\frac{\Delta t}{\Delta x}\delta \mathscr{R}^{\mathrm{Lag},n}_{k,i}. \tag{2.53}$$

- corrector-step:

$$\begin{bmatrix} \alpha \\ \alpha \mathbf{U} \end{bmatrix}^{n+1}_{k,i} = \begin{bmatrix} \alpha \\ \alpha \mathbf{U} \end{bmatrix}^{n}_{k,i} + \frac{\Delta t}{\Delta x}\left[(\mathscr{R}^{C,n+\frac{1}{2}}_{k,i-\frac{1}{2}} + \mathscr{R}^{\mathrm{Lag},n+\frac{1}{2}}_{k,i-\frac{1}{2},i}) - (\mathscr{R}^{C,n+\frac{1}{2}}_{k,i+\frac{1}{2}} + \mathscr{R}^{\mathrm{Lag},n+\frac{1}{2}}_{k,i+\frac{1}{2},i}) \right] + \frac{\Delta t}{\Delta x}\delta \mathscr{R}^{\mathrm{Lag},n+\frac{1}{2}}_{k,i}, \tag{2.54}$$

where the flux contributions in (2.54) are evaluated with intermediate step variables at time $t^{n+\frac{1}{2}}$ given by the predictor step (2.53).

A wide range of numerical experiments has established that the predictor-corrector DEM/RDEM scheme (2.53)-(2.54) is non-linearly stable for

$$\mathrm{CFL} \le \frac{1}{2}, \tag{2.55}$$

but this condition can be relaxed to

$$\mathrm{CFL} \le 1, \tag{2.56}$$

if assuming that no wave acceleration occurs [Toro 97] and that the elements discussed in Section 2.5.2 are taken into account.

Let us mention here that the second-order Hancock approach in the context of van Leer's second-order MUSCL technique (see [Toro 97]) is generally less expensive than the predictor-corrector RK2 scheme described above. However, the evolution step of Hancock's approach for boundary extrapolated variables remains unclear for the non-conservative two-fluid system. In addition, from an algorithmic viewpoint, the predictor-corrector approach is very simple to be implemented, since the predictor step (2.53) and corrector step (2.54) rely on an identical coding procedure.

2.7 Multi-dimensional extension

The extension of the DEM/RDEM method to multi-dimensional flow problems computed on general unstructured grids can be performed by following the key steps of a conventional finite volume method for conservation laws. Let us consider a two-dimensional polygonal control volume $\mathcal{C}_i$ such as the one displayed in Fig. 2.14. Index j indicates the j^{th} side or edge of $\mathcal{C}_i$, $\partial\mathcal{C}_{ij}$ being the length of this edge. The vector $\mathbf{n}_{ij}$ denotes the outward pointing unit normal vector while $\mathbf{t}_{ij}$ is the unit (anticlockwise) tangent vector.

The first-order DEM/RDEM method for phase Σ_k is expressed as follows:

$$\begin{bmatrix} \alpha \\ \alpha\mathbf{U} \end{bmatrix}_{k,i}^{n+1} = \begin{bmatrix} \alpha \\ \alpha\mathbf{U} \end{bmatrix}_{k,i}^{n} - \frac{\Delta t}{|\mathcal{C}_i|} \sum_j |\partial\mathcal{C}_{ij}| \left(\mathscr{R}^C_{k,j,i} + \mathscr{R}^{\mathrm{Lag}}_{k,j,i} \right), \tag{2.57}$$

where $\mathscr{R}^C_{k,j,i} + \mathscr{R}^{\mathrm{Lag}}_{k,j,i}$ denotes the flux contribution of boundary $\partial\mathcal{C}_{ij}$. The conservative and Lagrangian numerical fluxes are computed respectively by using formulae (2.28) and (2.30), applied in the direction defined by $\mathbf{n}_{ij}$. In other words, the Riemann problem is solved in a local frame $(\mathbf{n}_{ij},\ \mathbf{t}_{ij})$, with the tangent velocity component

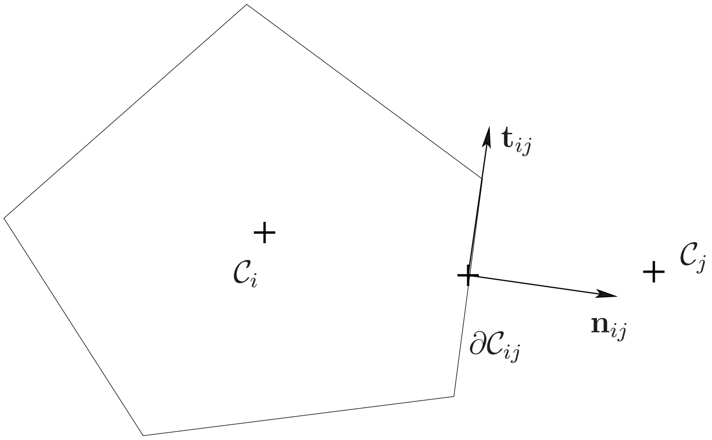

Figure 2.14: A polygonal cell $\mathcal{C}_i$ of volume $|\mathcal{C}_i|$ and boundary $\partial\mathcal{C}_{ij}$.

treated as a passive scalar.

The semi-discrete form of the second-order extension reads as follows for multidimensional problems:

$$\frac{\mathrm{d}}{\mathrm{d}t}\begin{bmatrix}\alpha\\ \alpha\mathbf{U}\end{bmatrix}_{k,i} = -\frac{1}{|\mathcal{C}_i|}\sum_j |\partial\mathcal{C}_{ij}|\left(\mathscr{R}^{C}_{k,j,i} + \mathscr{R}^{\mathrm{Lag}}_{k,j,i} - \delta\mathscr{R}^{\mathrm{Lag}}_{k,j,i}\right),$$

where the second-order Lagrangian-flux contribution $\delta\mathscr{R}^{\mathrm{Lag}}_{k,j,i}$ can be evaluated by using (2.47) with reconstructed data. Naturally, a multi-dimensional limiter must also be used (see for instance [Barth 89, Darwish 03]). In the present work, the limiter used in the reconstruction process is a variant of [Barth 89] (see [Beccantini 00]).

2.8 Numerical results for one-dimensional interfaces

This section reviews some typical results obtained for both non-reactive and reactive one-dimensional interface problems using the "standard" DEM/RDEM approach described in the present chapter. The objective of the section is to establish whether DEM/RDEM, as described up to now, is sufficient to obtain, in a robust way, accurate solutions for our applications of interest.

Note that only one phase physically exists inside each computational cell for interface problems, with the other phase occupying a very small volume (not zero for numerical reasons); this latter phase will be called the residual phase from now on. As far as the DEM/RDEM approach is concerned, mixture variables are not computed as such but can be easily obtained by post-processing the computed solutions. The numerical results for a mixture variable Q presented in this work are obtained from the following identity:

$$Q = \sum_k \alpha_k Q_k, \tag{2.58}$$

where Q_k can be either a conservative variable (such as the mass, momentum and energy per unit volume) or a physical non-conservative variable (such as the velocity, pressure and temperature) for phase Σ_k. When Q_k is a conservative quantity, Q can be regarded as the total amount of this quantity for the two phases. When Q_k is a non-conservative quantity, (2.58) aims at representing variables involving interface discontinuities. In fact, when α takes only the value of 0 or 1 for the interface problems, the quantity Q represents the variable either of phase Σ_1 or of Σ_2. On the other hand, when treating the numerical two-phase mixtures, *i.e.* when α can take an intermediate value between 0 and 1, the quantity Q represents qualitatively the numerical mixture variable, which does not have a physical meaning. However, this numerical mixture quantity Q can allow inspecting the method performance by examining the numerical dissipation or the occurrence of oscillation. Note that the representation of a non conservative variable in (2.58) is anyway consistent to the fact that the exact solution of α is 0 or 1.

2.8.1 Liquid-gas non-reactive interface

Let us consider the water-gas shock tube previously proposed in [Petitpas 07], similar to the one in [Abgrall 03], with stiffened gases thermodynamic closures. The main challenge of this test case is to overcome the numerical robustness problem which usually appears when computing the strong rarefaction wave created when the high pressurized water on the left is put in contact with the gas at atmospheric pressure on the right.

Initial conditions At the initial state, the high pressure (10^9 Pa) region on the left ($0 \leq x \leq 0.7$ m) contains nearly pure water and a small volume of gas (volume fraction $\varepsilon = 10^{-8}$) while the low pressure (10^5 Pa) region on the right contains nearly pure gas with a small amount of water (volume fraction $\varepsilon = 10^{-8}$). Note that the residual gas phase pressure on the left is set to 10^5 Pa, while the pressure of the residual water phase on the right is 10^9 Pa. The gas density is 10 kg/m^3 in the whole domain, while the water density is 1000 kg/m^3. Both fluids are initially at rest. The EOS parameters are set equal to $\gamma = 1.4$, $p_\infty = 0$ for the gas and $\gamma = 4.4$,

$p_\infty = 6.0 \times 10^8$ Pa for water.

Preliminary remarks The exact wave solution obtained by solving this Riemann problem of Euler equations is illustrated in Fig. 2.15. The results obtained with the first-order DEM approach and the limited second-order approach combined with the predictor-corrector time discretization are first analyzed. The volume fraction, density, velocity and pressure are reconstructed using the minmod limiter in order to achieve (quasi) second-order accuracy in space. The numerical variables of each single phase with first and second-order approaches are shown in Fig. 2.16 and 2.17, respectively, where the exact reference solution is also displayed for the sake of comparison. In fact, since the exact solution provides only pure phase variables of interface problem with no mixture, while DEM yields single phase variables with numerical mixtures, the comparison between first-order and second-order DEM results (also exact solution) will be performed on a third figure, Fig. 2.18, where (2.58) is used to display the mixture variables computed with the first and second-order DEM approach.

Analysis of the exact solution The exact solution of Riemann problem for Euler equations closed by SG-EOS for compressible liquids and gases can be obtained by following [Ivings 98, Toro 97]. Taking into account the initial conditions given above, we obtain the exact solution shown in Fig. 2.15 for selected variables. The liquid-gas interface velocity is evaluated by the speed of the contact discontinuity equal to 490.18 m/s. At time 220 μs, the interface, moving from its initial location at $x = 0.7$ m, reaches $x = 0.80784$ m. The right-traveling genuinely nonlinear wave (GNL) is a gas shock wave while the left-traveling GNL wave is a strong liquid rarefaction wave.

Analysis of the first and second-order DEM results It is first of all observed that each phase retains its own variables, including pressure and velocity, and both phases display very different profiles. On the left part of the interface, the water phase is nearly pure and its solution involves a strong rarefaction. This rarefaction solution is overall in good agreement with the exact solution. However, at the tail of the fan, negative pressure values are obtained (the pressure profile is plotted in logarithmic scale, so that negative values do not appear in the figures). We observe that the computed results are even worse with the second-order approach. Fortunately, these negative pressure values do not result in a negative square of sound speed, so the problem remains well-posed. On the right part of the interface, the gas phase is nearly pure and its shock solution is in good agreement with the exact solution. The residual liquid phase on the right and residual gas phase on the left also involve wave propagations. The phase interaction occurring on the interface is only computed by the non-conservative term in system (1.30), which should enforce the interface conditions (1.28)-(1.29). This is indeed verified by the pressure and velocity profiles in Fig. 2.16 and 2.17: p and v evolve differently, but at the interface, both quantities automatically fulfill the interface conditions.

Comparison of the exact and computed mixture variables Fig. 2.18 shows the computed mixture variables compared to the exact solution. We notice that the second-order approach is in general more accurate than the first-order method, except for the pressure wave associated with the strong rarefaction fan. We emphasize that the negative pressure values are linked to the stiffened gas equation of state. Interface conditions of continuous pressure and velocity are perfectly resolved. Examining the Mach number results, it is observed that, because of the numerical dissipation, spurious subsonic results are obtained for the supersonic part of flow using both the first and second-order DEM scheme. This clearly motivates the need for reducing the numerical dissipation. Additionally the weak right shock wave is not captured on the profiles of density and specific entropy.

Negative pressures can create serious numerical problems. Pressure and velocity relaxation procedures, presented in Appendix C with some associated numerical results, have the capability of preventing the occurrence of negative pressures by adding an internal phase interaction within a computational cell. We point here that no Newton type iterations are involved. Thus the relaxation solver here considered is computationally very efficient.

2.8.2 Chapman-Jouguet deflagration front

Test case description Let us consider the Chapman-Jouguet deflagration shock tube previously proposed in [Beccantini 10a]. This test case is interesting because it allows observing how the poor accuracy on the flame region can affect the accuracy on the flame-generated shock wave. The 20 meter long shock tube involves on the right (10 m $\leq x \leq$ 20 m) a stoichiometric mixture of hydrogen-air, with pressure and temperature equal to 1.013 bar and 290 K respectively. On the left, the burnt gas (due to the complete combustion of the stoichiometric mixture of hydrogen-air) is found with pressure and temperature equal to 2.013 bar and 2800 K. The specific heats are computed as fourth-degree polynomials of the temperature, obtained by interpolating data in JANAF tables [Stull 71]. For the modeling and numerical reasons already explained in [Abgrall 03], the right part contains a very small volume of burnt gas (volume fraction is $\varepsilon = 10^{-8}$) and the left part contains a very small volume of unburnt gas (volume fraction is $\varepsilon = 10^{-8}$). The gases are initially at rest and the fundamental flame speed is set equal to 200 m/s.

Analysis of the exact solution The exact Riemann problem solution for the reactive Euler equations closed by the thermally perfect gas EOS can be evaluated by following [Beccantini 10a] for deflagrations provided that the fundamental flame speed is given. Taking into account the introduced initial conditions, we obtain the exact solution of the problem as a Chapman-Jouguet deflagration shown in Fig. 2.19 for selected variables. The flame visible velocity, evaluated as the fundamental flame speed plus the unburnt gas velocity, is found to be equal to 1213.62 m/s. At time 4.0 ms, the reactive interface, moving from its initial location at $x = 10$ m, reaches $x = 14.85448$ m. In front of the flame interface, we have the right-traveling unburnt precursor shock wave while behind the reactive interface, the flow velocity is sonic with respect to the flame front, and we are interested in the burnt gas Taylor expansion wave. In addition, the left wave structure also incorporates the left-traveling contact discontinuity and shock wave of the burnt gas.

Analysis of the first and second-order RDEM solutions The exact solution of the reactive Euler equations and the numerical solutions obtained with the RDEM are compared. A uniform mesh of 100 cells is used. Fig. 2.20 and Fig. 2.21 show the results of individual phase variables for first and second-order approaches, respectively. As in the non-reacting water gas shock tube problem case, the 2-step Runge-Kutta stepping scheme is used for the time discretization for second-order approach; volume fraction, density, velocity and pressure are reconstructed using the minmod limiter. As already explained for the previous impermeable front problem, each phase retains its own variables. The computed behavior of the burnt phase on the left is in good agreement with the exact solution which involves a left-going shock wave, a left-going contact discontinuity, and a right-going Taylor expansion wave behind the Chapman-Jouguet deflagration front. On the right side, the behavior of the unburnt phase is also in good agreement with the right-going precursor shock wave.

Comparison of the exact and computed mixture variables Fig. 2.22 display the post-processed mixture variables compared to the exact solution of reactive Euler equations. The second-order minmod limited approach is clearly more accurate than the first-order upwind method, as expected.

2.8.3 Concluding remarks

Regarding the results obtained for the Chapman-Jouguet deflagration front test, even second-order calculations yield a very diffused interface which in turn exceedingly moderates the maximum over-pressure behind the non-reacting right-travelling shock wave. This makes the RDEM approach not sufficient to perform reliable investigations of fluid-structure interaction problems involving combustion-generated pressure waves. A more accurate scheme should be designed for this purpose. On the other hand, the CFL is set equal to 0.75 for this deflagration front test case. In fact, the second-order scheme does not work for CFL close to unity, the reason of which has been discussed in Section 2.5. Thus, robustness of DEM/RDEM should also be improved. The upwind downwind-controlled splitting (UDCS) which will be now presented in Chapter 3 is designed for improving both the accuracy and robustness of the DEM/RDEM approach.

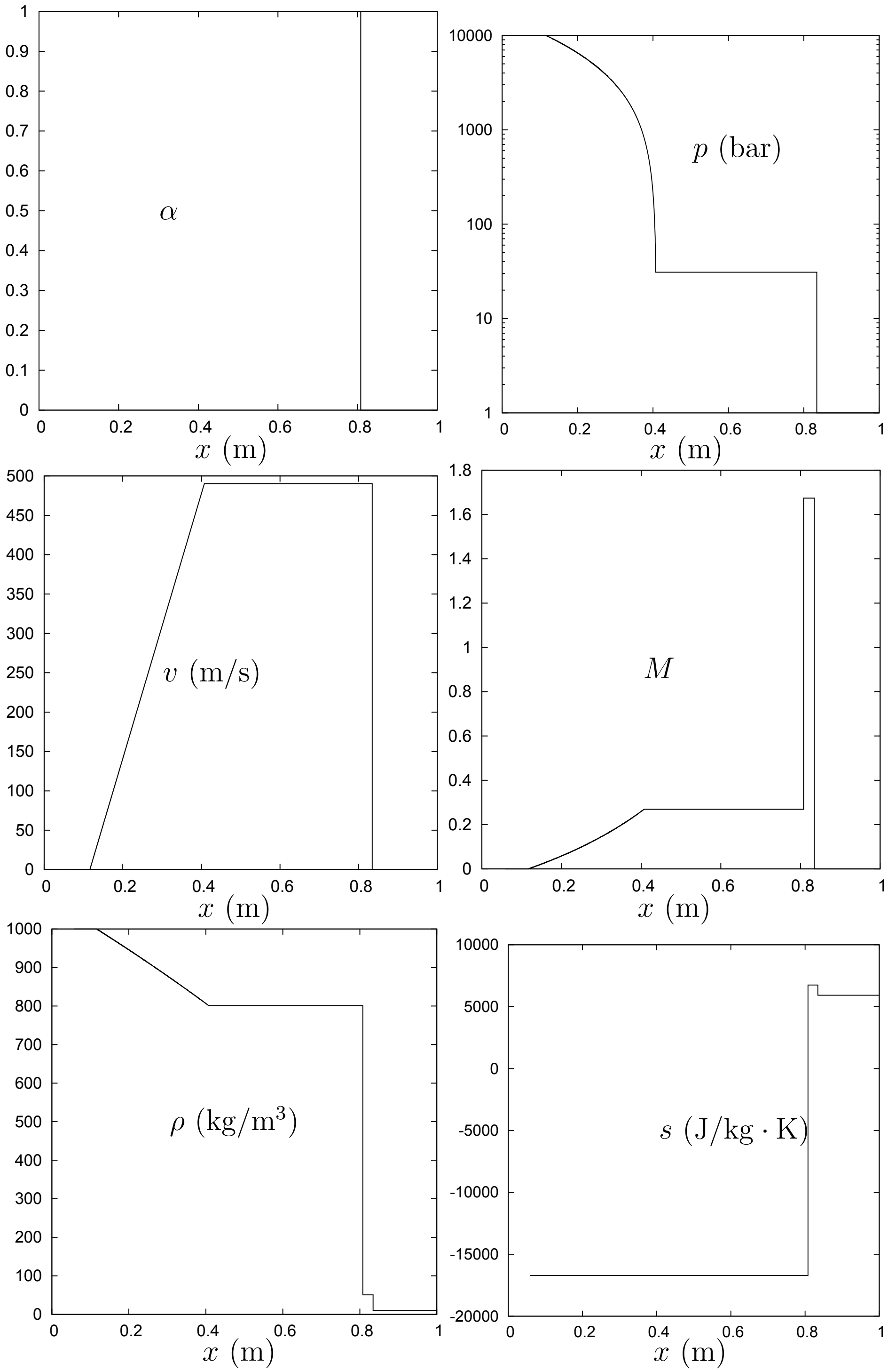

Figure 2.15: The exact solution of the Euler equations for water gas shock tube problem with interface separating pure phases at time $t = 220$ μs.

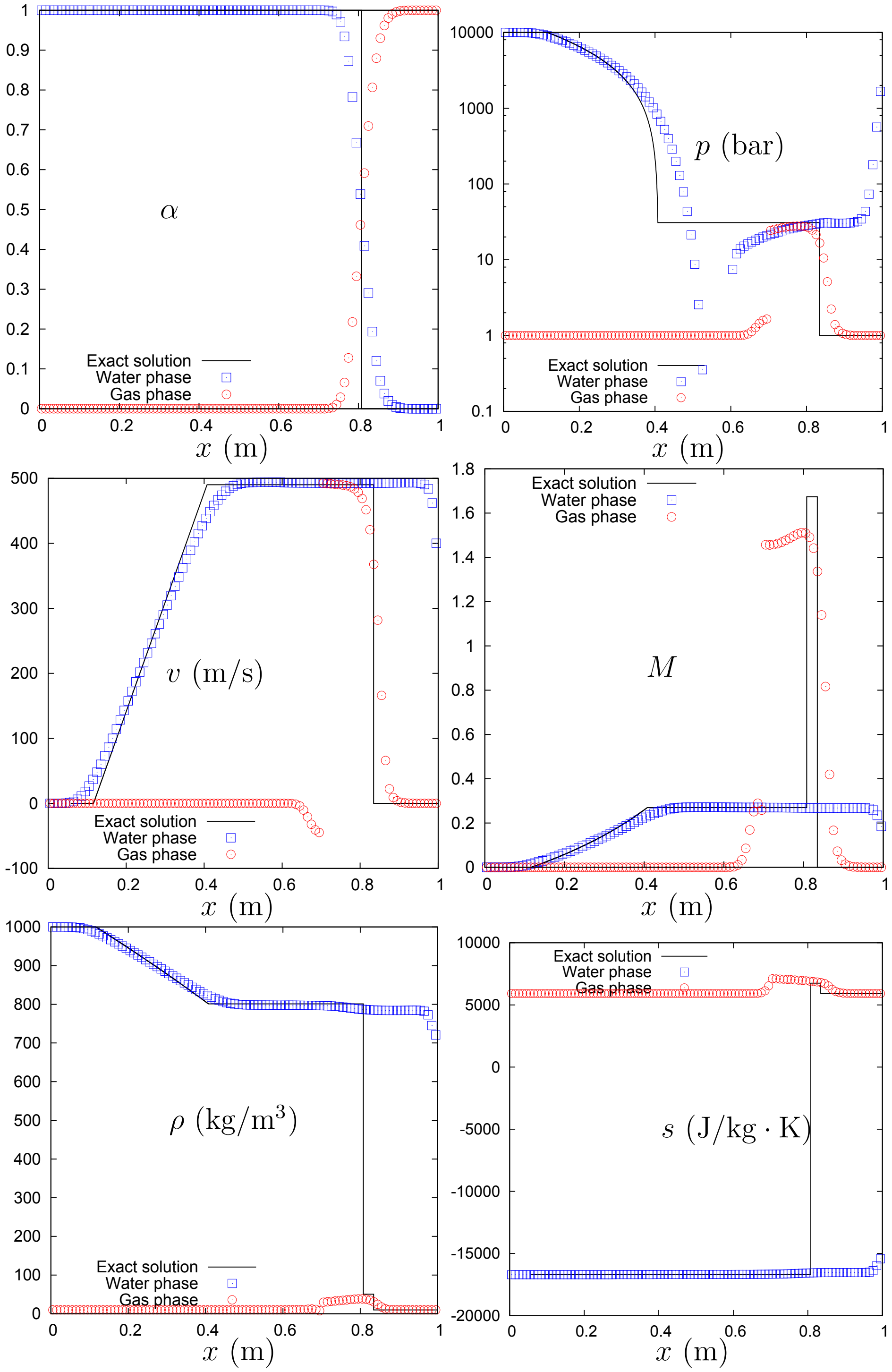

Figure 2.16: First-order DEM method is used for water gas shock tube problem with interface separating nearly pure phases. A 100 cells uniform mesh is used. CFL = 0.9. Time $t = 220$ μs. Individual phase variables are plotted.

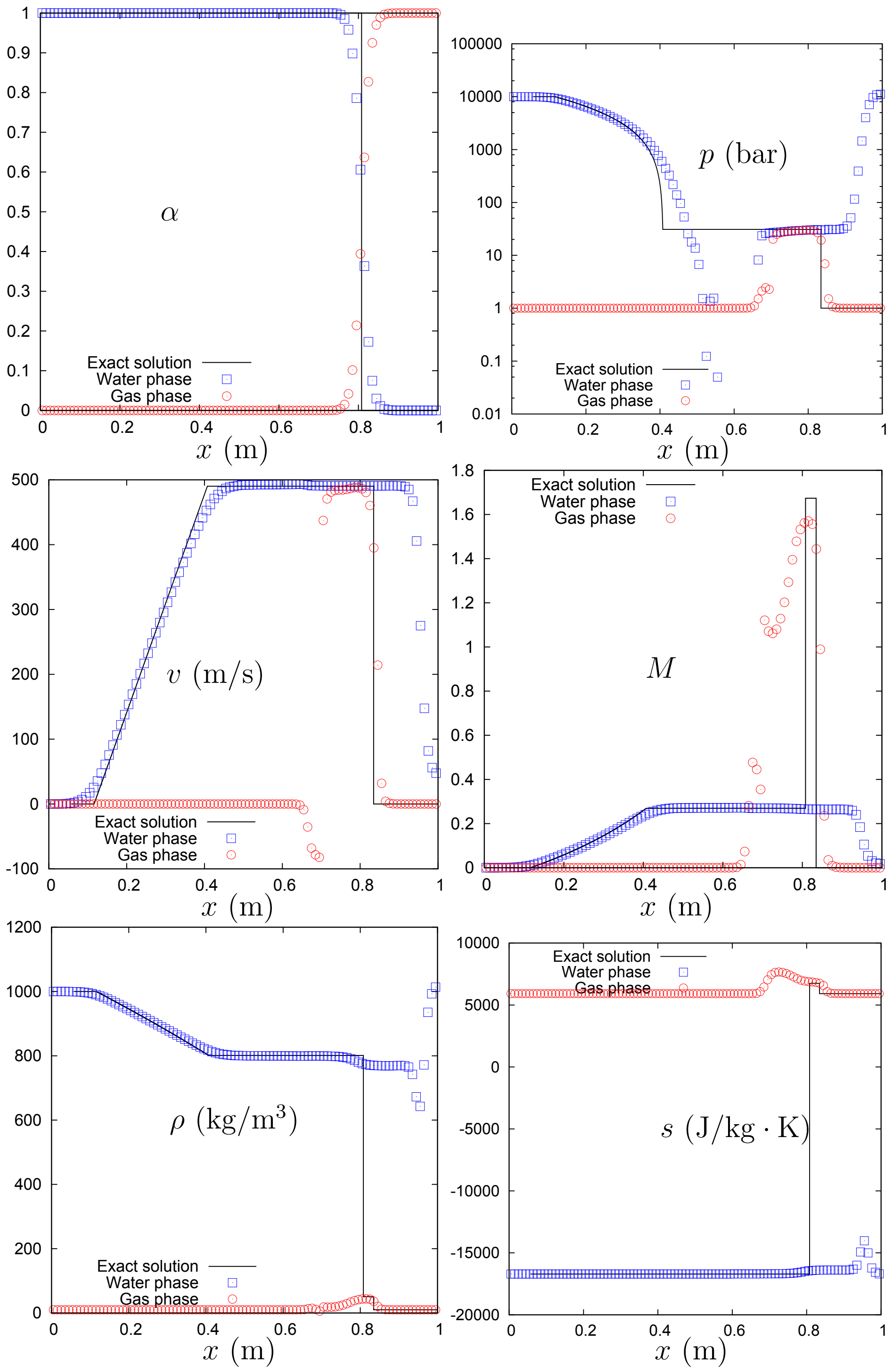

Figure 2.17: Second-order DEM method with minmod limiter is used for water gas shock tube problem with interface separating nearly pure phases. A 100 cells uniform mesh is used. CFL = 0.9. Time $t = 220$ μs. Individual phase variables are plotted.

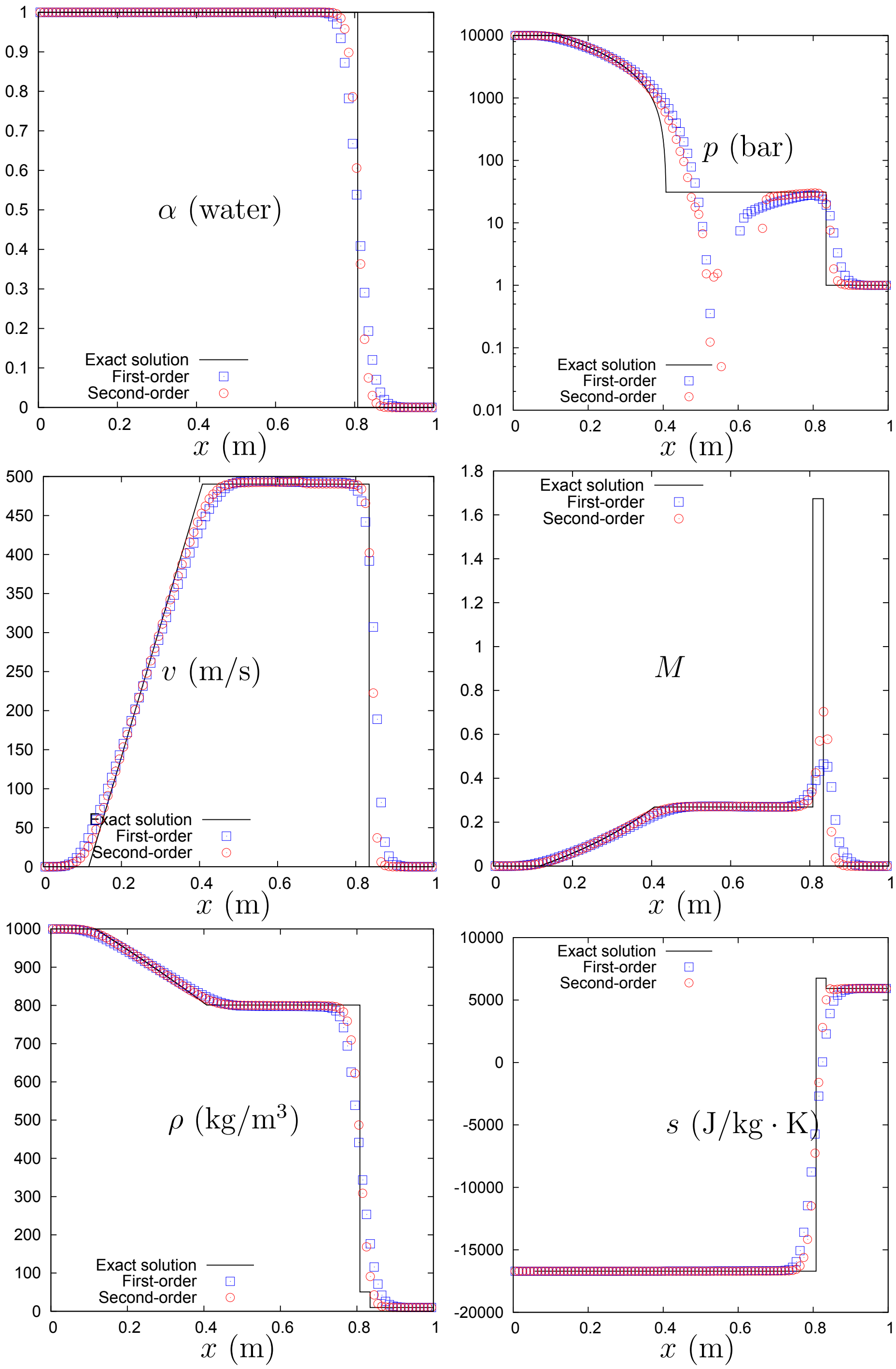

Figure 2.18: Second-order DEM method with minmod limiter and first-order method are compared for water gas shock tube problem with interface separating nearly pure phases. A 100 cells uniform mesh is used. CFL = 0.9. Time t = 220 μs. Phase mixture variables are plotted.

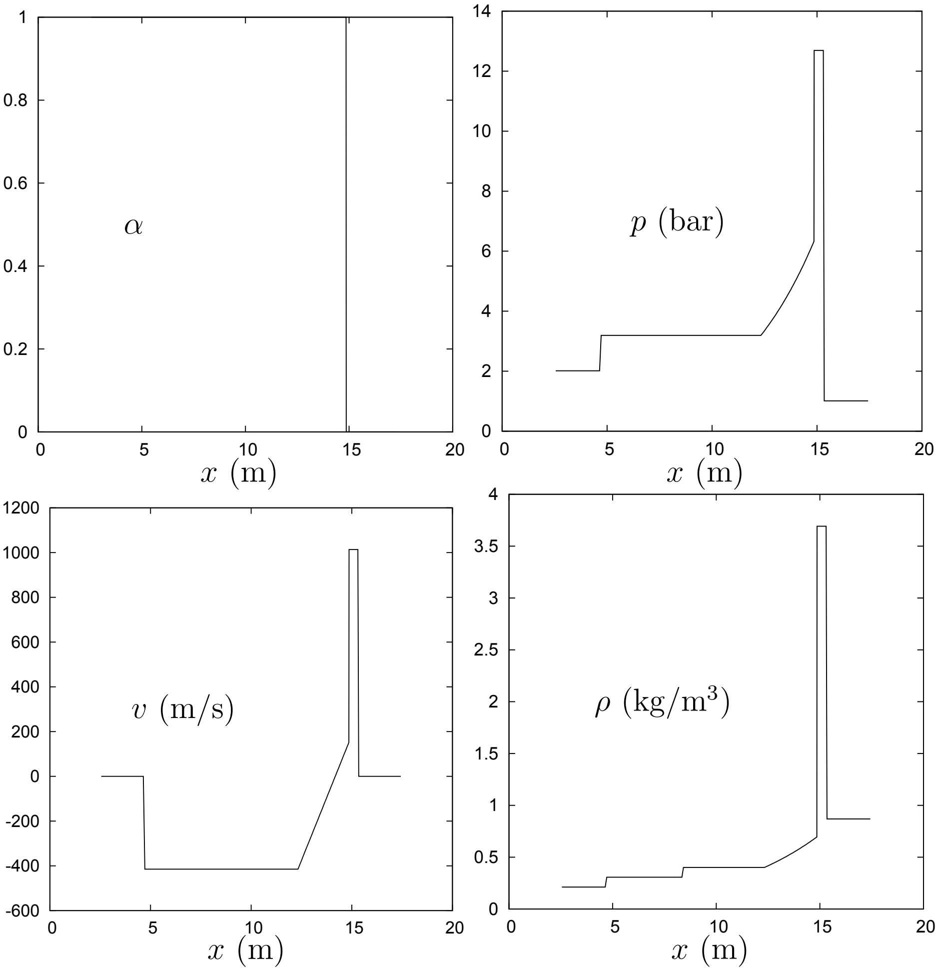

Figure 2.19: The exact solution of the reactive Euler equations for the shock tube of Chapman-Jouguet deflagration front at time $t = 4.0$ ms.

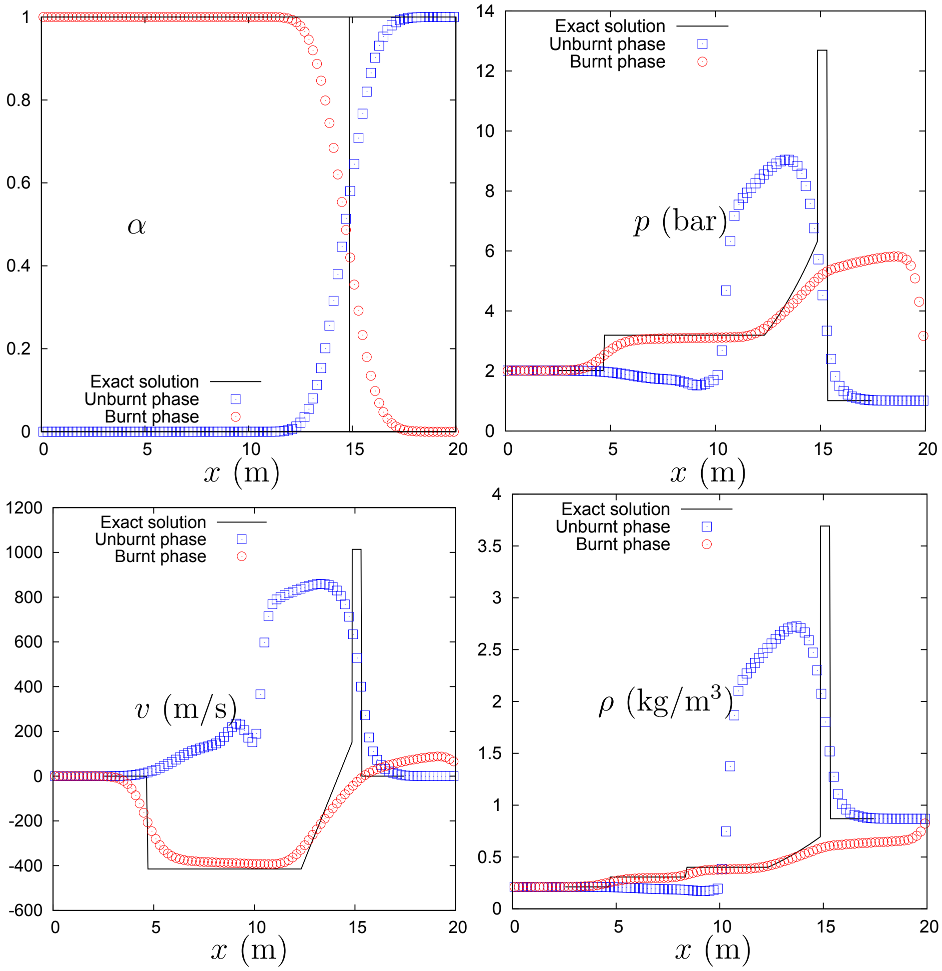

Figure 2.20: First-order RDEM method is used for the shock tube of Chapman-Jouguet deflagration front. A 100 cells uniform mesh is used. CFL = 0.75. Time $t = 4.0$ ms. Individual phase variables are plotted.

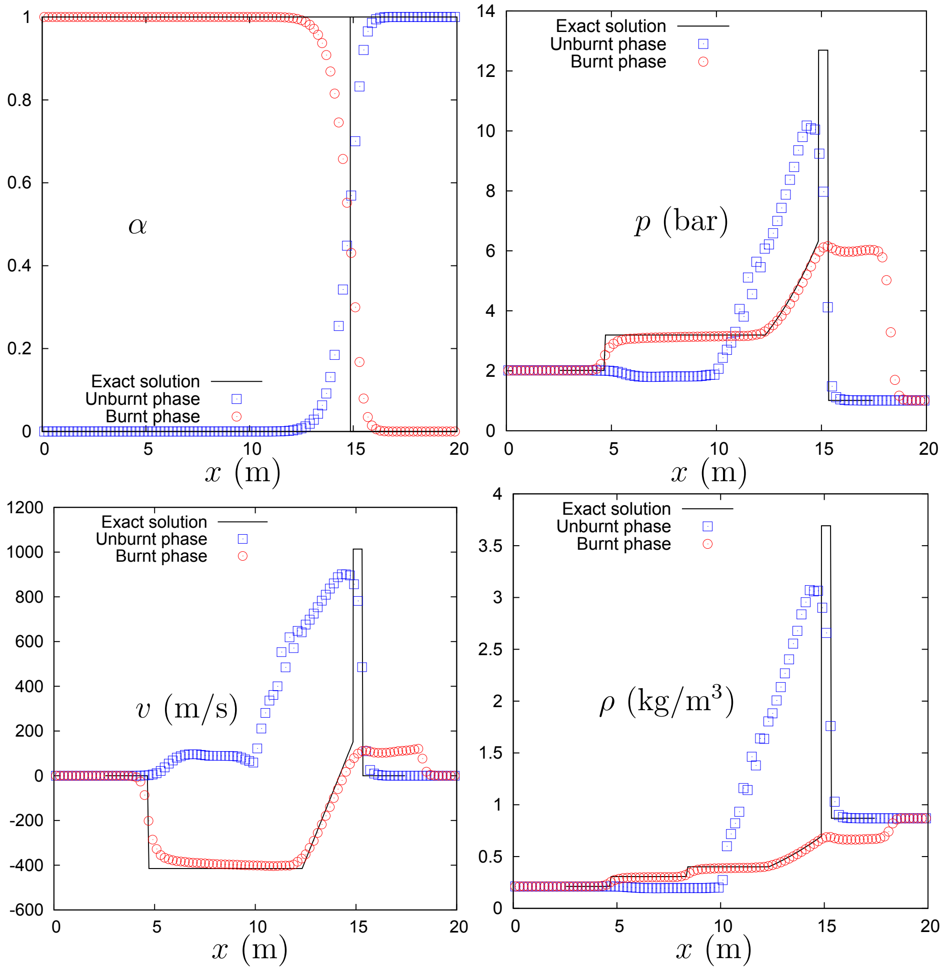

Figure 2.21: Second-order RDEM method with minmod limiter is used for the shock tube of Chapman-Jouguet deflagration front. A 100 cells uniform mesh is used. CFL = 0.75. Time $t = 4.0$ ms. Individual phase variables are plotted.

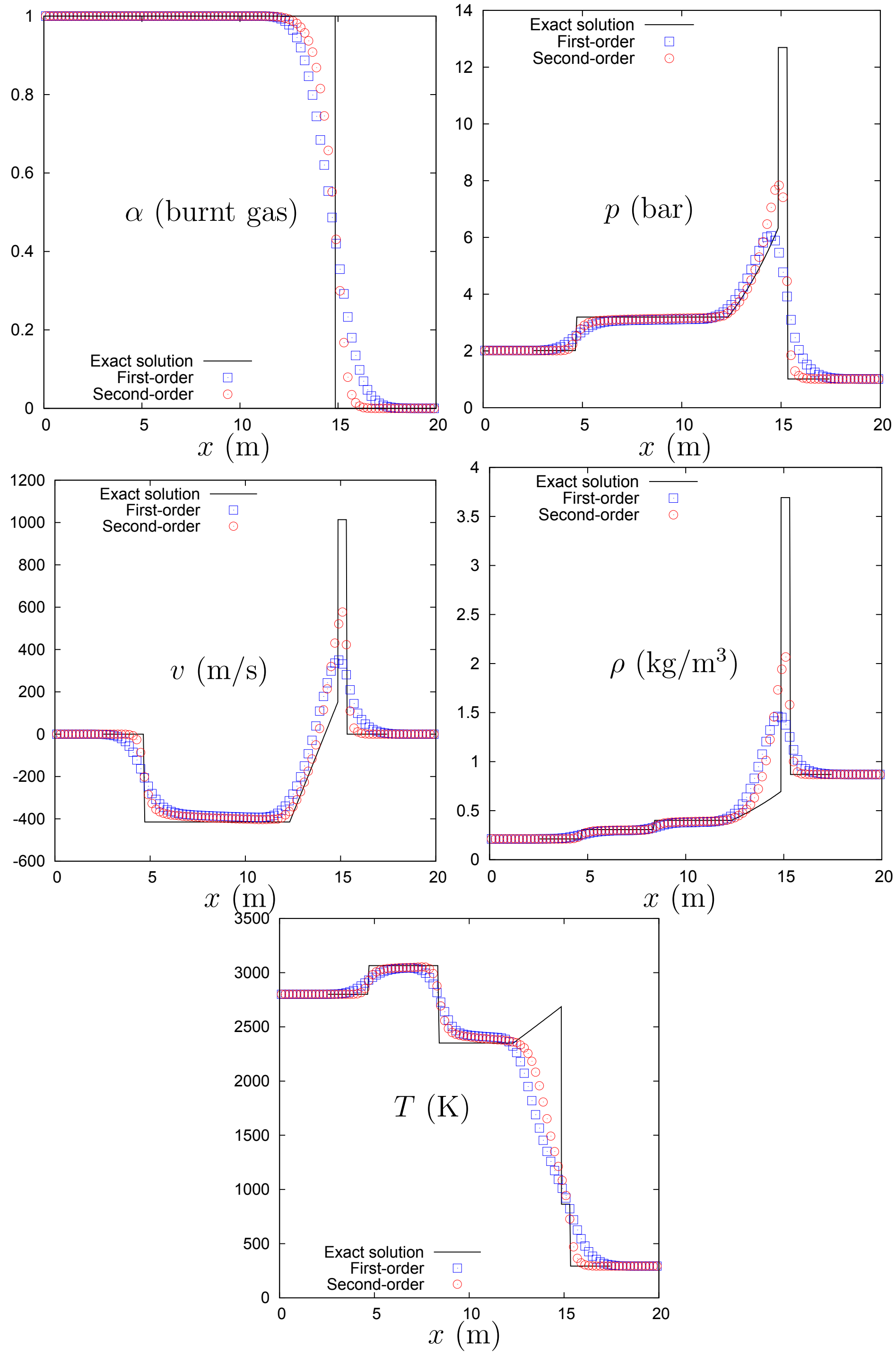

Figure 2.22: Second-order RDEM method with minmod limiter and first-order RDEM method are compared for the shock tube of Chapman-Jouguet deflagration front. A 100 cells uniform mesh is used. CFL = 0.75. Time t = 4.0 ms. Phase mixture variables are plotted.

Chapter 3

Upwind downwind-controlled splitting for interface discretization

With a first-order DEM/RDEM method, the volume generated at the intercell boundary is accumulated inside the downwind element, graphically translating the numerical dissipation for the topological equation (see Section 2.1). The predictor-corrector DEM scheme proposed in [Abgrall 03] (see Section 2.6) contains a second-order limited reconstruction for the volume fraction with the aim of improving the interface accuracy. Thanks to this reconstruction process, the interface is numerically less diffused since one part of the generated volume at the intercell boundary, which is accumulated inside the downwind element with the first-order method, is kept inside the upwind element.

A further extension of this volume fraction reconstruction approach has been performed in [Beccantini 10b]. The anti-diffusive (downwind-controlled) method proposed and used in [Lagoutière 00, Després 02, Kokh 10] is coupled with the RDEM method with the aim of accurately simulating reactive interface at all combustion regimes. Compared to the second-order approach, optimized reconstructed values of volume fractions are obtained at the intercell boundaries, which reduces more efficiently the numerical dissipation.

We emphasize that downwind-control and the anti-diffusion concept of the material interface make perfect sense because we are considering two-phase interfaces modeled with physical diffusive phenomena neglected. Thus, the discontinuity of the phase characteristic function X_k (or volume fraction α_k) is physically not diffused by the flow and interface motion - the physical interface remains a sharp front.

The downwind-controlled reconstruction method proposed in [Beccantini 10b] remains unstable for deflagrations, since it does not take into account the propagation of all the genuinely nonlinear waves. We present in this chapter an original approach, designed as "upwind downwind-controlled splitting" (UDCS), which further improves the strategy described in [Beccantini 10b]. Basically, the UDCS strategy combines two steps:

1. a first "Upwind" step fully contains the first-order upwind DEM/RDEM approach (density, velocity and pressure can be reconstructed following the slope limiter approach), and takes into account the propagation of all the waves, including the genuinely nonlinear waves.

2. a second "Downwind-controlled splitting" step aims at improving the accuracy of the linearly degenerate wave, *i.e.* contact discontinuity in non-reacting case and reactive shock in reacting case. The genuinely nonlinear waves having been treated within the "upwind" step, we thus recover the stability of the first-order upwind DEM/RDEM method.

In this chapter, we present in Section 3.1 the coupling of DEM/RDEM with an anti-diffusive approach such as proposed in [Beccantini 10b]. To overcome the robustness problem linked to this coupling for deflagrations, a first attempt with the use of a large time step marching scheme is proposed and presented in Section 3.2. However, we will show that this approach is not sufficiently robust for our targeted difficult test problems; moreover, its extension on unstructured grids is not straightforward. Thus, a new upwind downwind-controlled splitting (UDCS) approach is proposed afterwards in Section 3.3 to carry out accurate computations which are as robust as first-order upwind calculations. Concluding remarks follow in Section 3.4 where the computational efficiency derived from the anti-diffusive strategy within DEM/RDEM will be emphasized as an important feature of UDCS for two-fluid interface computations.

3.1 Coupling DEM/RDEM and anti-diffusive approach

3.1.1 Linear advection and the original anti-diffusive algorithm

We recall the main ingredients of the original anti-diffusive (downwind-controlled) method by way of the linear advection equation in one space dimension:

$$\frac{\partial \alpha}{\partial t} + \sigma \frac{\partial \alpha}{\partial x} = 0 \tag{3.1}$$

with constant propagation speed $\sigma > 0$. Note that the upwind and limited second-order DEM/RDEM scheme for a nonlinear advection equation (topological equation) can be found in Section 2.1 and Appendix B, respectively.

Riemann problem, upwind and downwind approaches.

The computational domain is divided into regular cells and the initial condition is defined as:

$$\alpha(x,0) = \begin{cases} 1 & \text{if } x < x_{i-\frac{1}{2}}, \\ 0 & \text{if } x > x_{i-\frac{1}{2}}. \end{cases}$$

as displayed in the figure below.

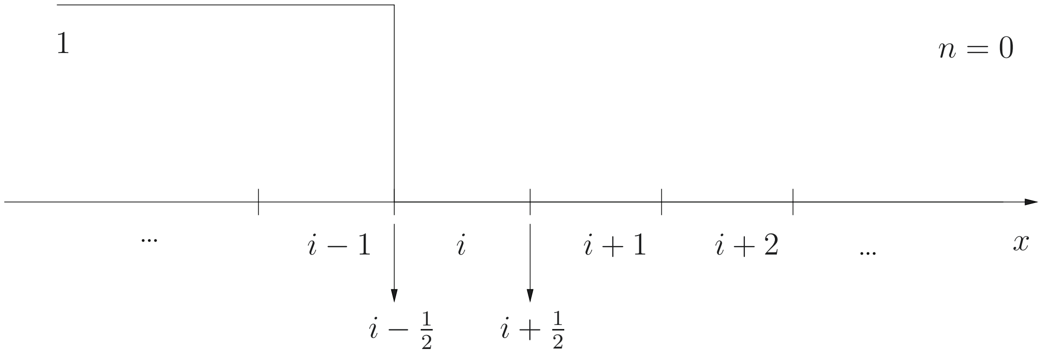

The unique weak solution of the problem at hand is given by:

$$\alpha(x,t) = \begin{cases} 1 & \text{if } x < x_{i-\frac{1}{2}} + \sigma t, \\ 0 & \text{if } x > x_{i-\frac{1}{2}} + \sigma t. \end{cases}$$

The first-order explicit upwind method for the advection equation reads

$$\alpha_i^{n+1} = \alpha_i^n + \frac{\sigma \Delta t}{\Delta x}(\alpha_{i-1}^n - \alpha_i^n), \tag{3.2}$$

and is stable provided that $|\frac{\sigma\Delta t}{\Delta x}| \leq 1$. At the intercell boundary $x_{i-\frac{1}{2}}$ its numerical flux is given by $\sigma\alpha_{i-1}$. The first-order explicit downwind method for the advection equation reads

$$\alpha_i^{n+1} = \alpha_i^n + \frac{\sigma \Delta t}{\Delta x}(\alpha_i^n - \alpha_{i+1}^n), \tag{3.3}$$

and is unconditionally unstable. At the intercell boundary $x_{i-\frac{1}{2}}$ its numerical flux is given by $\sigma\alpha_i$. It thus creates a new extremum in the cell element $i-1$.

Let us now discuss the numerical diffusion phenomenon which occurs when applying the first-order explicit upwind method (3.2) (see [Lagoutière 00]). We set for instance

$|\frac{\sigma \Delta t}{\Delta x}| = \frac{1}{4}$. In this case the analytical solution propagates one quarter of mesh size to the right at each time step.

1. After the first time step ($n = 1$), the analytical and numerical solution look like the plots displayed in the next figure:

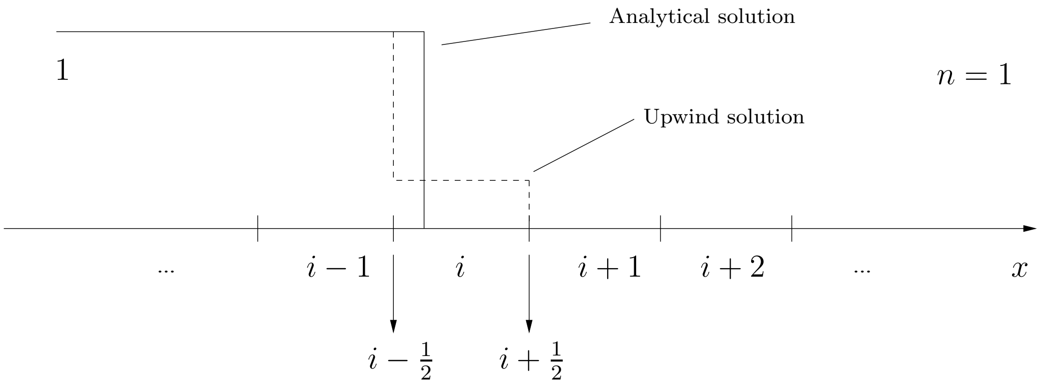

2. For the second time step, we obtain

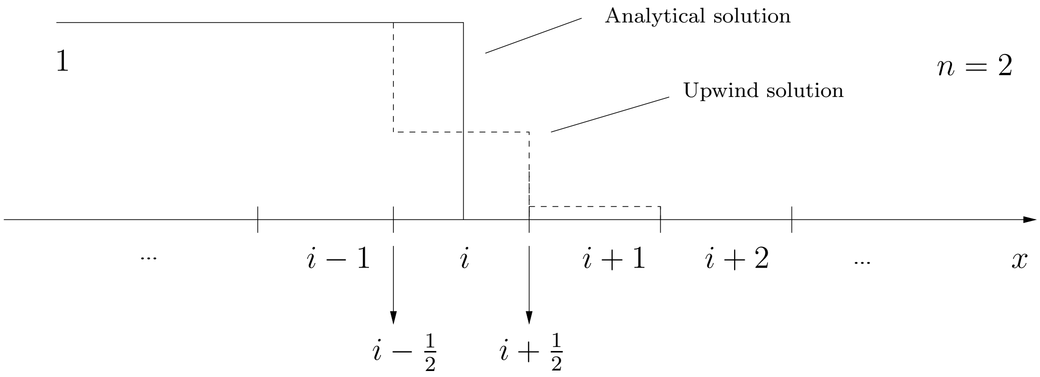

3. For the third time step, we obtain

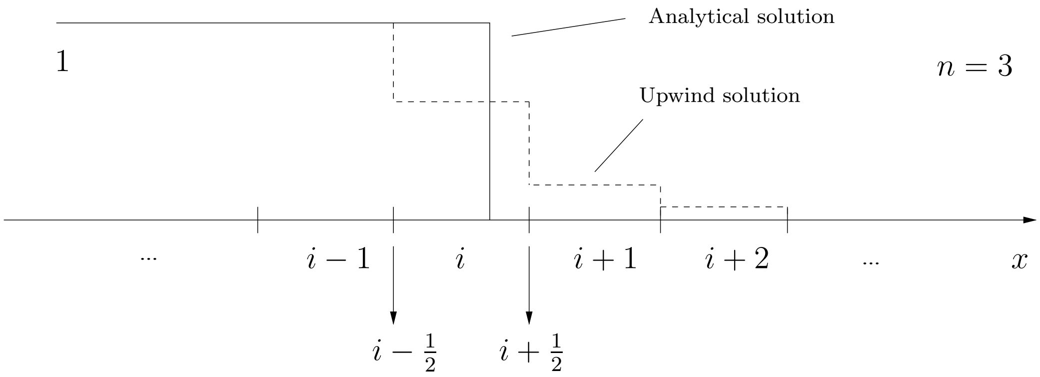

4. For the fourth time step, we obtain

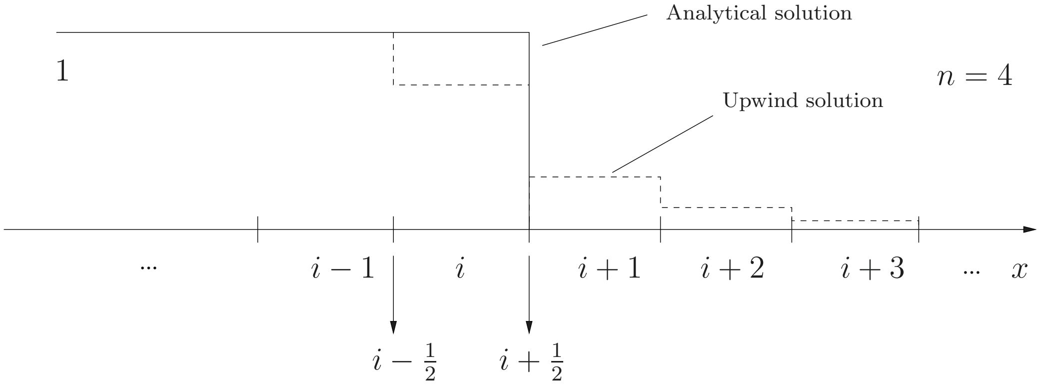

As can be deduced from the previous graphics, the front of the piecewise data has been diffused to other cells (i, $i+1$, $i+2$ and $i+3$) while the exact analytical solution never jumps outside of cell i. Moreover,

- At $n = 0$ the upwind fluxes in $x_{i-\frac{1}{2}}$ and fluxes in $x_{i+\frac{1}{2}}$ are equal to the ones of exact solution. From $n = 1$, the upwind fluxes in $x_{i-\frac{1}{2}}$ is still equal to the one of exact solution. However, the upwind fluxes in $x_{i+\frac{1}{2}}$ creates the numerical dissipation.

- From $n = 1$, if the downwind flux is used at $x_{i+\frac{1}{2}}$, the numerical solution obtained is identical to the averaged solution of the exact one.

The anti-diffusive approach proposed in [Lagoutière 00] is based on the above observation. It is also called downwind-controlled approach, since the selected numerical flux is downwind provided that certain nonlinear conditions are satisfied.

The original anti-diffusive algorithm

The general form of the numerical scheme for (3.1) reads

$$\alpha_i^{n+1} = \alpha_i^n + \frac{\sigma \Delta t}{\Delta x}(\alpha_{i-\frac{1}{2}}^n - \alpha_{i+\frac{1}{2}}^n). \tag{3.4}$$

Let us define

$$m_i^n = \min\left(\alpha_{i-1}^n, \alpha_i^n\right),$$
$$M_i^n = \max\left(\alpha_{i-1}^n, \alpha_i^n\right).$$

Applying the LED conditions (Section 2.5.1) for advection equation yields:

$$m_i^n \leq \alpha_i^{n+1} \leq M_i^n, \tag{3.5}$$

$$m_{i+1}^n \leq \alpha_{i+\frac{1}{2}}^n \leq M_{i+1}^n. \tag{3.6}$$

In [Lagoutière 00], a numerical approach is proposed in which the intercell numerical flux is close to the downwind value and, at the same time, satisfies conditions (3.5) and (3.6). Condition (3.5) is satisfied if

$$\begin{cases} m_i^n & \leq & \alpha_i^n + \dfrac{\sigma\Delta t}{\Delta x}(\alpha_{i-\frac{1}{2}}^n - \alpha_{i+\frac{1}{2}}^n), \\ M_i^n & \geq & \alpha_i^n + \dfrac{\sigma\Delta t}{\Delta x}(\alpha_{i-\frac{1}{2}}^n - \alpha_{i+\frac{1}{2}}^n). \end{cases}$$

or

$$\begin{cases} \alpha_{i+\frac{1}{2}}^n & \leq & \alpha_{i-\frac{1}{2}}^n + \dfrac{\Delta x}{\sigma\Delta t}(\alpha_i^n - m_i^n), \\ \alpha_{i+\frac{1}{2}}^n & \geq & \alpha_{i-\frac{1}{2}}^n + \dfrac{\Delta x}{\sigma\Delta t}(\alpha_i^n - M_i^n). \end{cases} \tag{3.7}$$

In order to avoid to deal with all the intercell boundaries at once, since $m_i^n \leq \alpha_{i-\frac{1}{2}}^n \leq M_i^n$, it follows that condition (3.7) is satisfied if

$$\begin{cases} \alpha_{i+\frac{1}{2}}^n & \leq & B_i^n & = & m_i^n + \dfrac{\Delta x}{\sigma\Delta t}(\alpha_i^n - m_i^n) & = & \alpha_i^n + \left(\dfrac{\Delta x}{\sigma\Delta t} - 1\right)(\alpha_i^n - m_i^n), \\ \alpha_{i+\frac{1}{2}}^n & \geq & b_i^n & = & M_i^n + \dfrac{\Delta x}{\sigma\Delta t}(\alpha_i^n - M_i^n) & = & \alpha_i^n - \left(\dfrac{\Delta x}{\sigma\Delta t} - 1\right)(M_i^n - \alpha_i^n). \end{cases} \tag{3.8}$$

Note that $b_i^n \leq \alpha_i^n \leq B_i^n$ if

$$\frac{\Delta x}{\sigma\Delta t} \geq 1.$$

Concluding, if we define

$$\begin{aligned} l_i^n &= \max(m_{i+1}^n, b_i^n), \\ L_i^n &= \min(M_{i+1}^n, B_i^n) \end{aligned}$$

with b_i^n and B_i^n given by (3.8), the numerical flux

$$\sigma\alpha_{i+\frac{1}{2}}^n = \begin{cases} \sigma L_i^n & \text{if } \alpha_{i+1}^n > L_i^n, \\ \sigma\alpha_{i+1}^n & \text{if } L_i^n \geq \alpha_{i+1}^n \geq l_i^n, \\ \sigma l_i^n & \text{if } l_i^n > \alpha_{i+1}^n \end{cases} \tag{3.9}$$

satisfies conditions (3.5) and (3.6).

3.1.2 Anti-diffusive reconstruction for DEM/RDEM

The anti-diffusive approach for the linear advection equation discussed in the previous section is now inserted into the DEM/RDEM method for a higher resolution of interface. For notation convenience, the phase index k is omitted for α in this section. The notations are illustrated in Fig. 2.13. Note that the Riemann problem solutions on sub-surfaces located at $x_{i,i-\frac{1}{2}}$ and $x_{i-1,i-\frac{1}{2}}$ are approximated by the solution at $x_{i-\frac{1}{2}}$ (see Section 2.6.2), with the aim of easily performing multi-dimensional computations. The numerical interface velocities at $x_{i-1,i-\frac{1}{2}}$, $x_{i,i-\frac{1}{2}}$ and $x_{i-\frac{1}{2}}$ are thus all denoted by $D_{I,i-\frac{1}{2}}$. We study in detail the case where $D_{I,i-\frac{1}{2}} > 0$ and $D_{I,i+\frac{1}{2}} > 0$. Let us define the local minimum and maximum variables as

$$\begin{aligned} m_i &= \min\left\{\alpha_{i-1}^n, \alpha_i^n\right\}, \\ M_i &= \max\left\{\alpha_{i-1}^n, \alpha_i^n\right\}. \end{aligned}$$

In this case, as shown in Fig. 3.1, we take

$$\begin{aligned} \alpha_{i,i-\frac{1}{2}} &= \alpha_i, \\ \alpha_{i+1,i+\frac{1}{2}} &= \alpha_{i+1}. \end{aligned} \tag{3.10}$$

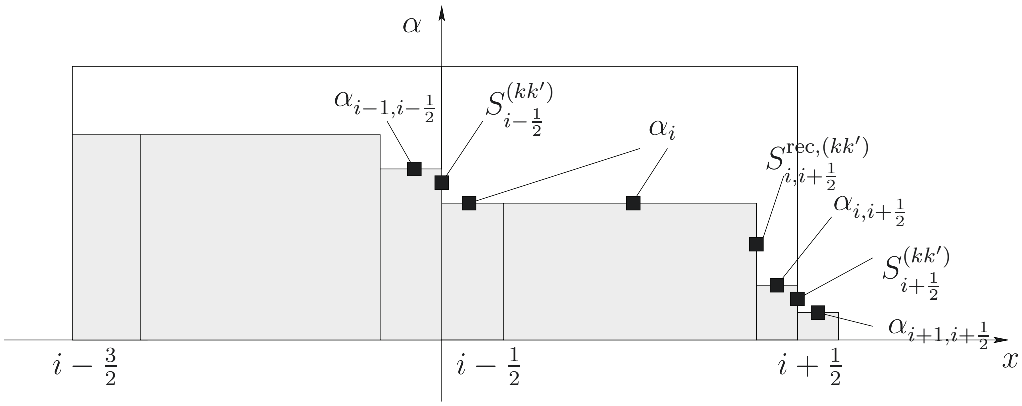

Figure 3.1: Anti-diffusive approach for RDEM. Case $D_{I,i-\frac{1}{2}} > 0$, $D_{I,i+\frac{1}{2}} > 0$. We have to determine $\alpha_{i,i+\frac{1}{2}}$ which can then determine $S^{\mathrm{rec},(kk')}_{i,i+\frac{1}{2}}$ and $S^{(kk')}_{i+\frac{1}{2}}$.

and we want to determine $\alpha_{i,i+\frac{1}{2}}$ which is able to satisfy the LED conditions (3.5) and (3.6), namely

$$m_i \leq \alpha_i^{n+1} \leq M_i, \tag{3.11}$$

$$m_{i+1} \leq \alpha_{i,i+\frac{1}{2}} \leq M_{i+1}. \tag{3.12}$$

Note that α can be different from α^n, for instance, if we use a predictor-corrector type stepping scheme. It is emphasized that (3.10) is imposed for the sake of simplicity. As one can observe from Fig. 2.13, the generated volumes of phase Σ_k from sub-surfaces $S_{i-\frac{1}{2}}^{(kk')}$ and $S_{i,i-\frac{1}{2}}^{\text{rec},(kk')}$ both enter into cell i. When the Riemann problem solution at $S_{i,i-\frac{1}{2}}^{\text{rec},(kk')}$ is approximated by the one at $S_{i-\frac{1}{2}}^{(kk')}$ (see Section 2.6.2), the numerical dissipation of volume fraction is in fact the same, whatever the value of $\alpha_{i,i-\frac{1}{2}}$ as long as it is between $\alpha_{i-1,i-\frac{1}{2}}$ and α_i according to LED properties. Thus, following $\alpha_{i,i-\frac{1}{2}} = \alpha_i$, we have

$$S_{i,i-\frac{1}{2}}^{\text{rec},(kk')} = S_{i,i-\frac{1}{2}}^{\text{rec},(k'k)} \equiv 0.$$

The numerical scheme for the averaged topological equation with the reconstruction shown in Fig. 3.1 can then be written as (see Section 2.2.1),

$$\alpha_i^{n+1} = \alpha_i^n + \frac{D_{I,i-\frac{1}{2}}\Delta t}{\Delta x}(S_{i-\frac{1}{2}}^{(kk')} - S_{i-\frac{1}{2}}^{(k'k)}) + \frac{D_{I,i+\frac{1}{2}}\Delta t}{\Delta x}(S_{i,i+\frac{1}{2}}^{\text{rec},(kk')} - S_{i,i+\frac{1}{2}}^{\text{rec},(k'k)})\ , \tag{3.13}$$

where

$$\begin{array}{rcl} S_{i-\frac{1}{2}}^{(kk')} & = & \max\{0, \alpha_{i-1,i-\frac{1}{2}} - \alpha_{i,i-\frac{1}{2}}\} \quad = \quad \max\{0, \alpha_{i-1,i-\frac{1}{2}} - \alpha_i\}, \\ S_{i-\frac{1}{2}}^{(k'k)} & = & \max\{0, -\alpha_{i-1,i-\frac{1}{2}} + \alpha_{i,i-\frac{1}{2}}\} \quad = \quad \max\{0, -\alpha_{i-1,i-\frac{1}{2}} + \alpha_i\}, \\ S_{i,i+\frac{1}{2}}^{\text{rec},(kk')} & = & \max\{0, \alpha_i - \alpha_{i,i+\frac{1}{2}}\}, \\ S_{i,i+\frac{1}{2}}^{\text{rec},(k'k)} & = & \max\{0, -\alpha_i + \alpha_{i,i+\frac{1}{2}}\}. \end{array} \tag{3.14}$$

As can be observed in Fig. 3.1, the numerical diffusion from cell i to cell $i+1$ is due to the intercell sub-surface $S_{i+\frac{1}{2}}^{(kk')}$ (or $S_{i+\frac{1}{2}}^{(k'k)}$). The idea of the anti-diffusive approach consists in reducing the maximum numerical diffusion on each intercell boundary, that is, in decreasing the surface of $S_{i+\frac{1}{2}}^{(kk')}$ (or $S_{i+\frac{1}{2}}^{(k'k)}$). If ideally letting $\alpha_{i,i+\frac{1}{2}} = \alpha_{i+1}$ (downwind approach, *i.e.* $S_{i+\frac{1}{2}}^{(kk')} = S_{i+\frac{1}{2}}^{(k'k)} = 0$ and $S_{i,i+\frac{1}{2}}^{\text{rec},(kk')} - S_{i,i+\frac{1}{2}}^{\text{rec},(k'k)} = \alpha_i - \alpha_{i+1}$), there would be absolutely no numerical diffusion from cell i to $i+1$ for the present time step. The phase volumes generated at $x_{i-\frac{1}{2}}$ by $S_{i-\frac{1}{2}}^{(kk')}$ (or $S_{i-\frac{1}{2}}^{(k'k)}$) and at $x_{i,i+\frac{1}{2}}$ by $S_{i,i+\frac{1}{2}}^{\text{rec},(kk')}$ (or $S_{i,i+\frac{1}{2}}^{\text{rec},(k'k)}$) are both stored inside the cell i. However, the LED properties

(3.11) and (3.12) should be considered for the reconstructed volume fraction $\alpha_{i,i+\frac{1}{2}}$. We are thus looking for $S^{(kk')}_{i-\frac{1}{2}} - S^{(k'k)}_{i-\frac{1}{2}}$ and $S^{\text{rec},(kk')}_{i,i+\frac{1}{2}} - S^{\text{rec},(k'k)}_{i,i+\frac{1}{2}}$ (which determines $S^{(kk')}_{i+\frac{1}{2}} - S^{(k'k)}_{i+\frac{1}{2}}$) in (3.13) that can give less numerical dissipation while fulfilling LED conditions. Using the definitions (3.14), equation (3.13) can also be written as

$$\alpha_i^{n+1} = \alpha_i^n + \frac{D_{I,i-\frac{1}{2}}\Delta t}{\Delta x}(\alpha_{i-1,i-\frac{1}{2}} - \alpha_i) + \frac{D_{I,i+\frac{1}{2}}\Delta t}{\Delta x}(\alpha_i - \alpha_{i,i+\frac{1}{2}}) \ . \tag{3.15}$$

As previously done in Section 3.1.1, we can first of all get rid of $\alpha_{i-1,i-\frac{1}{2}}$ in order to obtain a condition on $\alpha_{i,i+\frac{1}{2}}$. Observing that $m_i \leq \alpha_{i-1,i-\frac{1}{2}} \leq M_i$ yields

$$m_i - \alpha_i \leq \alpha_{i-1,i-\frac{1}{2}} - \alpha_i \leq S^{(kk')}_{i-\frac{1}{2}} - S^{(k'k)}_{i-\frac{1}{2}} \leq M_i - \alpha_i. \tag{3.16}$$

Using (3.15) and (3.16) allows to calculate $S^{(kk')}_{i-\frac{1}{2}}$ (or $S^{(k'k)}_{i-\frac{1}{2}}$) and $S^{\text{rec},(kk')}_{i,i+\frac{1}{2}}$ (or $S^{\text{rec},(k'k)}_{i,i+\frac{1}{2}}$), which can then be inserted into the full DEM/RDEM scheme (2.48) for two-fluid system.

3.2 Interpretation of the instability of anti-diffusive reconstruction and the correction

The anti-diffusive reconstruction approach presented in the previous section is able to compute a detonation front but does not work properly for a deflagration test case [Beccantini 10b]. In [Tang 11a, Tang 11b], a multifluid impermeable interface test case is considered to investigate this robustness issue. Some numerical tests show that relaxation procedures preventing from negative pressure occurrence can improve the robustness of the anti-diffusive approach. Unfortunately, for a wide range of cases, this relaxation technique remains delicate to apply. In the present section, we first analyze the stability conditions of the anti-diffusive reconstruction approach combined with DEM/RDEM by relying on wave propagation considerations. This analysis explains in a very clear way why the anti-diffusive approach is unstable for deflagration front. Then, based on this analysis, a correction is proposed, inspired from the large time stepping method proposed in [LeVeque 85], with the purpose of fulfilling the stability conditions for all possible wave tests. Note that the numerical interface velocities are all assumed positive in this section in order to simplify the presentation.

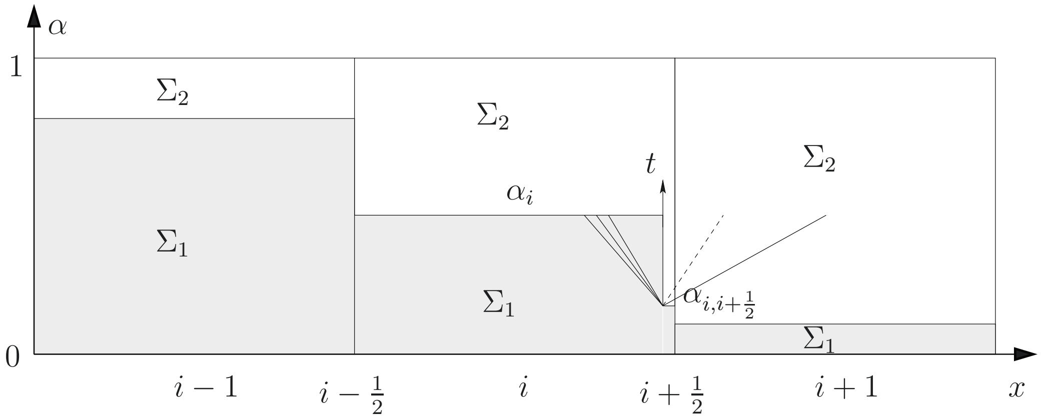

Figure 3.2: Reconstruction of anti-diffusive approach. Not only the contact wave but the nonlinear shock/rarefaction wave of the internal Riemann problem in cell i enter into the cell $i+1$.

3.2.1 Why is the anti-diffusive reconstruction approach not robust for DEM/RDEM?

The anti-diffusive reconstruction within DEM/RDEM described in the previous section is summarized in Fig. 3.2. The internal Lagrangian flux contribution in this approach can be evaluated by (2.46) or (2.47). The volume fraction in this reconstruction respects the LED conditions, and is thus stable. Together with the computed flux $\mathbf{F}^{\mathrm{Lag},(kk')}_{i+\frac{1}{2}}$ (or $\mathbf{F}^{\mathrm{Lag},(k'k)}_{i+\frac{1}{2}}$), the generated phase volume and the associated density, velocity and pressure obtained by solving the internal Riemann problem on $x_{i,i+\frac{1}{2}}$ are stored inside cell i.

A consequence of the anti-diffusive strategy is that the location of the internal discontinuity is restricted to be very close to the intercell boundary. This can be observed in the reconstruction shown in Fig. 3.2 after imposing $\alpha_{i,i-\frac{1}{2}} = \alpha_i$, since the volume conservation should always be maintained. We emphasize that this consequence is not linked to the specific approach followed but is encountered for any anti-diffusive volume fraction reconstruction concept. Let us consider the alternative approach displayed in Fig. 3.3 where the cell i contains two constant states for the volume fraction: the left α state is the same as the one in cell $i-1$, and the right α state is the same as the one in cell $i+1$[1]. The internal discontinuity thus goes closer and closer to the intercell boundary $x_{i-\frac{1}{2}}$ when the volume fraction front propagates to the right.

---

[1] Extending such a reconstruction principle to the multi-dimensional case on unstructured grids is clearly not straightforward.

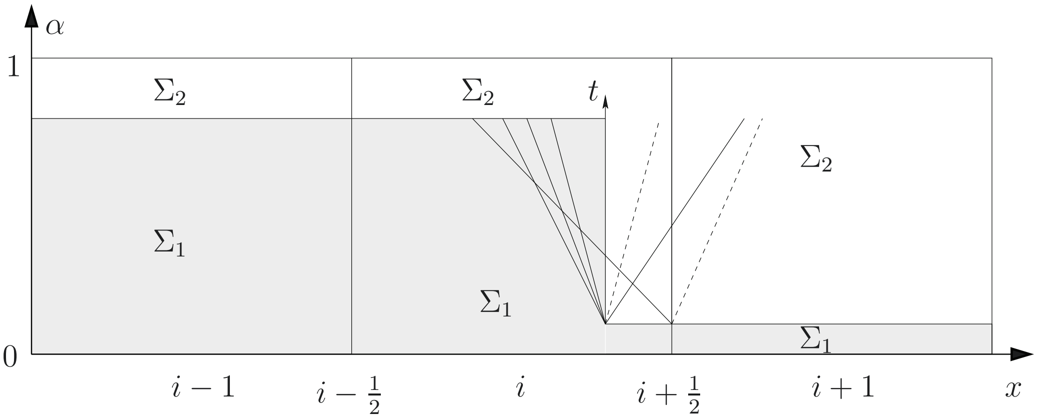

Figure 3.3: Alternative anti-diffusive reconstruction approach with DEM/RDEM. The internal discontinuity goes closer and closer to the intercell boundary when the volume fraction front propagates.

The wave-propagation form due to Leveque ([LeVeque 02]) is an alternative interpretation of the classical finite volume method. Briefly speaking, the cell average is only modified by the waves entering into the control volume from the cell boundaries. We can thus observe that

- the right-going nonlinear wave coming from $x_{i,i+\frac{1}{2}}$ in Fig. 3.2 modifies the cell average variables of phase Σ_2 in both cell i and cell $i+1$;
- the left-going nonlinear and/or linear wave coming from RP22 at $x_{i+\frac{1}{2}}$ can also alter the cell average variables for phase Σ_1 and Σ_2 in cell i.

These two wave propagation mechanisms are not taken into consideration in the anti-diffusive reconstruction approach described in Section 3.1.2. Neglecting these mechanisms leads to calculation failure when the residual phase volume fraction (phase Σ_2 in Fig. 3.2) tends to zero. In fact, the anti-diffusive approach can still work in many cases provided that an extremely low CFL value is used, simply because the impact of the nonlinear wave from the intercell boundary $x_{i+\frac{1}{2}}$ remains weak in that case. The success of the approach in a case of detonation can also be explained: the precursor shock wave is then absent, so that there is no wave impact from the intercell boundary $x_{i+\frac{1}{2}}$; besides, the relatively weak wave impact from the internal boundary $x_{i,i+\frac{1}{2}}$ is generally not sufficient to cause the computation failure.

Summary of numerical difficulties

The reason for the occurrence of instability when a “basic” anti-diffusive method is inserted into DEM/RDEM has been described. Several numerical difficulties must be overcome in order to achieve a stable coupling of an anti-diffusive approach and DEM/RDEM for all wave configurations:

- The internal phase discontinuity can be infinitely close to the intercell boundary and the variable averaging procedure (as the first version of Godunov's method [Toro 97]) remains unclear.
- Since the numerical interface also passes through the intercell boundary in Fig. 3.2, the evaluation of the modified numerical fluxes is not well defined.

We propose in Section 3.2.3 a modification of the intercell boundary's geometric definition to overcome these difficulties by using the large time stepping approach proposed in [LeVeque 85]. Let us briefly review in the next section the main ingredients of this large time stepping approach.

3.2.2 Large time step wave propagation method of Leveque

The standard Godunov method is stable under the condition CFL ≤ 1. This condition remains valid even though wave interaction takes place, under the assumption that no wave acceleration takes place as a consequence of wave interaction. This is in fact a linear assumption ([Toro 97]). In [LeVeque 85], a large time step generalization of Godunov's method is proposed for conservation laws, which can be applied for very large CFL values. The basic idea is that the waves simply pass through each other without any change in speed or strength. As illustrated in Fig. 3.4, the approximated solution at (x,t) can be interpreted as the initial value at (x,t^n) plus the jumps in the vector of conservative variables $\mathbf{u}$ across all waves that cross the line connecting (x,t^n) and (x,t).

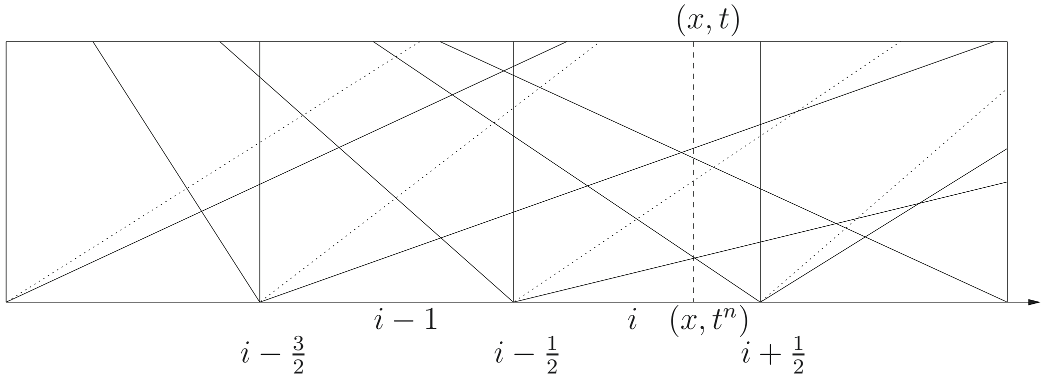

Figure 3.4: Large time wave propagation method.

3.2.3 Large time stepping correction in anti-diffusive approach for DEM/RDEM

As explained in Section 3.2.1, the robustness of an anti-diffusive approach can only be improved if taking into account the effects of the internal Riemann problem waves that enter the downwind cell (cell $i+1$ in Fig. 3.2). For the contribution of these waves to be clearly viewed and taken into consideration within the Large time stepping method, it is proposed to deform the intercell boundary $x_{i+\frac{1}{2}}$ as shown in Fig. 3.5. The red curve $ACC'D'D''E''EF$ is the newly constructed intercell boundary $x_{i+\frac{1}{2}}$ between cell i and cell $i+1$. The volume fraction reconstruction remains the same as before: α_i is the cell average and $\alpha_{i,i+\frac{1}{2}}$ at level CC' and $\alpha_{i-1,i-\frac{1}{2}}$ at level EE'' are calculated so as to limit the numerical interface diffusion as efficiently as possible (Section 3.1.2). Several useful metrics for the new intercell boundary in Fig. 3.5 are:

$$\begin{aligned}
\|AB\| &= S^{(11)}_{i+\frac{1}{2}}, \\
\|BC\| &= S^{(12)}_{i+\frac{1}{2}}, \\
\|CD\| &= \|C'D'\| = S^{\text{rec},(12)}_{i,i+\frac{1}{2}}, \\
\|DE\| &= \|D''E''\| = S^{(12)}_{i-\frac{1}{2}}, \\
\|EF\| &= S^{(22)}_{i-\frac{1}{2}}.
\end{aligned} \tag{3.17}$$

The remaining task, in order to determine the new intercell boundary $x_{i+\frac{1}{2}}$, is to define the two lengths L_p ($= \|DD'\|$) and L_m ($= \|DD''\|$). Let us denote the wave speeds

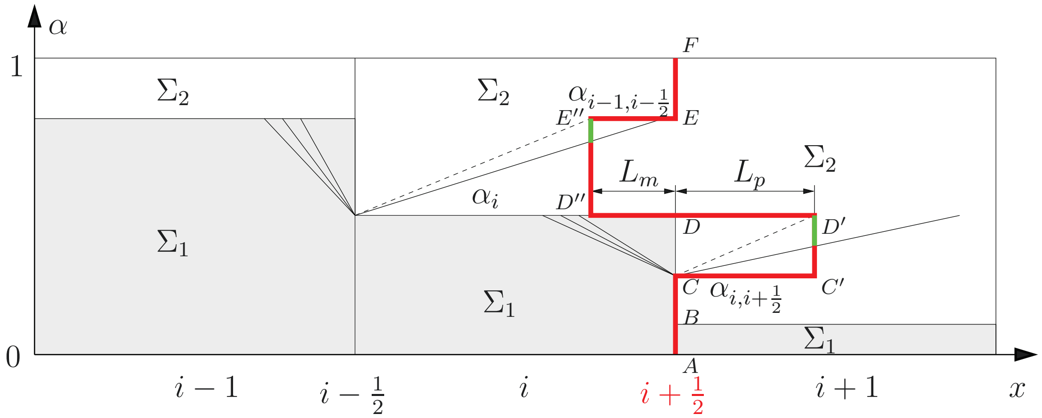

Figure 3.5: Intercell boundary deforming for anti-diffusive approach, with the aim of taking account of nonlinear wave propagation from internal Riemann problem on $x_{i,i+\frac{1}{2}}$. Red curve is the newly constructed intercell boundary. The flux correction will be realized on the green part of this new boundary.

from the internal Riemann problem at $x_{i,i+\frac{1}{2}}$ as $D_{I,i,i+\frac{1}{2}}$ (interface discontinuity) and $D^{\mathrm{GNL}}_{i,i+\frac{1}{2}}$ (right-going nonlinear wave); let us also denote the wave speeds of the two-fluid Riemann problem at intercell boundary $x_{i-\frac{1}{2}}$ as $D_{I,i-\frac{1}{2}}$ (interface discontinuity) and $D^{\mathrm{GNL}}_{i-\frac{1}{2}}$ (right-going nonlinear wave). In our work, the time stepping condition CFL ≤ 1 is always respected, so that a nonlinear wave does not perturb the neighboring intercell boundaries. The values of L_p and L_m are imposed as follows:

$$L_p = \|DD'\| = \|CC'\| = D_{I,i,i+\frac{1}{2}}\Delta t, \tag{3.18}$$

$$L_m = \|DD''\| = \|EE''\| = \frac{\alpha_i - \alpha_{i,i+\frac{1}{2}}}{\alpha_{i-1,i-\frac{1}{2}} - \alpha_i} L_p = \frac{S^{\mathrm{rec},(12)}_{i,i+\frac{1}{2}}}{S^{(12)}_{i-\frac{1}{2}}} L_p. \tag{3.19}$$

These formulae for L_p and L_m ensure that the volume of each element remains conserved, and the numerical interface on $x_{i,i+\frac{1}{2}}$ travels the distance measured by L_p. In the specific case where $S^{(12)}_{i-\frac{1}{2}} = S^{(21)}_{i-\frac{1}{2}} = 0$, we impose $L_p = 0$. As illustrated in Fig. 3.5, the flux correction can thus be realized on the two green parts of the newly constructed intercell boundary, by means of the large time stepping approach. We will next present some of the numerical results obtained using this strategy.

3.2.4 Numerical results of large time stepping correction

When applied to the liquid-gas non-reactive interface problem studied in Section 2.8.1, the baseline anti-diffusive reconstruction approach proposed in Section 3.1.2 allows to obtain numerical results (no calculation failure). However, the approach requires a CFL much lower than unity [Tang 11a] for reasons which have been explained in Section 3.2.1. The numerical results presented in this section are obtained using the above described large time stepping correction for the anti-diffusive approach within DEM/RDEM and clearly demonstrate the achieved robustness improvement.

Let us take 10^{-6} as the residual phase volume fraction for both liquid and gas. The numerical results of the first-order method coupled with the corrected anti-diffusive approach are shown in Fig. 3.6 with a 100-cell uniform mesh. Note the anti-diffusive reconstruction is only applied to the non-conservative averaged topological equation, so that the method is only first-order accurate in space and time for the nonlinear shock and rarefaction waves. The method works very well for the standard time stepping condition CFL < 1.0. These original results are compared with the pure first-order DEM method (upwind method for the topological equation). It can be observed the interface zone is much better resolved with the anti-diffusive strategy. In fact, the interface is described by a single intermediate point - the interface resolution

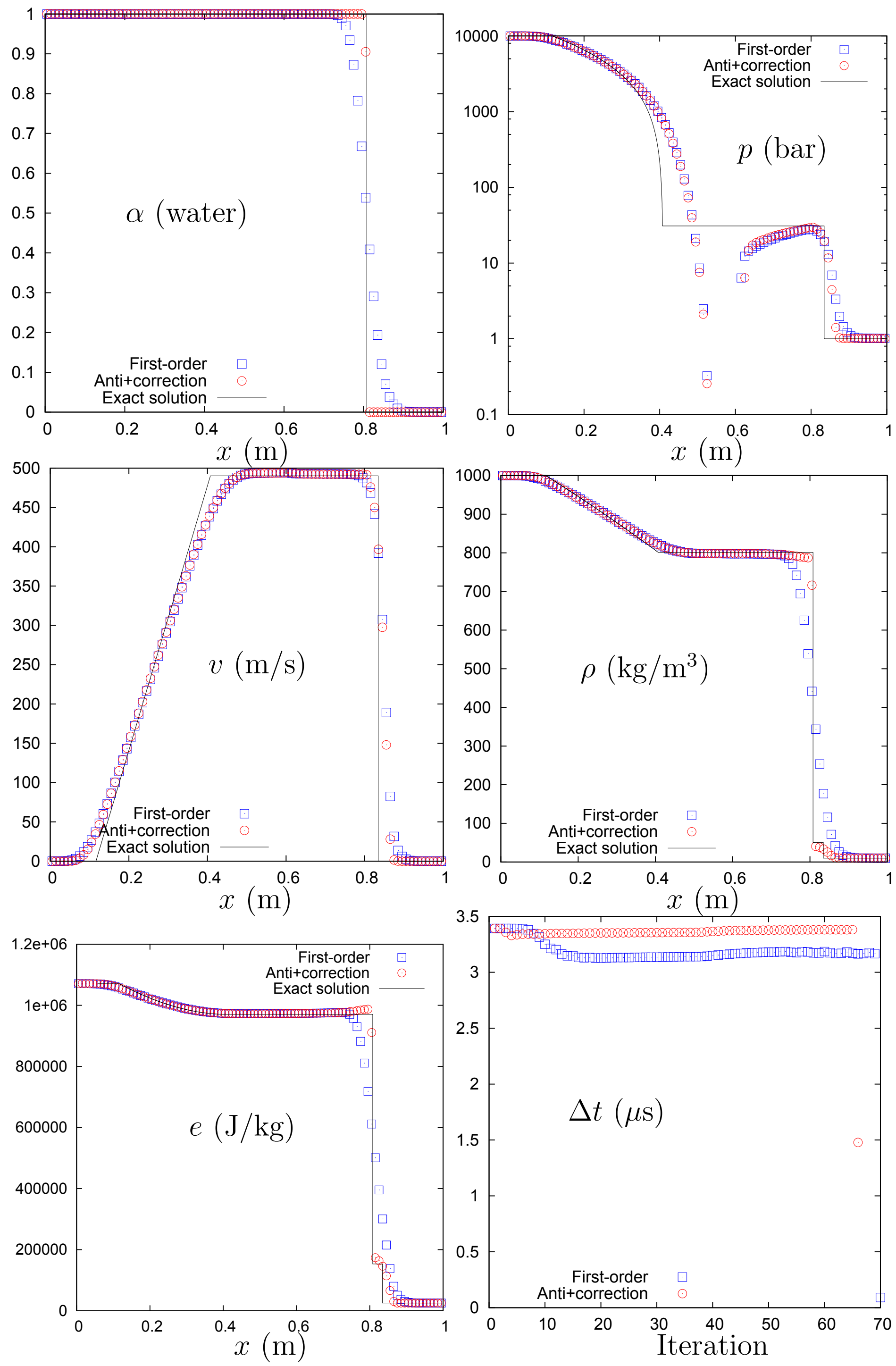

Figure 3.6: First-order DEM method with corrected anti-diffusive approach for water gas shock tube with impermeable interface ([Petitpas 07]). 100 computational cells. $t = 220$ μs. CFL $= 0.9$. Residual phase volume fraction is set as 10^{-6}.

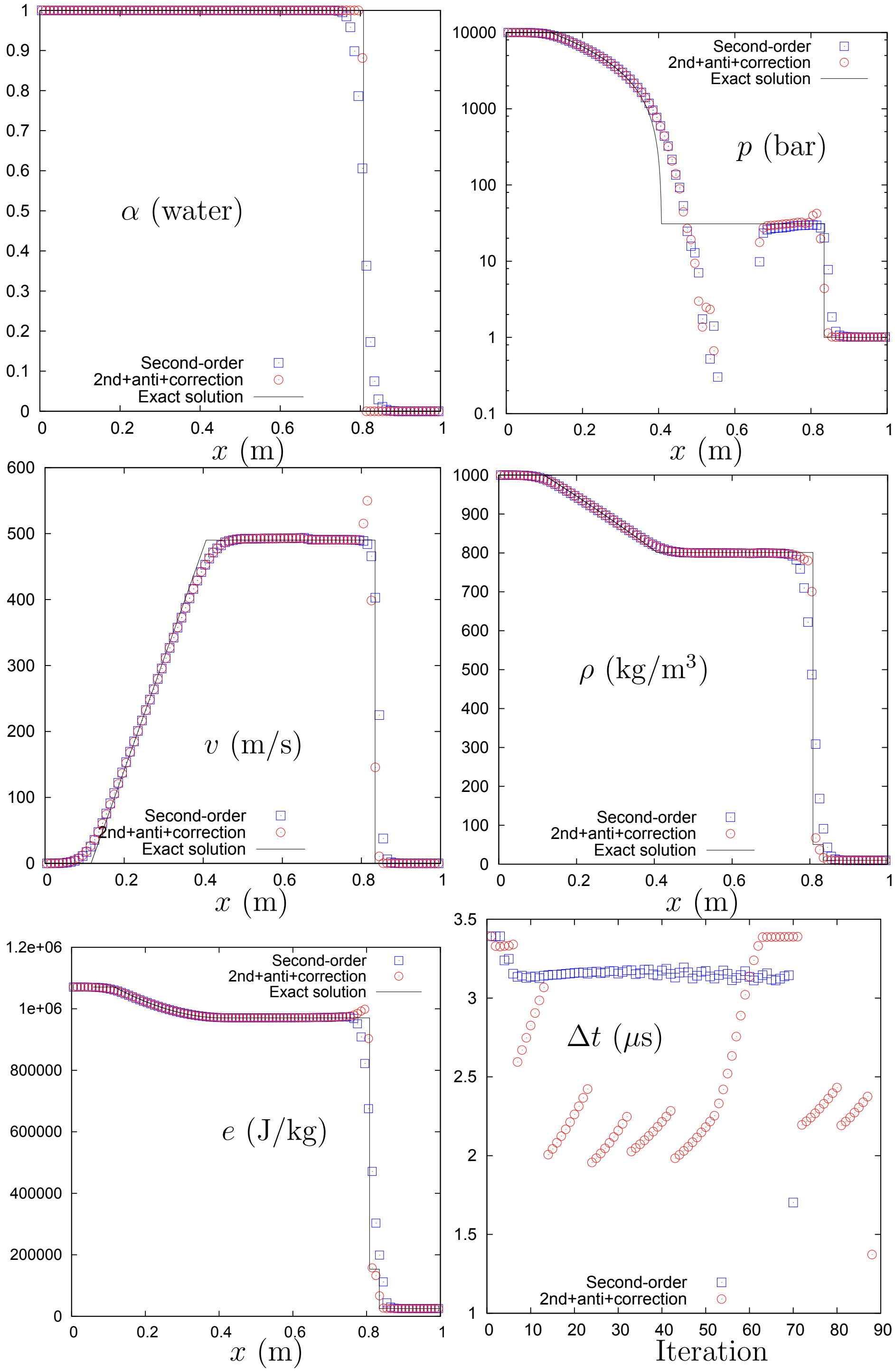

Figure 3.7: Limited second-order DEM method (minmod) with corrected anti-diffusive approach for water gas shock tube with impermeable interface ([Petitpas 07]). 100 computational cells. $t = 220$ μs. CFL $= 0.9$. Residual phase volume fraction is set as 10^{-6}.

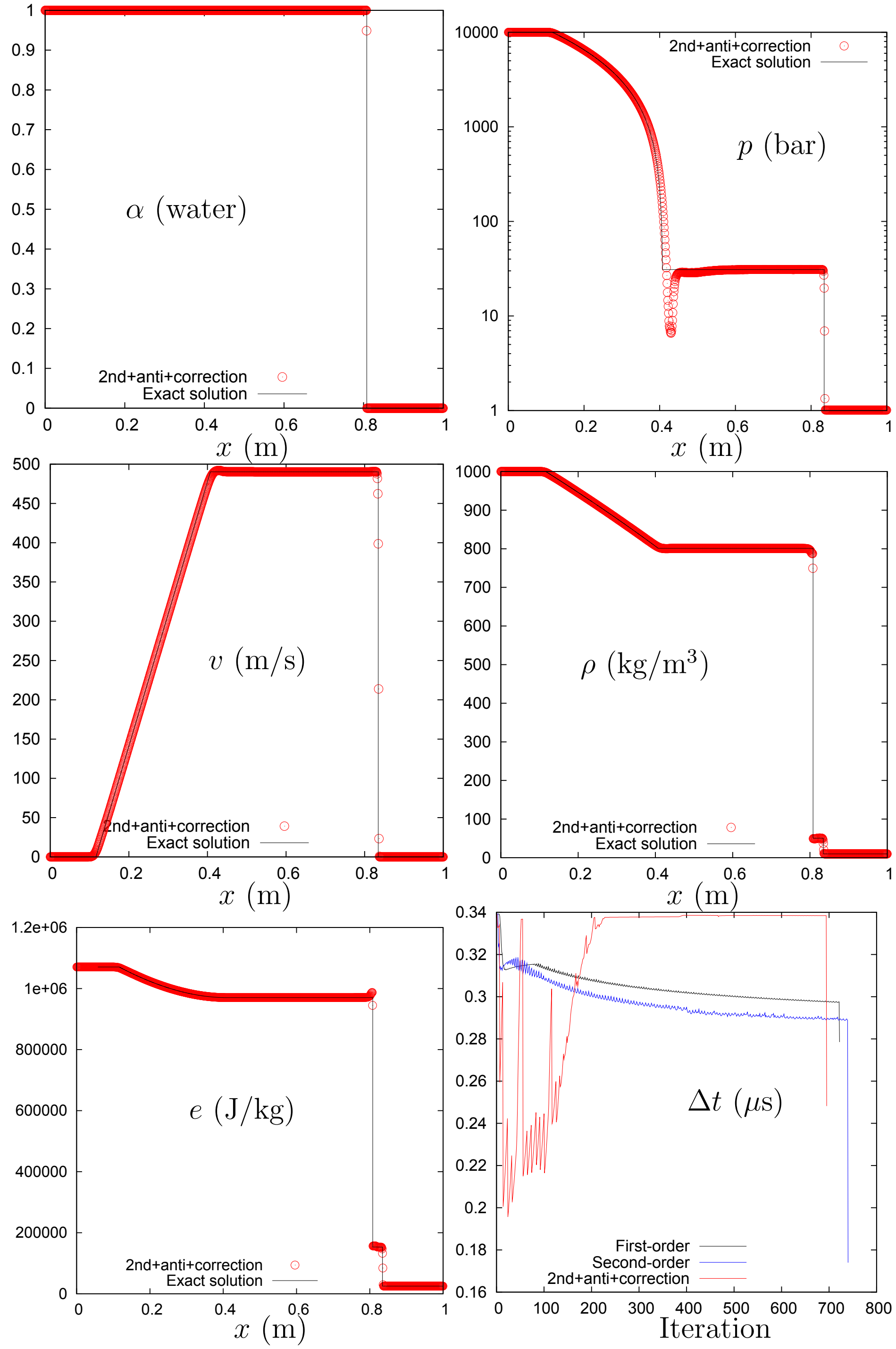

Figure 3.8: Limited second-order DEM method (minmod) with corrected anti-diffusive approach for water gas shock tube with impermeable interface ([Petitpas 07]). 1000 computational cells. $t = 220$ μs. CFL $= 0.9$. Residual phase volume fraction is set as 10^{-6}.

is almost exact. Moreover, the more accurate anti-diffusive approach also requires less time steps than the first-order calculation.

The numerical results computed with the minmod limited second-order method coupled with the corrected anti-diffusive approach are displayed in Fig. 3.7. The second-order accuracy in time is obtained by a Runge-Kutta method. Since the anti-diffusive approach is only applied to the topological equation, the method degenerates into a limited second-order approach for the shock wave and rarefaction wave. We observe that the method works well for CFL < 1.0. These original results are compared with the state-of-the-art[2] (limited) second-order DEM method. It is observed that the corrected anti-diffusive approach is in general more accurate than the second-order method. However, a non-physical overshoot appears at the contact discontinuity for the velocity profile (see Fig. 3.7). This error vanishes very quickly when the mesh is refined (see the results obtained with 1000 elements in Fig. 3.8). We have also checked that all the conservative variables are in good agreement with the exact solution without any oscillations (figure not shown). The robustness of the approach should be improved: as can be observed in Fig. 3.7 the time steps must be reduced at the beginning of the anti-diffusive computation in order to ensure positive physical variables. Note however that after a while the time steps become quasi-constant with values greater than the ones used with the first-order and limited second-order method (Fig. 3.8).

3.3 Upwind downwind-controlled splitting

The anti-diffusive reconstruction for the DEM/RDEM approach which includes the stability correction presented in Section 3.2 considerably improves the robustness of this accurate strategy for interface problems. A persistent drawback of the approach is its multi-dimensional extension which is far from straightforward on unstructured grids.

The upwind downwind-controlled splitting (UDCS) is thus now proposed with the purpose of constructing a robust and accurate method, simple enough to lend itself to a multi-dimensional extension on general unstructured grids. One of the key underlying ideas in devising UDCS is to set robustness as a main priority in the solution procedure. With this idea in mind, the first-order upwind method is first employed in the DEM/RDEM approach for the discretization of the volume fraction (Fig. 3.9(a), thus called the "upwind" step). The separated averaging of conservative variables and volume fraction for both phases is then carried out (Fig. 3.9(b)). At this point,

---

[2] Prior to the present PhD work.

the genuinely nonlinear waves are already taken into account in the first-order upwind approach for the volume fraction. Next, with the aim of improving the volume fraction accuracy, the numerically diffused volume is rearranged: a fraction of this volume is displaced back to its upwind cell element, preserving the conservative properties of all conservative variables for both phases. Furthermore, this displacement process of the phase volumes should, at the same time, respect the Local Extremum Diminishing (LED) property [Jameson 01] of the numerical scheme. Additionally, the corresponding conservative variables assigned to these volumes should also be determined. This step, illustrated in Fig. 3.9(c), is called "downwind-controlled splitting". We emphasize that the "downwind-controlled splitting" step only aims at improving the accuracy of the linearly degenerate wave (contact discontinuity in non-reacting case and reactive shock in reacting case). We note that the "downwind-controlled splitting" step does not involve any robustness issue: as already mentioned above, the genuinely nonlinear waves are no longer of concern, since they have been considered in the "upwind" step.

The principles of the idea being exposed, the original UDCS approach is now described in detail: the main concept is described at first for the topological equation in a 1D situation; its extension to full two-fluid calculations using DEM/RDEM is then introduced; the multi-dimensional case is eventually discussed.

3.3.1 UDCS for the averaged topological equation - downwind factor

The upwind downwind-controlled splitting (UDCS) approach is described in this section for the scalar topological equation in one space dimension. The phase index k is omitted in the following. Let us first assume, for the sake of demonstration, that the interface velocities at location $x_{i-\frac{1}{2}}$ and $x_{i+\frac{1}{2}}$ are both positive. The general case is discussed at the end of this section. Thus, the intercell boundary $x_{i-\frac{1}{2}}$ is an inlet for both phases in cell i; on its other side, $x_{i+\frac{1}{2}}$ is an outlet. According to the first-order upwind method for (1.16) (scheme (2.5) and (2.8)), the inlet and the outlet interfaces at each time step globally "generate" the following volumes (Fig. 3.9(a)):

$$\begin{aligned}
\Delta \mathrm{up}^n_{i-\frac{1}{2}} &= \left(\alpha^n_{i-1} - \alpha^n_i\right) D^n_{I,i-\frac{1}{2}} \Delta t = \left(S^{\mathrm{fir},(kk')}_{i-\frac{1}{2}} - S^{\mathrm{fir},(k'k)}_{i-\frac{1}{2}}\right) D^n_{I,i-\frac{1}{2}} \Delta t, \\
\Delta \mathrm{up}^n_{i+\frac{1}{2}} &= \left(\alpha^n_{i} - \alpha^n_{i+1}\right) D^n_{I,i+\frac{1}{2}} \Delta t = \left(S^{\mathrm{fir},(kk')}_{i+\frac{1}{2}} - S^{\mathrm{fir},(k'k)}_{i+\frac{1}{2}}\right) D^n_{I,i-\frac{1}{2}} \Delta t,
\end{aligned} \tag{3.20}$$

where $D^n_{I,j}$ is the interface velocity at time t^n given by the local two-phase Riemann problem at intercell boundary x_j (Section 2.3.2 and 2.3.3). $S^{\mathrm{fir},(kk')}_j$ (or $S^{\mathrm{fir},(k'k)}_j$) is the two-phase sub-surface defined on intercell boundary x_j by the first-order DEM/RDEM approach (see formulae (2.13)-(2.14)). The "upwinded" state $\alpha_i^{n+1,\mathrm{up}}$ is thus given by

$$\alpha_i^{n+1,\mathrm{up}} = \alpha_i^n + \frac{1}{\Delta x}\Delta \mathrm{up}^n_{i-\frac{1}{2}}. \tag{3.21}$$

The volume quantity kept inside cell i is imposed as follows:

$$\alpha_i^{n+1} = \alpha_i^n + \frac{1-\lambda^n_{i,\mathrm{in},i-\frac{1}{2}}}{\Delta x}\Delta \mathrm{up}^n_{i-\frac{1}{2}} + \frac{\lambda^n_{i,\mathrm{out},i+\frac{1}{2}}}{\Delta x}\Delta \mathrm{up}^n_{i+\frac{1}{2}}, \tag{3.22}$$

or

$$\alpha_i^{n+1} = \alpha_i^{n+1,\mathrm{up}} + \frac{-\lambda^n_{i,\mathrm{in},i-\frac{1}{2}}}{\Delta x}\Delta \mathrm{up}^n_{i-\frac{1}{2}} + \frac{\lambda^n_{i,\mathrm{out},i+\frac{1}{2}}}{\Delta x}\Delta \mathrm{up}^n_{i+\frac{1}{2}}, \tag{3.23}$$

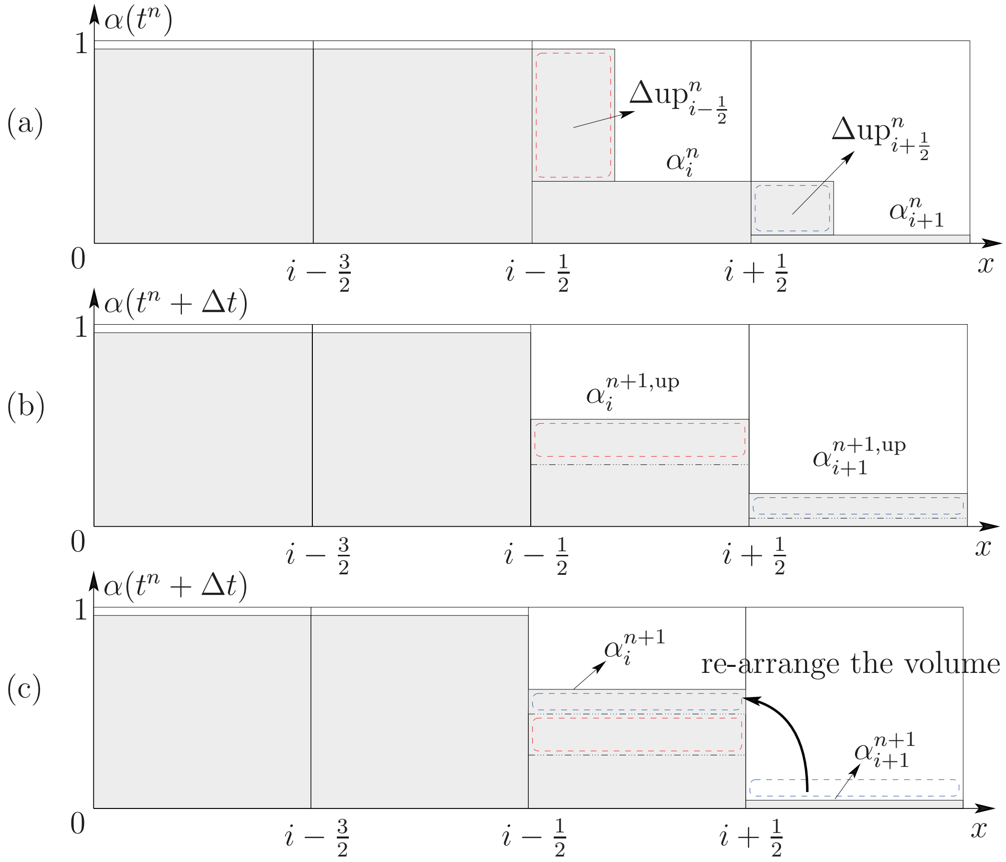

Figure 3.9: UDCS approach. (*a*) first-order upwind DEM approach involving interface evolution according to the two-phase Riemann problem solution. (*b*) separated averaging procedures for each phase. (*c*) phase displacement of UDCS approach determined by the LED property.

where $\lambda^n_{i,\mathrm{in/out},j}$ is the downwind factor defined on the intercell boundary x_j for the instant t^n. We impose that $0 \le \lambda^n_{i,\mathrm{in/out},j} \le 1$ for all j. Note that if setting $\lambda^n_{i,\mathrm{in},i-\frac{1}{2}} = \lambda^n_{i,\mathrm{out},i+\frac{1}{2}} = 0$, formulation (3.22) degenerates to the first-order upwind scheme for (1.16), and if setting $\lambda^n_{i,\mathrm{in},i-\frac{1}{2}} = \lambda^n_{i,\mathrm{out},i+\frac{1}{2}} = 1$ in (3.22), an unconditionally unstable downwind scheme is recovered for (1.16). The UDCS approach (3.22) for the volume fraction topological equation (1.16) consists now in determining the downwind factors $\lambda^n_{i,\mathrm{in},i-\frac{1}{2}}$, $\lambda^n_{i,\mathrm{out},i+\frac{1}{2}}$ in (3.22) for a high resolution of the interface. Two approaches are presented in what follows for this purpose.

- **UDCS second-order approach**

First of all, a second-order reconstruction can be used to calculate these downwind factors:

$$\begin{aligned}
\lambda^n_{i,\mathrm{in},i-\frac{1}{2}} &= \frac{\alpha^n_{i-1} - \alpha^n_{i-1,i-\frac{1}{2}}}{\alpha^n_{i-1} - \alpha^n_i} = \frac{S^{\mathrm{sec},(kk')}_{i-1,i-\frac{1}{2}} - S^{\mathrm{sec},(k'k)}_{i-1,i-\frac{1}{2}}}{S^{\mathrm{fir},(kk')}_{i-\frac{1}{2}} - S^{\mathrm{fir},(k'k)}_{i-\frac{1}{2}}}, \text{ when } D^n_{I,i-\frac{1}{2}} > 0, \alpha^n_{i-1} \neq \alpha^n_i,\\
\lambda^n_{i,\mathrm{out},i+\frac{1}{2}} &= \frac{\alpha^n_i - \alpha^n_{i,i+\frac{1}{2}}}{\alpha^n_i - \alpha^n_{i+1}} = \frac{S^{\mathrm{sec},(kk')}_{i,i+\frac{1}{2}} - S^{\mathrm{sec},(k'k)}_{i,i+\frac{1}{2}}}{S^{\mathrm{fir},(kk')}_{i+\frac{1}{2}} - S^{\mathrm{fir},(k'k)}_{i+\frac{1}{2}}}, \text{ when } D^n_{I,i+\frac{1}{2}} > 0, \alpha^n_i \neq \alpha^n_{i+1}.
\end{aligned} \tag{3.24}$$

Inserting (3.24) into (3.22) yields the UDCS second-order scheme for the averaged topological equation:

$$\alpha^{n+1}_i = \alpha^n_i + \frac{\Delta t}{\Delta x}\left[D^n_{I,i-\frac{1}{2}}(\alpha^n_{i-1,i-\frac{1}{2}} - \alpha^n_i) + D^n_{I,i+\frac{1}{2}}(\alpha^n_i - \alpha^n_{i,i+\frac{1}{2}})\right], \tag{3.25}$$

or equivalently in terms of partitioned sub-surfaces:

$$\begin{aligned}
\alpha^{n+1}_i = \alpha^n_i + \frac{\Delta t}{\Delta x}\Bigg[D^n_{I,i-\frac{1}{2}}\Big((S^{\mathrm{sec},(kk')}_{i-\frac{1}{2}} - S^{\mathrm{sec},(k'k)}_{i-\frac{1}{2}}) + (S^{\mathrm{sec},(kk')}_{i,i-\frac{1}{2}} - S^{\mathrm{sec},(k'k)}_{i,i-\frac{1}{2}})\Big)&\\
+D^n_{I,i+\frac{1}{2}}\Big(S^{\mathrm{sec},(kk')}_{i,i+\frac{1}{2}} - S^{\mathrm{sec},(k'k)}_{i,i+\frac{1}{2}}\Big)\Bigg]&,
\end{aligned} \tag{3.26}$$

where $(S^{\mathrm{sec},(kk')}_{i-\frac{1}{2}} - S^{\mathrm{sec},(k'k)}_{i-\frac{1}{2}})$ is given by (2.37) for second-order intercell two-phase contact. Note that (3.26) makes use of the identity:

$$S^{\mathrm{fir},(kk')}_{i-\frac{1}{2}} - S^{\mathrm{fir},(k'k)}_{i-\frac{1}{2}} = (S^{\mathrm{sec},(kk')}_{i-1,i-\frac{1}{2}} - S^{\mathrm{sec},(k'k)}_{i-1,i-\frac{1}{2}}) + (S^{\mathrm{sec},(kk')}_{i-\frac{1}{2}} - S^{\mathrm{sec},(k'k)}_{i-\frac{1}{2}}) + (S^{\mathrm{sec},(kk')}_{i,i-\frac{1}{2}} - S^{\mathrm{sec},(k'k)}_{i,i-\frac{1}{2}}).$$

Stability condition

An interesting point of the scalar UDCS scheme (3.25) or (3.26) is that it is first-order accurate in time by the forward Euler method and (quasi) second-order accurate in space via a limiting TVD approach; however, it is stable under the condition CFL ≤ 1, since its stability is determined by the first-order upwind method. We emphasize that this is not the case for the state-of-the-art limited second-order method described in Appendix B. Because of the internal reconstruction, this scheme is stable for CFL $\leq \frac{1}{2}$ if time is discretized by using the first-order Euler method. We mention that these two schemes are equivalent to each other if the propagation velocity D_I is constant. However, when D_I is obtained by resolving local Riemann problems in DEM/RDEM, these two second-order approaches differ from each other.

- **UDCS anti-diffusive approach**

Alternatively, the downwind-controlled (anti-diffusive) approach [Després 02] (see Section 3.1) can be used to evaluate the downwind factors in UDCS scheme (3.22), with values in general larger than the ones obtained with TVD limiters. With this aim, we compute, using the inlet interfaces, the minimum and maximum volume fractions m^n and M^n for each cell element i:

$$\begin{aligned} m_i^n &= \min\Big\{\alpha_i^n, \alpha_{i-1}^n\Big\}, \\ M_i^n &= \max\Big\{\alpha_i^n, \alpha_{i-1}^n\Big\}. \end{aligned}$$

The LED property requires to ensure $m_i^n \leq \alpha_i^{n+1} \leq M_i^n$, that is:

$$m_i^n \leq \alpha_i^n + \frac{1-\lambda^n_{i,\text{in},i-\frac{1}{2}}}{\Delta x}\Delta\text{up}^n_{i-\frac{1}{2}} + \frac{\lambda^n_{i,\text{out},i+\frac{1}{2}}}{\Delta x}\Delta\text{up}^n_{i+\frac{1}{2}} \leq M_i^n. \tag{3.27}$$

Formula (3.27) represents a linear system of inequalities which is difficult to solve since it globally involves all the downwind factors λ^n in the computational domain. As already done in Section 3.1, tolerated values can be used as sufficient conditions to satisfy these linear inequalities. Details about the tolerated values of λ^n used in this work can be found in Section 3.3.3 where the general multi-dimensional case is fully studied. In brief, one of the two downwind factors involved in (3.27) is replaced by a fixed value still guaranteeing these inequalities, which allows to simply determine the largest value of the other downwind factor locally. The values of λ^n thus obtained are certainly not the largest ones in the algebraic sense, but this approach gives the practical possibility of determining the required downwind factors locally.

Stability condition

Like the UDCS second-order approach, the UDCS anti-diffusive method is also stable under the condition CFL ≤ 1 when the first-order Euler method is used for time discretization, since its stability is still determined by the first-order upwind method. We thus notice that, with the purpose of high resolution and unlike the conventional reconstruction approach, the splitting idea involved in UDCS does not reduce the stability region of the numerical scheme.

Keeping the notations of (3.20), the UDCS scheme (3.22) for the volume fraction topological equation can be extended to the general case of interface velocity propagations:

$$\begin{aligned}\alpha_i^{n+1} = \alpha_i^n &+ \frac{\Delta\mathrm{up}_{i-\frac{1}{2}}^n}{\Delta x}\left[(1-\lambda_{i,\mathrm{in},i-\frac{1}{2}}^n)\beta_{i-\frac{1}{2}} + \lambda_{i,\mathrm{out},i-\frac{1}{2}}^n(1-\beta_{i-\frac{1}{2}})\right] \\ &+ \frac{\Delta\mathrm{up}_{i+\frac{1}{2}}^n}{\Delta x}\left[(1-\lambda_{i,\mathrm{in},i+\frac{1}{2}}^n)(1-\beta_{i+\frac{1}{2}}) + \lambda_{i,\mathrm{out},i+\frac{1}{2}}^n\beta_{i+\frac{1}{2}}\right],\end{aligned} \tag{3.28}$$

or using $\alpha_i^{n+1,\mathrm{up}}$ which is the upwinded state given by (2.8),

$$\begin{aligned}\alpha_i^{n+1} = \alpha_i^{n+1,\mathrm{up}} &+ \frac{\Delta\mathrm{up}_{i-\frac{1}{2}}^n}{\Delta x}\left[-\lambda_{i,\mathrm{in},i-\frac{1}{2}}^n\beta_{i-\frac{1}{2}} + \lambda_{i,\mathrm{out},i-\frac{1}{2}}^n(1-\beta_{i-\frac{1}{2}})\right] \\ &+ \frac{\Delta\mathrm{up}_{i+\frac{1}{2}}^n}{\Delta x}\left[-\lambda_{i,\mathrm{in},i+\frac{1}{2}}^n(1-\beta_{i+\frac{1}{2}}) + \lambda_{i,\mathrm{out},i+\frac{1}{2}}^n\beta_{i+\frac{1}{2}}\right],\end{aligned} \tag{3.29}$$

where the interface velocity propagation indicator β is defined by (2.7). We emphasize that (3.28) or (3.29) degenerates into the first-order approach (2.8) if setting all the downwind factors to zero. For the UDCS second-order approach, completing the definitions in (3.24), we calculate similarly for other cases:

$$\begin{aligned}\lambda_{i,\mathrm{out},i-\frac{1}{2}}^n &= \frac{\alpha_{i,i-\frac{1}{2}}^n - \alpha_i^n}{\alpha_{i-1}^n - \alpha_i^n} = \frac{S_{i,i-\frac{1}{2}}^{\mathrm{sec},(kk')} - S_{i,i-\frac{1}{2}}^{\mathrm{sec},(k'k)}}{S_{i-\frac{1}{2}}^{\mathrm{fir},(kk')} - S_{i-\frac{1}{2}}^{\mathrm{fir},(k'k)}}, \text{ when } D_{I,i-\frac{1}{2}}^n < 0, \alpha_{i-1}^n \neq \alpha_i^n, \\ \lambda_{i,\mathrm{in},i+\frac{1}{2}}^n &= \frac{\alpha_{i+1}^n - \alpha_{i+1,i+\frac{1}{2}}^n}{\alpha_i^n - \alpha_{i+1}^n} = \frac{S_{i+1,i+\frac{1}{2}}^{\mathrm{sec},(kk')} - S_{i+1,i+\frac{1}{2}}^{\mathrm{sec},(k'k)}}{S_{i+\frac{1}{2}}^{\mathrm{fir},(kk')} - S_{i+\frac{1}{2}}^{\mathrm{fir},(k'k)}}, \text{ when } D_{I,i+\frac{1}{2}}^n < 0, \alpha_i^n \neq \alpha_{i+1}^n.\end{aligned} \tag{3.30}$$

These downwind factors can be further evaluated using the strategy presented in Section 3.3.3 for UDCS anti-diffusive approach. The compact UDCS scheme (3.28) can be written for phase Σ_k in terms of intercell partitioned sub-surfaces as

$$\begin{aligned}\alpha_{k,i}^{n+1} = \alpha_{k,i}^{n} + \frac{\Delta t}{\Delta x}\Big[&\Big((1-\lambda^n_{i,\mathrm{in},i-\frac{1}{2}})\beta_{i-\frac{1}{2}} + \lambda^n_{i,\mathrm{out},i-\frac{1}{2}}(1-\beta_{i-\frac{1}{2}})\Big) D^n_{I,i-\frac{1}{2}} \Big(S^{\mathrm{fir},(kk')}_{i-\frac{1}{2}} - S^{\mathrm{fir},(k'k)}_{i-\frac{1}{2}}\Big) \\ &+ \Big((1-\lambda^n_{i,\mathrm{in},i+\frac{1}{2}})(1-\beta_{i+\frac{1}{2}}) + \lambda^n_{i,\mathrm{out},i+\frac{1}{2}}\beta_{i+\frac{1}{2}}\Big) D^n_{I,i+\frac{1}{2}} \Big(S^{\mathrm{fir},(kk')}_{i+\frac{1}{2}} - S^{\mathrm{fir},(k'k)}_{i+\frac{1}{2}}\Big)\Big].\end{aligned} \tag{3.31}$$

or using $\alpha_{k,i}^{n+1,\mathrm{up}}$ given by (2.18),

$$\begin{aligned}\alpha_{k,i}^{n+1} = \alpha_{k,i}^{n+1,\mathrm{up}} + \frac{\Delta t}{\Delta x}\Big[&\Big(-\lambda^n_{i,\mathrm{in},i-\frac{1}{2}}\beta_{i-\frac{1}{2}} + \lambda^n_{i,\mathrm{out},i-\frac{1}{2}}(1-\beta_{i-\frac{1}{2}})\Big) D^n_{I,i-\frac{1}{2}} \Big(S^{\mathrm{fir},(kk')}_{i-\frac{1}{2}} - S^{\mathrm{fir},(k'k)}_{i-\frac{1}{2}}\Big) \\ &+ \Big(-\lambda^n_{i,\mathrm{in},i+\frac{1}{2}}(1-\beta_{i+\frac{1}{2}}) + \lambda^n_{i,\mathrm{out},i+\frac{1}{2}}\beta_{i+\frac{1}{2}}\Big) D^n_{I,i+\frac{1}{2}} \Big(S^{\mathrm{fir},(kk')}_{i+\frac{1}{2}} - S^{\mathrm{fir},(k'k)}_{i+\frac{1}{2}}\Big)\Big],\end{aligned} \tag{3.32}$$

3.3.2 UDCS for the two-fluid system

The UDCS scheme (3.29) developed in Section 3.3.1 for the volume fraction topological equation (1.16) can be easily implemented into the (Reactive) Discrete Equations Method for the full two-fluid system. As previously mentioned, in order to guarantee the method robustness, the first-order upwind DEM/RDEM method is, first of all, processed for the whole two-phase system (Fig. 3.9(a)). The conservative variables of each phase are consequently updated after upwinding (state denoted $\mathbf{U}_k^{n+1,\mathrm{up}}$) using the separated averaging procedure described in Chapter 2 (Fig. 3.9(b)). Then, following the strategy described in Section 3.3.1, the corresponding volumes of each phase are globally rearranged in the computational domain using the formulae (3.28) or (3.29) with the computed downwind factors (UDCS second-order approach or UDCS anti-diffusive approach) at each intercell boundary (Fig. 3.9(c)).

The only remaining issue in the upwind downwind-controlled splitting approach is to determine how to assign the conservative variables to the corresponding displaced volumes of each phase. A possible approach is to associate these phase volumes being displaced and rearranged with the conservative variables $\mathbf{U}_k^{n+1,\mathrm{up}}$ after the first-order upwind approach of DEM/RDEM. This numerical technique takes advantage of the stability property of the upwind scheme, and a wide range of numerical experiments involving both reacting and non-reacting flows shows that this simple association is numerically efficient since the corresponding results are oscillation free and very accurate near the interface.

Considering for instance the first-order forward Euler time discretization, the solution procedure of UDCS can be summarized as follows:

1. The first-order upwind DEM/RDEM method is processed in order to obtain the intermediate "upwinded" state $\begin{bmatrix}\alpha\\ \alpha\mathbf{U}\end{bmatrix}_{k,i}^{n+1,\text{up}}$ of each cell i:

$$\begin{bmatrix}\alpha\\ \alpha\mathbf{U}\end{bmatrix}_{k,i}^{n+1,\text{up}} = \begin{bmatrix}\alpha\\ \alpha\mathbf{U}\end{bmatrix}_{k,i}^{n} + \frac{\Delta t}{\Delta x}\left[\left(\mathscr{R}^{C}_{k,i-\frac{1}{2}} + \mathscr{R}^{\text{Lag}}_{k,i-\frac{1}{2},i}\right) - \left(\mathscr{R}^{C}_{k,i+\frac{1}{2}} + \mathscr{R}^{\text{Lag}}_{k,i+\frac{1}{2},i}\right)\right], \tag{3.33}$$

   and the generated volume $\Delta\text{up}^{n}_{j-\frac{1}{2}}$ on each intercell boundary $x_{j-\frac{1}{2}}$:

$$\Delta\text{up}^{n}_{j-\frac{1}{2}} = \left(\alpha^{n}_{j-1} - \alpha^{n}_{j}\right) D^{n}_{I,j-\frac{1}{2}}\Delta t = \left(S^{\text{fir},(kk')}_{j-\frac{1}{2}} - S^{\text{fir},(k'k)}_{j-\frac{1}{2}}\right) D^{n}_{I,j-\frac{1}{2}}\Delta t.$$

2. Using either the UDCS second-order approach or the UDCS anti-diffusive approach, compute the downwind factors at intercell boundaries: $\lambda^{n}_{i,\text{in},i-\frac{1}{2}}$ if $D^{n}_{I,i-\frac{1}{2}} > 0$ or $\lambda^{n}_{i,\text{out},i-\frac{1}{2}}$ if $D^{n}_{I,i-\frac{1}{2}} < 0$, and $\lambda^{n}_{i,\text{in},i+\frac{1}{2}}$ if $D^{n}_{I,i+\frac{1}{2}} < 0$ or $\lambda^{n}_{i,\text{out},i+\frac{1}{2}}$ if $D^{n}_{I,i+\frac{1}{2}} > 0$.

3. Evaluate the new volume fraction state $\alpha^{n+1}_{k,i}$ by the UDCS approach (3.28) or (3.29).

4. Evaluate the new state for other variables $(\alpha\mathbf{U})^{n+1}_{k,i}$ by the "downwind-controlled splitting" idea:

$$\begin{aligned}
(\alpha\mathbf{U})^{n+1}_{k,i} &= (\alpha\mathbf{U})^{n+1,\text{up}}_{k,i} \\
&+ \frac{\Delta\text{up}^{n}_{i-\frac{1}{2}}}{\Delta x}\left[-\lambda^{n}_{i,\text{in},i-\frac{1}{2}}\beta_{i-\frac{1}{2}}\mathbf{U}^{n+1,\text{up}}_{k,i} + \lambda^{n}_{i,\text{out},i-\frac{1}{2}}(1-\beta_{i-\frac{1}{2}})\mathbf{U}^{n+1,\text{up}}_{k,i-1}\right] \qquad (3.34)\\
&+ \frac{\Delta\text{up}^{n}_{i+\frac{1}{2}}}{\Delta x}\left[-\lambda^{n}_{i,\text{in},i+\frac{1}{2}}(1-\beta_{i+\frac{1}{2}})\mathbf{U}^{n+1,\text{up}}_{k,i} + \lambda^{n}_{i,\text{out},i+\frac{1}{2}}\beta_{i+\frac{1}{2}}\mathbf{U}^{n+1,\text{up}}_{k,i+1}\right].
\end{aligned}$$

Discussion

As observed from (3.34) where the system variables $\mathbf{U}^{n+1}_{k,i}$ are updated by the first-order "upwinded" data $\alpha^{n+1,\text{up}}_{k,i}$ and $\mathbf{U}^{n+1,\text{up}}_{k,i}$, the "downwind-controlled splitting" step does not involve any genuinely nonlinear waves, since those have been considered in the "upwind" step 1. For this reason, the stability of the UDCS approach (3.34) combined with (3.29) is the same as the stability of the scheme calculating $\alpha^{n+1,\text{up}}_{k,i}$ and $\mathbf{U}^{n+1,\text{up}}_{k,i}$. This feature plays a key role in preventing the occurrence of robustness problems for UDCS.

3.3.3 UDCS for multi-dimensional case and the downwind factor determination

Topological equation and downwind factor calculation

For the sake of simplicity, a two-dimensional case is presented here but the ideas which are developed hold for 3D problems. The phase index k is omitted in this section since the UDCS scheme is the same for both phases.

An unstructured two-dimensional element $\mathcal{C}_i$ is presented in Fig. 3.10. Its boundaries $\{\partial\mathcal{C}_{i,j}\}$ are divided into two categories: *inlet* (noted as $\{\partial\mathcal{C}_{i,\text{in},j}\}$) and *outlet* (noted as $\{\partial\mathcal{C}_{i,\text{out},j}\}$) ones. An inlet boundary $\partial\mathcal{C}_{i,\text{in},j}$ for phase Σ_k is characterized by $\mathbf{D}^n_{i,\text{in},j} \cdot \mathbf{n}_{i,\text{in},j} < 0$, with $\mathbf{n}_{i,\text{in},j}$ the normal vector pointing toward the outside of $\mathcal{C}_i$. That is, the interface enters inside $\mathcal{C}_i$, which generates a (positive or negative) volume of Σ_k. On the other hand, an outlet boundary $\partial\mathcal{C}_{i,\text{out},j}$ is such that $\mathbf{D}^n_{i,\text{out},j} \cdot \mathbf{n}_{i,\text{out},j} > 0$.

The first-order upwind DEM/RDEM scheme (Chapter 2) for the multi-dimensional topological equation (1.16) can be written as

$$\alpha_i^{n+1,\text{up}} = \alpha_i^n + \sum_j \frac{\Delta \text{up}^n_{i,\text{in},j}}{|\mathcal{C}_i|}, \tag{3.35}$$

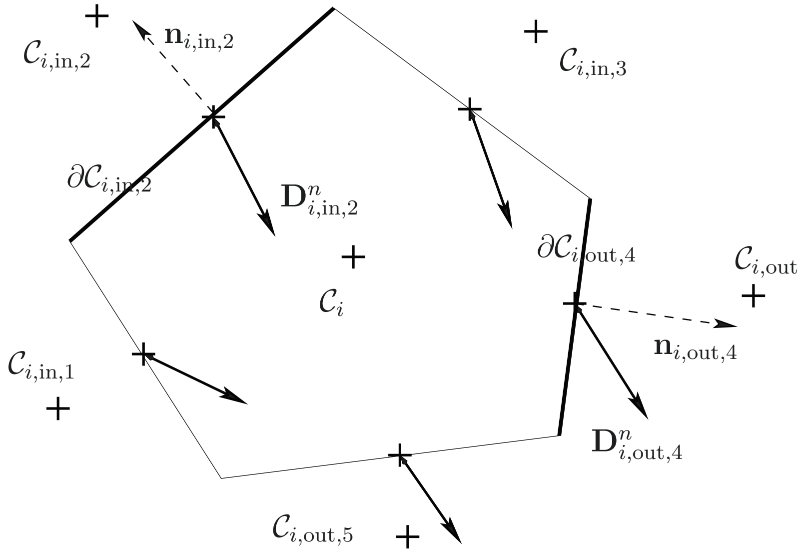

Figure 3.10: Two dimensional finite volume cell. Illustration for numerical resolution of topological equation.

with $|\mathcal{C}_i|$ the volume of $\mathcal{C}_i$ and $\Delta\mathrm{up}^n_{i,\mathrm{in},j}$ the volume of Σ_k entering into $\mathcal{C}_i$ through the inlet boundary $\partial\mathcal{C}_{i,\mathrm{in},j}$ and defined by

$$\Delta\mathrm{up}^n_{i,\mathrm{in},j} = \left(\alpha^n_{i,\mathrm{in},j} - \alpha^n_i\right) |\partial\mathcal{C}_{i,\mathrm{in},j}| \left|\mathbf{D}^n_{i,\mathrm{in},j} \cdot \mathbf{n}_{i,\mathrm{in},j}\right| \Delta t, \tag{3.36}$$

with $|\partial\mathcal{C}_{i,\mathrm{in},j}|$ the interfacial surface area of $\partial\mathcal{C}_{i,\mathrm{in},j}$. The upwind formulation (3.35) can be rearranged as follows:

$$\alpha^{n+1,\mathrm{up}}_i = \alpha^n_i \Big(1 - \frac{\Delta t}{|\mathcal{C}_i|} \sum_j |\partial\mathcal{C}_{i,\mathrm{in},j}| \left|\mathbf{D}^n_{i,\mathrm{in},j} \cdot \mathbf{n}_{i,\mathrm{in},j}\right|\Big) + \sum_j \alpha^n_{i,\mathrm{in},j} \Big(\frac{\Delta t}{|\mathcal{C}_i|} |\partial\mathcal{C}_{i,\mathrm{in},j}| \left|\mathbf{D}^n_{i,\mathrm{in},j} \cdot \mathbf{n}_{i,\mathrm{in},j}\right|\Big). \tag{3.37}$$

When imposing, in practical computations, the time step Δt such that

$$\Delta t \leq \min_i \frac{|\mathcal{C}_i|}{\displaystyle\sum_j |\partial\mathcal{C}_{i,\mathrm{in},j}| \left|\mathbf{D}^n_{i,\mathrm{in},j} \cdot \mathbf{n}_{i,\mathrm{in},j}\right|}, \tag{3.38}$$

$\alpha^{n+1,\mathrm{up}}_i$ in (3.37) can thus be viewed as an average value among α^n_i and the set $\{\alpha^n_{i,\mathrm{in},j}\}$ of its inlet neighbors $\{\mathcal{C}_{i,\mathrm{in},j}\}$, which obviously respect the local Extremum Diminishing (LED) property [Jameson 01]:

$$\alpha^{n+1}_i \in [m^n_i, M^n_i]. \tag{3.39}$$

The local maximum and minimum values for $\mathcal{C}_i$ in (3.39) are computed as follows:

$$\begin{aligned} m^n_{i,\mathrm{in},j} &= \min\{\alpha^n_i, \alpha^n_{i,\mathrm{in},j}\}, \\ M^n_{i,\mathrm{in},j} &= \max\{\alpha^n_i, \alpha^n_{i,\mathrm{in},j}\}, \\ m^n_i &= \min_j\{m^n_{i,\mathrm{in},j}\}, \\ M^n_i &= \max_j\{M^n_{i,\mathrm{in},j}\}. \end{aligned} \tag{3.40}$$

It is worthwhile to notice that, if only viewing the scalar equation (1.16), the time step restriction (2.35) is a sufficient (but not necessary) condition to satisfy (3.39). Indeed, due to the inequality $\left|\sum_j \Delta\mathrm{up}^n_{i,\mathrm{in},j}\right| \leq \sum_j \left|\Delta\mathrm{up}^n_{i,\mathrm{in},j}\right|$, a larger Δt than the one given by (2.35) could still be able to ensure the LED condition (3.39). Furthermore, it is emphasized that, within the framework of the DEM/RDEM approach, the time step Δt is additionally restricted by acoustic wave speeds.

Using the first-order upwind DEM/RDEM scheme, the volume fraction contribution of the outlet boundary $\partial\mathcal{C}_{i,\mathrm{out},j}$ to the neighboring cell $\mathcal{C}_{i,\mathrm{out},j}$ is quantified by the exiting volume:

$$\Delta\text{up}^n_{i,\text{out},j} = \left(\alpha^n_i - \alpha^n_{i,\text{out},j}\right) |\partial\mathcal{C}_{i,\text{out},j}|\, \mathbf{D}^n_{i,\text{out},j} \cdot \mathbf{n}_{i,\text{out},j}\Delta t. \tag{3.41}$$

Following the downwind factor idea introduced in Section 3.3.1, and using the first-order Euler time discretization, the high resolution UDCS scheme designed for the multi-dimensional case reads:

$$\alpha^{n+1}_i = \alpha^n_i + \sum_j (1 - \lambda^n_{i,\text{in},j}) \frac{\Delta\text{up}^n_{i,\text{in},j}}{|\mathcal{C}_i|} + \sum_j \lambda^n_{i,\text{out},j} \frac{\Delta\text{up}^n_{i,\text{out},j}}{|\mathcal{C}_i|}, \tag{3.42}$$

or if including the "upwinded" state $\alpha^{n+1,\text{up}}_i$,

$$\alpha^{n+1}_i = \alpha^{n+1,\text{up}}_i + \sum_j (-\lambda^n_{i,\text{in},j}) \frac{\Delta\text{up}^n_{i,\text{in},j}}{|\mathcal{C}_i|} + \sum_j \lambda^n_{i,\text{out},j} \frac{\Delta\text{up}^n_{i,\text{out},j}}{|\mathcal{C}_i|}. \tag{3.43}$$

(3.42) and (3.43) degenerate into the first-order upwind scheme when setting all the downwind factors to zero. On the other hand, an unstable downwind scheme is recovered if putting all downwind factors to unity. Schemes (3.42) and (3.43) can be understood as follows: a part of the volume Δup^n_j generated and transported across the boundary $\partial\mathcal{C}_{i,j}$ by the first-order upwind method is returned back to its upwind cell (this volume percentage is precisely the downwind factor λ^n_j) . That is, based on the upwind result in $\mathcal{C}_i$, we return the amount of $\lambda^n_{i,\text{in},j}\Delta\text{up}^n_{i,\text{in},j}$ to its inlet neighbor $\mathcal{C}_{i,\text{in},j}$, and on the other side, fetch the amount of $\lambda^n_{i,\text{out},j}\Delta\text{up}^n_{i,\text{out},j}$ from its outlet neighbor $\mathcal{C}_{i,\text{out},j}$. Obviously, with larger values for the downwind factors $\lambda^n_{i,\text{in},j}, \lambda^n_{i,\text{out},j}$, the scheme will be more accurate; however, the local LED condition (3.39) should remain satisfied.

- **UDCS second-order approach**

  As done in Section 3.3.1, the UDCS second-order accurate scheme can be obtained by using the slope limiting strategy. In this framework, the value of the downwind factor $\lambda^n_{i,\text{out},j}$ for an outlet boundary is determined by

$$\lambda^n_{i,\text{out},j} = \frac{\alpha^n_i - \alpha^n_{\text{f},\text{out},j}}{\alpha^n_i - \alpha^n_{i,\text{out},j}}, \text{ when } \alpha^n_i \neq \alpha^n_{i,\text{out},j}. \tag{3.44}$$

  $\alpha^n_{\text{f},\text{out},j}$ in (3.44) is the reconstructed value at the boundary $\partial\mathcal{C}_{i,\text{out},j}$ within cell $\mathcal{C}_i$ using slope limiter. The value of the downwind factor $\lambda^n_{i,\text{in},j}$ for an inlet boundary is determined analogously:

$$\lambda^n_{i,\text{in},j} = \frac{\alpha^n_{i,\text{in},j} - \alpha^n_{\text{f},i,\text{in},j}}{\alpha^n_{i,\text{in},j} - \alpha^n_i}, \text{ when } \alpha^n_i \neq \alpha^n_{i,\text{in},j}. \tag{3.45}$$

$\alpha^n_{\text{f},i,\text{in},j}$ in (3.45) is the reconstructed value at the boundary $\partial\mathcal{C}_{i,\text{in},j}$ within cell $\mathcal{C}_{i,\text{in},j}$ using slope limiter.

- **UDCS anti-diffusive approach**

For simplicity, a unique value of the downwind factor $\lambda^n_{i,\text{out}}$ defined for cell $\mathcal{C}_i$ is imposed for all the outlet boundaries $\{\partial\mathcal{C}_{i,\text{out},j}\}$:

$$\lambda^n_{i,\text{out},j} = \lambda^n_{i,\text{out}}, \text{ for any } j.$$

Thus, by defining

$$\Delta\text{up}^n_{i,\text{out}} = \sum_j \Delta\text{up}^n_{i,\text{out},j}$$

for cell $\mathcal{C}_i$, (3.39) is rewritten as follows:

$$\alpha^{n+1}_i = \alpha^n_i + \sum_j (1 - \lambda^n_{i,\text{in},j}) \frac{\Delta\text{up}^n_{i,\text{in},j}}{|\mathcal{C}_i|} + \lambda^n_{i,\text{out}} \frac{\Delta\text{up}^n_{i,\text{out}}}{|\mathcal{C}_i|} \geq m^n_i, \tag{3.46}$$

$$\alpha^{n+1}_i = \alpha^n_i + \sum_j (1 - \lambda^n_{i,\text{in},j}) \frac{\Delta\text{up}^n_{i,\text{in},j}}{|\mathcal{C}_i|} + \lambda^n_{i,\text{out}} \frac{\Delta\text{up}^n_{i,\text{out}}}{|\mathcal{C}_i|} \leq M^n_i. \tag{3.47}$$

It is easy to verify that, when setting $\lambda^n_{i,\text{out}} = 0$, both (3.46) and (3.47) are fulfilled for any value of $\lambda^n_{i,\text{in},j}$, by writing α^{n+1}_i as an average among α^n_i and the values of its inlet neighbors $\{\alpha^n_{i,\text{in},j}\}$ as done in (3.37):

$$\begin{aligned} \alpha^{n+1}_i = {} & \alpha^n_i \Big(1 - \frac{\Delta t}{|\mathcal{C}_i|} \sum_j (1 - \lambda^n_{i,\text{in},j}) \, |\partial\mathcal{C}_{i,\text{in},j}| \, \big|\mathbf{D}^n_{i,\text{in},j} \cdot \mathbf{n}_{i,\text{in},j}\big|\Big) \\ & + \sum_j \alpha^n_{i,\text{in},j} \Big(\frac{\Delta t}{|\mathcal{C}_i|} (1 - \lambda^n_{i,\text{in},j}) \, |\partial\mathcal{C}_{i,\text{in},j}| \, \big|\mathbf{D}^n_{i,\text{in},j} \cdot \mathbf{n}_{i,\text{in},j}\big|\Big), \end{aligned} \tag{3.48}$$

where we have used the result below coming from the stability condition (3.38):

$$
\begin{aligned}
& \frac{\Delta t}{|\mathcal{C}_i|}(1-\lambda^n_{i,\mathrm{in},j})\,|\partial\mathcal{C}_{i,\mathrm{in},j}|\,\left|\mathbf{D}^n_{i,\mathrm{in},j}\cdot\mathbf{n}_{i,\mathrm{in},j}\right| \\
\leq\ & \frac{\Delta t}{|\mathcal{C}_i|}\sum_j(1-\lambda^n_{i,\mathrm{in},j})\,|\partial\mathcal{C}_{i,\mathrm{in},j}|\,\left|\mathbf{D}^n_{i,\mathrm{in},j}\cdot\mathbf{n}_{i,\mathrm{in},j}\right| \\
\leq\ & \frac{\Delta t}{|\mathcal{C}_i|}\sum_j|\partial\mathcal{C}_{i,\mathrm{in},j}|\,\left|\mathbf{D}^n_{i,\mathrm{in},j}\cdot\mathbf{n}_{i,\mathrm{in},j}\right| \\
\leq\ & 1.
\end{aligned}
\tag{3.49}
$$

Furthermore, the following results can also be established: if $\Delta\mathrm{up}^n_{i,\mathrm{out}} < 0$, (3.47) is satisfied; on the other hand, if $\Delta\mathrm{up}^n_{i,\mathrm{out}} > 0$, (3.46) is satisfied. It thus follows the restrictive conditions for the downwind factors can be summarized as:

$$
\begin{cases}
0 \leq \lambda^n_{i,\mathrm{out}} \leq 1; \\
0 \leq \lambda^n_{i,\mathrm{in},j} \leq 1,\ \forall j; \\
\lambda^n_{i,\mathrm{out}} \leq \begin{cases}
\dfrac{1}{\left|\Delta\mathrm{up}^n_{i,\mathrm{out}}\right|}\left[|\mathcal{C}_i|\,(\alpha^n_i - m^n_i) + \displaystyle\sum_j(1-\lambda^n_{i,\mathrm{in},j})\Delta\mathrm{up}^n_{i,\mathrm{in},j}\right], & \text{if } \Delta\mathrm{up}^n_{i,\mathrm{out}} < 0; \\
\dfrac{1}{\left|\Delta\mathrm{up}^n_{i,\mathrm{out}}\right|}\left[|\mathcal{C}_i|\,(M^n_i - \alpha^n_i) - \displaystyle\sum_j(1-\lambda^n_{i,\mathrm{in},j})\Delta\mathrm{up}^n_{i,\mathrm{in},j}\right], & \text{if } \Delta\mathrm{up}^n_{i,\mathrm{out}} > 0.
\end{cases}
\end{cases}
\tag{3.50}
$$

It is certain that the system of inequalities (3.50) admits some solutions $\{\lambda^n_{i,\mathrm{out}}\}$ (for instance, $\lambda^n_{i,\mathrm{out}} = 0$ is inside its solution region for any $\lambda^n_{i,\mathrm{in},j}$). Unfortunately (3.50) involves almost all the intercell boundaries in the whole domain considered, which creates serious algebraic difficulties to find the full solution region for the downwind factor $\lambda^n_{i,\mathrm{out}}$. As done in Section 3.3.1 for the one-dimensional case (following the technique proposed in [Després 02]), we use a sub-region of the solution of (3.50) as follows:

$$
\begin{cases}
0 \leq \lambda^n_{i,\mathrm{out}} \leq 1; \\
\lambda^n_{i,\mathrm{out}} \leq \Lambda^n_i = \begin{cases}
\dfrac{1}{\left|\Delta\mathrm{up}^n_{i,\mathrm{out}}\right|}\left[|\mathcal{C}_i|\,(\alpha^n_i - m^n_i) + \displaystyle\sum_j\frac{1}{2}\Big(1-\mathrm{sign}(\Delta\mathrm{up}^n_{i,\mathrm{in},j})\Big)\Delta\mathrm{up}^n_{i,\mathrm{in},j}\right], \\
\hfill \text{if } \Delta\mathrm{up}^n_{i,\mathrm{out}} < 0; \\
\dfrac{1}{\left|\Delta\mathrm{up}^n_{i,\mathrm{out}}\right|}\left[|\mathcal{C}_i|\,(M^n_i - \alpha^n_i) - \displaystyle\sum_j\frac{1}{2}\Big(1+\mathrm{sign}(\Delta\mathrm{up}^n_{i,\mathrm{in},j})\Big)\Delta\mathrm{up}^n_{i,\mathrm{in},j}\right], \\
\hfill \text{if } \Delta\mathrm{up}^n_{i,\mathrm{out}} > 0.
\end{cases}
\end{cases}
\tag{3.51}
$$

Hence, the optimized downwind factor $\lambda^n_{i,\text{out}}$ can be determined locally.

UDCS for two-fluid system

With the first-order Euler time discretization, the solution procedure for the multi-dimensional UDCS applied to the full two-fluid system can be summarized as follows:

1. The first-order upwind DEM/RDEM method is applied with the aim to obtain the intermediate "upwinded" state $\begin{bmatrix}\alpha \\ \alpha\mathbf{U}\end{bmatrix}^{n+1,\text{up}}_{k,i}$ of each cell i:

$$\begin{bmatrix}\alpha \\ \alpha\mathbf{U}\end{bmatrix}^{n+1}_{k,i} = \begin{bmatrix}\alpha \\ \alpha\mathbf{U}\end{bmatrix}^{n}_{k,i} - \frac{\Delta t}{|\mathcal{C}_i|}\sum_j |\partial\mathcal{C}_{ij}| \left(\mathscr{R}^C_{k,j,i} + \mathscr{R}^{\text{Lag}}_{k,j,i}\right), \tag{3.52}$$

   and the generated volume $\Delta\text{up}^n_{i,\text{in/out},j}$ on its intercell boundary $\partial\mathcal{C}_{i,\text{in/out},j}$:

$$\Delta\text{up}^n_{i,\text{in/out},j} = \left(\alpha^n_i - \alpha^n_{i,\text{in/out},j}\right)\left|\partial\mathcal{C}_{i,\text{in/out},j}\right| \mathbf{D}^n_{i,j}\cdot\mathbf{n}_{i,j}\Delta t. \tag{3.53}$$

2. Using either the UDCS second-order approach or the UDCS anti-diffusive approach, compute the downwind factors at intercell boundaries $\lambda^n_{i,\text{in},j}$ and $\lambda^n_{i,\text{out},j}$. We note that for the UDCS anti-diffusive approach, a unique downwind factor $\lambda^n_{i,\text{out}}$ is computed for all outlet boundaries. $\lambda^n_{i,\text{in},j}$ is determined by the outlet downwind factor in cell $\mathcal{C}_{i,\text{in},j}$:

$$\lambda^n_{i,\text{in},j} = \lambda^n_{(i,\text{in},j),\text{out}}, \tag{3.54}$$

   where $\lambda^n_{(i,\text{in},j),\text{out}}$ is computed in the cell $\mathcal{C}_{i,\text{in},j}$.

3. Evaluate the new volume fraction state $\alpha^{n+1}_{k,i}$ by the UDCS approach (3.42) or (3.43).

4. Evaluate the new state for the other variables $(\alpha\mathbf{U})^{n+1}_{k,i}$ by

$$\begin{aligned}(\alpha\mathbf{U})^{n+1}_{k,i} = (\alpha\mathbf{U})^{n+1,\text{up}}_{k,i} &+ \sum_j (-\lambda^n_{i,\text{in},j})\frac{\Delta\text{up}^n_{i,\text{in},j}}{|\mathcal{C}_i|}\mathbf{U}^{n+1,\text{up}}_{k,i} \\ &+ \sum_j \lambda^n_{i,\text{out},j}\frac{\Delta\text{up}^n_{i,\text{out},j}}{|\mathcal{C}_i|}\mathbf{U}^{n+1,\text{up}}_{k,(i,\text{out},j)}.\end{aligned} \tag{3.55}$$

   where $\mathbf{U}^{n+1,\text{up}}_{k,(i,\text{out},j)}$ is the "upwinded" vector of variables for phase Σ_k in cell $\mathcal{C}_{i,\text{out},j}$.

As discussed in Section 3.3.2, the stability of the UDCS approach (3.55) combined with (3.43) is the same as the stability of the scheme calculating $\alpha^{n+1,\text{up}}_{k,i}$ and $\mathbf{U}^{n+1,\text{up}}_{k,i}$.

3.4 Concluding remarks

In this chapter, we have first studied in Section 3.1 the direct coupling of the DEM /RDEM method with an anti-diffusive approach in order to achieve accurate interface propagation. This coupling yields a very accurate flame profile for detonation fronts, but is unstable for deflagrations. Next, in Section 3.2, the instability of deflagration computations has been analyzed from a wave propagation viewpoint. A corrected version of the coupling between DEM/RDEM and the anti-diffusive method was then proposed. However, the complexity of this approach does not allow a straightforward extension to multi-dimensional problems on unstructured grids. Eventually in Section 3.3, we have presented the upwind downwind-controlled splitting (UDCS) approach which is the main contribution of the thesis. Applied either with a second-order or an anti-diffusive type downwind factor, the phase splitting idea within the UDCS does not reduce the scheme stability, which can be verified throughout the UDCS solution procedure for two-fluid system. In fact, its stability is similar to that of the upwind method (note that it can be the second-order upwinding approach, since the density, velocity and pressure can be reconstructed), because the "downwind-controlled splitting" step does not incorporate genuinely nonlinear wave propagations which are already considered in the previous "upwind" step. Finally, the UDCS idea has been extended to multi-dimensional case.

An extra benefit of the UDCS anti-diffusive approach lies in its computational efficiency, derived from its capability to accurately solve reactive interfaces. Indeed, when the interface is numerically dissipated, the DEM/RDEM approach computes (numerous) expensive reactive Riemann problems which are involved inside the interface diffusion zone. On the other hand, a less dissipated front requires, within the DEM/RDEM strategy, a considerably reduced number of reactive Riemann problems to be solved. This feature of UDCS is of crucial importance when performing multi-dimensional numerical investigations on refined grids.

In the following Chapter 4, one-dimensional numerical results obtained with the UDCS approach will be presented on a selection of non-reacting and reacting problems. Chapter 5 will be devoted to the presentation and analysis of two-dimensional numerical experiments with UDCS.

Chapter 4

One-dimensional test problems

The properties of the UDCS scheme developed in the previous chapter will be now assessed on a few selected one-dimensional test problems. The first non-reactive test problem will be the liquid-gas non-reactive interface initially introduced in Section 2.8. Let us recall this test problem is made difficult by the high pressure and density ratio existing between the two phases. The initial conditions give rise to a powerful expansion wave that often leads the numerical methods to produce states with negative pressures thus causing the failure of the calculation for many state-of-the-art methods. Additionally to this, the Mach number distributions computed in [Petitpas 07] display some undesirable numerical oscillations. The second reactive test-problem for the new UDCS strategy will be the Chapman-Jouguet fast deflagration configuration also introduced in Section 2.8. Let us recall this problem is of particular interest for nuclear safety related applications since the numerical computation of a smeared reactive shock wave can significantly affect the pressure wave description and hence lead to poor load estimates when performing fluid-structure interaction studies for instance. In fact, be it in fast deflagration regime or in detonation regime, the accurate computation of a reactive shock is critical when aiming at a reliable numerical tool for nuclear safety assessment.

What has been established up to now with these 1D non-reacting and reacting test cases is that both first-order and limited second-order DEM/RDEM approaches do not yield sufficiently accurate results on coarse grids (see Section 2.8 in Chapter 2) to be good candidates for numerical applications involving large geometries (up to the full reactor scale). It was also pointed out, in the first part of Chapter 3, that coupling DEM/RDEM with an anti-diffusive approach could potentially capture a contact discontinuity and a reactive shock with a much better accuracy than the previous methods but with a certain lack of robustness, which was not acceptable for practical applications.

The present chapter will demonstrate the very good accuracy and robustness properties which can be achieved with the newly proposed UDCS strategy implemented into the DEM/RDEM framework, be it in its second-order or anti-diffusive version. Section 4.1 will be devoted to the application of UDCS to the non-reactive interface problem and Section 4.2.1 and 4.2.2 will deal respectively with the Chapman-Jouguet fast deflagration front test and a Chapman-Jouguet detonation problem, for which the non-reactive precursor shock wave and the reactive shock wave collapse in space. Concluding remarks will be provided in Section 4.3.

4.1 Liquid-gas non-reactive interface

We reproduce the liquid-gas non-reactive interface problem studied in Section 2.8.1 with the residual phase volume fraction set equal to 10^{-8} for both the liquid and the gas. The initial conditions are those described in Section 2.8.1.

A two-step Runge-Kutta method is used for the time discretization; density, velocity and pressure are reconstructed using the minmod limiter in order to achieve (quasi) second-order accuracy in space. As far as the the phase volume fraction is concerned, two numerical strategies are investigated:

- *UDCS anti-diff* refers to the anti-diffusive version of UDCS which combines DEM, UDCS and the anti-diffusive approach as detailed in Chapter 3
- *UDCS 2nd-order* refers to the second-order version of UDCS which combines DEM and UDCS second-order method with minmod reconstruction.

The computed results are systematically compared to the available exact solution of the problem.

The results displayed in Fig. 4.1 for the individual phase variables and in Fig. 4.2 for the mixture variables are obtained on a uniform mesh of 100 cells. With a single point only in the material interface zone, the UDCS anti-diffusive approach demonstrates its capacity to almost exactly capture the interface, which makes it more accurate than the UDCS second-order DEM scheme. Numerical results obtained with the "standard" second-order DEM scheme using a minmod reconstruction (initially proposed in [Abgrall 03] and reviewed in Section 2.6) were already shown in Section 2.8 and are not reproduced here because they almost coincide with the results provided by the UDCS second-order version. Examining the Mach number distribution, it is observed that the supersonic part of the flow is well resolved by the UDCS anti-diffusive

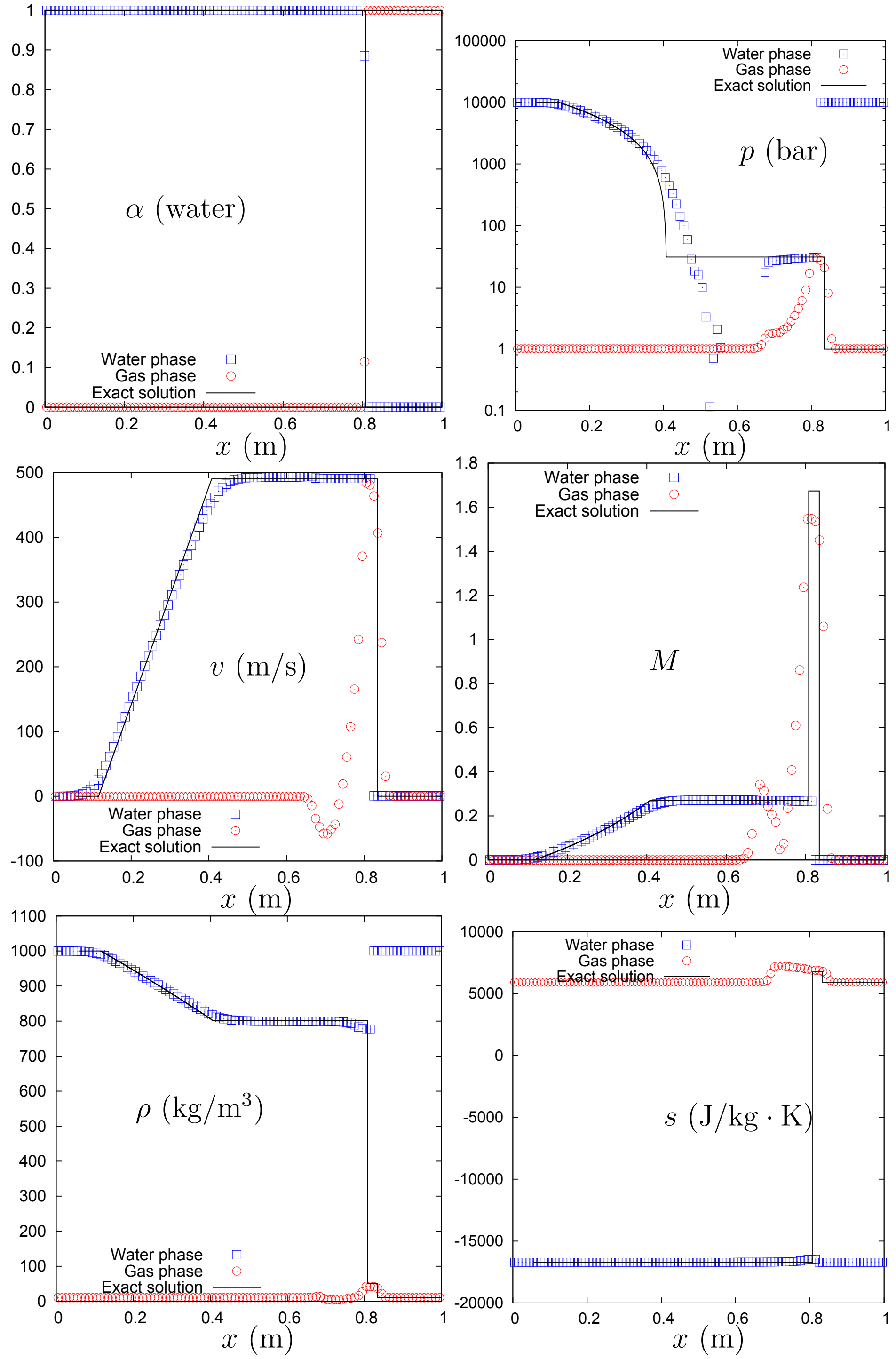

Figure 4.1: UDCS anti-diffusive DEM method (minmod for ρ, v and p) for water gas shock tube problem with impermeable interface. A 100 cells uniform mesh is used. CFL = 0.9. Time $t = 220$ μs. Residual phase volume fraction is set as 10^{-8}. Individual phase variables are plotted.

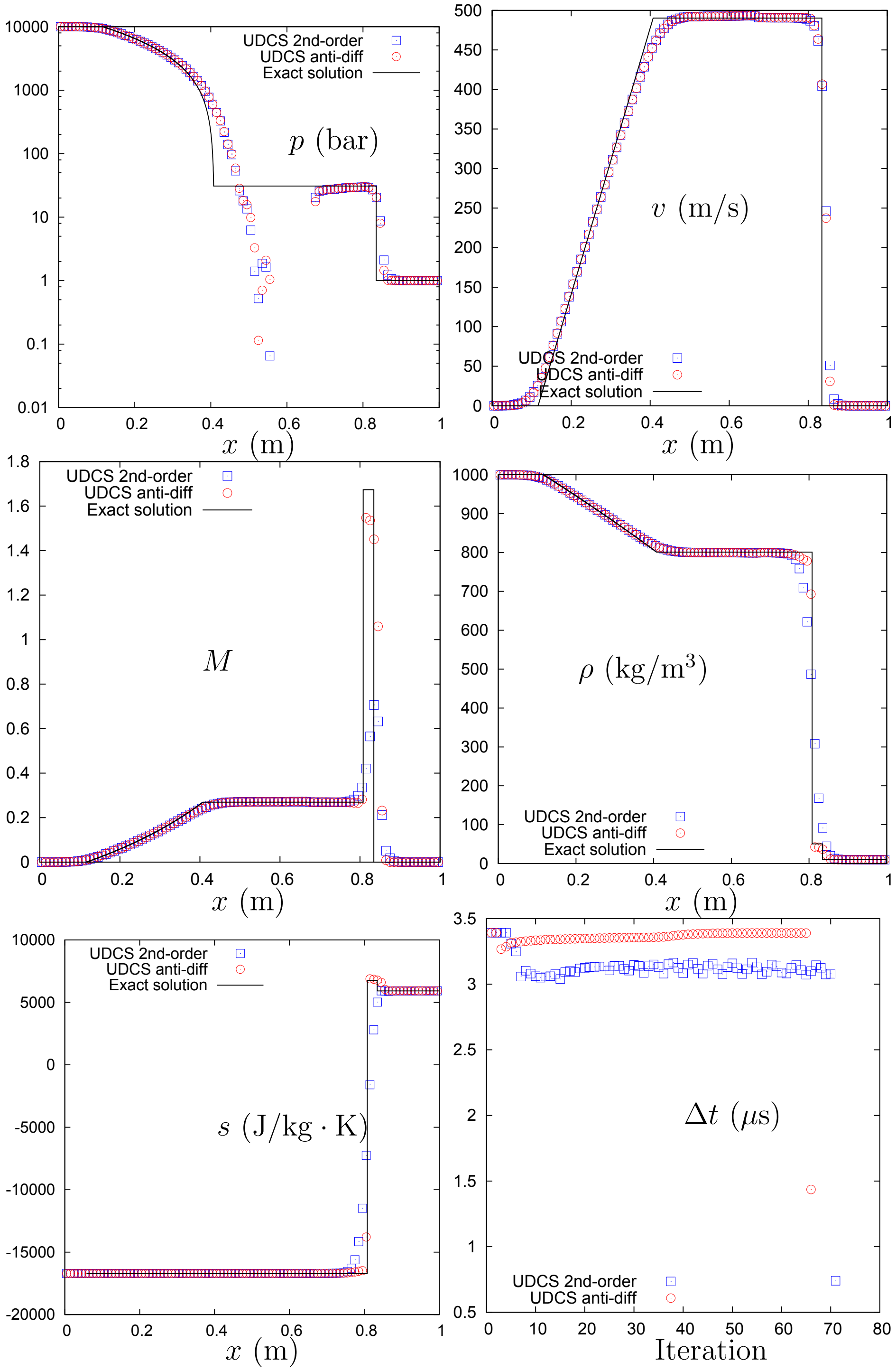

Figure 4.2: UDCS anti-diffusive DEM method (minmod for ρ, v and p) and UDCS second-order method are compared for water gas shock tube problem with impermeable interface. A 100 cells uniform mesh is used. CFL = 0.9. Time $t = 220\ \mu$s. Residual phase volume fraction is set as 10^{-8}. Phase mixture variables are plotted.

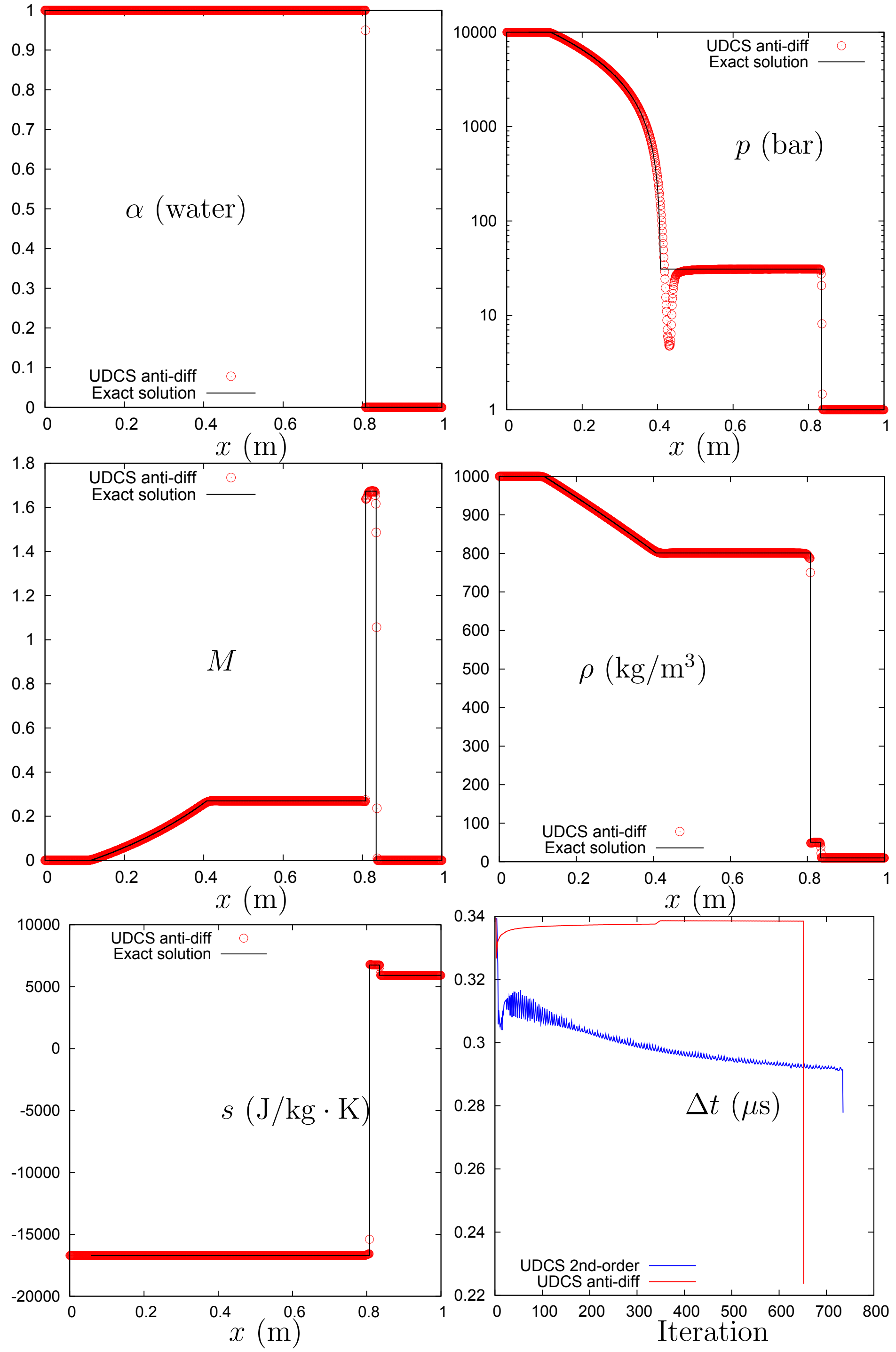

Figure 4.3: UDCS anti-diffusive DEM method (minmod for ρ, v and p) for water gas shock tube problem with impermeable interface. A 1000 cells uniform mesh is used. CFL = 0.9. Time $t = 220$ μs. Residual phase volume fraction is set as 10^{-8}. Phase mixture variables are plotted.

method while the results obtained using the second-order DEM scheme display a spurious subsonic flow region. If using a uniform mesh with 1000 cells (Fig. 4.3) perfect agreement is obtained between the numerical and exact solutions. The numerical results obtained at the interface using the UDCS anti-diffusive method are more accurate than those presented in [Petitpas 07] and obtained with a relaxation-projection method. All the computed variables are oscillation free, including the Mach number. The phenomenon of negative pressure occurrence in Fig. 4.2 is significantly improved when refining the grid, as observed in Fig. 4.3.

When comparing the results obtained in Section 3.2.4 with the corrected anti-diffusive reconstruction approach proposed in Section 3.2.3 and the present UDCS anti-diffusive results, it can be observed that no velocity overshoots are observed with the UCDS anti-diffusive approach and that the time steps remain almost constant. Furthermore, it is also interesting to notice that the less diffused interface front leads to a reduced number of time steps for the UDCS anti-diffusive approach, compared to the second-order approach. In fact, the numerical diffusion in the second-order scheme yields more two-phase Riemann problem solutions and thus the associated time stepping conditions become more restrictive. The greater accuracy of the UDCS anti-diffusive approach is consequently also beneficial as far as computational efficiency is concerned.

When more accurate limiters (such as “superbee”) are employed for the volume fraction reconstruction, the standard second-order DEM approach introduces numerical oscillations in the vicinity of the material interface, while no numerical oscillation is observed for the UDCS second-order approach. This is a direct benefit of the phase splitting involved in the UDCS approach as *a priori* explained in Section 3.3 and experimentally observed in the present numerical tests.

4.2 Chapman-Jouguet deflagration and detonation front

4.2.1 Fast deflagration case

The UDCS method is now applied to the computation of the Chapman-Jouguet deflagration front test already studied in Section 2.8.2. The predictor-corrector time-stepping scheme is still used for the time discretization; density, velocity and pressure also remain reconstructed using the minmod limiter. As far as the the numerical treatment of the phase volume fraction is concerned, the denominations *UDCS anti-diff* and *UDCS 2nd-order* introduced in the non-reactive case retain the same meaning. A uniform mesh of 100 cells is used and the CFL number is set equal to 0.9. Note this choice of CFL is improved over the standard second-order approach used in Section 2.8.2 which allows a maximum CFL number equal to about 0.75.

Fig. 4.4 displays the numerical results for the individual phase variables obtained with the UDCS anti-diffusive RDEM method, compared to the exact solution of the reactive Riemann problem for the Euler equations. With the RDEM method, the interaction between the burnt and unburnt gas mixture is only driven by the non-conservative term including mass transfer phenomenon in the two-fluid model on the interface. For this reason, each phase has very different wave profiles in general, but the interface conditions are fulfilled in the computed interface zone. The burnt gas mixture on the left of the reactive shock is in good agreement with the exact solution in terms of Taylor expansion wave, contact discontinuity and left traveling shock. The unburnt gas mixture on the right of the reactive shock displays a better capture of the precursor shock wave than the standard second-order RDEM approach shown in Fig. 2.21, thanks to the much higher resolution of the reactive shock wave.

Fig. 4.5 displays the computed mixture variables and compares the UDCS anti-diffusive approach with the UDCS second-order method. It can be observed the UDCS anti-diffusive method yields a much better resolution of the reactive interface. As in the non-reacting liquid-gas shock tube problem, the numerical results obtained by the standard second-order DEM method are not shown since they almost coincide with the ones obtained using the UDCS second-order approach. It can also be checked that the UDCS anti-diffusive approach can almost exactly capture the flame interface, which substantially improves the results on the maximum over-pressure following the non-reactive shock wave. This makes the UDCS anti-diffusive approach especially attractive to perform, for instance, investigations of fluid-structure interaction problems involving combustion-generated pressure waves.

4.2.2 Detonation case

The UDCS scheme is also applied to the computation of a Chapman-Jouguet detonation front test. Apart from the fundamental flame speed K_0, the flow initial conditions are the same as the Chapman-Jouguet deflagration front test. Indeed, in the case of a Chapman-Jouguet detonation, the fundamental flame speed corresponds to the one which makes the reactive shock speed identical to the one of the precursor shock ([Beccantini 10a]). Thus, it is not necessary to specify K_0. In other words, the Chapman-Jouguet detonation can be considered as a a Chapman-Jouguet deflagration in which the precursor shock and the reactive shock travel at the same speed. See also [Ciccarelli 08], pages 503 - 507.

In this detonation model we have assumed an infinitely fast chemical reaction with zero induction time. As for the deflagration test case, a uniform mesh of 100 cells is used and the CFL is taken equal to 0.9. The predictor-corrector time-stepping scheme is used for time discretization, while density, velocity and pressure are reconstructed using the minmod limiter.

The exact Riemann problem solution for the reactive Euler equations closed by the thermally perfect gas EOS can be evaluated for this case by following [Beccantini 10a]. Taking into consideration the initial conditions, we obtain this exact solution as the Chapman-Jouguet detonation shown in Fig. 4.6 for selected variables. The detonation front velocity is found to be equal to 2088.73 m/s. At time 3.2 ms, the reactive shock, moving from its initial location at $x = 10$ m, reaches $x = 16.68394$ m. The right-traveling precursor shock and the detonation front collapse while, behind the reactive interface, the flow velocity is sonic in the reactive shock frame, and the burnt gas Taylor expansion wave develops. In addition, the left wave structure also incorporates the left-traveling contact discontinuity and the shock wave of burnt gas.

Computed results are shown in Fig. 4.7 for the individual phase variables using UDCS anti-diffusive approach and in Fig. 4.8 for the mixture variables comparing UDCS anti-diffusive and UDCS second-order approaches to each other as well as to the exact solution. We observe that the scheme performance is as good as for the deflagration case. In this case again, each phase displays very different wave profiles in general, but with interface conditions which are automatically fulfilled in the interface zone thanks to the calculation of non-conservative term including mass transfer phenomenon. The burnt gas mixture on the left of the reactive shock is in good agreement with the exact solution. Here again also the UDCS anti-diffusive approach can almost exactly capture the detonation front which incorporates the nonlinear shock wave. Thus, the Chapman-Jouguet state for the detonation can be quasi-exactly captured. As a consequence, the UDCS anti-diffusive approach yields a much higher resolution of the detonation front than the UDCS second-order method. Note also that the numerical results obtained with the standard second-order RDEM method are not shown since they almost coincide with the ones obtained using the UDCS second-order approach.

4.3 Concluding remarks

One-dimensional test cases including non-reactive and reactive interfaces have been computed with the newly proposed UDCS scheme. The UDCS second-order DEM /RDEM approach provides a solution accuracy which is similar to that of the standard second-order DEM/RDEM method but can be used with larger values of the CFL number thanks to its increased robustness. The UDCS anti-diffusive approach clearly appears as the best method developed so far in this work since it both significantly improves the robustness and the accuracy of the original DEM approach. In fact, the coupling between the newly proposed UDCS anti-diffusive method and DEM/RDEM has the capability of almost exactly capturing both non-reactive and reactive interfaces in a very robust way. To the best of our knowledge, the UDCS anti-diffusive method is the first approach displaying the capability of quasi-exactly capturing, in both deflagration and detonation regimes, the reactive shock wave that incorporates the mass transfer phenomenon on the interface where significant pressure and velocity jump can also be present. It is emphasized that these very nice properties of the UDCS anti-diffusive approach are closely related to the separate phase averaging in the numerical mixture within the framework of DEM/RDEM method. In other words, the accuracy and robustness properties achieved with the UDCS anti-diffusive approach within the DEM/RDEM framework are the outcome of the full combination between the DEM/RDEM framework, the anti-diffusive strategy and the UDCS technique. The last step to perform in this work is to assess the properties of this same combination when applied to multidimensional problems on unstructured grids: this is the topic of the next and last Chapter of the thesis.

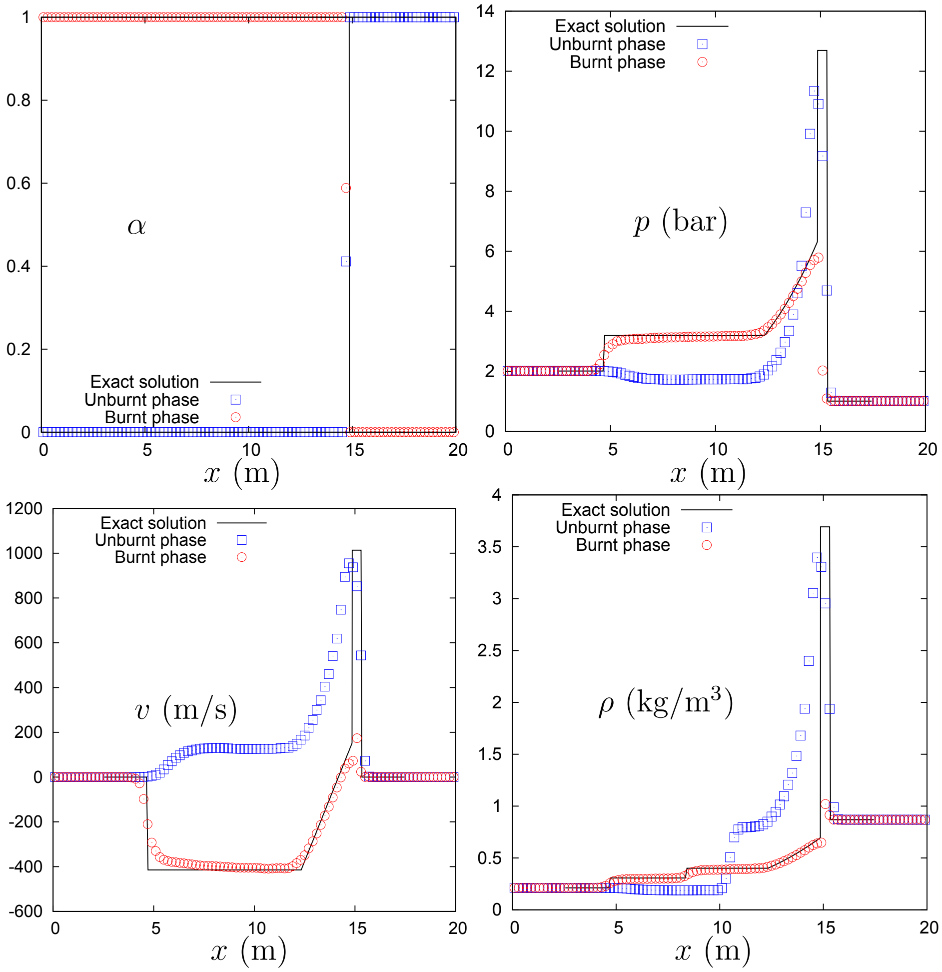

Figure 4.4: UDCS anti-diffusive RDEM method (minmod for ρ, v, p) is used for shock tube of Chapman-Jouguet deflagration front. A 100 cells uniform mesh is used. CFL = 0.9. Time $t = 4.0$ ms. Individual phase variables are plotted.

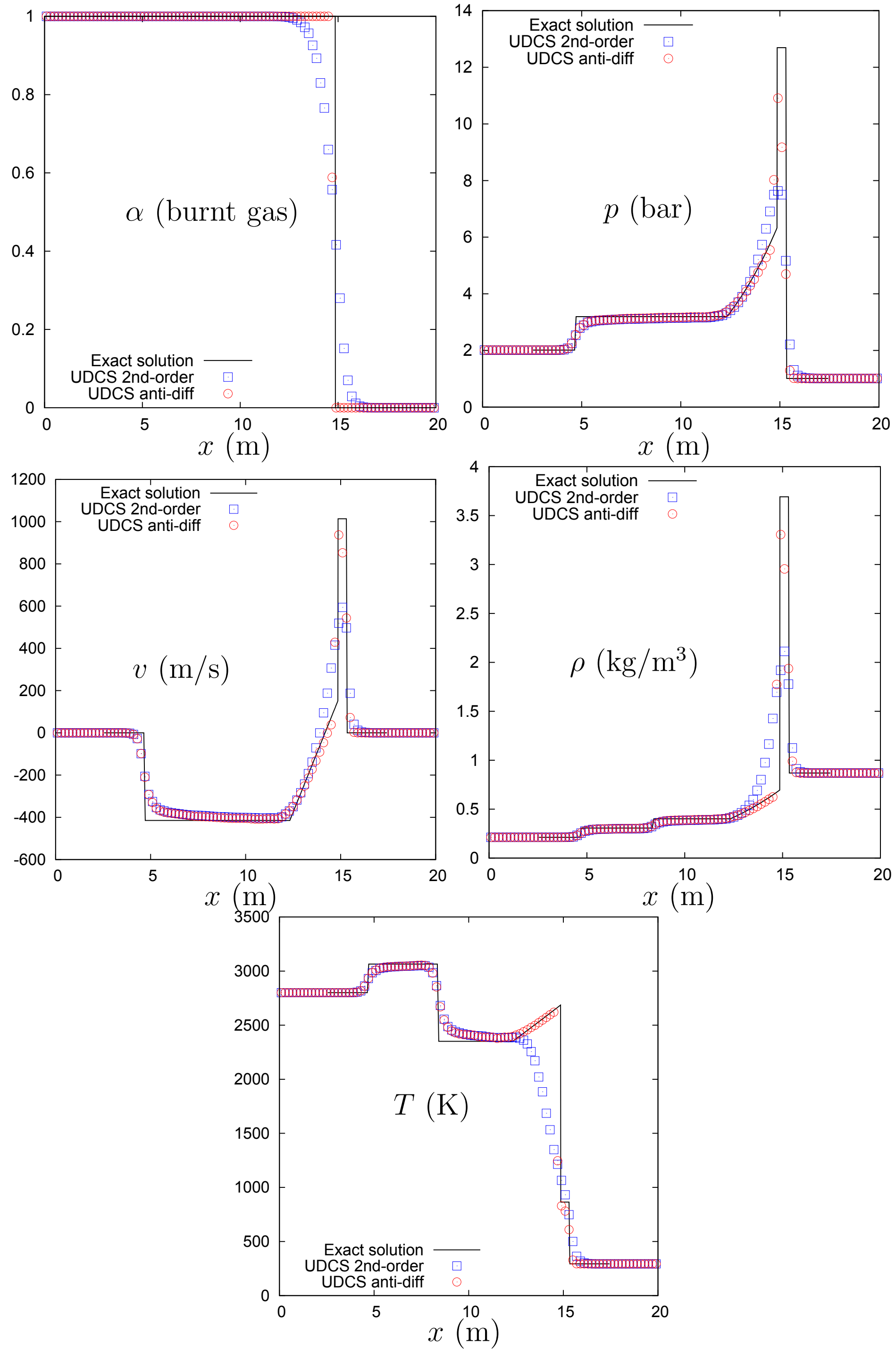

Figure 4.5: UDCS anti-diffusive RDEM method (minmod for ρ, v, p) and UDCS second-order RDEM method are compared for shock tube of Chapman-Jouguet deflagration front. A 100 cells uniform mesh is used. CFL = 0.9. Time t = 4.0 ms. Mixture phase variables are plotted.

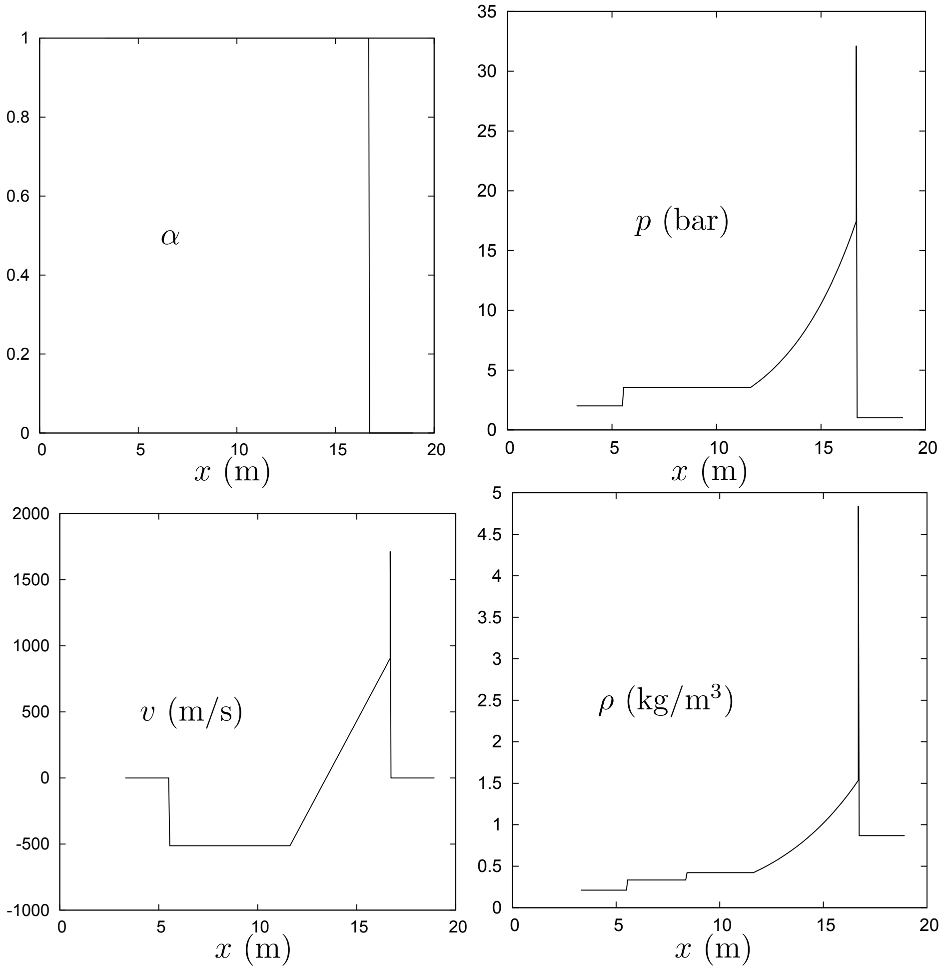

Figure 4.6: The exact solution of the reactive Euler equations for shock tube of Chapman-Jouguet detonation front at time $t = 3.2$ ms.

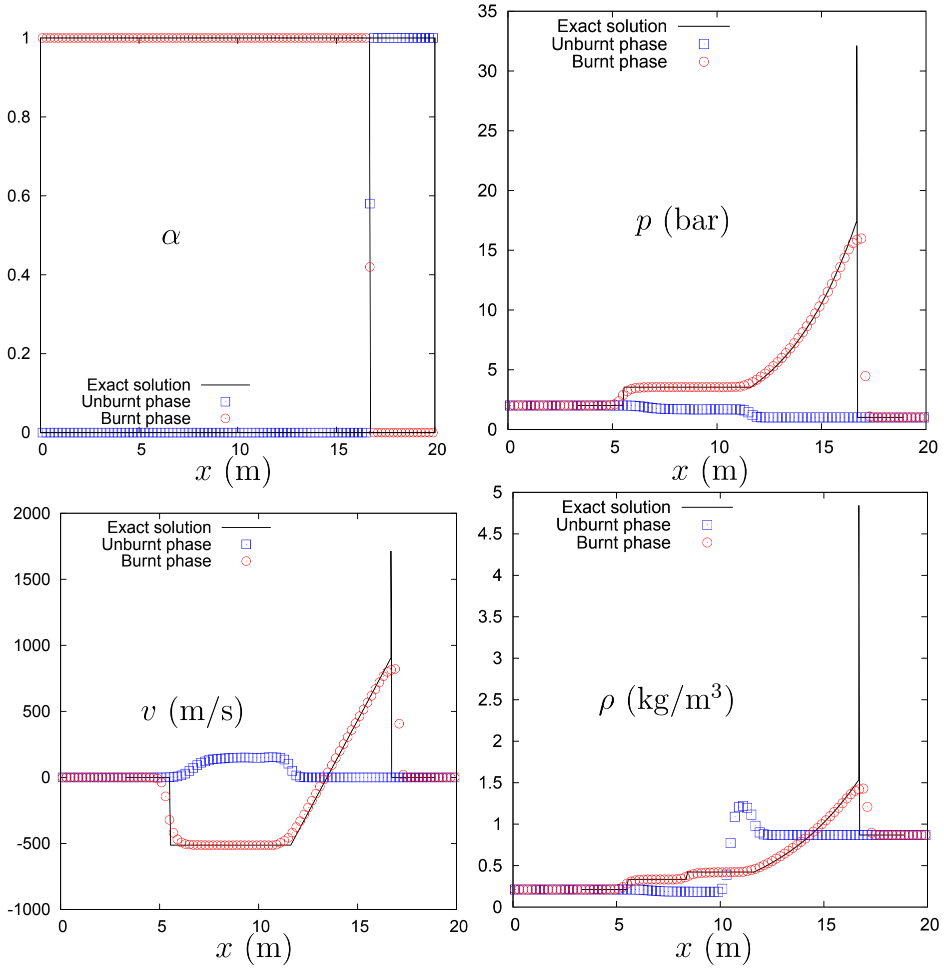

Figure 4.7: UDCS anti-diffusive RDEM method (minmod for ρ, v, p) is used for shock tube of Chapman-Jouguet detonation front. A 100 cells uniform mesh is used. CFL $= 0.9$. Time $t = 3.2$ ms. Individual phase variables are plotted.

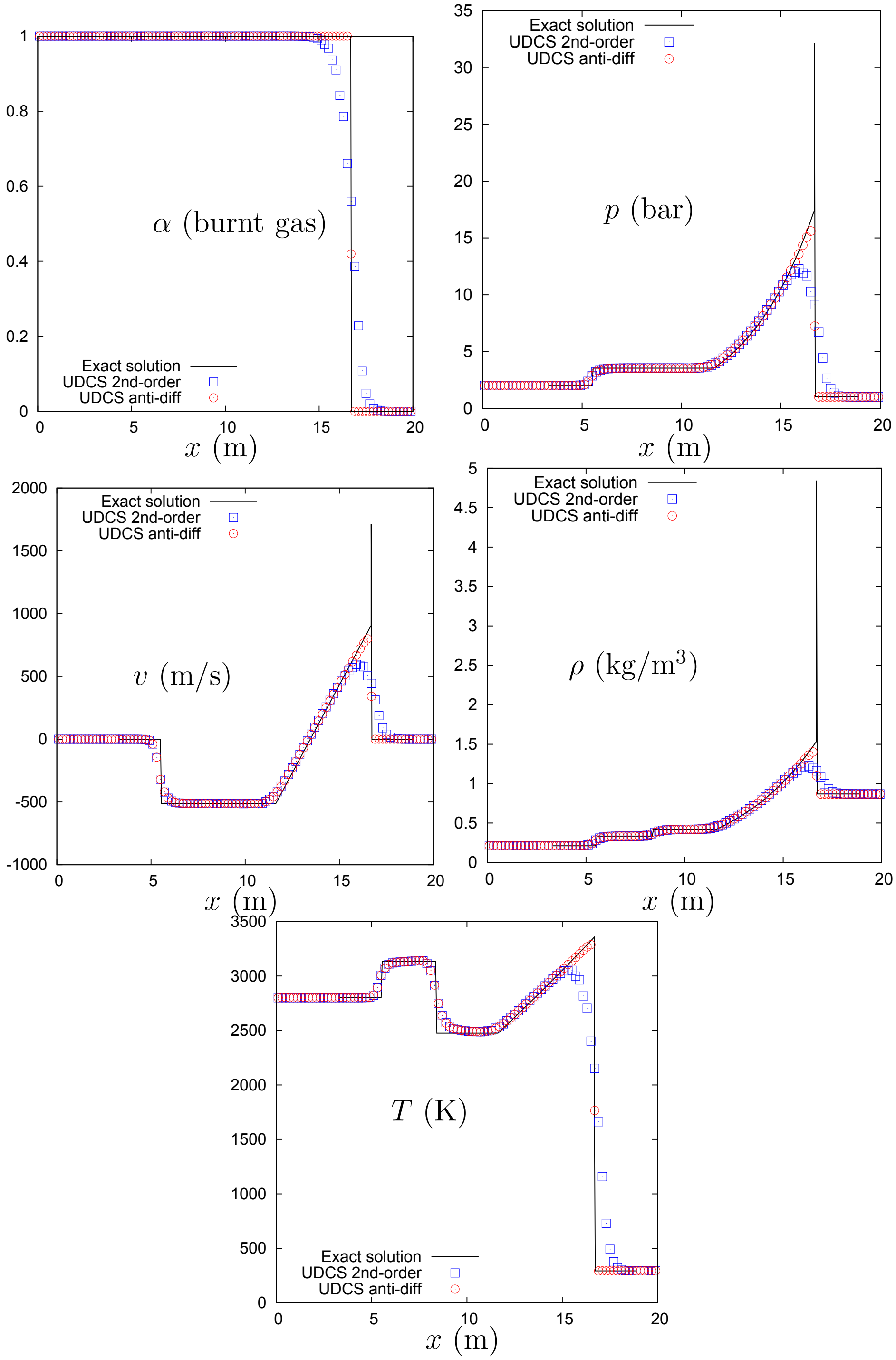

Figure 4.8: UDCS anti-diffusive RDEM method (minmod for ρ, v, p) and UDCS second-order RDEM method are compared for shock tube of Chapman-Jouguet detonation front. A 100 cells uniform mesh is used. CFL = 0.9. Time t = 3.2 ms. Mixture phase variables are plotted.

Chapter 5

Two-dimensional test problems

This final chapter is devoted to the application of the UDCS DEM/RDEM scheme to two-dimensional non-reactive and reactive interface problems computed on unstructured grids. The study is restricted to academic problems: no complex geometries, such as a full reactor containment, are involved. Still, unstructured grids (made of quadrangular or triangular elements) will be systematically used in order to assess the general implementation of the UDCS DEM/RDEM approach. Moreover, the computed test cases have been selected so that they display physical features and numerical difficulties representative of those encountered for real-life applications.

The first non-reacting test case is the interaction between a shock moving through air and a bubble of heavy gas initially at rest in the surrounding air. This classical test problem for multiphase solvers has been previously computed for instance in [Quirk 96, Shyue 06, Nourgaliev 06, Banks 07, Chertock 08, Kokh 10, Kreeft 10]. The computed solutions obtained using UDCS and DEM will be compared to available experimental data and comments will also be provided with respect to some of these previous numerical results of the literature.

The second non-reacting test problem is, again, the interaction between a shock and a bubble but this time the bubble is made of a light gas and immersed in a liquid medium. This problem has been analyzed in [Kokh 10] using an anti-diffusive strategy applied to a reduced two-fluid model with a single pressure and a single velocity. Note that, similarly as the one-dimensional liquid-gas interface computed in Chapter 4, this two-phase shock bubble problem is made especially difficult by the very high ratio of both pressure and density between the liquid and gaseous phases. In addition, the multidimensional expansion wave appearing in the liquid phase may often produce negative pressures which are likely to cause in turn serious numerical difficulties. Note that only Cartesian grid calculations will be performed with UDCS for this demanding test case; the ability of the approach to be applied on general unstructured grids will be considered as established from the previous test case.

Finally, a one-dimensional line-symmetric steady deflagration test problem will be computed as a reacting demonstration test problem, using UDCS and RDEM on a two-dimensional Cartesian grid. The numerical results obtained will be compared with an available one-dimensional reference solution. Note that, physically speaking, this reference solution for the multi-dimensional reactive Euler equations is in fact unstable, since the stability of a cylindrical/spherical flame is guaranteed by the competition between thermal and species diffusion effects which are neglected in the reactive Euler equations. This inviscid solution can be used anyway for the sake of an analytical/numerical comparison.

The chapter is organized as follows: Section 5.1 is devoted to the gaseous non-reacting shock bubble interaction problem and Section 5.2 to the liquid-gas non-reacting problem. Section 5.3 deals with the cylindrical combustion propagation case. Concluding remarks are provided in Section 5.4.

5.1 Gaseous non-reacting shock bubble interaction

As previously mentioned, this shock bubble test case is well documented, both from a numerical viewpoint (previous computational investigations performed in [Quirk 96, Shyue 06, Kokh 10]) and an experimental (qualitative) viewpoint (visualizations provided by [Haas 87]).

The flow problem consists in simulating the impact of a Mach 1.22 shock traveling through air (light gas) onto a cylinder of R22 gas (heavy gas). The configuration is described in Fig. 5.1. The cylinder of R22 gas is surrounded by air within a 445 mm × 89 mm rectangular computational domain. At $t = 0$, the cylinder is at rest and its center is located at $(x, y) = (225 \text{ mm}, 44.5 \text{ mm})$. The initial radius of the cylinder (or gas bubble) is $r = 25$ mm. The planar shock is initially located at $x = 275$ mm and moves from right to left towards the cylinder. The interaction between the material interface and the shock wave, coming from the light gas region into the heavy gas region, generates a system of waves which includes, at the early stage of the interaction, a transmitted shock wave in air, a refracted shock wave in the R22 bubble, a material interface and a reflected shock wave in air. Due to the smaller speed of sound in the R22 gas, the refracted shock wave in R22 propagates more slowly than the transmitted shock wave in air.

Both fluids (air and R22) are described by a polytropic EOS. The initial conditions

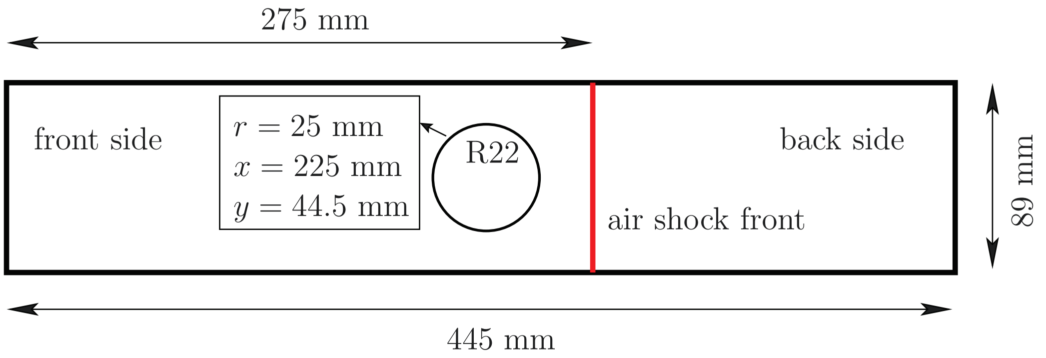

Figure 5.1: Initial configuration of air-R22 shock problem.

and the fluid properties are summarized in Table 5.1. The top and bottom boundary conditions are set as solid walls while constant state boundary conditions are imposed on the left and right boundaries which are not reached by the propagating waves at the final time of the simulation.

In Fig. 5.2, experimental Schlieren images taken from [Haas 87] are displayed on the first column and compared with the numerical solutions provided by 2 different numerical strategies, relying on DEM and UDCS for the volume fraction equation but with a second-order approach (minmod reconstruction) or anti-diffusive approach, each of these strategies being applied on a quadrangular or triangular grid. The presentation of the results in Fig. 5.2 is organized as follows:

- column 2: UDCS with minmod reconstruction (quasi second order), on a 1000×200 Cartesian mesh.
- column 3: UDCS with minmod reconstruction, on a $1000 \times 200 \times 2$ triangular mesh.
- column 4: UDCS and anti-diffusive approach, on a 1000×200 Cartesian mesh.

Location	ρ (kg m^{-3})	p (Pa)	u_x (m s^{-1})	u_y (m s^{-1})	γ
Air (back side)	1.686	1.59×10^5	-113.5	0	1.4
Air (front side)	1.225	1.01325×10^5	0	0	1.4
R22	3.863	1.01325×10^5	0	0	1.249

Table 5.1: Air-R22 shock cylinder interaction test. EOS coefficients and initial data.

- column 5: UDCS and anti-diffusive approach, on a $1000 \times 200 \times 2$ triangular mesh.

In all cases, the Euler explicit scheme is used for time discretization, with a CFL value set to 0.4. No reconstruction on the primitive variables is performed. As done in [Haas 87], the results are shown around the R22 gas bubble at several time instants (measured relative to the moment when the shock wave first interacts with the bubble boundary at time $t = 60$ μs). For the sake of conciseness, only a selection of the experimental snapshots has been retained but the reference used to design each instant is kept consistent with the one used in the experimental work [Haas 87], namely: (b) $t = 115$ μs, (d) $t = 187$ μs, (g) $t = 342$ μs, (h) $t = 417$ μs, (i) $t = 1020$ μs. A first qualitative analysis of the UDCS/DEM numerical results, on both triangular and

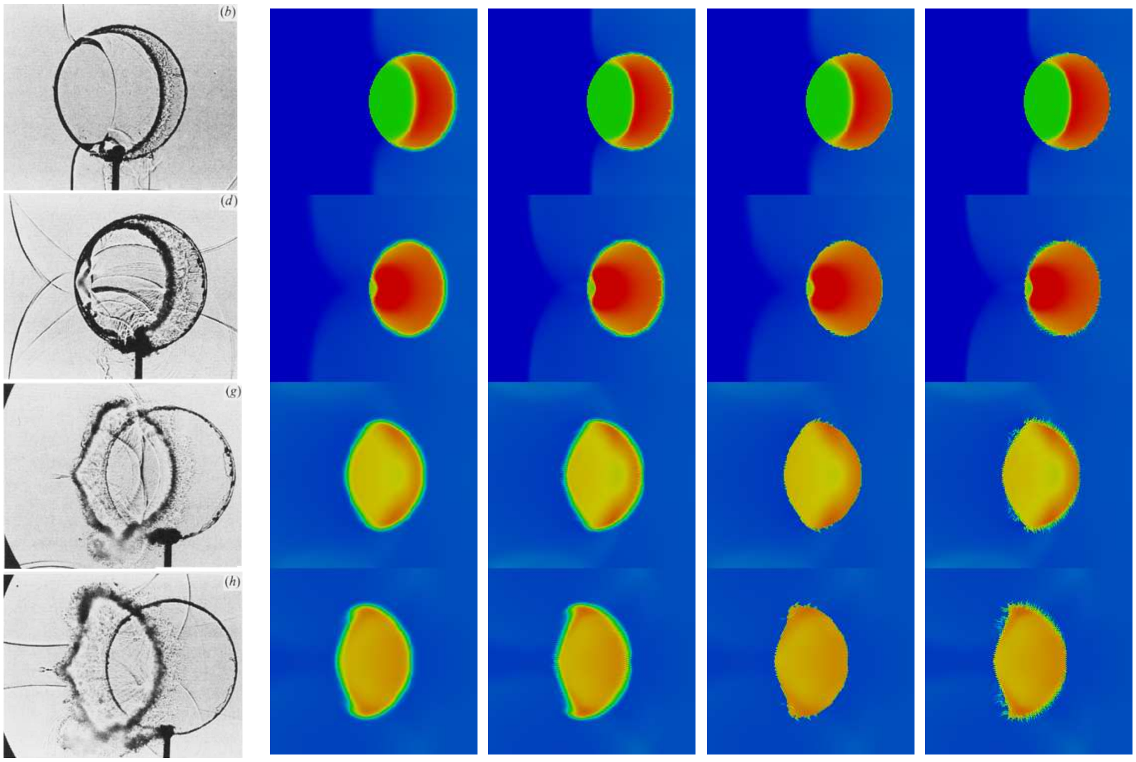

Figure 5.2: Air-R22 shock cylinder interaction test. Numerical results of density profile. From left to right: experimental results in [Haas 87], UDCS minmod method with 1000×200 Cartesian mesh, UDCS minmod method with triangular mesh of $1000 \times 200 \times 2$ cells, UDCS anti-diffusive method with 1000×200 Cartesian mesh, and UDCS anti-diffusive method with triangular mesh of $1000 \times 200 \times 2$ cells. Five instants are selected from [Haas 87]: (b) $t = 115$ μs, (d) $t = 187$ μs, (g) $t = 342$ μs, (h) $t = 417$ μs, (i) $t = 1020$ μs.

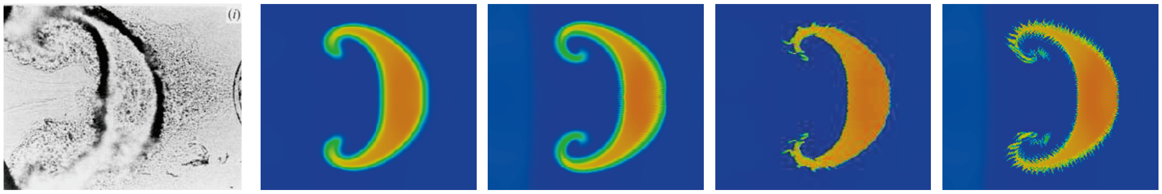

Figure 5.2: (*continued*)

quadrangular meshes, allows to conclude the computed solutions are globally in good agreement with the experimental data in [Haas 87] (and also with previous numerical results such as [Quirk 96, Shyue 06, Kokh 10]). Moreover, it can be observed on the density contours that the interface resolution is significantly improved when the UDCS anti-diffusive method is employed, be it on the quadrangular or triangular grid. It is in particular interesting to notice that the UDCS anti-diffusive method works well on the unstructured triangular mesh: the interface instabilities (of Richtmyer-Meshkov and Kelvin-Helmholtz type, see [Nourgaliev 06]) is clearly observed in Fig. 5.2 *(i)*. The UDCS anti-diffusive approach is proved capable of resolving vortex structure and interface instability on a relatively coarse mesh while a (much) higher grid resolution would be required for many state-of-the-art methods (see for instance [Nourgaliev 06] or even the more smeared interface computed using UDCS in its second-order version instead of the anti-diffusive version).

The different numerical approaches are more quantitatively compared by analyzing the volume fraction and the mixture density at the final computational time. The results in Fig. 5.3 are plotted along the axis of symmetry ($+x$ direction), in the region occupied by the bubble. Three increasingly refined Cartesian meshes (250×50, 500×100, 1000×200) and three increasingly refined triangular meshes are used for accuracy comparison. Each triangular mesh is built from one of the Cartesian mesh by dividing each cell in two triangles so that the triangular grid is twice finer than the corresponding Cartesian mesh. On each grid, the UDCS second-order approach and UDCS anti-diffusive approach have been applied. The first line of Fig. 5.3 demonstrates the achievement of grid-convergence for the computations (using the UDCS anti-diffusive approach). The results displayed on the second line show that, on quadrangular grids, the UDCS anti-diffusive approach with 500×100 Cartesian mesh produces (much) more accurate results than the UDCS minmod approach with 1000×200 cells. A similar trend is observed with the triangular grids, when analyzing the results displayed on the third line: the UDCS anti-diffusive approach yields again more accurate results than the UDCS minmod approach.

Further plots (Fig. 5.5 and Fig. 5.6) are drawn along the two lines perpendicular to the axis of symmetry (y direction) whose location over the final time bubble shape is indicated in Fig. 5.4. The grid-convergence of the results can be qualitatively observed and the UDCS anti-diffusive approach still proves to be more accurate than the UDCS minmod approach. In line with the triangular mesh results shown in Fig. 5.2 for the UDCS anti-diffusive approach, the interface instability is visible in the third column of Fig. 5.5 and Fig. 5.6.

Finally, the pressure time-history is displayed in Fig. 5.7 for the sake of comparison with [Quirk 96, Shyue 06, Kokh 10, Haas 87]. Three locations are retained: $x_p = 3,\ 27,\ 67$ mm, downstream of the R22 gas bubble along the axis of symmetry. Time is measured from the first communication of the shock wave with the bubble at time $t = 60\ \mu s$. The UDCS anti-diffusive results on triangular grids made of $250 \times 50 \times 2$, $500 \times 100 \times 2$, and $1000 \times 200 \times 2$ elements are presented so that grid convergence can be qualitatively checked. Note that as far this pressure time-history along the symmetry axis is concerned, no noticeable difference is observed when comparing the results obtained with the UDCS minmod method and the UDCS anti-diffusive method on the same mesh. Note also that the pressure peaks are not as accurately resolved as in [Kokh 10], where a more refined (5000×1000) Cartesian grid was used. Moreover, it is worthwhile to mention that, with the same CFL value, a larger number of time steps is required for computing the flow evolution with a ful non-equilibrium two-fluid flow model than with a sub-model, such as the one used in [Kokh 10] (more information can be found in [Zein 10]). This can generally make the results of the full two-fluid model more diffused than the ones obtained with a sub-model. However, it is emphasized that the full two-fluid model must be assessed in this work since it will be necessarily used in order to compute reactive fronts on which the pressure and velocity jumps can be significant.

5.2 Liquid-gas non-reacting shock bubble interaction

In this section, the two-dimensional shock bubble interaction test involves now a lighter gas bubble surrounded by (heavier) liquid water. The geometry of the initial configuration is described in Fig. 5.8. Both fluids are thermodynamically described by the stiffened gas EOS ($P_\infty = 0$ for the gas). The EOS parameters and the initial fluids states are given in Table 5.2. Solid wall boundary conditions are applied for the top and bottom boundaries while constant states are imposed at the left and right boundaries. The computational domain is discretized using a 300×100 Cartesian grid. The first-order Euler method is used for time discretization.

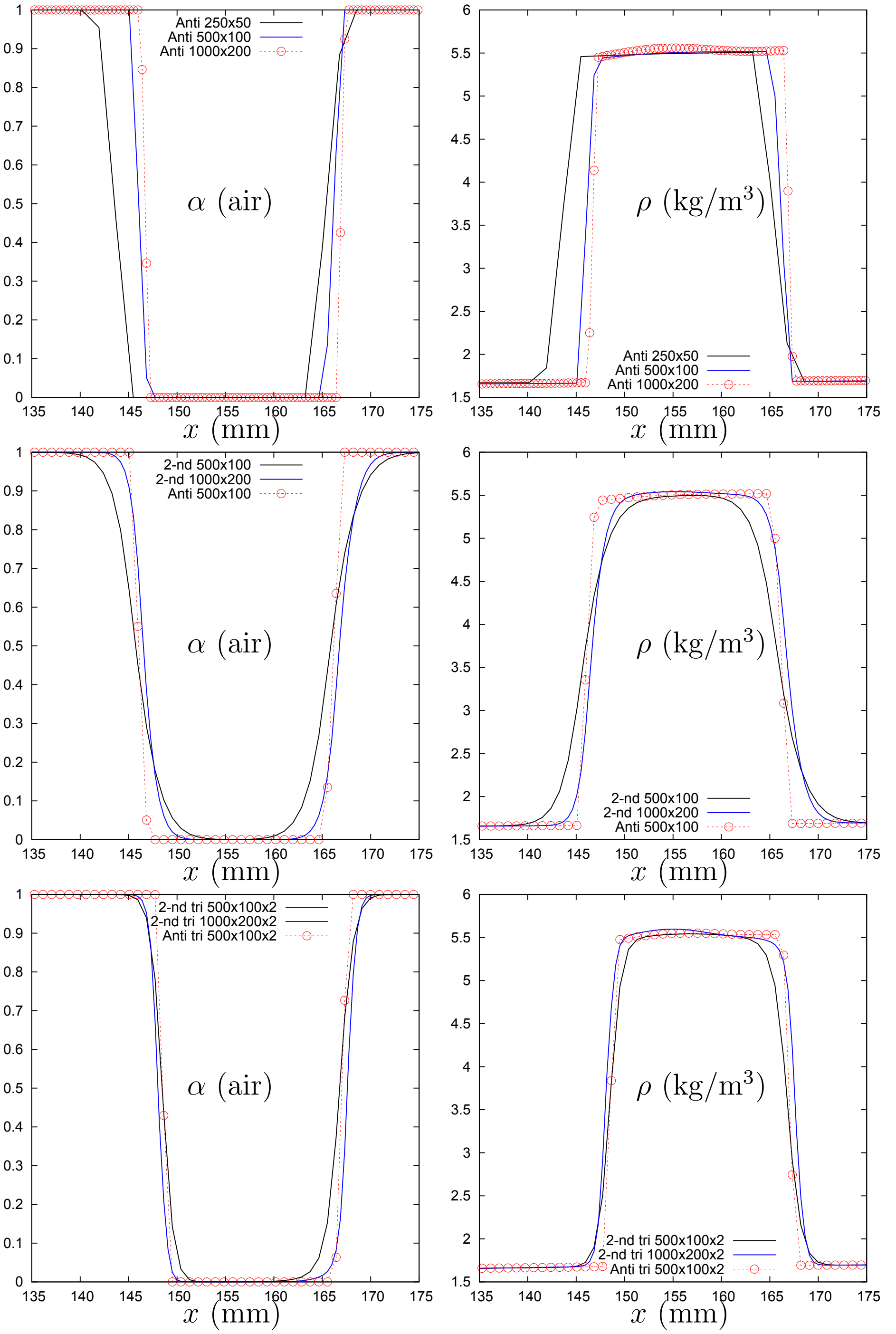

Figure 5.3: Air-R22 shock cylinder interaction test. Plots of volume fraction and mixture density over the axis of symmetry (x direction) around the R22 bubble. Anti stands for UDCS anti-diffusive approach. 2-nd stands for UDCS minmod approach (which is quasi second order). tri stands for triangular mesh.

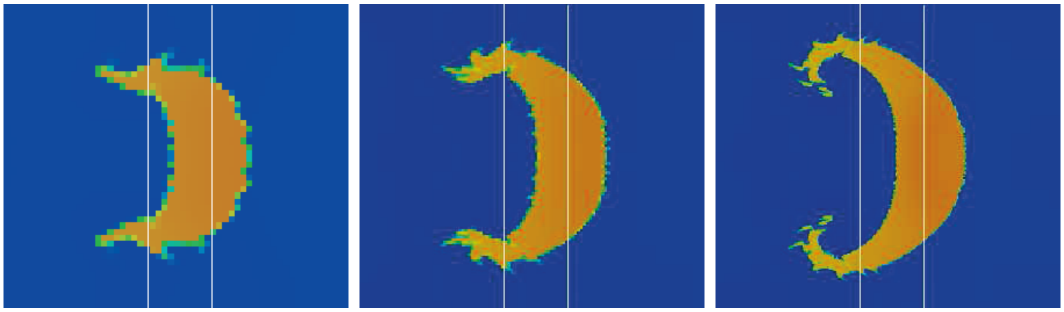

Figure 5.4: Air-R22 shock cylinder interaction test. Positions of y direction lines for plots of volume fraction and mixture density in Fig. 5.5 and Fig. 5.6. From left to right: UDCS anti-diffusive approach with Cartesian mesh of 250×50, 500×100, and 1000×200 cells. Left line is located at $x = 136$ mm, and right line at $x = 155$ mm (measured from the left boundary of the whole domain).

Fig. 5.9 and Fig. 5.10 display the computed solutions (volume fraction and mixture density contours) using UDCS and DEM at four time instants. The gas bubble is transformed into two symmetrical vortices at the end of the computational period, as also observed in [Saurel 99b, Kokh 10]. Compared to the second-order scheme, the UDCS anti-diffusive approach yields a much sharper interface profile. This can be further (quantitatively) verified by visualizing volume fraction and mixture density distributions along the axis of symmetry; such distributions are plotted in Fig. 5.11 at time $t = 375$ μs and in Fig. 5.12 at $t = 450$ μs. This latter time instant corresponds to the time at which the numerically diffused interface computed with the UDCS second-order approach interacts with the front side of the bubble. The sharper interface computed with the UDCS anti-diffusive approach is well demonstrated. At $t = 450$ μs, the anti-diffusive and second-order approaches start to yield significant difference for the pressure and density distributions along the symmetry axis; in particular, the UDCS anti-diffusive method predicts a higher pressure in the bubble zone while the UDCS second-order method tends to underestimate this pressure level.

Location	ρ (kg m^{-3})	p (Pa)	u_x (m s^{-1})	u_y (m s^{-1})	γ	P_∞ (Pa)
Water (back side)	1030.9	3×10^9	300.0	0	4.4	6.8×10^8
Water (front side)	1000.0	10^5	0	0	4.4	6.8×10^8
Air	1.0	10^5	0	0	1.4	0

Table 5.2: liquid-gas shock bubble interaction test. EOS coefficients and initial data.

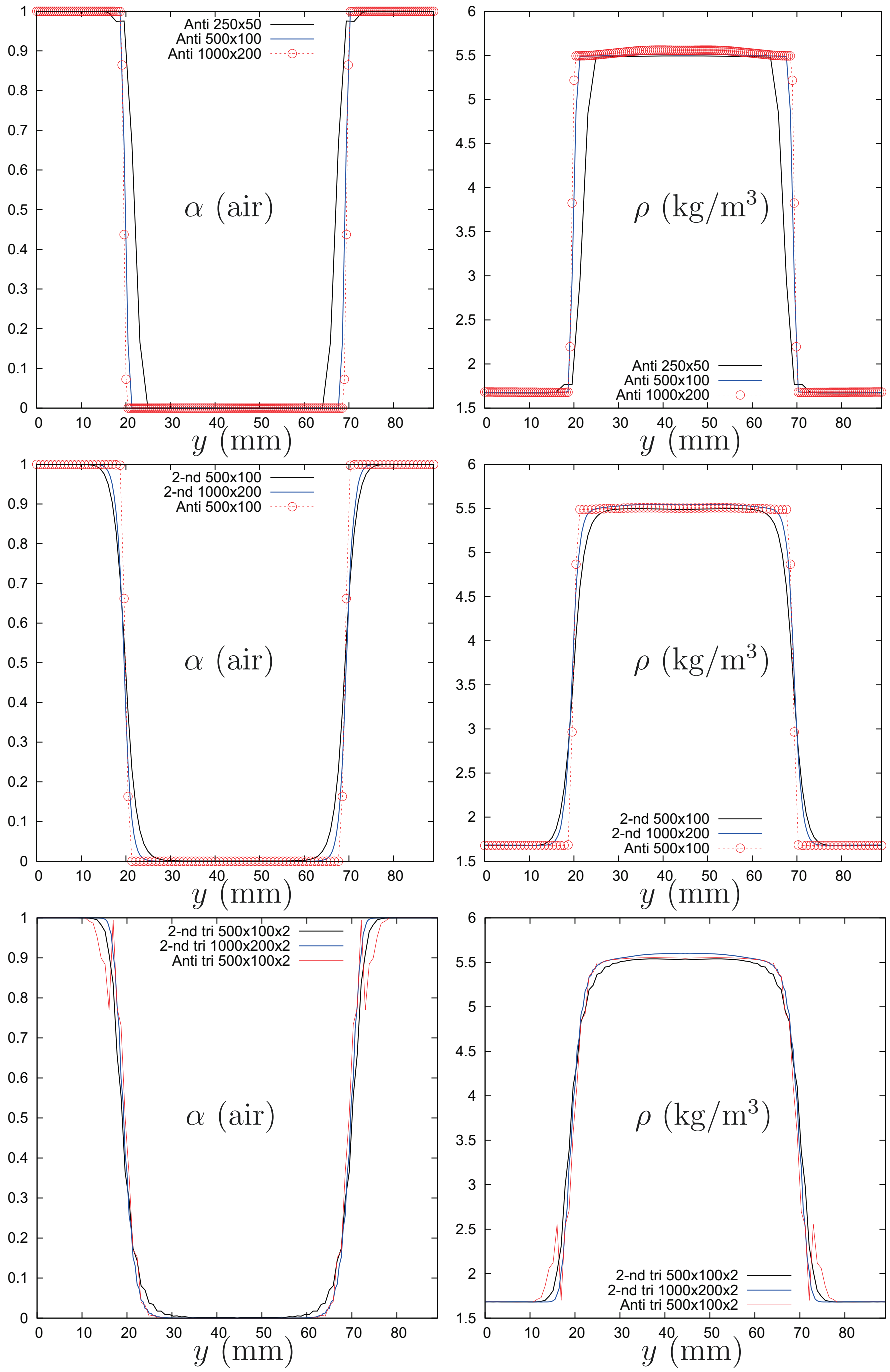

Figure 5.5: Air-R22 shock cylinder interaction test. Plots of volume fraction and mixture density over the line situated at $x = 155$ mm (Fig. 5.4). Anti stands for UDCS anti-diffusive approach. 2-nd stands for UDCS minmod approach (which is quasi second order). tri stands for triangular mesh.

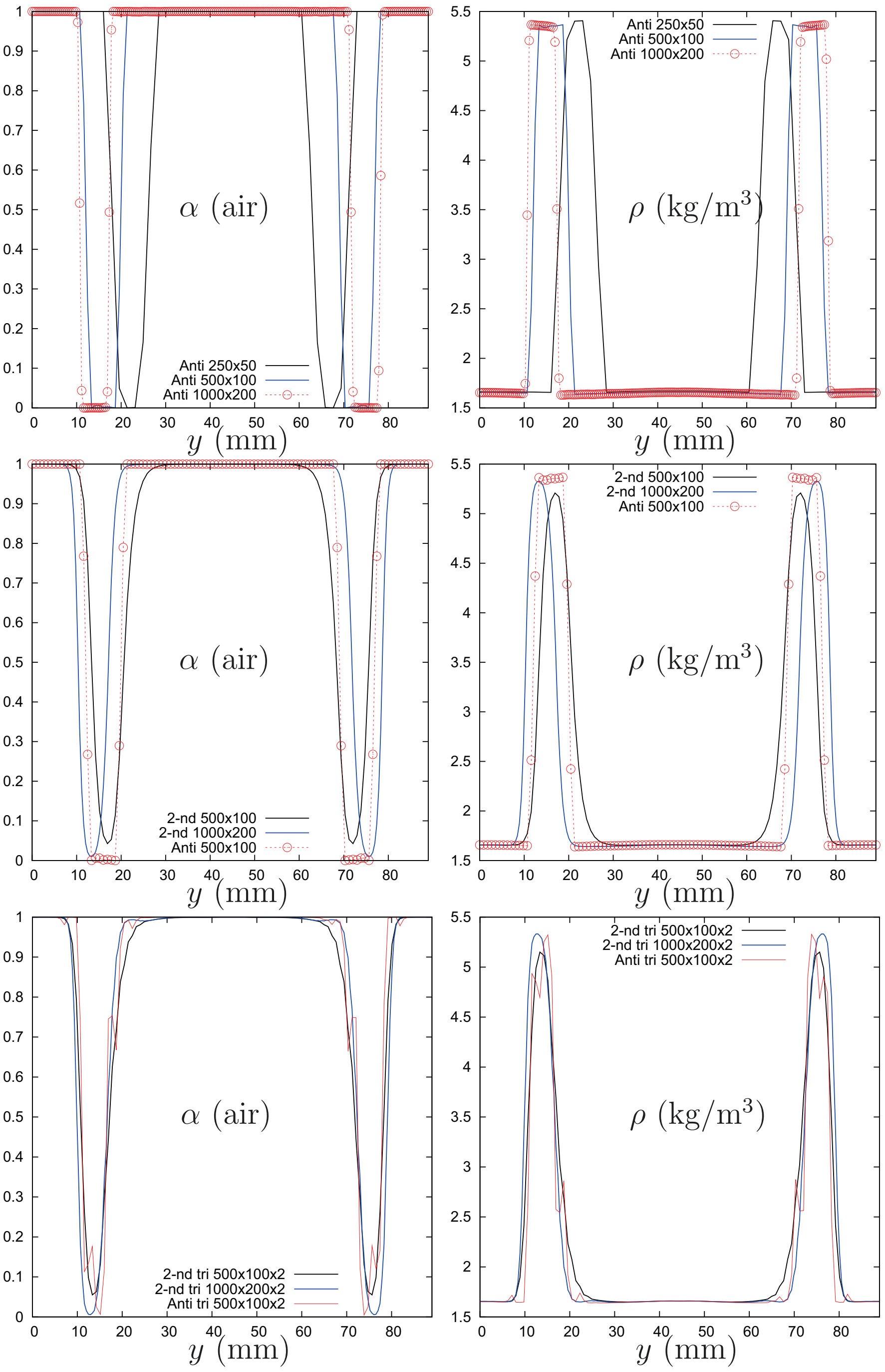

Figure 5.6: Air-R22 shock cylinder interaction test. Plots of volume fraction and mixture density over the line situated at $x = 136$ mm (Fig. 5.4). Anti stands for UDCS anti-diffusive approach. 2-nd stands for UDCS minmod approach (which is quasi second order). tri stands for triangular mesh.

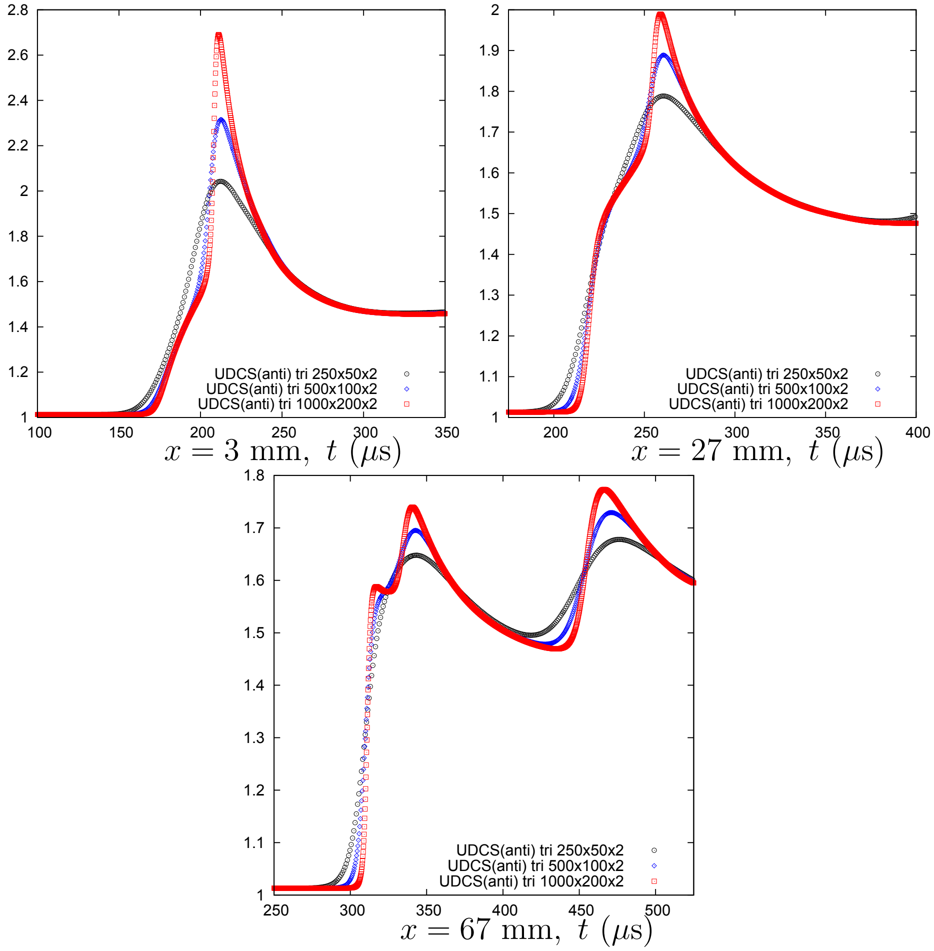

Figure 5.7: Air-R22 shock cylinder interaction test. Time history of pressure in three locations: $x = 3$ mm, $x = 27$ mm, and $x = 67$ mm downstream of the R22 gas bubble along the axis of symmetry. Anti stands for UDCS anti-diffusive approach. tri stands for triangular mesh.

5.3 2D computation of 1D line-symmetric steady combustion

This test case has been previously considered in [Beccantini 10a], Section 6.3, page 300. A 2D (theoretically) unbounded domain is filled with a stoichiometric mixture of (thermally perfect) hydrogen-air at rest. At $t = 0$, combustion is initiated in a single point (the lower left corner of the computational domain) and the test case studies the propagation of the 1D line-symmetric deflagration wave thus generated.

The computational domain is a square of side length equal to 1 m, discretized with a regular grid of 400×400 quadrangles; the CFL number is set equal to 0.4. As far as initial conditions are concerned, initial pressure and temperature are assumed respectively equal to 1.013 bar and 290 K. The fundamental speed is given by $K_0 = 45.2$ m/s. The combustion is "numerically initiated" by supposing that the hydrogen-air mixture is burnt in the closest element to the center of symmetry (the left bottom corner of the square domain here considered). The initial pressure and temperature of the burnt gas mixture are equal to 2.013 bar and 2800 K respectively.

An analytical solution is available for this problem (see in particular [Kuhl 73]). Alternatively, a reference solution can be obtained by performing a 1D line-symmetric computation (as done here) and offers therefore a point of reference for the numerical results computed using the UDCS anti-diffusive approach and RDEM. As already mentioned in the introduction of the chapter, this solution is not physically meaningful since diffusion effects should be necessarily included for a realistic description of a cylindrical/spherical flame. Still, this solution remains a valid point of reference for our computed inviscid solutions. From now on, the 1D line-symmetric solution will be referred to as the "reference solution".

In Fig. 5.13-5.15 we present the computed solution at 1.2 ms, obtained with different approaches: the original RDEM approach (explicit Euler scheme for time discretization), the (RDEM) UDCS approach with minmod reconstruction on pressure, density, velocity and volume fraction (second-order explicit Runge-Kutta scheme for time discretization), and the (RDEM) UDCS anti-diffusive approach (explicit Euler scheme for time discretization). For each method, contours of the volume fraction of the

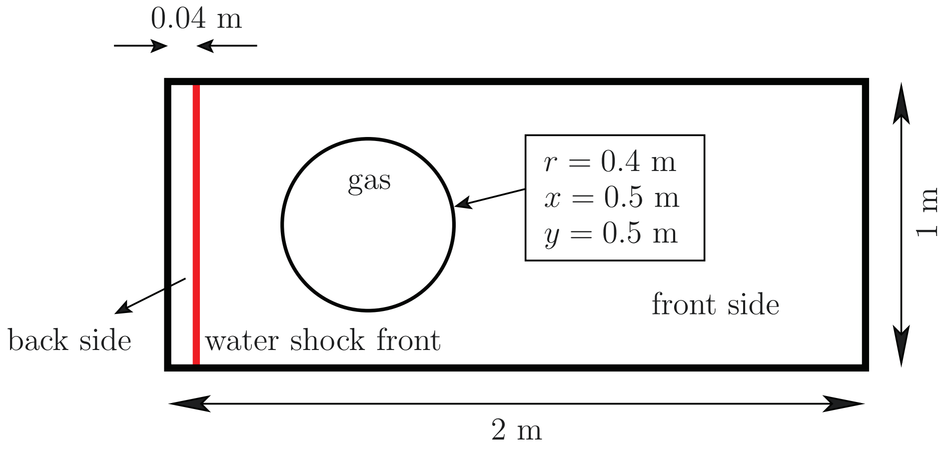

Figure 5.8: Initial configuration of liquid-gas shock tube [Kokh 10].

burnt gas and the pressure are respectively displayed on the left part and right part of the top line. On the bottom line, we plot the density (left) and pressure (right) distributions computed along the x-axis and the diagonal ($x = y$) of the computational domain and compare these distributions extracted from the 2D solution to the reference 1D computation. Before analyzing the various numerical solutions, we

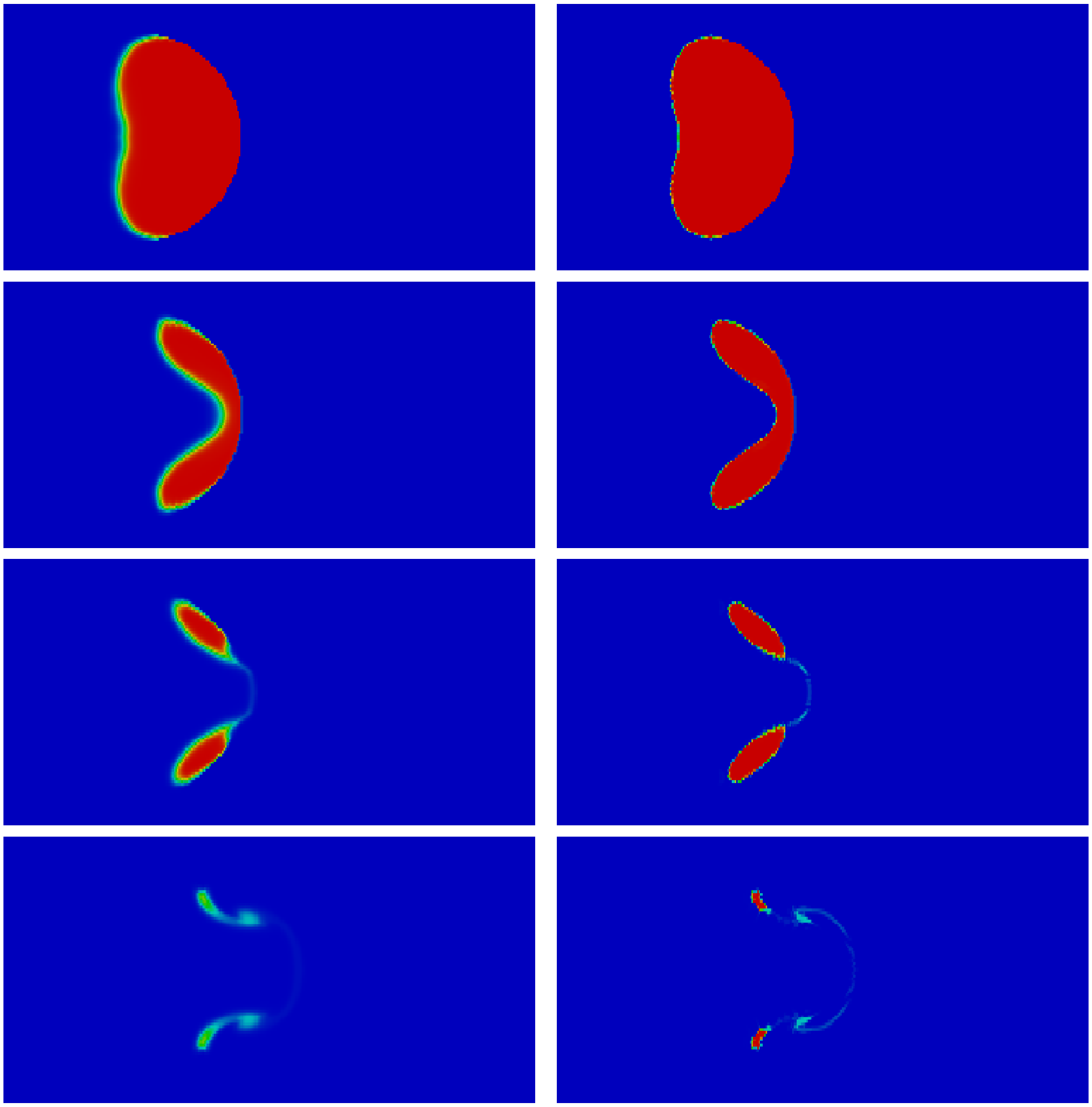

Figure 5.9: Liquid-gas shock bubble interaction test. Mapping of the volume fraction. On the left: UDCS second-order DEM scheme; on the right: UDCS anti-diffusive DEM scheme. Four instants from top to bottom: $t = 225\ \mu s$, $375\ \mu s$, $450\ \mu s$, $600\ \mu s$.

want to point out that, whatever the method used, the flame propagates at different speeds along the diagonal and along the axis of the domain. Such a phenomenon was already observed in [Beccantini 10a], where the solution was obtained using the original RDEM on a quadrangular regular mesh. In our opinion, using the original RDEM approach, this behavior was due to the fact that, when studying 1D reactive Riemann problems at the intercell boundaries, the cell interface normal $\mathbf{n}_f$ can be

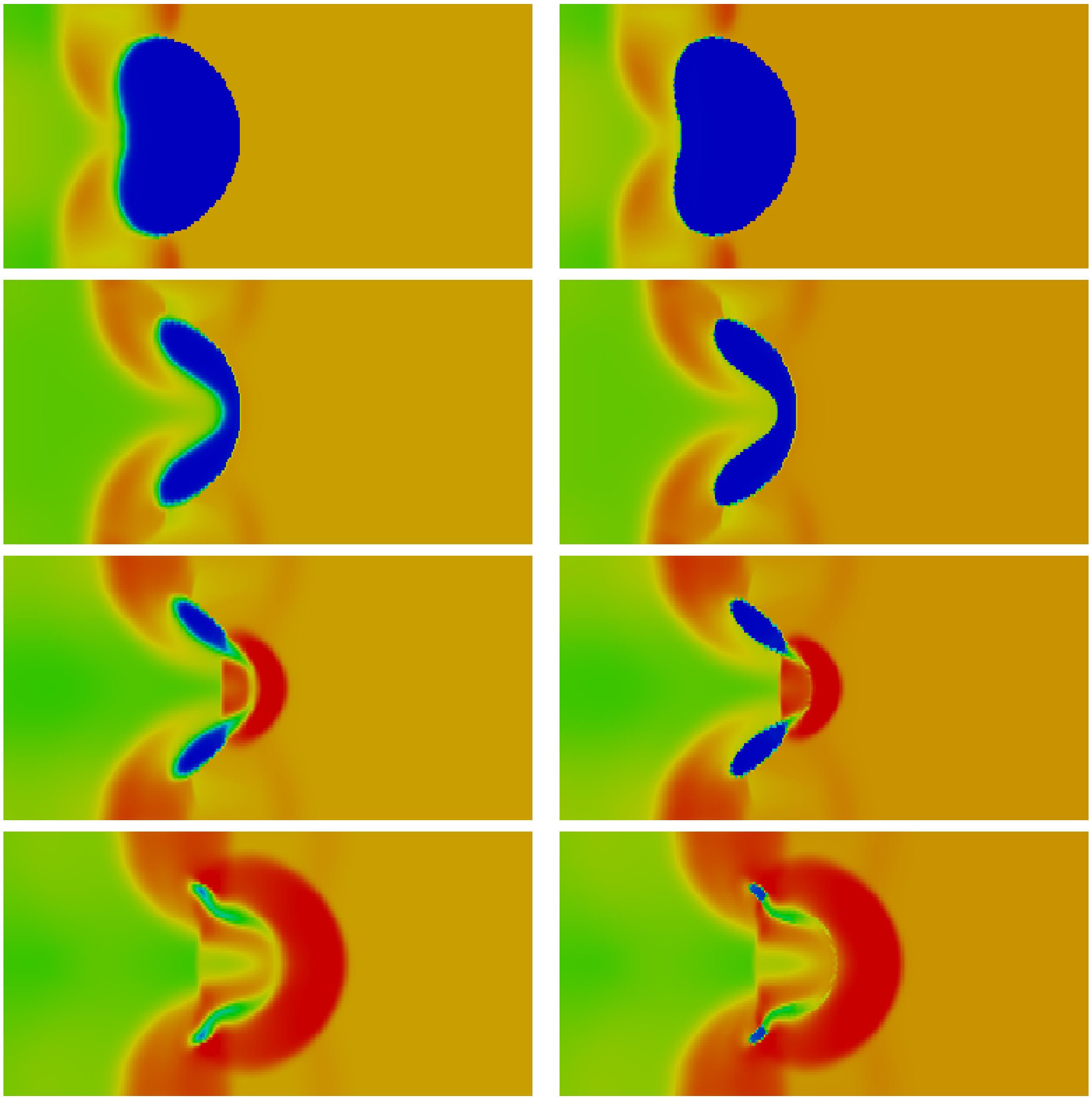

Figure 5.10: Liquid-gas shock bubble interaction test. Mapping of the mixture density. On the left: UDCS second-order DEM scheme; on the right: UDCS anti-diffusive DEM scheme. Four instants from top to bottom: $t = 225\ \mu s$, $375\ \mu s$, $450\ \mu s$, $525\ \mu s$.

different from the flame surface normal. Let us recall that the total flame velocity is $\mathbf{D}_I = \mathbf{v}^{\mathrm{u}} + K_0\mathbf{n}$ (see equation (2.20)) where $\mathbf{n}$ is the flame surface normal (here computed with the formula $\mathbf{n} = \frac{\nabla\alpha}{|\nabla\alpha|}$). As shown in [Beccantini 10a], if in evaluating the solution of the 1D reactive Riemann problem, the fundamental flame speed is supposed to be given by $K_0|\mathbf{n}\cdot\mathbf{n}_f|$ (instead of K_0), directional effects drastically reduce but do not disappear. This is not so astonishing. Indeed, if the normal to the intercell boundary and the normal to the flame are not aligned, we change the solution of the reactive Riemann problem at the interface. For instance, a detonation ($K_{0,\mathrm{det}}$ given by the merging of the precursor shock and the reactive shock in the flame frame) becomes a deflagration because of the scalar product $|\mathbf{n}\cdot\mathbf{n}_f|$ which reduces the value of the fundamental flame speed ($K_{0,\mathrm{det}}|\mathbf{n}\cdot\mathbf{n}_f|$ instead of $K_{0,\mathrm{det}}$). Numerical

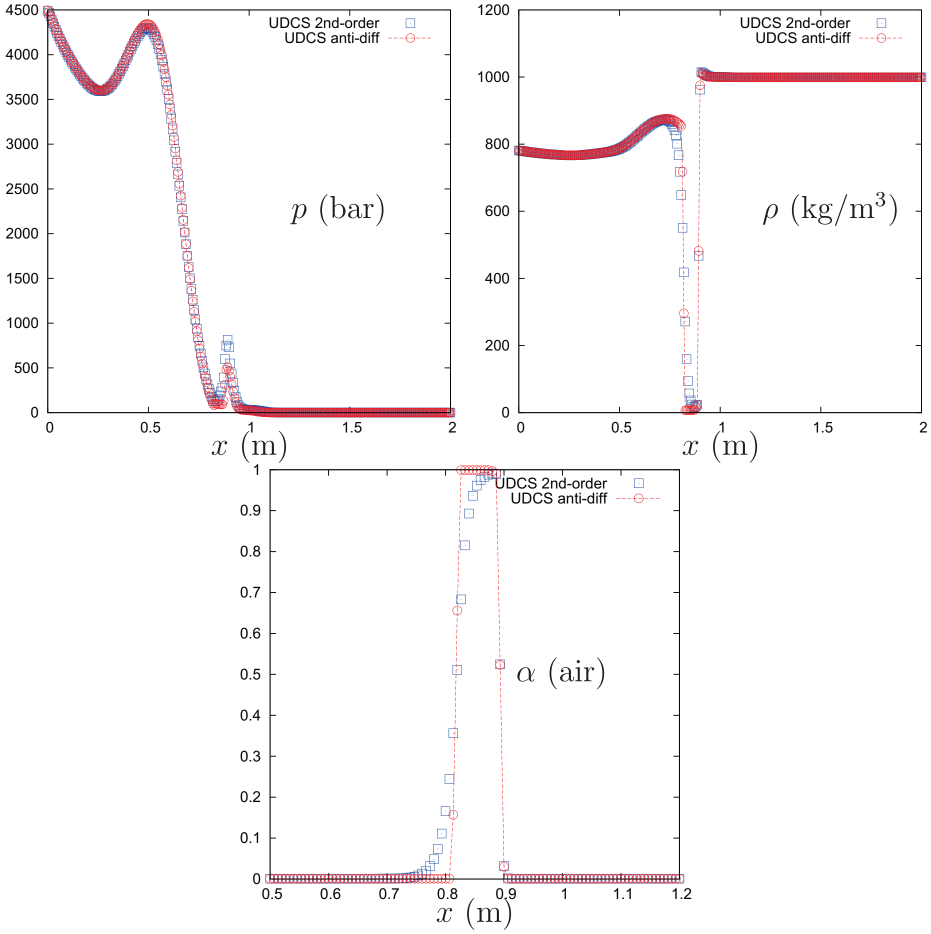

Figure 5.11: Liquid-gas shock bubble interaction test. Plots of pressure, density and air volume fraction over the axis of symmetry (x direction) at time $t = 375$ μs.

experiments (not shown here) for different values of K_0 from fast deflagration to detonation on cylindrical and spherical flows have shown that the solution, even though not converging to the exact one, is acceptably close to it for the applications we have to deal with (computed pressure waves are slightly higher than the exact ones but this can be considered as normal since due to the reactive wave instability). Since this problem is related to RDEM, let us go on with our investigation on UDCS. In what follows, except when differently mentioned, we compute the normal to the flame interface with the formula $\mathbf{n} = \frac{\nabla\alpha}{|\nabla\alpha|}$ and we use $K_0|\mathbf{n}\cdot\mathbf{n}_f|$ as the fundamental flame speed.

As one can see in Fig. 5.13-5.15 , the numerical results which are the closest to the reference solution are the ones obtained using the first-order RDEM (which present the highest numerical diffusion) in Fig. 5.13. The results obtained using UDCS with minmod reconstruction and RDEM in Fig. 5.14 are less diffused than the ones given by the first-order reconstruction. The propagation speed of the flame along the axis and the diagonal remains almost the same. The flame interface shape is not circular; this is expected since the reference solution is unstable. The pressure level in the burnt gas appears higher than the one given by the first-order approach. This is due to the fact that as the flame surface wrinkles, the quantity of unburnt gas which burns per time unit increases. This phenomenon increases in turn the release of chemical energy per time unit and thus the pressure. Finally, in the UDCS anti-diffusive solution shown in Fig. 5.15, it can be noticed that the volume fraction is less diffused than in the other solutions but the flame is much faster on the axis than on the diagonal. Our guess is that the flame interface normal evaluation with the formula

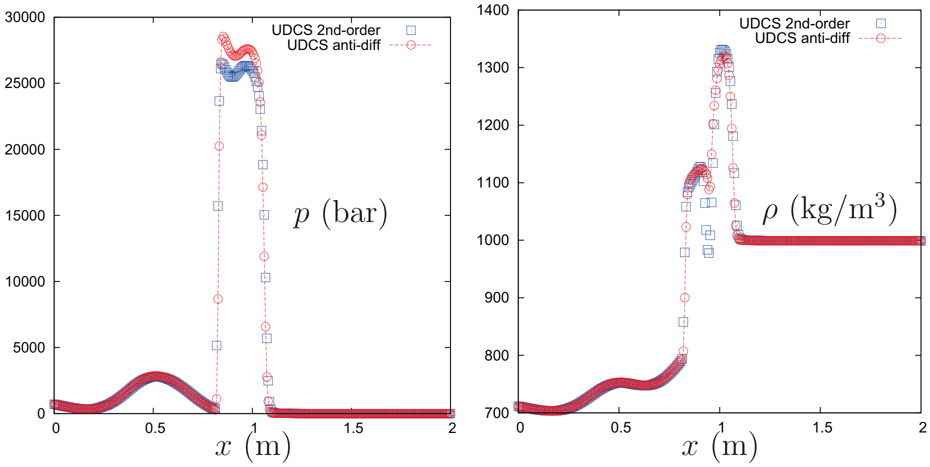

Figure 5.12: Liquid-gas shock bubble interaction test. Plots of pressure and density over the axis of symmetry (x direction) at time $t = 450$ μs.

$\frac{\nabla\alpha}{|\nabla\alpha|}$ creates problems when α is not smooth enough. In order to distinguish between the front capturing properties of the UDCS anti-diffusive approach and the numerical flame propagation issue, a last set of results was obtained using RDEM and UDCS anti-diffusive approach with the flame interface normal artificially set equal to the one of the 1D line-symmetric solution (namely $\mathbf{n} = (\frac{x}{r}, \frac{y}{r})$). As observed in Fig. 5.16, the propagation velocities are almost the same in all directions in that case and the solution is less diffused than in the other approaches (first-order RDEM and RDEM with UDCS second-order approach), as expected.

5.4 Concluding remarks

Two-dimensional non-reactive and reactive interface problems have been studied with the UDCS and DEM/RDEM schemes.

Several numerical strategies have been employed and compared:

- computations using UDCS anti-diffusive DEM/RDEM approach and UDCS second-order DEM/RDEM method which provides an interface accuracy similar to that of the standard second-order method. Note however that UDCS + DEM/RDEM is computationally more robust than the standard DEM/RDEM, due to the fact that its stability is comparable to that of first-order calculations.
- computations on regular grids made of quadrangles or fully unstructured grids made of triangles.

The UDCS anti-diffusive approach was found able to give a much higher resolution of both non-reactive and reactive material interfaces than the UDCS second-order approach, with no restriction on stability with respect to this second-order approach. In fact, we have also noticed that the UDCS anti-diffusive is more efficient than the second-order method. As already mentioned, the reason for this better overall efficiency comes from the reduced number of two-phase (non-reactive or reactive) Riemann problems which have to be solved when the material interface is numerically less diffused thanks to the UDCS anti-diffusive strategy.

The key features of the UDCS anti-diffusive DEM/RDEM approach established at this stage are the following ones:

- the method works well on unstructured grids.
- it resolves material or reactive interfaces in a very accurate way. This point is crucial since rather coarse grids are hardly avoidable when treating very large geometry compared to the combustion front size.

- it is more robust than the standard second-order DEM/RDEM approach;
- it costs considerably less CPU computational time than the second-order DEM /RDEM approach, which makes its implementation in industrial purpose CFD codes attractive.

Based on the present 2D results, what still needs to be improved for real-life combustion problems is the numerical computation of the flame normal, through the computation of the volume fraction gradient, in the case of reactive fronts for the UDCS/RDEM approach.

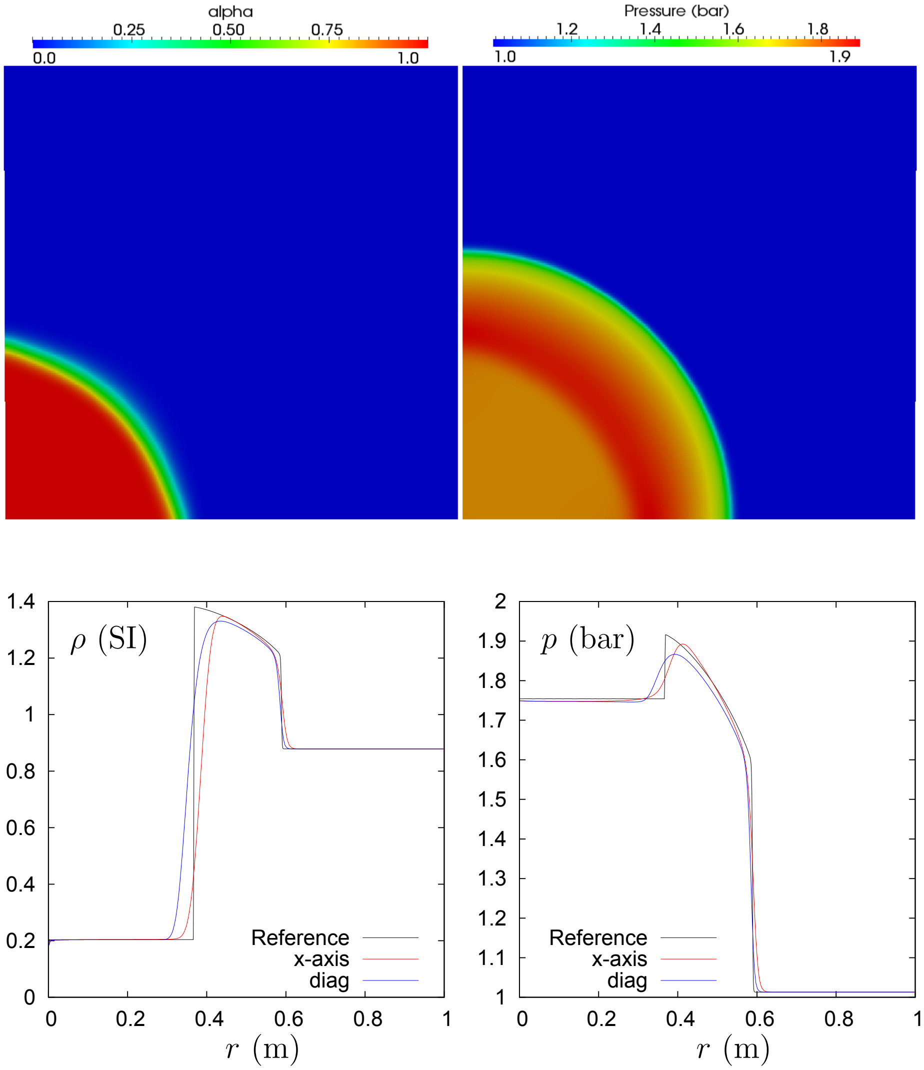

Figure 5.13: Propagation of a 1D line-symmetric steady flame. First-order RDEM (explicit Euler scheme for time discretization). On the top: the volume fraction of the burnt gas and the pressure. On the bottom: the plots of density over axis and diagonal, and that of pressure. The reference solution is obtained using a 1D line-symmetric solver and the UDCS anti-diffusive approach.

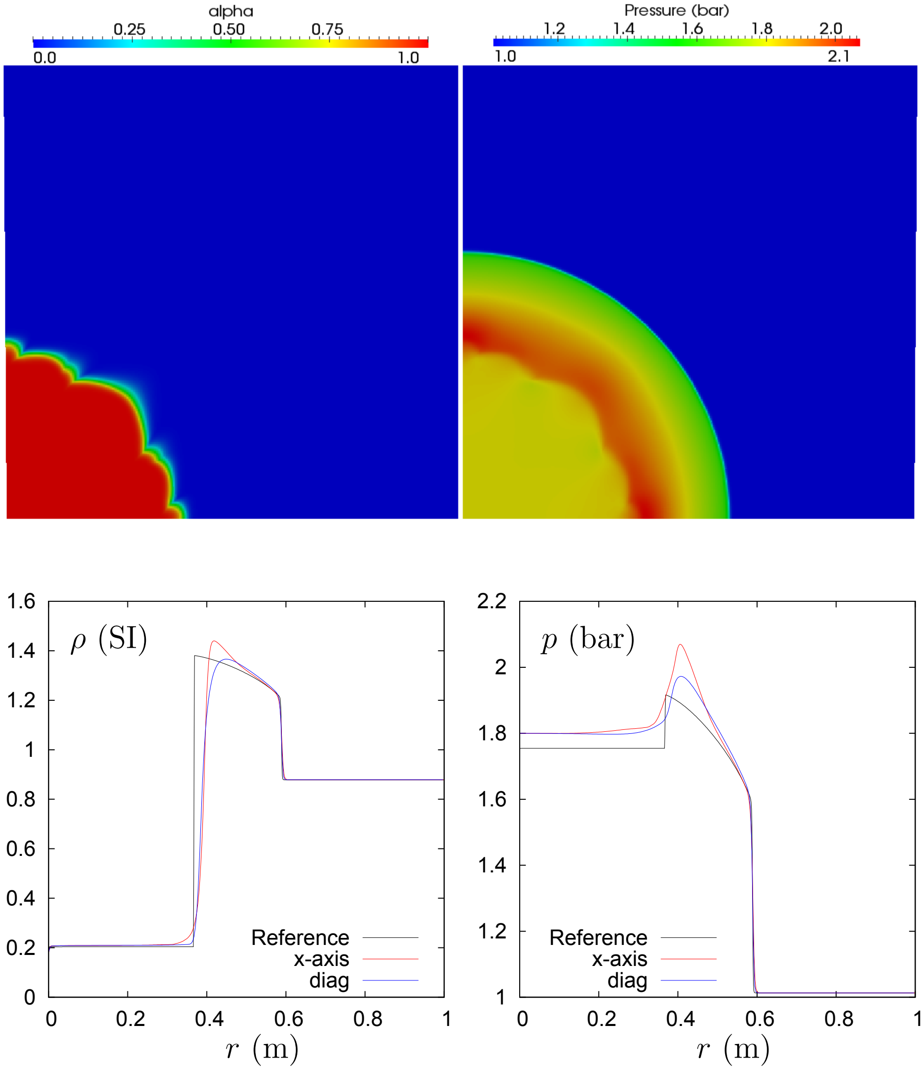

Figure 5.14: Propagation of a 1D line-symmetric steady flame. (Quasi) second-order UDCS + RDEM, with minmod reconstruction for all primitive variables (second-order explicit Runge-Kutta scheme for time discretization). On the top: the volume fraction of the burnt gas and the pressure. On the bottom: the plots of density over axis and diagonal, and that of pressure. The reference solution is obtained using a 1D line-symmetric solver and the UDCS anti-diffusive approach.

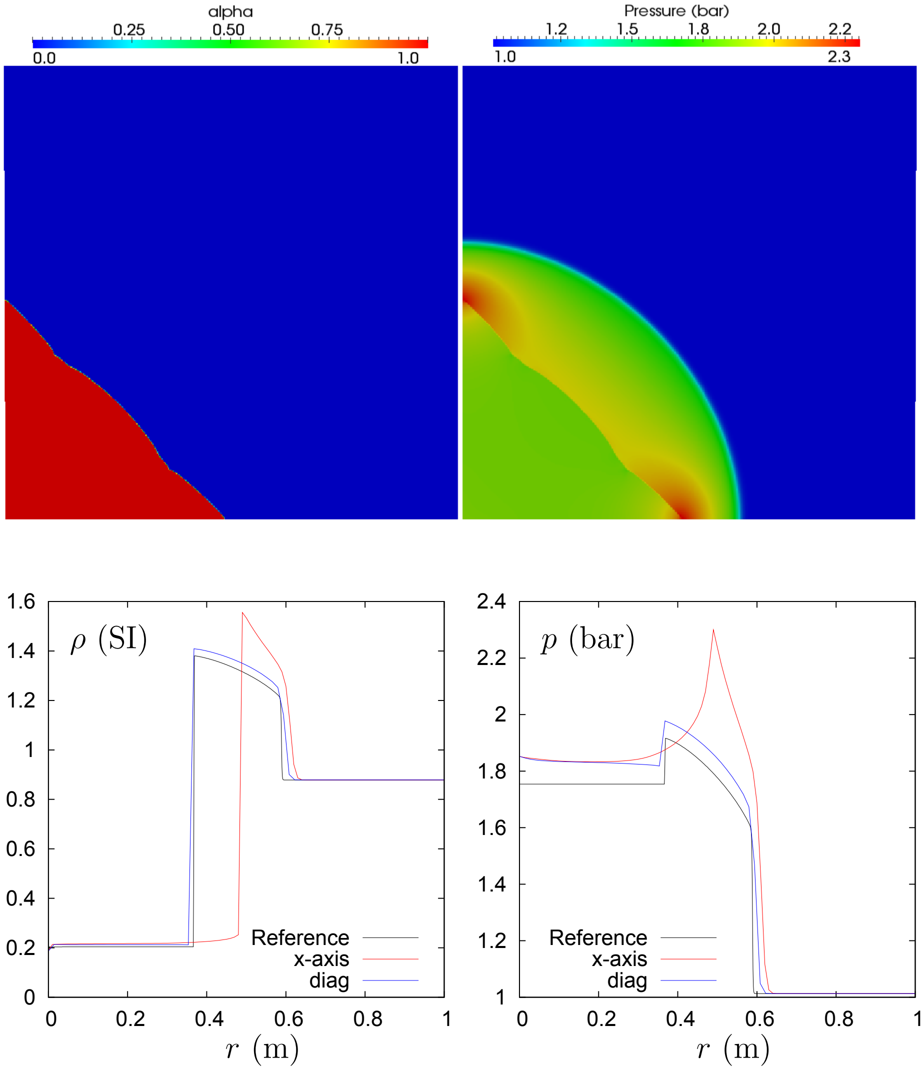

Figure 5.15: Propagation of a 1D line-symmetric steady flame. UDCS anti-diffusive + RDEM approach (explicit Euler scheme for time discretization). On the top: the volume fraction of the burnt gas and the pressure. On the bottom: the plots of density over axis and diagonal, and that of pressure. The reference solution is obtained using a 1D line-symmetric solver and the UDCS anti-diffusive approach.

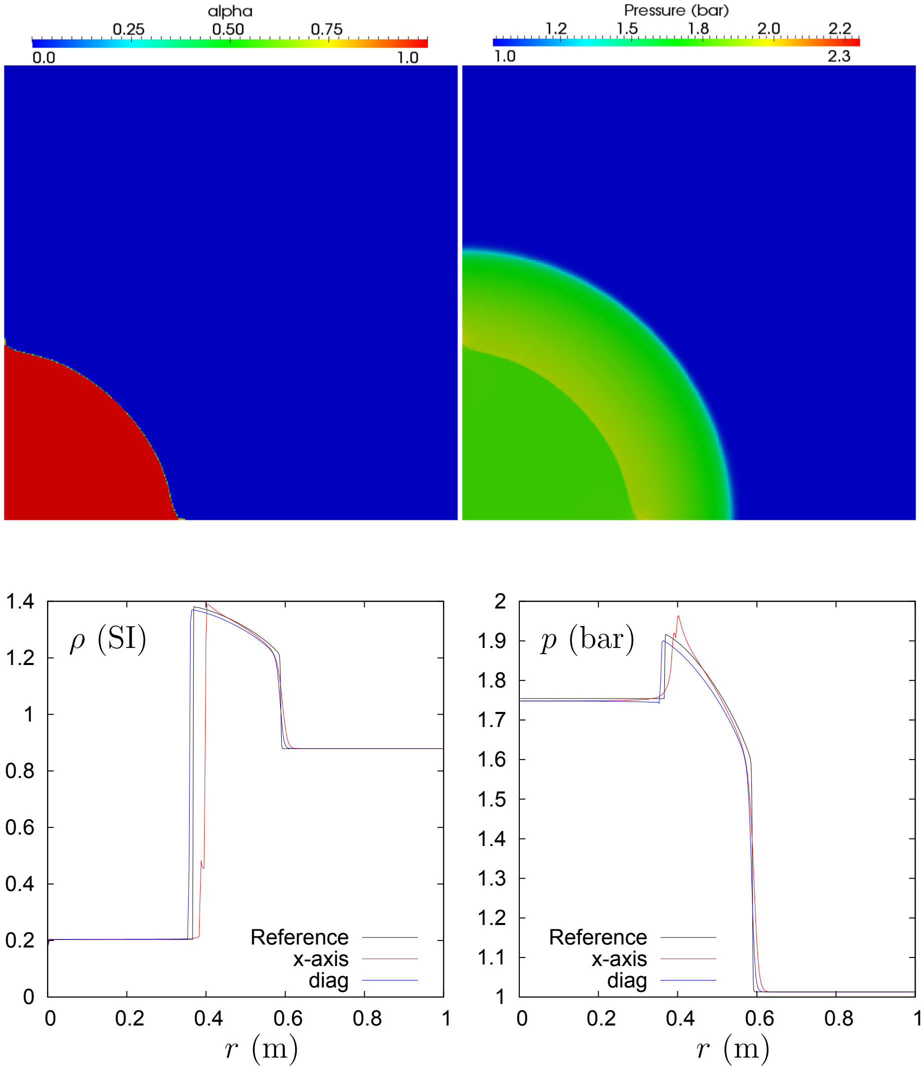

Figure 5.16: Propagation of a 1D line-symmetric steady flame. UDCS anti-diffusive + RDEM approach (explicit Euler scheme for time discretization), in which normals at the flame interface are forced to be equal to the ones of the reference solution (namely $\mathbf{n} = (x/r, y/r)$). On the top: the volume fraction of the burnt gas and the pressure. On the bottom: the plots of density over axis and diagonal, and that of pressure. The reference solution is obtained using a 1D line-symmetric solver and the UDCS anti-diffusive approach.

Summary, conclusions and perspectives

A CFD methodology capable of sharply resolving both two-fluid non-reactive and reactive interfaces has been developed within a finite volume framework. With attention given to the accuracy but also robustness and efficiency of the methodology, a new *upwind downwind-controlled splitting* scheme has been proposed to be combined with the (Reactive) Discrete Equations Method (DEM/RDEM), and an implementation of the approach in multiple space dimensions on general unstructured meshes has been performed in the EUROPLEXUS code.

This thesis conclusion proposes a summary of the work development, followed by the main outcomes to keep in mind and a few suggestions for future work.

Summary of the method development

Our final goal was to perform the numerical investigation of combustion safety issues occurring for instance during a postulated Loss of Coolant Accident in a nuclear reactor containment.

The (Reactive) Discrete Equations Method has been retained in this work as a general development framework. An analysis of the advantages and disadvantages of DEM/RDEM has been made in the light of the final objective, namely the development of an accurate, robust and efficient methodology able to resolve, on complex geometry, reactive sharp interfaces where a significant jump of variable values takes place, *e.g.* pressure and velocity, together with mass transport phenomena. We emphasize that this is a difficult two-fluid problem, since many state-of-the-art two-phase models and methods are only able to solve impermeable fronts. A remarkable property of the Reactive Discrete Equations Method lies in its capability of preserving the conservation of mass, momentum and energy which is of crucial importance when dealing with long-term combustion simulations. On the other hand, it was also known at the start of the work that both first-order and second-order RDEM calculations did not provide satisfactory interface accuracy in fast deflagration and detonation configurations. This was of course not acceptable since it is crucial to obtain an acceptable accuracy on these reactive fronts if one has to take into account for instance the combustion generated pressure wave when investigating reactor containment safety.

With the aim of improving the reactive front resolution, RDEM was first coupled with an anti-diffusive approach, which can potentially capture in a very accurate way the contact discontinuity and the reactive shock wave. However, this coupling was found to be insufficiently stable in general. Our research effort was then focused on developing a so-called upwind downwind-controlled splitting (UDCS) method which can solve sharp fluid/fluid interfaces both accurately and in a very robust way. The method derivation demonstrates that the stability of UDCS is similar to the stability of the first-order upwind DEM/RDEM approach with piecewise constant volume fractions. The best accuracy is achieved with the anti-diffusive version of UDCS, be it with DEM or RDEM that is for non-reacting or reacting flows.

The implementation of UDCS + DEM/RDEM in multiple dimensions has been performed in the fast dynamic fluid-structure interaction code EUROPLEXUS. Several calculated one and two-dimensional examples over a wide spectrum of physical conditions incorporating both non-reactive and reactive interfaces have been presented, illustrating the attractive features of the methodology developed in this work with, in particular:

- almost exact capturing of contact discontinuity and reactive shock wave in one space dimension
- calculation of both impermeable and permeable fronts on irregular unstructured meshes in a very accurate and robust way.

Main outcomes

Inserting the UDCS anti-diffusive approach inside the DEM/RDEM framework significantly improves the accuracy, robustness and efficiency properties of the DEM/RDEM strategy which was available in the literature at the start of this work. Systematic comparison between the proposed specific methodology and other approaches available in the literature is not necessarily easy to perform because both the choice of the physical model and the key design principles of the numerical treatment can be very different. We can nonetheless draw some interesting conclusions when comparing the UDCS anti-diffusive approach + DEM/RDM with the anti-diffusive type method developed in [Kokh 10]. Let us recall [Kokh 10] is focused on the numerical solution of a reduced two-fluid model with a single pressure and a single velocity, which is not capable of representing high speed combustion waves in which a significant jump in pressure and velocity occurs. For impermeable (non reactive) fronts (gaseous and liquid-gas shock bubble interactions), the methodology developed in this work compares well with [Kokh 10]. The added value of our strategy is that it is capable of successfully dealing with permeable fronts, particularly all speed reactive fronts in our applications. Moreover, the presented methodology works also on irregular unstructured grids, which is of essential importance for applications involving complex geometry (such as a reactor containment).

Anti-diffusive UDCS resolves the interface in a very accurate way. This point is crucial, because rather coarse grids are hardly avoidable when treating very large geometry with respect to the combustion front size. In particular, to the best of our knowledge, the UDCS anti-diffusive method combined with RDEM is the first approach able to quasi-exactly capture (in one space dimension), for both deflagration and detonation regimes, a reactive shock wave.

Robustness has also been successfully ensured. Indeed, the UDCS approach (either limited second-order or anti-diffusive) with DEM/RDEM is proved as stable as the first-order DEM/RDEM version for the volume fraction. The approach is made of two main steps: the first “upwind” step fully contains the first-order upwind DEM/RDEM approach, which takes account of all first-order wave propagations, including in particular the genuinely nonlinear waves; the second “downwind-controlled splitting” step aims at improving the accuracy of the linearly degenerate wave (*i.e.*, the contact discontinuity for non-reacting stiffened gas flow and the reactive shock for reacting gas flow), by splitting the phase volumes and rearranging them in space. Since this step does not involve the time evolution and since the genuinely nonlinear waves have been taken into consideration within the previous step by upwind strategy, we thus recover the stability of the first-order DEM/RDEM method with piecewise constant volume fraction data.

As an extra benefit, higher computational efficiency is also achieved. The internal Riemann problem calculated within the state-of-the-art limited second-order approach [Abgrall 03] is not needed, since we are no longer concerned with the internal discontinuity of volume fraction when using UDCS method. In addition, the steeper representation of the phase interface obtained by UDCS anti-diffusive approach considerably reduces the zone where expensive two-phase Riemann problems have to be computed within DEM/RDEM. This feature can lead to computations that become more efficient than both first-order and second-order simulations. The efficiency of anti-diffusive UDCS is emphasized as a very attractive property for its implementation in industrial purpose CFD codes.

Future research

UDCS has been proposed in the context of permeable sharp interfaces with chemical reactions. Note however that the combination UDCS/RDEM is not limited to reactive fronts and can be implemented for the simulation of other physical phenomena, such as evaporation fronts [Le Métayer 05].

Additionally, although the UDCS idea has been exclusively proposed and developed for the full non-equilibrium two-fluid model in the present work, we believe that it would be worthwhile to extend this concept to sub-models of two-phase flow for interface computations.

On a more technical note, let us emphasize the UDCS limited second-order method has already been combined with the explicit two-stepping Runge-Kutta scheme for time discretization. This allows to work with large enough CFL numbers when using a limited second-order reconstruction on all primitive variables (achieving quasi second-order accuracy in space and time). Unfortunately, it was found more difficult to couple the anti-diffusive UDCS approach with the second-order Runge-Kutta scheme so that this point requires further investigaton.

Finally, as observed on the final 2D combustion problem, it will also be necessary to improve the approach used to compute the normal at the flame interface so as to avoid that this normal computation spoils the accuracy improvement brought by the anti-diffusive UDCS/RDEM.

Appendix A

Basic notions on reconstruction approach

Basic notions of space reconstruction with slope-limiter method are recalled in what follows. We take for instance the single phase Euler equations and let the function θ_i measure the data smoothness of a primitive variable $W \in (\rho,\ v,\ p)^{\mathrm{T}}$,

$$\theta_i = \frac{W_i - W_{i-1}}{W_{i+1} - W_i},$$

The slope Δ_i inside the cell i related to the primitive variable W can be written as

$$\Delta_i(W) = \frac{W_{i+1} - W_i}{\Delta x} \phi\left(\theta_i\right), \tag{A.1}$$

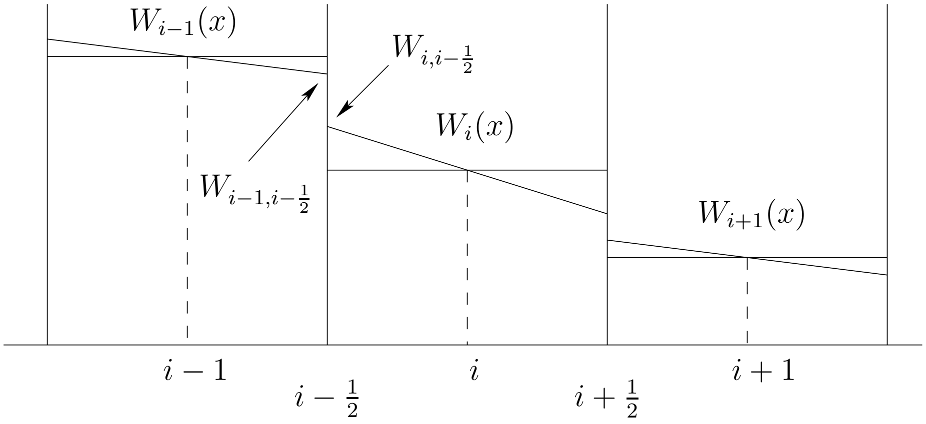

Figure A.1: Piecewise linear reconstruction in (quasi) second-order slope limiter approach.

with $\phi(\theta_i)$ the limiter function. Note that when $\phi(\theta_i) = 1$, (A.1) is Lax-Wendroff method with downwind slope, while when $\phi(\theta_i) = \theta_i$ it is Beam-Warming method with upwind slope. In this work, if not specified, the minmod limiter is used which is defined by

$$\phi(\theta_i) = \max(0, \min(1, \theta_i)) = \begin{cases} 0 & \text{if } \theta_i \leq 0, \\ \theta_i & \text{if } 0 \leq \theta_i \leq 1, \\ 1 & \text{if } \theta_i \geq 1. \end{cases}$$

Constructing a piecewise linear approximation for the primitive variable W with the slope $\Delta_i(W)$ defined in (A.1), the local value of W inside the cell i is,

$$W_i(x,t) = W_i + (x - x_i)\Delta_i, \; x_{i-\frac{1}{2}} \leq x \leq x_{i+\frac{1}{2}}.$$

The values at the intercell boundary $x_{i-\frac{1}{2}}$ (illustrated in Fig. A.1) can then be written as

$$\begin{aligned} W_{i-1,i-\frac{1}{2}} &= W_{i-1} + \frac{1}{2}\Delta x \Delta_{i-1}, \\ W_{i,i-\frac{1}{2}} &= W_i - \frac{1}{2}\Delta x \Delta_i. \end{aligned} \tag{A.2}$$

When computing the intercell Godunov-type numerical flux $\mathbf{F}_{i-\frac{1}{2}}$ with the reconstruction shown in Fig. A.1, it is noted that the Riemann problem at $x_{i-\frac{1}{2}}$ is no longer with constant data and a single discontinuity. Rigorously speaking, we should consider a so-called Generalised Riemann Problem [Ben-Artzi 84, Godlewski 96, Toro 97], with piecewise linear data. Unfortunately, the solution of Generalised Riemann Problem for the Euler equations is extremely complicated, and is thus not attractive enough for deriving high order methods with simplicity. Alternatively, we consider to modify the reconstruction shown in Fig. A.1 so as to use the solution of conventional

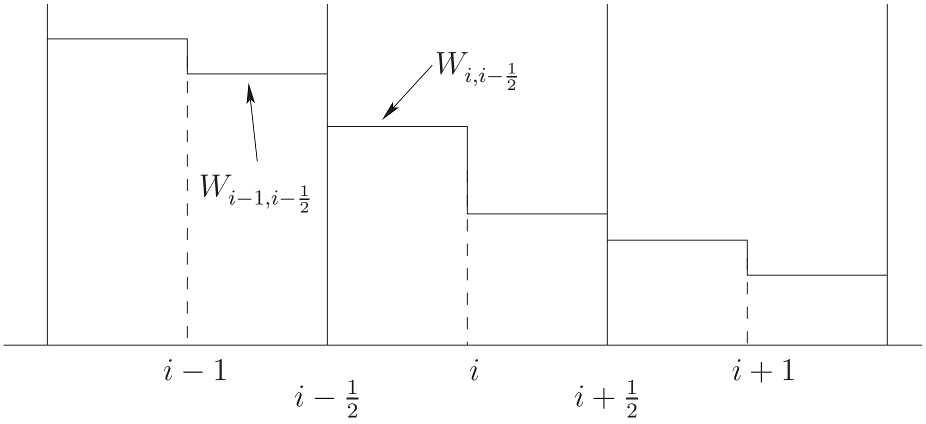

Figure A.2: Modified reconstruction in (quasi) second-order slope limiter approach.

Riemann problems with piecewise constant data. This modification is illustrated in Fig. A.2. That is, inside a cell element i, we reconstruct two constant states $W_{i,i-\frac{1}{2}}$ and $W_{i,i+\frac{1}{2}}$, with an internal discontinuity located at x_i. Consequently, conventional Riemann problem solution can be utilized to compute intercell numerical fluxes.

Comments on stability condition of first-order Euler stepping method The simplest approach for the time discretization is the first-order forward Euler method, as used in the work of [Kolgan 72]. That is, for the Euler equations,

$$\mathbf{U}_i^{n+1} = \mathbf{U}_i^n - \frac{\Delta t}{\Delta x}(\mathbf{f}(\mathbf{U}_{i+\frac{1}{2}}(x_{i+\frac{1}{2}},t)) - \mathbf{f}(\mathbf{U}_{i-\frac{1}{2}}(x_{i-\frac{1}{2}},t))), \tag{A.3}$$

where

$$\mathbf{U}_{i-\frac{1}{2}}(x_{i-\frac{1}{2}},t),\ t^n < t \leq t^{n+1}$$

is the exact solution of the intercell local Riemann problem

$$\mathrm{RP}(\mathbf{W}^n_{i-1,i-\frac{1}{2}}, \mathbf{W}^n_{i,i-\frac{1}{2}}) \tag{A.4}$$

with reconstructed primitive variables. It is emphasized that the solution of internal Riemann problem defined at x_i and denoted by

$$\mathrm{RP}(\mathbf{W}^n_{i,i-\frac{1}{2}}, \mathbf{W}^n_{i,i+\frac{1}{2}}) \tag{A.5}$$

indeed does not contribute to the final solution of the numerical scheme, because the numerical flux defined on internal discontinuity x_i exits from cell i, and enters into

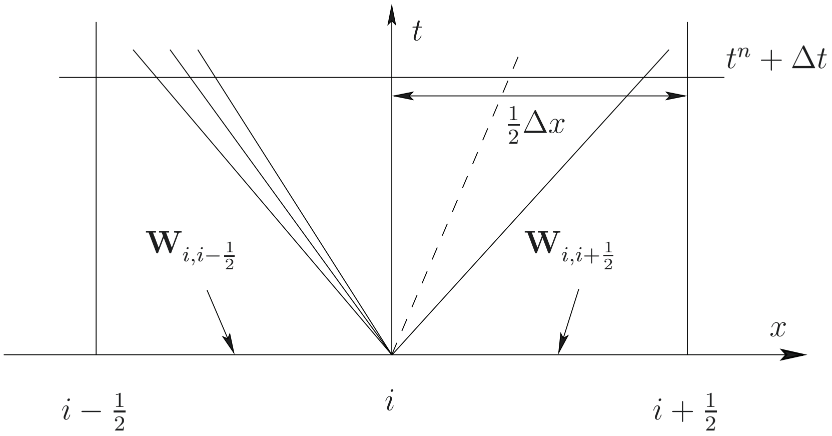

Figure A.3: Wave propagations of cell-internal Riemann problem $\mathrm{RP}(\mathbf{W}_{i,i-\frac{1}{2}}, \mathbf{W}_{i,i+\frac{1}{2}})$.

the same cell i. However, the associated wave propagations of the internal Riemann problem determines the stability condition. In fact, in order for the scheme (A.3) to be stable, any wave involved in the reconstruction illustrated in Fig. A.2 should not modify the time-averaged flux defined on intercell boundaries. Considering the cell-internal discontinuity defined at x_i, the wave propagations incorporated in the resolution of (A.5) are illustrated in Fig. A.3. In order to fulfill the stability condition that the fastest nonlinear wave generated from cell-internal discontinuity cannot reach the intercell boundary, there should be

$$\Delta t \leq \frac{1}{2} \frac{\Delta x}{\delta^n_{\max}}, \; \textit{i.e.} \; \text{CFL} \leq \frac{1}{2} \tag{A.6}$$

where $\delta^n_{\max}$ represents the maximum wave speed in the whole domain. Note that in (A.6) we have made the assumption of no wave acceleration resulting from wave interaction [Toro 97]. A wide range of numerical experiments shows that a predictor-corrector scheme [Toro 97, Abgrall 03] is capable of relaxing the CFL to unity.

Appendix B

Limited second-order DEM/RDEM approach for averaged topological equation

This section is devoted to the state-of-the-art second-order DEM/RDEM scheme for the scalar averaged topological equation (1.16) in one space dimension. The phase Σ_k is concerned and its phase indicator k is omitted for α for notation convenience. Following the reconstruction approach described in Appendix A (see also Section 2.6.1), the reconstructed values of α inside cell i are given by

$$\alpha_{i,i-\frac{1}{2}} = \alpha_i - \frac{1}{2}\Delta x \Delta_i,$$
$$\alpha_{i,i+\frac{1}{2}} = \alpha_i + \frac{1}{2}\Delta x \Delta_i,$$

as illustrated in Fig. 2.12. Here Δ_i is the slope function in cell i defined by (2.36). As already mentioned, the numerical solution $\alpha(x,t)$ can be approximated by a piecewise constant reconstruction function $\alpha(x,t)$, such that

$$\alpha(x,t) = \begin{cases} \alpha_{i,i-\frac{1}{2}}, \ x_{i-\frac{1}{2}} < x < x_i, \\ \alpha_{i,i+\frac{1}{2}}, \ x_i < x < x_{i+\frac{1}{2}}. \end{cases}$$

Analogously as done in Section 2.1, we discretize the modified topological equation (2.2). The conservative term can be discretized by the same way as (2.3):

$$\left[\frac{\partial(\alpha D_I)}{\partial x}\right]_i = \frac{\alpha_{i+\frac{1}{2}} D_{I,i+\frac{1}{2}} - \alpha_{i-\frac{1}{2}} D_{I,i-\frac{1}{2}}}{\Delta x}.$$

There existing two constant states of volume fraction inside cell element i, the non-conservative term can be discretized by calculating the average of these two parts:

$$\left[\alpha \frac{\partial D_I}{\partial x}\right]_i = \frac{1}{2}\left(\left[\alpha \frac{\partial D_I}{\partial x}\right]_{i,i-\frac{1}{2}} + \left[\alpha \frac{\partial D_I}{\partial x}\right]_{i,i+\frac{1}{2}}\right),$$

where $\left[\alpha \frac{\partial D_I}{\partial x}\right]_{i,i-\frac{1}{2}}$ and $\left[\alpha \frac{\partial D_I}{\partial x}\right]_{i,i+\frac{1}{2}}$ can be computed analogously as in (2.4),

$$\begin{aligned}\left[\alpha \frac{\partial D_I}{\partial x}\right]_{i,i-\frac{1}{2}} &= \alpha_{i,i-\frac{1}{2}} \frac{D_{I,i} - D_{I,i-\frac{1}{2}}}{\frac{1}{2}\Delta x},\\ \left[\alpha \frac{\partial D_I}{\partial x}\right]_{i,i+\frac{1}{2}} &= \alpha_{i,i+\frac{1}{2}} \frac{D_{I,i+\frac{1}{2}} - D_{I,i}}{\frac{1}{2}\Delta x},\end{aligned}$$

where $D_{I,i}$ is given by the internal Riemann problem solution. Thus, using either first-order Euler method or predictor-corrector method (only the corrector step is presented) for the time discretization in (2.2) leads to

$$\alpha_i^{n+1} = \alpha_i^n + \frac{\Delta t}{\Delta x}\left[D_{I,i-\frac{1}{2}}(\alpha_{i-\frac{1}{2}} - \alpha_{i,i-\frac{1}{2}}) + D_{I,i}(\alpha_{i,i-\frac{1}{2}} - \alpha_{i,i+\frac{1}{2}}) + D_{I,i+\frac{1}{2}}(\alpha_{i,i+\frac{1}{2}} - \alpha_{i+\frac{1}{2}})\right]. \tag{B.1}$$

The intercell value $\alpha_{j-\frac{1}{2}}$ at $x = x_{j-\frac{1}{2}}$ is given by

$$\alpha_{j-\frac{1}{2}} = \begin{cases} \alpha_{j-1,j-\frac{1}{2}}, \text{ if } D_{I,j-\frac{1}{2}} > 0, \\ \alpha_{j,j-\frac{1}{2}}, \text{ if } D_{I,j-\frac{1}{2}} < 0. \end{cases} \tag{B.2}$$

Employing the intercell interface velocity indicator β defined by (2.7), the second-order DEM/RDEM scheme (B.1) can be rewritten as

$$\begin{aligned}\alpha_i^{n+1} = \alpha_i^n + \frac{\Delta t}{\Delta x}\Big[&\beta_{i-\frac{1}{2}} D_{I,i-\frac{1}{2}}(\alpha_{i-1,i-\frac{1}{2}} - \alpha_{i,i-\frac{1}{2}}) + D_{I,i}(\alpha_{i,i-\frac{1}{2}} - \alpha_{i,i+\frac{1}{2}}) \\ &+(1-\beta_{i+\frac{1}{2}}) D_{I,i+\frac{1}{2}}(\alpha_{i,i+\frac{1}{2}} - \alpha_{i+1,i+\frac{1}{2}})\Big].\end{aligned} \tag{B.3}$$

In terms of partitioned sub-surfaces within the framework of DEM/RDEM approach (see Section 2.6.1), the scheme (B.3) can be written as

$$\begin{aligned}\alpha_i^{n+1} = \alpha_i^n + \frac{\Delta t}{\Delta x}\Big[&\beta_{i-\frac{1}{2}} D_{I,i-\frac{1}{2}}(S_{i-\frac{1}{2}}^{(kk')} - S_{i-\frac{1}{2}}^{(k'k)}) + D_{I,i}(S_i^{\text{sec},(kk')} - S_i^{\text{sec},(k'k)}) \\ &+(1-\beta_{i+\frac{1}{2}}) D_{I,i+\frac{1}{2}}(S_{i+\frac{1}{2}}^{(kk')} - S_{i+\frac{1}{2}}^{(k'k)})\Big].\end{aligned} \tag{B.4}$$

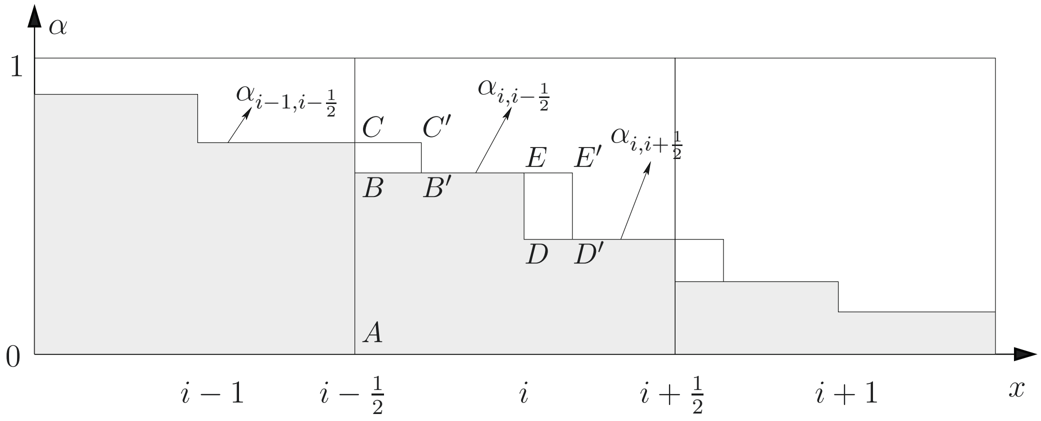

Figure B.1: Second-order DEM/RDEM method for averaged topological equation.

The second-order DEM/RDEM method (B.4) for topological equation is illustrated graphically in Fig. B.1 in case of positive propagation speed. It follows that the flux contribution of intercell boundary $x_{i+\frac{1}{2}}$ vanishes. That is,

$$(1-\beta_{i+\frac{1}{2}})D_{I,i+\frac{1}{2}}(S^{(kk')}_{i+\frac{1}{2}}-S^{(k'k)}_{i+\frac{1}{2}})=0.$$

Moreover, the term of

$$\beta_{i-\frac{1}{2}}D_{I,i-\frac{1}{2}}\Delta t(S^{(kk')}_{i-\frac{1}{2}}-S^{(k'k)}_{i-\frac{1}{2}})$$

in numerical scheme (B.4) can be represented by the area $A_{BB'C'C}$ in Fig. B.1 to stand for the flux contribution of intercell boundary $x_{i-\frac{1}{2}}$, while the term of

$$D_{I,i}\Delta t(S^{\mathrm{sec},(kk')}_{i}-S^{\mathrm{sec},(k'k)}_{i})$$

can be represented by the area $A_{DD'E'E}$ which means the flux contribution of internal numerical interface on x_i. Thus, we can express (B.4) graphically as

$$\alpha_i^{n+1}=\alpha_i^n+\frac{A_{BB'C'C}}{\Delta x}+\frac{A_{DD'E'E}}{\Delta x}. \tag{B.5}$$

Appendix C

Relaxation solver

This section concerns only the two-fluid system (1.21) with no molecular flux involved on the interface. That is, $\Gamma_{k,I}$ defined in (1.22) vanishes. With stiffened gas thermodynamic closures, this system is able to stand for compressible liquid-gas interface motions, such as the test case studied in Section 2.8.1. The relaxation source terms introduced in [Saurel 99a] represents, additionally to the two-fluid system (1.21) where interface conditions are calculated by the non-conservative Lagrangian flux terms, an internal phase interaction inside each cell element, with the aim of "relaxing" the system till both phases contain the same pressure and velocity. Note that the global mass, momentum and energy conservation should be maintained throughout these relaxation procedures. We emphasize that the relaxation procedures here considered is not able to improve the robustness of the straightforward coupling between DEM/RDEM and anti-diffusive approach (see Section 3.1). However, it is useful to prevent the numerical calculations from producing negative pressures. In fact, the liquid phase pressure is allowed to be negative according to the stiffened gas EOS, while the gas phase is not. Another utility of the relaxation procedures consists in taking account of the two-phase physical mixtures. We refer to [Saurel 99a, Saurel 01, Abgrall 03, Murrone 05] for these issues.

The stiffness of the relaxation terms [Saurel 99a] implies that the full system can be solved by standard splitting method (Strang splitting [Strang 68]). Let $\mathbb{L}_h^{\Delta t}$ denote the hyperbolic operator (for the first-order method, it is (2.27)), containing the non-conservative Lagrangian flux terms, and $\mathbb{L}_r^{\Delta t}$ the integration operator for relaxation source terms. Thus for the first-order method the solution is obtained by a succession of operators,

$$\begin{bmatrix} \alpha \\ \alpha \mathbf{U} \end{bmatrix}_{k,i}^{n+1} = \mathbb{L}_r^{\Delta t} \mathbb{L}_h^{\Delta t} \begin{bmatrix} \alpha \\ \alpha \mathbf{U} \end{bmatrix}_{k,i}^{n} . \tag{C.1}$$

The pressure and velocity non-equilibrium effects in two-phase flow regions are often not essential [Saurel 99a], so it can simply be assumed that the pressure and velocity relaxation parameters (see [Saurel 99a]) are infinite everywhere. The paper [Saurel 99a] gives a very detailed description of the infinite rate relaxation process. We follow their method in this section. In what follows we give a relatively simple explanation of the numerical approximation of the relaxation process. Note that the relaxation solver is considered after each time step. The velocity relaxation is processed at first. In fact, if the pressure relaxation is processed before the velocity one, the phase pressures become different again after the whole relaxation process. Note also that the method of pressure relaxation here presented is a simplified version of the one introduced in [Saurel 99a]. In fact, no Newton type iterative method is required to find the equilibrium pressure. A quadratic equation is proposed to be solved analytically for this purpose, which makes the relaxation procedures less time-consuming.

C.1 Instantaneous velocity relaxation

We denote the system primitive variables obtained at time t^n as

$$(\alpha^0,\ \mathbf{W}^0)_k^{\mathrm{T}} = (\alpha^0,\ \rho^0,\ \mathbf{v}^0,\ p^0)_k^{\mathrm{T}}. \tag{C.2}$$

After the velocity relaxation, they are denoted by

$$(\alpha,\ \mathbf{W})_k^{\mathrm{T}} = (\alpha,\ \rho,\ \mathbf{v},\ p)_k^{\mathrm{T}}. \tag{C.3}$$

In the velocity relaxation process, according to [Saurel 99a], it is assumed that the fluids are incompressible and act as rigid bodies. Since mass is conserved, there are obviously

$$\alpha_k = \alpha_k^0, \tag{C.4}$$

$$\rho_k = \rho_k^0. \tag{C.5}$$

The conservation of momentum gives

$$\sum_{k=1}^{2} \alpha_k \rho_k \mathbf{v}_k = \sum_{k=1}^{2} \alpha_k^0 \rho_k^0 \mathbf{v}_k^0. \tag{C.6}$$

Hence, the final velocity reads,

$$\mathbf{v}_k = \frac{\sum_{k=1}^{2} \alpha_k^0 \rho_k^0 \mathbf{v}_k^0}{\sum_{k=1}^{2} \alpha_k^0 \rho_k^0}. \tag{C.7}$$

It follows, from the conservation of total energy, that

$$\frac{\mathrm{d}\alpha_1 \rho_1 \left(\frac{\mathbf{v}_1^2}{2} + e_1 \right)}{\mathrm{d}t} = \mathbf{f}_{\text{int}} \cdot \mathbf{v}_{\text{int}}, \quad \frac{\mathrm{d}\alpha_2 \rho_2 \left(\frac{\mathbf{v}_2^2}{2} + e_2 \right)}{\mathrm{d}t} = -\mathbf{f}_{\text{int}} \cdot \mathbf{v}_{\text{int}}. \tag{C.8}$$

Here $\mathbf{f}_{\text{int}}$ is the interfacial force and $\mathbf{v}_{\text{int}}$ the interfacial velocity. In [Saurel 99a], it is modelled as

$$\mathbf{v}_{\text{int}} = \frac{\sum_{k=1}^{2} \alpha_k \rho_k \mathbf{v}_k}{\sum_{k=1}^{2} \alpha_k \rho_k}. \tag{C.9}$$

So the initial interfacial velocity is

$$\mathbf{v}_{\text{int}}^0 = \frac{\sum_{k=1}^{2} \alpha_k^0 \rho_k^0 \mathbf{v}_k^0}{\sum_{k=1}^{2} \alpha_k^0 \rho_k^0}. \tag{C.10}$$

From (C.7), the final interfacial velocity is given by

$$\mathbf{v}_{\text{int}}^{\mathbf{f}} = \mathbf{v}_{\text{int}}^0 = \frac{\sum_{k=1}^{2} \alpha_k^0 \rho_k^0 \mathbf{v}_k^0}{\sum_{k=1}^{2} \alpha_k^0 \rho_k^0}. \tag{C.11}$$

Approximating the equations (C.8) gives,

$$\begin{aligned}\alpha_1\rho_1(\frac{\mathbf{v}_1^2}{2}+e_1)-\alpha_1^0\rho_1^0(\frac{(\mathbf{v}_1^0)^2}{2}+e_1^0) &= \int_t \mathbf{f}_{\text{int}}\cdot\mathbf{v}_{\text{int}}\,\mathrm{d}t\\ &\doteq \overline{\mathbf{v}_{\text{int}}}\cdot\int_t \mathbf{f}_{\text{int}}\,\mathrm{d}t\\ &= \overline{\mathbf{v}_{\text{int}}}\cdot\left(\alpha_1\rho_1\mathbf{v}_1-\alpha_1^0\rho_1^0\mathbf{v}_1^0\right),\end{aligned} \tag{C.12}$$

$$\begin{aligned}\alpha_2\rho_2(\frac{\mathbf{v}_2^2}{2}+e_2)-\alpha_2^0\rho_2^0(\frac{(\mathbf{v}_2^0)^2}{2}+e_2^0) &= -\int_t \mathbf{f}_{\text{int}}\cdot\mathbf{v}_{\text{int}}\,\mathrm{d}t\\ &\doteq \overline{\mathbf{v}_{\text{int}}}\cdot\left(-\int_t \mathbf{f}_{\text{int}}\,\mathrm{d}t\right)\\ &= \overline{\mathbf{v}_{\text{int}}}\cdot\left(\alpha_2\rho_2\mathbf{v}_2-\alpha_2^0\rho_2^0\mathbf{v}_2^0\right).\end{aligned} \tag{C.13}$$

Approximating the average interfacial velocity as

$$\overline{\mathbf{v}_{\text{int}}}=\frac{\mathbf{v}_{\text{int}}^0+\mathbf{v}_{\text{int}}^{\mathbf{f}}}{2}=\mathbf{v}_k=\frac{\sum_{k=1}^{2}\alpha_k^0\rho_k^0\mathbf{v}_k^0}{\sum_{k=1}^{2}\alpha_k^0\rho_k^0}, \tag{C.14}$$

gives the results for e_k as follows:

$$e_k=e_k^0+\frac{1}{2}\left(\mathbf{v}_k-\mathbf{v}_k^0\right)^2. \tag{C.15}$$

Taking account of the corresponding EOS, the final pressure is given by

$$p_k=\left(\gamma_k-1\right)\rho_k e_k-\gamma_k p_{\infty,k}. \tag{C.16}$$

C.2 Instantaneous pressure relaxation

The primitive variables after velocity relaxation are denoted as

$$(\alpha^{0'},\ \mathbf{W}^{0'})_k^{\mathrm{T}}=(\alpha^{0'},\ \rho^{0'},\ \mathbf{v}^{0'},\ p^{0'})_k^{\mathrm{T}}. \tag{C.17}$$

After the pressure relaxation, they are denoted by

$$(\alpha,\ \mathbf{W})_k^{\mathrm{T}}=(\alpha,\ \rho,\ \mathbf{v},\ p)_k^{\mathrm{T}}. \tag{C.18}$$

Considering the computational cell as a closed system, and supposing the pressure relaxation process is an adiabatic process of thermodynamics, there is then

$$\mathbf{v}_k = \mathbf{v}_k^{0'}. \tag{C.19}$$

The mass conservation gives

$$\alpha_k \rho_k = \alpha_k^{0'} \rho_k^{0'}. \tag{C.20}$$

Thus,

$$\rho_k = \frac{\alpha_k^{0'} \rho_k^{0'}}{\alpha_k}. \tag{C.21}$$

The first law of thermodynamics implies

$$\mathrm{d}\left(\alpha_k \rho_k e_k\right) = -p_{\text{int}}\, \mathrm{d}\alpha_k, \tag{C.22}$$

where p_{int} is the interfacial pressure that has to be modelled. One restriction for modelling is that it should be equal for both phases, otherwise the energy is no longer conserved. Several options exist in the literature. The one in [Saurel 99a] is used in this work:

$$p_{\text{int}} = \sum_{k=1}^{2} \alpha_k p_k. \tag{C.23}$$

Approximately integrating (C.22) gives

$$\alpha_k \rho_k e_k - \alpha_k^{0'} \rho_k^{0'} e_k^{0'} = -\int_\alpha p_{\text{int}}\, \mathrm{d}\alpha_k \doteq -\overline{p_{\text{int}}} \int_\alpha \mathrm{d}\alpha_k = -\overline{p_{\text{int}}}(\alpha_k - \alpha_k^{0'}). \tag{C.24}$$

Rearranging the equation gives the value of internal energy as below,

$$e_k = e_k^{0'} - \frac{\overline{p_{\text{int}}}}{\alpha_k^{0'} \rho_k^{0'}} \left(\alpha_k - \alpha_k^{0'}\right). \tag{C.25}$$

The pressure average[1] can be simply set as

$$\overline{p_{\text{int}}} = \frac{p_{\text{int}}^{0'} + p_{\text{int}}}{2}. \tag{C.26}$$

The EOS reads at the equilibrium state,

$$p_{\text{int}} = p_k = \left(\gamma_k - 1\right) \rho_k e_k - \gamma_k p_{\infty,k}. \tag{C.27}$$

---

[1] According to [Saurel 09], other possible estimates can be $\overline{p_{\text{int}}} = p_{\text{int}}^{0'}$ or $\overline{p_{\text{int}}} = p_{\text{int}}$ (the initial or relaxed interfacial pressure, respectively). The resulting difference in practical computations is negligible.

From equations (C.21), (C.25), (C.26) and (C.27), one can find the relation between the pressure and the volume fraction as follows,

$$\begin{aligned} p_k(\alpha_k) &= \frac{\alpha_k^{0'}\rho_k^{0'}e_k^{0'} - \dfrac{1}{2}(\alpha_k - \alpha_k^{0'})p_{\text{int}}^{0'} - \dfrac{\alpha_k\gamma_k p_{\infty,k}}{\gamma_k - 1}}{\dfrac{\alpha_k}{\gamma_k - 1} + \dfrac{1}{2}(\alpha_k - \alpha_k^{0'})} \\ &= \frac{\alpha_k^{0'}p_k^{0'} - (\alpha_k - \alpha_k^{0'})\left(\gamma_k p_{\infty,k} + \dfrac{\gamma_k - 1}{2}p_{\text{int}}^{0'}\right)}{\alpha_k + \dfrac{\gamma_k - 1}{2}(\alpha_k - \alpha_k^{0'})}. \end{aligned} \tag{C.28}$$

The remaining task now is to find α_1 satisfying the following equation,

$$p_1(\alpha_1) = p_2(1 - \alpha_1). \tag{C.29}$$

The equation (C.29) can be resolved analytically. In fact, it is equivalent to the following quadratic equation

$$a(\alpha_1 - \alpha_1^{0'})^2 + b(\alpha_1 - \alpha_1^{0'}) + c = 0. \tag{C.30}$$

The equation's coefficients in (C.30) are given as below,

$$a = B_1\frac{\gamma_2 + 1}{2} - B_2\frac{\gamma_1 + 1}{2}, \tag{C.31}$$

$$b = -\left(B_1(1 - \alpha_1^{0'}) + B_2\alpha_1^{0'} + A_1\frac{\gamma_2 + 1}{2} + A_2\frac{\gamma_1 + 1}{2}\right), \tag{C.32}$$

$$c = \alpha_1^{0'}(1 - \alpha_1^{0'})(p_1^{0'} - p_2^{0'}), \tag{C.33}$$

with the constants $A_1,\ A_2,\ B_1,\ B_2$ defined as

$$A_1 = \alpha_1^{0'}p_1^{0'}, \tag{C.34}$$

$$A_2 = (1 - \alpha_1^{0'})p_2^{0'}, \tag{C.35}$$

$$B_1 = \gamma_1 p_{\infty,1} + \frac{\gamma_1 - 1}{2}p_{\text{int}}^{0'}, \tag{C.36}$$

$$B_2 = \gamma_2 p_{\infty,2} + \frac{\gamma_2 - 1}{2}p_{\text{int}}^{0'}. \tag{C.37}$$

When $a \neq 0$, one can easily find the correct solution of (C.30) for pressure relaxation process:

$$\alpha_1 = \alpha_1^{0'} + \frac{-b - \sqrt{b^2 - 4ac}}{2a}.$$

Thus, the pressure of each phase is given by (C.28),

$$p_1 = p_1(\alpha_1),\ p_2 = p_2(1 - \alpha_1). \tag{C.38}$$

Until here, all primitive variables have been determined.

C.3 Numerical results with relaxation

Following the Section 2.8.1, this part is devoted to the numerical results of relaxation solver for liquid-gas non-reactive interface problem. The numerical results of Section 2.8.1, in spite of the success of no computational failure, present negative pressures, which can create serious problems in many situations. Thus, pressure and velocity relaxation procedures are employed here with the aim of improving the scheme, by adding an internal phase interaction within a computational cell.

Using the state-of-the-art second-order DEM approach with relaxations, Fig. C.1 and Fig. C.2 show the results of individual and mixture phase variables, respectively. As expected, liquid phase and gas phase have a unique pressure and velocity, which prevents the negative pressures. This results in that the second-order method is now also more accurate on pressure profile than the first-order calculation, compared to the results shown in Section 2.8.1 without relaxation. An extra benefit of the relaxation procedures is that the Mach number is better resolved than the DEM/RDEM without relaxation.

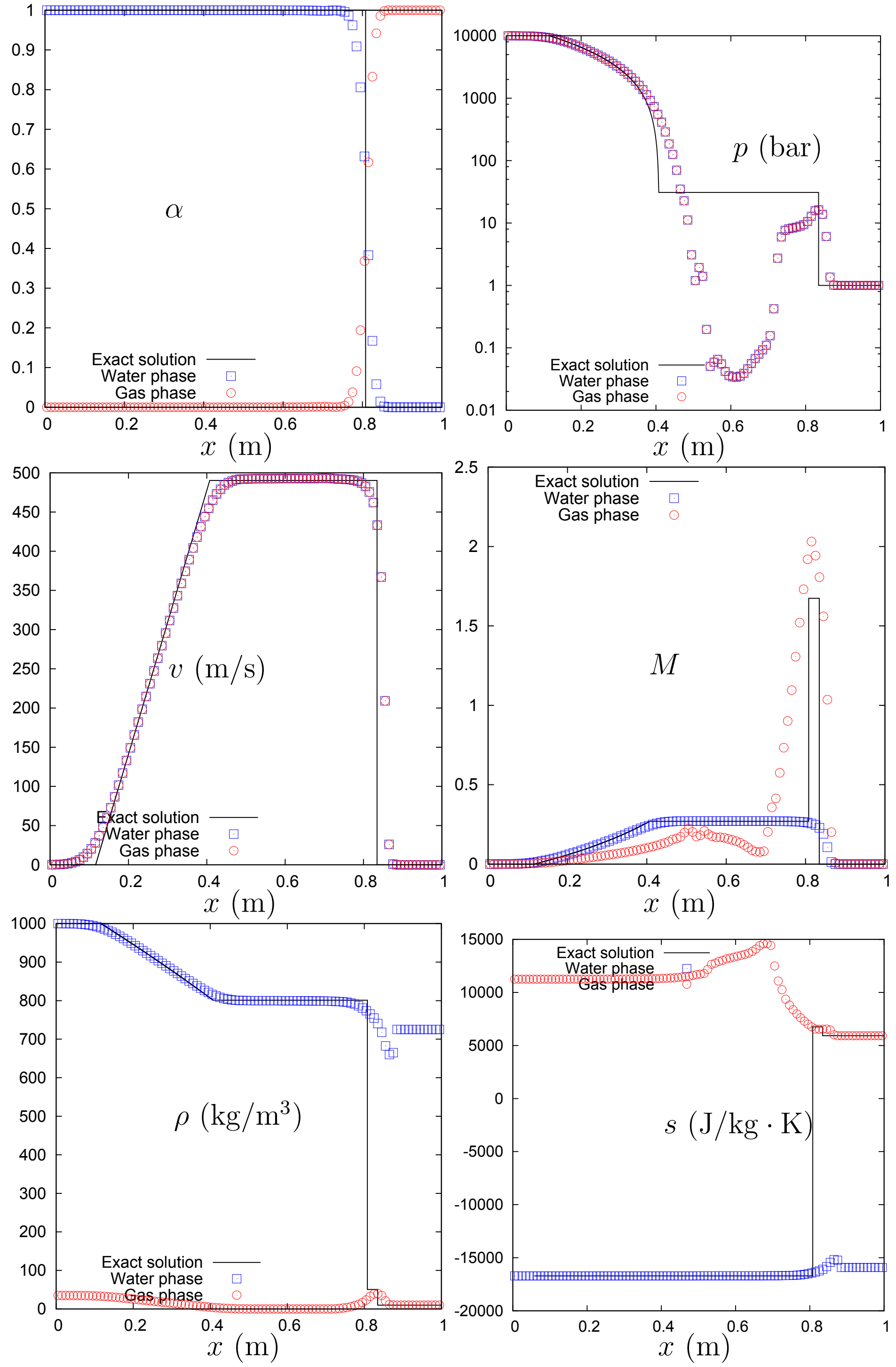

Figure C.1: Second-order DEM method with minmod limiter is used for water gas shock tube problem with interface separating nearly pure phases. Relaxations are used. A 100 cells uniform mesh is used. CFL $= 0.9$. Time $t = 220$ μs. Individual phase variables are plotted.

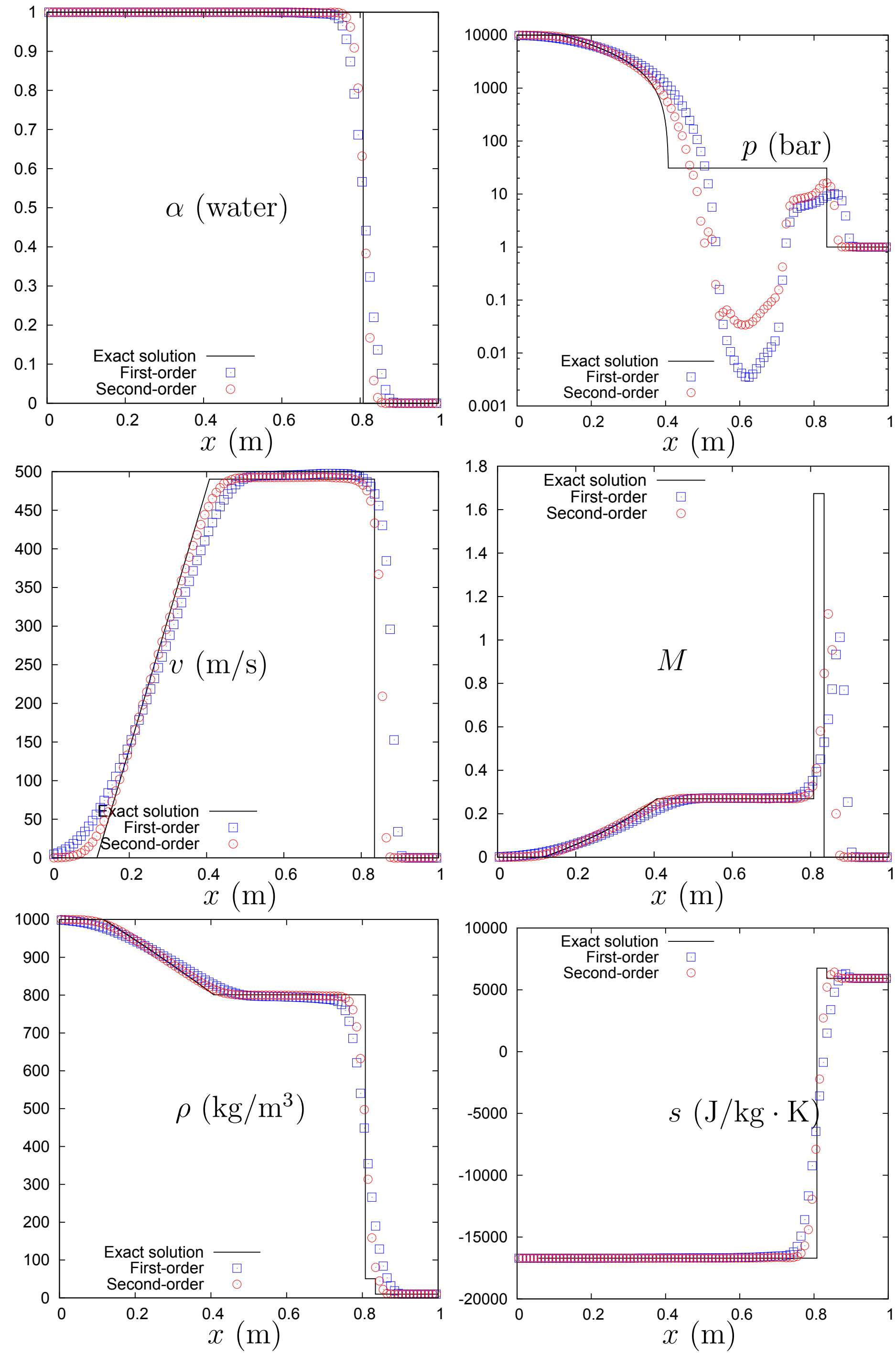

Figure C.2: Second-order DEM method with minmod limiter and first-order method are compared for water gas shock tube problem with interface separating nearly pure phases. Relaxations are used. A 100 cells uniform mesh is used. CFL = 0.9. Time $t = 220\ \mu$s. Phase mixture variables are plotted.

Bibliography

[Abgrall 96] R. Abgrall. *How to Prevent Pressure Oscillations in Multicomponent Flow Calculations: A Quasi Conservative Approach.* Journal of Computational Physics, vol. 125, no. 1, pages 150–160, April 1996.

[Abgrall 01] R. Abgrall & S. Karni. *Computations of Compressible Multifluids.* Journal of Computational Physics, vol. 169, no. 2, pages 594–623, May 2001.

[Abgrall 03] R. Abgrall & R. Saurel. *Discrete equations for physical and numerical compressible multiphase mixtures.* Journal of Computational Physics, vol. 186, pages 361–396, 2003.

[Banks 07] J.W. Banks, D.W. Schwendeman, a.K. Kapila & W.D. Henshaw. *A high-resolution Godunov method for compressible multi-material flow on overlapping grids.* Journal of Computational Physics, vol. 223, no. 1, pages 262–297, April 2007.

[Barth 89] T. J. Barth & D. C. Jespersen. *The design and application of upwind schemes on unstructured meshes.* AIAA paper 89-0366, 1989.

[Beccantini 00] A. Beccantini. *Upwind Splitting Schemes for Ideal Gases Mixtures with Temperature-Dependent Specific Heat Capacities.* PhD thesis, Université d'Evry, 2000.

[Beccantini 10a] A. Beccantini & E. Studer. *The reactive Riemann problem for thermally perfect gases at all combustion regimes.* International Journal for Numerical Methods in Fluids, vol. 64, pages 269–313, 2010.

[Beccantini 10b] A. Beccantini & K. Tang. *The Reactive Discrete Equations Method for the (reactive) Euler Equations: the minmod reconstruction versus the antidiffusive approach.* Technical report, CEA Saclay DM2S/SFME/LTMF/RT/10-007/A, 2010.

[Ben-Artzi 84] M. Ben-Artzi & J. Falcovitz. *A second-order Godunov-type scheme for compressible fluid dynamics.* Journal of Computational Physics, vol. 55, no. 1, pages 1–32, 1984.

[Bestion 11] D. Bestion. *Applicability of two-phase CFD to nuclear reactor thermalhydraulics and elaboration of Best Practice Guidelines.* Nuclear Engineering and Design, pages 1–11, November 2011.

[Bielert 01] U. Bielert, W. Breitung, A. Kotchourko, P. Royl, W. Scholtyssek, A. Veser, A. Beccantini, F. Dabbene, H. Paillere, E. Studer, T. Huld, H. Wilkening, B. Edlinger, C. Poruba & M. Mohaved. *Multi-dimensional simulation of hydrogen distribution and turbulent combustion in severe accidents.* Nuclear Engineering and Design, vol. 209, pages 165–172, November 2001.

[Buyevich 71] Y. A. Buyevich. *Statistical Hydrodynamics of Disperse Systems, Physical Background and General Equations.* Journal of Fluid Mechanics, vol. 49, pages 489–507, 1971.

[Chang 07] C.-H. Chang & M.-S. Liou. *A robust and accurate approach to computing compressible multiphase flow: Stratified flow model and AUSM+-up scheme.* Journal of Computational Physics, vol. 225, no. 1, pages 840–873, 2007.

[Chertock 08] A. Chertock, S. Karni & A. Kurganov. *Interface tracking method for compressible multifluids.* ESAIM : Mathematical Modelling and Numerical Analysis, vol. 42, pages 991–1019, 2008.

[Ciccarelli 08] G. Ciccarelli & S. Dorofeev. *Flame acceleration and transition to detonation in ducts.* Progress in Energy and Combustion Science, vol. 34, no. 4, pages 499–550, August 2008.

[Darwish 03] M. S. Darwish & F. Moukalled. *TVD schemes for unstructured grids.* International Journal of Heat and Mass Transfer, vol. 46, pages 599–611, 2003.

[Delhaye 68] J.-M. Delhaye. *Équations fondamentales des écoulements diphasiques.* Technical report, Commissariat à l'énergie atomique, CEA-R-3429, 1968.

[Després 02] B. Després & F. Lagoutière. *Contact Discontinuity Capturing Schemes for Linear Advection and Compressible Gas Dynamics.* Journal of Scientific Computing, vol. 16, no. 4, pages 479–524, 2002.

[Drew 98] D. A. Drew & S. L. Passman. Theory of Multicomponent Fluids, Applied Mathematical Sciences, Vol. 135. Springer, New York, 1998.

[Efimenko 01] A.A. Efimenko & S.B. Dorofeev. *CREBCOM code system for description of gaseous combustion.* Journal of Loss Prevention in the Process Industries, vol. 14, no. 6, pages 575–581, November 2001.

[Farhat 08] C. Farhat, A. Rallu & S. Shankaran. *A higher-order generalized ghost fluid method for the poor for the three-dimensional two-phase flow computation of underwater implosions.* Journal of Computational Physics, vol. 227, no. 16, pages 7674–7700, 2008.

[García 10] J. García, D. Baraldi, E. Gallego, A. Beccantini, A. Crespo, O.R. Hansen, S. Hø iset, A. Kotchourko, D. Makarov & E. Migoya. *An intercomparison exercise on the capabilities of CFD models to reproduce a large-scale hydrogen deflagration in open atmosphere.* International Journal of Hydrogen Energy, vol. 35, no. 9, pages 4435–4444, May 2010.

[Godlewski 96] E. Godlewski & P.-A. Raviart. Numerical Approximation of Hyperbolic Systems of Conservation Laws. Springer, 1996.

[Godunov 59] S. K. Godunov. *A Difference Scheme for Numerical Solution of Discontinuous Solution of Hydrodynamic Equations.* Math. Sbornik, vol. 47, pages 271–306, 1959.

[Haas 87] J.-F. Haas & B. Sturtevant. *Interaction of weak shock waves with cylindrical and spherical gas inhomogeneities.* Journal of Fluid Mechanics, vol. 181, pages 41–76, 1987.

[Harlow 71] F. Harlow & A. Amsden. *Fluid dynamics.* Technical report, Los Alamos National Laboratory, LA-4700, 1971.

[Ishii 75] M. Ishii. Thermo-fluid Dynamic Theory of Two-phase Flow. Eyrolles, Paris, 1975.

[Ivings 98] M. J. Ivings, D. M. Causon & E. F. Toro. *On Riemann solvers for compressible liquids.* International Journal for Numerical Methods in Fluids, vol. 28, no. 3, pages 395–418, September 1998.

[Jameson 95] A. Jameson. *Analysis and Design of Numerical Schemes for Gas Dynamics, 1: Artificial Diffusion, Upwind Biasing, Limiters and Their Effect on Accuracy and Multigrid Convergence.* International

Journal of Computational Fluid Dynamics, vol. 4, no. 3, pages 171–218, 1995.

[Jameson 01] A. Jameson. *A perspective on computational algorithms for aerodynamic analysis and design.* Progress in Aerospace Sciences, vol. 37, pages 197–243, 2001.

[Kapila 01] A. K. Kapila, R. Menikoff, J. B. Bdzil, S. F. Son & D. S. Stewart. *Two-phase modeling of deflagration-to-detonation transition in granular materials: Reduced equations.* Physics of Fluids, vol. 13, no. 10, page 3002, 2001.

[Kokh 10] S. Kokh & F. Lagoutière. *An anti-diffusive numerical scheme for the simulation of interfaces between compressible fluids by means of a five-equation model.* Journal of Computational Physics, vol. 229, no. 8, pages 2773–2809, April 2010.

[Kolgan 72] V. P. Kolgan. *Numerical schemes for discontinuous problems of gas dynamics based on minimization of the solution gradient.* Technical report, Uch. Zap.TsAGI, 1972.

[Kreeft 10] Jasper J. Kreeft & Barry Koren. *A new formulation of Kapilas five-equation model for compressible two-fluid flow, and its numerical treatment.* Journal of Computational Physics, vol. 229, no. 18, pages 6220–6242, September 2010.

[Kudriakov 07] S. Kudriakov, F. Dabbene, E. Studer, A. Beccantini, J. Magnaud, H. Paillere, A. Bentaib, A. Bleyer, J. Malet & E. Porcheron. *The TONUS CFD code for hydrogen risk analysis: Physical models, numerical schemes and validation matrix.* Nuclear Engineering and Design, vol. 238, pages 551–565, June 2007.

[Kuhl 73] A. L. Kuhl, M. M. Kamel & A. K. Oppenheim. *Pressure waves generated by steady flames.* Symposium (International) on Combustion, vol. 14, no. 1, pages 1201–1215, 1973.

[Lagoutière 00] F. Lagoutière. *Modélisation mathématique et résolution numérique de problèmes de fluides compressibles à plusieurs constituants.* PhD thesis, Université Pierre et Marie CURIE, 2000.

[Le Métayer 03] O. Le Métayer. *Modélisation et résolution de la propagation de fronts perméables. Application aux fronts d'évaporation et de détonation.* PhD thesis, Aix Marseille 1, 2003.

[Le Métayer 05] O. Le Métayer, J. Massoni & R. Saurel. *Modelling evaporation fronts with reactive Riemann solvers.* Journal of Computational Physics, vol. 205, pages 567–610, 2005.

[Lennon 94] F. Lennon. *Shock Wave Propagation in Water.* PhD thesis, Manchester Metropolitan University, 1994.

[LeVeque 85] R. J. LeVeque. *A Large Time Step Generalization of Godunov's Method for Systems of Conservation Laws.* SIAM Journal on Numerical Analysis, vol. 22, no. 6, pages 1051–1073, 1985.

[LeVeque 02] R. J. LeVeque. Finite Volume Methods for Hyperbolic Problems. Cambridge University Press, 2002.

[Murrone 05] A. Murrone & H. Guillard. *A five equation reduced model for compressible two phase flow problems.* Journal of Computational Physics, vol. 202, pages 664–698, 2005.

[Nigmatulin 79] R.I. Nigmatulin. *Spatial averaging in the mechanics of heterogeneous and dispersed systems.* International Journal of Multiphase Flow, vol. 5, no. 5, pages 353–385, 1979.

[Nourgaliev 06] R.R. Nourgaliev, T.N. Dinh & T.G. Theofanous. *Adaptive characteristics-based matching for compressible multifluid dynamics.* Journal of Computational Physics, vol. 213, no. 2, pages 500–529, April 2006.

[Perrier 07] V. Perrier. *Modélisation et simulation d'écoulements multiphasiques compressibles avec ou sans changement de phase. Application à l'interaction laser-plasma.* PhD thesis, Université Bordeaux 1, 2007.

[Petitpas 07] F. Petitpas, E. Franquet, R. Saurel & O. Le Métayer. *A relaxation-projection method for compressible flows. Part II: Artificial heat exchanges for multiphase shocks.* Journal of Computational Physics, vol. 225, no. 2, pages 2214–2248, August 2007.

[Quirk 96] J. J. Quirk & S. Karni. *On the dynamics of a shock-bubble interaction.* Journal of Fluid Mechanics, vol. 318, pages 129–163, 1996.

[Saurel 99a] R. Saurel & R. Abgrall. *A multiphase Godunov method for compressible multifluid and multiphase flows.* Journal of Computational Physics, vol. 150, pages 425–467, 1999.

[Saurel 99b] R. Saurel & R. Abgrall. *A Simple Method for Compressible Multifluid Flows.* SIAM Journal on Scientific Computing, vol. 21, no. 3, page 1115, 1999.

[Saurel 01] R. Saurel & O. Le Métayer. *A multiphase model for compressible flows with interfaces, shocks, detonation waves and cavitation.* Journal of Fluid Mechanics, vol. 431, pages 239–271, March 2001.

[Saurel 08] R. Saurel, F. Petitpas & R. Abgrall. *Modelling phase transition in metastable liquids: application to cavitating and flashing flows.* Journal of Fluid Mechanics, vol. 607, pages 313–350, June 2008.

[Saurel 09] R. Saurel, F. Petitpas & R. Berry. *Simple and efficient relaxation methods for interfaces separating compressible fluids, cavitating flows and shocks in multiphase mixtures.* Journal of Computational Physics, vol. 228, no. 5, pages 1678–1712, 2009.

[Shyue 06] K.-M. Shyue. *A wave-propagation based volume tracking method for compressible multicomponent flow in two space dimensions.* Journal of Computational Physics, vol. 215, pages 219–244, 2006.

[Strang 68] G. Strang. *On the construction and comparison of difference schemes.* SIAM Journal on Numerical Analysis, vol. 5, no. 3, pages 506–517, 1968.

[Stull 71] D. R. Stull & H. Prophet. JANAF thermochemical tables. U.S. Dept. of Commerce, National Bureau of Standards, Washington, D.C., second edition, 1971.

[Tang 11a] K. Tang. *Discrete Equations Method for 1D stiffened gas flows I: Interface problems.* Technical report, CEA Saclay DM2S/STMF/LATF/RT/11-002/A, 2011.

[Tang 11b] K. Tang. *Discrete Equations Method for 1D stiffened gas flows II: Multiphase mixtures.* Technical report, CEA Saclay DM2S/STMF/LATF/RT/11-003/A, 2011.

[Tang 12] K. Tang, A. Beccantini & C. Corre. *Combining Discrete Equations Method and upwind downwind-controlled splitting for non-reacting and reacting two-fluid computations.* In Seventh International Conference on Computational Fluid Dynamics (ICCFD7), Big Island, Hawaii, July 9-13, 2012.

[Tokareva 10] S. A. Tokareva & E. F. Toro. *HLLC-type Riemann solver for the Baer-Nunziato equations of compressible two-phase flow.* Journal of Computational Physics, vol. 229, no. 10, pages 3573–3604, May 2010.

[Toro 97] E. F. Toro. Riemann Solvers and Numerical Methods for Fluid Dynamics: A Practical Introduction. Springer-Verlag, 1997.

[Yadigaroglu 05] G. Yadigaroglu. *Computational Fluid Dynamics for nuclear applications: from CFD to multi-scale CMFD.* Nuclear Engineering and Design, vol. 235, no. 2-4, pages 153–164, February 2005.

[Zein 10] A. Zein, M. Hantke & G. Warnecke. *Modeling phase transition for compressible two-phase flows applied to metastable liquids.* Journal of Computational Physics, vol. 229, no. 8, pages 2964–2998, April 2010.